



MRI IMAGE BASED MEASUREMENT, MODELLING
AND DIAGNOSTIC INTERPRETATION OF PRESSURE
AND FLOW IN THE PULMONARY ARTERIES:
APPLICATIONS IN PULMONARY HYPERTENSION

Angela Lungu

School of Medicine and Biomedical Sciences
Department of Cardiovascular Science
Medical Physics Group

Submitted for the degree of PhD

Submission Date
October 2015

ABSTRACT

Pulmonary hypertension (PH) is a clinical condition characterised by an increased mean pulmonary arterial pressure (mPAP) of over 25 mmHg measured, at rest, by right heart catheterisation (RHC). RHC is currently considered the gold standard for diagnosis, follow-up and measurement of response to treatment. Although the severe complications and mortality risk associated with the invasive procedure are reduced when it is performed in a specialist centre, finding non-invasive PH diagnosis methods is highly desirable.

Non-invasive, non-ionising imaging techniques, based on magnetic resonance imaging (MRI) and on echocardiography, have been integrated into the clinical routine as means for PH assessment. Although the imaging techniques can provide valuable information supporting the PH diagnosis, accurately identifying patients with PH based upon images alone remains challenging. Computationally based models can bring additional insights into the haemodynamic changes occurring under the manifestation of PH.

The primary hypothesis of this thesis is that the physiological status of the pulmonary circulation can be inferred using solely non-invasive flow and anatomy measurements of the pulmonary arteries, measured by MRI and interpreted by 0D and 1D mathematical models.

The aim was to implement a series of simple mathematical models, taking the inputs from MRI measurements, and to evaluate their potential to support the non-invasive diagnosis and monitoring of PH. The principal objective was to develop a tool that can readily be translated into the clinic, requiring minimum operator input and time and returning meaningful and accurate results.

Two mathematical models, a 3 element Windkessel model and a 1D model of an axisymmetric straight elastic tube for wave reflections were implemented and clinically tested on a cohort of healthy volunteers and of patients who were clinically investigated for PH. The latter group contained some who were normotensive, and those with PH were stratified according to severity. A 2D semi-automatic image segmentation workflow was developed to provide patient specific, simultaneous flow and anatomy measurements of the main pulmonary artery (MPA) as input to the mathematical models.

Several diagnostic indices are proposed, and of these distal resistance (R_d), total vascular compliance (C) and the ratio of reflected to total wave power (W_b/W_{tot}) showed statistically significant differences between the analysed groups, with good accuracy in PH classification.

A machine learning classifier using the derived computational metrics and several other PH metrics computed from MRI images of the MPA and of the right ventricle alone, proposed in the literature as PH surrogate markers, was trained and validated with leave-one-out cross-validation to improve the accuracy of non-invasive PH diagnosis. The results accurately classified 92% of the patients, and furthermore the misclassified 8% were patients with mPAP close to the 25 mmHg (at RHC) threshold (within the range of clinical uncertainty).

The individual analysis of all PH surrogate markers emphasised that wave reflection quantification, although with lower diagnosis accuracy (75%) than the machine learning model embedding multiple markers, has the potential to distinguish between multiple PH categories.

A finite element method (FEM) based model to solve a 1D pulmonary arterial tree linear system, has been implemented to contribute further to the accurate, non-invasive assessment of pulmonary hypertension.

The diagnostic protocols, including the analysis work flow, developed and reported in this PhD thesis can be integrated into the clinical process, with the potential to reduce the need for RHC by maximising the use of available MRI data.

ACKNOWLEDGEMENTS

This thesis would not have been completed without the invaluable academic, educational, organisational and psychological support of my supervisors, project's collaborators, colleagues, friends and family, to whom I would like to thank:

I would like to express in debt gratitude to my supervisors, Prof. Rod Hose and Prof. Jim Wild for their irreplaceable guidance, help and dedication throughout my entire PhD. To Prof. Hose, for the long and in depth discussions on computational modelling, for his patience for me to solve trivial problems which in the end were 'just implementation problems' and his valuable mentorship. To Prof. Wild for his encouragements and support on the MR unit, critical to the success of this project.

I would like to thank Dr. Andy Swift for his help and guidance in interpreting the clinical data, to Dr. David Kiely for further, in depth clinical insights and enthusiasm on *in silico* modelling and to Dave Capener for supporting the process of image acquisition.

My acknowledgements are extended to all Medical Physics staff members and students, who are still part of the group and to those who left, for making me feel welcomed and appreciated. To Prof. Pat Lawford, the group's leader, for her genuine care and attention she showed to me since joining the group, to Steve Parkin, for the administrative and technical support in the office, to Iwona and her 'my Blazej', for a bowl of warm soup and an open door at any time and to Claudia for walking in my shoes during thesis writing.

I would like to address a special thank you to Prof. Dan Rafiroiu and Conf. Simona Vlad who believed in me and encouraged me to start a PhD in this group.

I would like to thank to all my friends and family who regardless of understanding or not what my PhD is about, were supportive and encouraged me to carry on at difficult times.

My final thoughts are going to my closest family members who had the strongest taste of what being away meant. To my mother, for all her supportive, loving and caring words which only a mother could give. To my loving husband, Radu, for always being there, listening to my complaints and sharing my successful moments, for his confidence, encouragements and interest for my research – thank you for taking this journey alongside me.

CONTENTS

ABSTRACT	I
ACKNOWLEDGEMENTS	III
LIST OF FIGURES	VII
LIST OF TABLES.....	XI
1 INTRODUCTION & LITERATURE REVIEW.....	1
INTRODUCTION AND MOTIVATION	1
PULMONARY STRUCTURE	2
PULMONARY HYPERTENSION	3
1.1.1 <i>Definition, classification, diagnosis</i>	3
1.1.2 <i>Alternative, non-invasive diagnosis methods in PH</i>	5
1.1.2.1 The direct approach.....	6
1.1.2.2 The model-based approach	7
MATHEMATICAL MODELS OF THE PULMONARY CIRCULATION	7
1.1.3 <i>0D models- underlying concepts</i>	8
1.1.4 <i>One dimensional distributed models</i>	13
1.1.5 <i>Examples of pulmonary circulation 0D and 1D models</i>	15
THESIS OUTLINE	20
2 FROM MRI IMAGES TO AREA, FLOW AND PRESSURE WAVEFORMS.....	22
MOTIVATION.....	22
PULMONARY ARTERY MR IMAGE ACQUISITION	23
2.1.1 <i>Pulse sequences</i>	23
2.1.2 <i>Sequences parameters</i>	26
PROCESSING OF MR IMAGES TO DERIVE AREA, FLOW AND PRESSURE WAVEFORMS	27
2.1.3 <i>Image segmentation</i>	27
2.1.3.1 Manual segmentation.....	30
2.1.3.2 Semi-automatic segmentation.....	31
2.1.4 <i>Area computation</i>	37
2.1.5 <i>Flow computation</i>	38
2.1.6 <i>From area to pressure waveforms</i>	38
RESULTS AND DISCUSSION	44
2.1.7 <i>Image segmentation</i>	44
2.1.7.1 Segmentation efficiency	45

2.1.7.2	Segmentation reproducibility	47
2.1.8	<i>Influence of area segmentation of derived pressure waveforms</i>	62
SUMMARY AND CONCLUSIONS		64
3	OD AND 1D MODEL OF A THIN WALLED STRAIGHT ELASTIC TUBE FOR PULMONARY	
	HYPERTENSION ASSESSMENT	63
	MOTIVATION.....	63
	MATERIALS AND METHODS	65
3.1.1	<i>Subjects</i>	65
3.1.2	<i>MRI images</i>	65
3.1.3	<i>OD Windkessel model</i>	66
3.1.3.1	Optimisation problem for computing Windkessel electrical parameters	66
3.1.3.2	Searching algorithm	67
3.1.3.3	Defining the cost function.....	68
3.1.3.4	Analytical solution for the Windkessel inlet pressure.....	69
3.1.3.5	Four element Windkessel model	72
3.1.4	<i>1D model of a straight elastic tube</i>	73
3.1.5	<i>Coupled 1D and OD models</i>	76
3.1.6	<i>Statistical analysis of the results</i>	79
	RESULTS AND DISCUSSION	80
3.1.7	<i>OD model</i>	81
3.1.7.1	Results.....	81
3.1.7.2	Discussion	90
3.1.8	<i>1D model</i>	96
3.1.8.1	Results.....	96
3.1.8.2	Discussion	98
3.1.9	<i>Coupled 1D and OD models</i>	99
3.1.9.1	Results and discussions.....	99
3.1.10	<i>OD and 1D models results' influence factors</i>	101
3.1.10.1	Influence of choosing the pressure model.....	101
3.1.10.2	Inter and intra operator variability	104
3.1.10.3	PC vs bSSPF parameters.....	108
	SUMMARY AND CONCLUSIONS	110
4	NON-INVASIVE PH DIAGNOSIS USING COMPUTATIONAL AND IMAGE BASED INDICES	
	INTEGRATED INTO CLASSIFICATION ALGORITHMS	112
	MOTIVATION.....	112
	MATERIALS AND METHODS	113
4.1.1	<i>Subjects</i>	113
4.1.2	<i>Right heart catheterisation</i>	114

4.1.3	<i>MRI images</i>	114
4.1.4	<i>Diagnosis metrics derivation</i>	115
4.1.4.1	Physiology-based computational modelling from image data.....	115
4.1.4.2	2D MPA metrics	115
4.1.4.3	CMR metrics.....	116
4.1.5	<i>Clinical diagnosis test</i>	117
4.1.5.1	Individual metric classifier	117
4.1.5.2	Multiple metrics classification	118
4.1.6	<i>Statistical analysis of the results</i>	121
RESULTS	122
4.1.7	<i>Demographics and non-invasive metrics group values</i>	122
4.1.8	<i>Performance of individual parameters</i>	124
4.1.9	<i>Random forest classifier performance</i>	126
DISCUSSION	130
4.1.9.1	Individual metrics	130
4.1.9.2	Machine learning classifier	131
SUMMARY AND CONCLUSIONS	131
5	FINITE ELEMENT MODEL FOR A 1D BRANCHING TREE OF PULMONARY ARTERIAL CIRCULATION	132
	MOTIVATION.....	132
	DEFINING THE PULMONARY ARTERIAL TREE	134
	LINEARISED PRESSURE AND FLOW SOLUTION FOR A SINGLE 1D ELEMENT	136
	PRESSURE AND FLOW SOLUTIONS FOR A BRANCHING TREE ENSEMBLE	140
5.1.1	<i>Recursive impedance method</i>	141
5.1.2	<i>Direct method</i>	144
5.1.2.1	Direct method solver based on element's degrees of freedom	145
5.1.2.2	Direct method solver based on nodal degrees of freedom	150
RESULTS AND DISCUSSION	159
SUMMARY AND CONCLUSIONS	163
6	CONCLUSIONS, LIMITATIONS AND FUTURE WORK	166
	CONCLUSIONS AND LIMITATIONS.....	167
	FUTURE WORK	171
	FINAL THOUGHTS.....	172
REFERENCES	173
APPENDIX	182
	PUBLICATIONS LIST	182
	THIRD PARTY COPYRIGHT PERMISSIONS	184

List of Figures

FIGURE 1.1 PULMONARY HYPERTENSION GROUPS AND SUB-GROUPS CLASSIFICATION [9]	4
FIGURE 1.2 OD (WINDKESSEL) MODELS IN CONFIGURATION OF 2 (A), 3 (B) AND 4 (C-D) ELECTRICAL PARAMETERS	9
FIGURE 1.3 THE FOUR NETWORK CONFIGURATION FOR COMPARTMENTAL MODELS, DESCRIBE BY FORMAGGIA [61]	13
FIGURE 2.1 PHASE CONTRAST (PC) SEQUENCE DIAGRAM BASED ON A SPOILED GRADIENT ECHO SEQUENCE (SPGR)	24
FIGURE 2.2 TYPICAL PC MAGNITUDE AND BSSFP IMAGES OF THE MPA, DURING THE PEAK SYSTOLE AND LATE DIASTOLE	25
FIGURE 2.3 BALANCED STEADY STATE FREE PRECESSION (BSSFP) SEQUENCE DIAGRAM FROM [98]	26
FIGURE 2.4 ECG GATED ACQUISITION WITH FOUR VIEW PER CARDIAC CYCLE	26
FIGURE 2.5 THE CHOICE OF THE LOCALIZER PLANS AND THE CORRESPONDING AXIAL VIEW FOR MPA, LPA AND RPA....	27
FIGURE 2.6 MR IMAGE OF THE MAIN PULMONARY ARTERY	28
FIGURE 2.7 MATLAB SEGMENTATION GUI	29
FIGURE 2.8 MAPPING FUNCTION FOR A POINT PRESENT IN 2 IMAGES	33
FIGURE 2.9 REGISTRATION-BASED SEGMENTATION: CASE 1, PEAK SYSTOLIC FIXED IMAGE	36
FIGURE 2.10 REGISTRATION-BASED SEGMENTATION, CASE 3, SEQUENTIAL SEGMENTATION OF THE TIME SERIES.	37
FIGURE 2.11 SIMULTANEOUS RECORDINGS OF PRESSURE AND DIAMETER IN THE PULMONARY CIRCULATION.....	39
FIGURE 2.12 PRESSURE-DIAMETER CORRELATION FOR THE PULMONARY CIRCULATION.....	40
FIGURE 2.13 RELATIONSHIP BETWEEN PETERSON’S ELASTICITY MODULUS (E_p) AND DIASTOLIC PRESSURE (P_0) WITH RELATIVE AREA CHANGE (RAC) IN THE HUMAN MPA	44
FIGURE 2.14 AREA VARIATION OBTAINED FOR EACH OPERATOR AND EVERY SEGMENTATION APPROACH, TOGETHER WITH AVERAGE AREA AND STANDARD DEVIATION FOR MPA.....	49
FIGURE 2.15 AREA VARIATION OBTAINED FOR EACH OPERATOR AND EVERY SEGMENTATION APPROACH, TOGETHER WITH AVERAGE AREA AND STANDARD DEVIATION FOR RPA.....	50
FIGURE 2.16 AREA VARIATION OBTAINED FOR EACH OPERATOR AND EVERY SEGMENTATION APPROACH, TOGETHER WITH AVERAGE AREA AND STANDARD DEVIATION FOR LPA	51
FIGURE 2.17 COEFFICIENT OF VARIATION FOR INTER AND INTRA-OPERATOR VARIABILITY	52
FIGURE 2.18 AREA VARIATION OBTAINED FOR OPERATOR’S 1 SEGMENTATIONS FOR EVERY SEGMENTATION APPROACH, TOGETHER WITH AVERAGE AREA AND STANDARD DEVIATION FOR MPA	54
FIGURE 2.19 AREA VARIATION OBTAINED FOR OPERATOR’S 1 SEGMENTATIONS FOR EVERY SEGMENTATION APPROACH, TOGETHER WITH AVERAGE AREA AND STANDARD DEVIATION FOR RPA	55
FIGURE 2.20 AREA VARIATION OBTAINED FOR OPERATOR’S 1 SEGMENTATIONS FOR EVERY SEGMENTATION APPROACH, TOGETHER WITH AVERAGE AREA AND STANDARD DEVIATION FOR LPA.....	56
FIGURE 2.21 FLOW WAVEFORMS AS REPORTED IN THE MR SCANNER REPORT FOR MPA (RED), LPA (GREEN) AND RPA (BLUE) OF THE SAME PATIENT	57

FIGURE 2.22 FLOW VARIATION OBTAINED FOR EACH OPERATOR AND EVERY SEGMENTATION APPROACH, TOGETHER WITH AVERAGE FLOW AND STANDARD DEVIATION FOR MPA.....	58
FIGURE 2.23 FLOW VARIATION OBTAINED FOR EACH OPERATOR AND EVERY SEGMENTATION APPROACH, TOGETHER WITH AVERAGE FLOW AND STANDARD DEVIATION FOR RPA.....	59
FIGURE 2.24 FLOW VARIATION OBTAINED FOR EACH OPERATOR AND EVERY SEGMENTATION APPROACH, TOGETHER WITH AVERAGE FLOW AND STANDARD DEVIATION FOR LPA.....	60
FIGURE 2.25 PRESSURE VARIATION IN MPA OBTAINED FOR EACH OPERATOR, FOR CASES 1 AND 2 OF THE SEMI-AUTOMATIC SEGMENTATION, TOGETHER WITH AVERAGED PRESSURE AND STANDARD DEVIATION.....	63
FIGURE 3.1 THREE ELEMENT WINDKESSEL MODEL (R_cCR_D) USED FOR THE ANALYSIS OF PULMONARY CIRCULATION IN PH.....	66
FIGURE 3.2 FOUR ELEMENT WINDKESSEL MODEL (R_cLCR_D) USED FOR THE ANALYSIS OF PULMONARY CIRCULATION IN PH.....	72
FIGURE 3.3 A 1D MODEL OF A STRAIGHT ELASTIC TUBE COUPLED WITH A OD R_cCR_D MODEL.....	77
FIGURE 3.4 RELATIONSHIP BETWEEN INVASIVELY MEASURED (RHC) AND MODEL DERIVED MEAN (MPAP), SYSTOLIC (SPAP) AND DIASTOLIC (DPAP) PRESSURES.....	81
FIGURE 3.5 FITTING QUALITY OF A 3 ELEMENT WINDKESSEL MODEL: ORIGINAL WAVEFORM (CONTINUOUS BLUE) AND FITTED (DASHED RED).	82
FIGURE 3.6 THE RESULTS FOR THE OD WINDKESSEL MODEL ON THE 80 PATIENT COHORT: (A) DISTAL RESISTANCE R_D , (B) CHARACTERISTIC RESISTANCE R_c , (C) TOTAL RESISTANCE R_{TOTAL} , (D) TOTAL COMPLIANCE C	83
FIGURE 3.7 TOTAL RESISTANCE COMPUTED AS RATIO OF INVASIVELY MEASURED MPAP (RHC) AND MEAN FLOW (MRI) $R_{TOTAL}RHC$	85
FIGURE 3.8 RELATIONSHIP BETWEEN TOTAL RESISTANCES MEASURED AS MEAN PRESSURE TO MEAN FLOW AND CLINICALLY DERIVED PVR.	86
FIGURE 3.9 RELATIONSHIP BETWEEN THE TOTAL COMPLIANCE, C AND TOTAL R_{TOTAL} AND DISTAL R_D RESISTANCES COMPUTED FROM THE OD MODEL AND TOTAL COMPLIANCE C , AND CLINICALLY MEASURED PVR, DISPLAYED ON LOG-LOG GRAPHS	87
FIGURE 3.10 THE VARIATION OF DISTAL RESISTANCE-TOTAL COMPLIANCE PRODUCT WITHIN THE ANALYSED GROUPS: (A) ENTIRE COHORT (B) DATA FROM (A) WITHOUT THE MARKER OUTLIERS.....	88
FIGURE 3.11 SOURCE OF OUTLIERS IN THREE AND FOUR ELEMENT WINDKESSEL MODEL.....	89
FIGURE 3.12 (TOP): WAVE POWER HARMONIC CONTENT QUANTIFIED FOR THE FORWARD (GREEN) AND BACKWARD (RED) PRESSURE COMPONENTS OF A NOPH PATIENT. (BOTTOM): DECOMPOSITION OF THE PRESSURE WAVEFORM IN FORWARD AND BACKWARD TIME VARYING COMPONENTS	97
FIGURE 3.13 (TOP): WAVE POWER HARMONIC CONTENT QUANTIFIED FOR THE FORWARD (GREEN) AND BACKWARD (RED) PRESSURE COMPONENTS OF A PH PATIENT. (BOTTOM): DECOMPOSITION OF THE PRESSURE WAVEFORM IN FORWARD AND BACKWARD TIME VARYING COMPONENTS	97
FIGURE 3.14 RESULTS OF THE 1D MODEL, WITHIN THE ANALYSED GROUPS.....	98
FIGURE 3.15 FITTING QUALITY OF THE 3 ELEMENT WINDKESSEL MODEL: ORIGINAL WAVEFORM (CONTINUOUS BLUE) AND FITTED (DASHED RED).	100

FIGURE 3.16 DISTRIBUTION ACROSS GROUPS OF THE LENGTH OF THE 1D DOMAIN.....	101
FIGURE 3.17 RELATIONSHIP BETWEEN W_B/W_{TOT} DETERMINED USING MIXED DATA SET (GG+RHC) AND FROM SOLELY FROM RHC AND GREENFIELD AND GRIGGS [96].....	102
FIGURE 3.18 RELATIONSHIP BETWEEN R_D DETERMINED USING THE MIXED DATA SET (RHC+GG) AND SOLELY RHC AND GREENFIELD AND GRIGGS [96]	103
FIGURE 3.19 RELATIONSHIP BETWEEN R_C DETERMINED USING MIXED THE DATA SET (RHC+GG) AND SOLELY FROM RHC AND GREENFIELD AND GRIGGS [96].....	103
FIGURE 3.20 RELATIONSHIP BETWEEN C DETERMINED USING THE MIXED DATA SET AND SOLELY FROM RHC AND GREENFIELD AND GRIGGS [96]	104
FIGURE 3.21 INTER-OBSERVER VARIABILITY. BLAND-ALTMAN (LEFT) AND REGRESSION ANALYSIS (RIGHT), SHOWED FOR RELATIVE AREA CHANGE (RAC), RATIO OF WAVES POWER (W_B/W_{TOT}), DISTAL RESISTANCE (R_D) AND PULMONARY COMPLIANCE (C) PERFORMED ON 20 CASES SELECTED AT RANDOM (USING MATLAB) FROM THE 72 PATIENT COHORT.....	106
FIGURE 3.22 INTRA-OBSERVER VARIABILITY. BLAND-ALTMAN (LEFT) AND REGRESSION ANALYSIS (RIGHT), SHOWED FOR RELATIVE AREA CHANGE (RAC), RATIO OF WAVES POWER (W_B/W_{TOT}), DISTAL RESISTANCE (R_D) AND PULMONARY COMPLIANCE (C) PERFORMED ON 20 CASES SELECTED AT RANDOM (USING MATLAB) FROM THE 72 PATIENT COHORT.....	107
FIGURE 3.23 CORRELATION AND AGREEMENT BETWEEN W_B/W_{TOTAL} DERIVED FROM SOLELY PC IMAGES AND BSSF AND PC IMAGES.....	108
FIGURE 3.24 CORRELATION AND AGREEMENT BETWEEN R_D DERIVED FROM SOLELY PC IMAGES AND BSSF AND PC IMAGES.	109
FIGURE 3.25 CORRELATION AND AGREEMENT BETWEEN C DERIVED FROM SOLELY PC IMAGES AND BSSF AND PC IMAGES.	109
FIGURE 3.26 CORRELATION AND AGREEMENT BETWEEN R_C DERIVED FROM SOLELY PC IMAGES AND BSSF AND PC IMAGES.	110
FIGURE 4.1 SCHEMATIC DIAGRAM OF THE SINGLE TREE CLASSIFICATION ALGORITHM.....	119
FIGURE 4.2 SCHEMATIC DIAGRAM OF THE RANDOM FOREST CLASSIFICATION ALGORITHM.	120
FIGURE 4.3 LEAVE-ONE-OUT CROSS-VALIDATION DIAGRAM	122
FIGURE 4.4 ROC AND AUC OF THE PHYSIOLOGY-BASED COMPUTATIONAL METRICS.....	125
FIGURE 4.5 ROC AND AUC OF THE MPA DERIVED METRICS	125
FIGURE 4.6 ROC AND AUC OF THE CMR DERIVED METRICS	126
FIGURE 4.7 INDIVIDUAL AND RANDOM FOREST MODEL'S ACCURACIES	128
FIGURE 4.8 THE PATIENT CLASSIFICATION RETURNED BY THE ENSEMBLE MODEL WITH THE SMALLEST MISCLASSIFICATION ERROR AND HIGHEST SENSITIVITY, AT LEAVE-ONE-OUT CROSS-VALIDATION.	129
FIGURE 5.1 BRANCHING TREE CONNECTIVITY AND TERMINOLOGY	136
FIGURE 5.2 COMPUTATION OF THE INPUT IMPEDANCE, Z_L FOR A VASCULAR ELEMENT USING THE CHARACTERISTIC Z_C AND TERMINAL IMPEDANCE Z_0	141
FIGURE 5.3 WAVE DIRECTION IN ONE ELEMENT	145

FIGURE 5.4 PRESSURE WAVE COMPONENTS AT THE INTERFACE OF A THREE MEDIA SYSTEM DESCRIBED IN TERMS OF A)
 INLET AND OUTLET COMPONENTS B) INCIDENT, TRANSMITTED AND REFLECTED..... 147

FIGURE 5.5 POPULATING THE GLOBAL STIFFNESS MATRIX WITH THE INDIVIDUAL ELEMENT STIFFNESS 154

FIGURE 5.6 SCHEMATIC OF THE INTERIOR DEGREES OF FREEDOM CONDENSATION IN THE SUPERELEMENT APPROACH.. 157

FIGURE 5.7 THE EFFECT OF REDUCING THE RADIUS AT A GENERATION AT THE TIME, ON THE INLET MEASURED W_B/W_{TOT}
 161

List of Tables

TABLE 2.1 TOTAL SEGMENTATION TIMES (T_{TOTAL}) FOR EACH OF THE PROPOSED APPROACHES	46
TABLE 2.2 'AFTER-TRAINING' MEAN \pm SD OF COEFFICIENT OF VARIATION (C.V)	53
TABLE 2.3 MEAN AND SD OF COEFFICIENT OF VARIATION (C.V)-INTRA-OPERATOR	57
TABLE 2.4 RELATIVE ERRORS IN FLOW QUANTIFICATION	61
TABLE 2.5 COEFFICIENT OF VARIATION FOR MINIMUM AND MAXIMUM AREA	63
TABLE 3.1 GA PARAMETERS' INTERVAL	68
TABLE 3.2 COMPARISON BETWEEN PARAMETERS VALUES OF THE THREE AND FOUR ELEMENT WINDKESSEL MODEL	88
TABLE 3.3 BIAS AND LIMITS OF AGREEMENT FOR THE INTRA AND INTER-OPERATOR VARIABILITY	105
TABLE 4.1 PATIENTS DEMOGRAPHICS, RHC DATA, MATHEMATICAL MODEL AND IMAGES DERIVED PARAMETERS	123
TABLE 4.2 NON-INVASIVE METRICS' INDIVIDUAL ACCURACIES EVALUATED FOR A CUT-OFF VALUE CORRESPONDING TO MAXIMUM YODEN INDEX	124
TABLE 4.3 CLASSIFICATION ACCURACIES FOR THE COUPLED-PH-METRICS MODELS	127

CHAPTER 1

Introduction & Literature Review

INTRODUCTION AND MOTIVATION

The pulmonary circulation is a low-pressure, high-flow vascular network, characterised by a multiple-branching circuit running from the right ventricle to the left atrium [1]. Under normal conditions, the right heart circulation has to accommodate the same amount of blood as the systemic circulation. Despite this common feature, the two have distinct anatomical and functional characteristics: the pulmonary system has shorter, tapered, more compliant vessels, that are less resistive to blood flow, with the flow driven by a significantly lower pressure than its left counterpart [2]. For many cardiovascular diseases, the onset or presence of the disease is manifested in haemodynamic and anatomical modifications. Due to the convoluted vessel network, with arteries and veins closely following the airways [3] and its hidden position, behind the thorax, the pulmonary circulation structure and function can be difficult to image effectively.

Pulmonary hypertension (PH) is a condition, clinically defined by an increased mean pulmonary arterial pressure (mPAP), $\geq 25\text{mmHg}$ at rest, measured by invasive right heart catheterisation (RHC)[4]. The RHC procedure is currently considered the gold standard for diagnosis, follow-up and response to treatment and the patient is often exposed to multiple

investigations [5]. RHC presents risks to the patient, including bleeding, hematoma formation, vessel puncture, reaction to the contrast dye, abnormal heart rate and, in extreme cases, heart attack, stroke and death [6], [7]. Although the severe complications are reduced when the procedure is performed in a specialist centre [8], [6], non-invasive methods for PH assessment are highly desirable.

PH is a complex disease, with multiple classifications (reviewed in Section 1.3 of this chapter), and with pathophysiological features that include intimal proliferation, vascular remodelling, vasoconstriction and increase in the vascular stiffness. Beside structural and morphological changes, evaluated usually through imaging techniques (Doppler Echocardiography, MR, PET, CT)[9], [10], [11], these phenomena are intimately related to: increase of the pulmonary vascular resistance (PVR), decrease of the vessel compliance (C), leading to increase in the ventricular afterload, followed by ventricular failure and death [9],[12].

The hypothesis of this PhD thesis is that the physiological status of the pulmonary circulation can be assessed using solely non-invasive measurements of the flow and anatomy of the pulmonary arteries measured by Magnetic Resonance Imaging (MRI), interpreted by simple mathematical models (Windkessel models and 1D wave transmission models).

The aim of the project is to implement and to clinically evaluate the above mentioned models, operating on MRI derived input data, as a non-invasive alternative to right heart catheterisation for diagnosis and monitoring of pulmonary hypertension.

PULMONARY STRUCTURE

The pulmonary circulation is a multiple branching circuit, extending from the pulmonary valve to the left atrium [13]. The main pulmonary artery (MPA) is tapered, about 5 cm long, with a diameter of approximately 3 cm, although the dimensions vary between the sexes [14]. The pulmonary trunk is divided into the right and left branches, continuing to branch into smaller pulmonary arteries until they reach the capillary level, where gas exchange takes place. From there, oxygenated blood is transported to the left side of the heart through a system of pulmonary veins, which empty into the left atrium through the 4 pulmonary veins [13].

The pulmonary arteries and veins closely follow the topology of the airways, with the number of the blood vessels exceeding the airways (supernumerary vessels). Chang *et al* [15] state that there are 28 generations of arterial branches, with vessel diameters as small as 100 μ m.

The intricacy of the pulmonary vasculature and importance of computer modelling in assessing its mechanics in health and diseased cases was emphasised by Burrowes [3] through a complex structured anatomical model of the distribution of arteries and veins in the human lung.

PULMONARY HYPERTENSION

1.1.1 Definition, classification, diagnosis

Pulmonary hypertension is a condition that is clinically defined by an increase of the mean pulmonary arterial pressure (mPAP) ≥ 25 mmHg, measured, at rest, by invasive right heart catheterisation [12]. Although a 30 mmHg value was proposed as an exercise threshold [1], it was showed [16] that even higher values can be found in healthy people during exercise.

For healthy volunteers, the normal pressure range at rest was reported to be 14.3 ± 3.3 mmHg [17], giving rise to debate regarding the patients whose mPAP is higher than normal but smaller than the PH diagnosis definition [12]. The term 'borderline PH' defines patients with mPAP between 20 and 24mmHg [18] and remains an area that is not effectively covered by the official guidelines.

The most recent classification was done in 2008 at Dana Point, California. According to the pathophysiological modification, clinical presentation, and therapeutic approaches, PH was divided into 5 groups [12] as follows:

- Group 1: Pulmonary arterial hypertension (PAH)
- Group 2: Pulmonary hypertension due to left heart disease (PH-LHD)
- Group 3: Pulmonary hypertension owing to lung disease and/or hypoxia (PH-Lung)
- Group 4: Chronic thromboembolic pulmonary hypertension (CTEPH)
- Group 5: Pulmonary hypertension with unclear or multifactorial etiologies

These five groups can be divided into two major categories: pre-capillary PH (groups 1,3, 4 and 5) and post-capillary PH (group 2), the names being suggestive of the site of the disease. A pulmonary wedge pressure (PWP) higher than 15 mmHg is clinically attributed to post-capillary PH, whereas smaller values are considered to characterise pre-capillary PH [4]. Although unreported in the guidelines, the situation where the patient has $PWP > 15$ mmHg but also presents signs of pre-capillary PH is clinically possible, being attributed to a 'mixed PH' category [19].

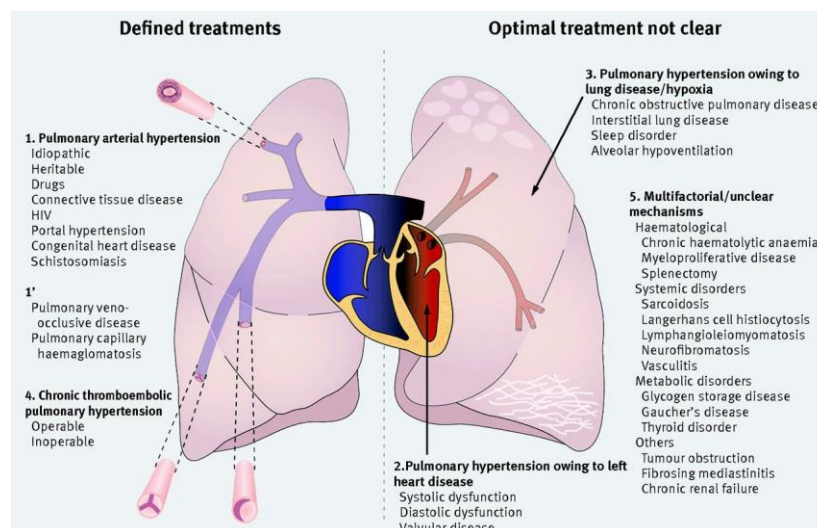


Figure 1.1 Pulmonary hypertension groups and sub-groups classification [9]

Figure 1 from [9] reproduced with permission given through Copyright Clearance Center's RightsLink service.

Characteristics shared by the PH groups include vascular remodelling, vasoconstriction and intimal proliferation [4]. These features contribute to an increase in pulmonary vascular resistance (PVR) and decrease of pulmonary compliance (C) [20]. To overcome this increase in the ventricular afterload, the energy expended by the right ventricle increases, often leading to right heart failure, recognised as one of the most common causes of death in PH [21], [22].

The pathology specific to each of the five PH groups, along with their sub-groups, is illustrated in Figure 1.1. As graphically highlighted in this comprehensive diagram from [9], only group 1 (PAH) and 4 (CTEPH) have a defined clinical treatment. Whereas for the other three groups, the optimal treatment is not clear, being determined mainly by the treatment of the underlying cause.

As PH is a disorder with no specific symptoms [4], a complete series of tests is often undertaken. Imaging techniques (Echocardiography, CT, MR) play an important role in visualising the internal pulmonary structures and supporting the PH diagnosis within the groups [10]. However, the diagnosis is currently confirmed by the RHC method as the only clinical gold standard. The procedure is not used solely to measure the mPAP but also to determine the pulmonary wedge pressure (PWP) and the cardiac output (CO), and to compute the pulmonary vascular resistance (PVR): all of these parameters are important for PH sub-group classification, follow-up and treatment.

The PWP represents a marker used for the correct diagnosis of PH-LHD [23] and for exclusion of pre-capillary PH [4]. Despite its importance in the decision process, PWP does not always represent a good estimate for the left arterial pressure [24]. The erroneous computation of PWP can further lead to the erroneous estimation of PVR (Eq. 1.1), since the latter depends upon the PWP.

Clinically, PVR is defined as the ratio of the difference between mPAP and left arterial pressure (approximated by the PWP) and the CO.

$$PVR = \frac{mPAP - PWP}{CO} \quad (\text{Eq. 1.1})$$

The measure, usually expressed in Wood units (WU) (equivalent to 80 dyn s cm^{-5}) corresponds to the Poiseuille resistance (Eq. 1.2), defined as the ratio between pressure drop (ΔP) and volumetric flow rate (Q) through cylindrical pipes for incompressible, Newtonian fluids.

$$R_{\text{Poiseuille}} = \frac{\Delta P}{Q} = \frac{8l\mu}{\pi r^4} \quad (\text{Eq. 1.2})$$

where l is the vessel length, r is the vessel radius and μ is the dynamic blood viscosity.

Normal PVR values lie between 0.13 and 1.24 WU, with an average of 0.7 WU [25], whereas values above 2-3 WU are indicative of PH [5]. Increased PVR values were associated in some studies [26], [27], [28], [29] with PH severity, and with a lower survival rate after heart transplantation [29], [28]. Different values have been adopted as a threshold between mild and severe PH: 4 WU [26], [27], 5 WU [28] or 6 WU [29].

1.1.2 Alternative, non-invasive diagnosis methods in PH

Non-invasive imaging techniques (Echocardiography, MRI) are currently used both for the clinical screening of the PH-suspect patients and in follow-up monitoring [4].

Furthermore, research has been conducted [26], [30], [31], [32], [33], [34], [35], [36], [37], [27] to derive non-invasive clinical significant parameters for the assessment of PH. The derivation of these 'RHC surrogate markers' seems to follow two trends, which might be classified as direct or model-based approaches. The latter constitutes the focus of the present PhD thesis and it is extensively reviewed in Section 0.

1.1.2.1 The direct approach

In the direct approach, parameters are derived solely based on the measured outputs (no further modelling is required).

Some of these studies propose qualitative/observational markers: Swift *et al.* [38] suggested that the artefacts from black blood images caused by slow flowing blood in the pulmonary trunk have diagnostic potential in the discrimination between PAH and no PH patients. Kitabatake *et al.* [39] observed changes in the shape of the pulmonary flow curve, obtained through Doppler Echocardiography, in patients with normal, moderate and elevated mPAP. Although showing promising results, these studies have the limitation of being subject to operator interpretation.

Other studies, falling under the same 'direct approach', propose quantitative anatomical or haemodynamic markers, derived in most cases from 2D pulmonary artery (PA) phase contrast and/or CINE cardiac MR images. These markers include: maximum, minimum and relative area change of the vessel, average and peak blood flow velocity, and acceleration and ejection times.

Measurements of the anatomy and function of pulmonary arteries (relative area change-RAC, pulsatility/ distensibility and minimum area) were reported [26], [30], [31], [32] as having the potential to classify PH from no PH patients. Values of 15%, 24% and 40% RAC were indicated [26], [30] as thresholds to separate PH patients with and without the condition. A cut-off value of 10% was able to differentiate between responders and non-responders to vasodilators in IPAH patients [40]. The same parameter, measured for the RPA, was proposed [31] as a mortality predictor for a 16% threshold.

A series of studies based this time on cine cardiac MR images were conducted for the assessment of right ventricle mass (RVM) and ventricle mass index (VMI) [33], [34], interventricular septal curvature [35], right ventricle function (end systolic/diastolic volume) [36], peak and average velocity [41], [32], [34], acceleration (AT) and ejection times (ET) [32], [42]. Each of these has shown potential in differentiating patients without PH from those with the disease. It is however known that changes in right heart structure and function manifest late in the evaluation of PH. Hence, it is desirable to identify PH markers that are able to diagnose the presence of the disease in its earlier stages.

1.1.2.2 The model-based approach

A second, more indirect, approach for non-invasive PH assessment uses the output from the imaging techniques, in general flow and area measurements, as input for mathematically formulated models [43],[44],[45], [27], [46].

However, the majority of the model-based approaches that are reported in the literature are almost invariably based on invasive pressure and flow measurements in animals and humans, under normal as well as under induced PH conditions. There are very few published studies that use exclusively non-invasive measures, which constitute the major focus of this thesis.

MATHEMATICAL MODELS OF THE PULMONARY CIRCULATION

Finding alternative, non-invasive methods to assess pulmonary hypertension has received increasing interest in the pulmonary research community, [26], [30], [31], [32], [33], [34], [35], [36], [37], [43],[44],[45], [27]. Although the direct methods of determining PH markers have been shown to have clinical potential, their interpretation could be enriched by introducing additional knowledge from the application of mathematical models, which can bring insights into the haemodynamic system behaviour in health and disease.

Based on mathematical and physical principles including electrical circuit theory and wave transmission theory, cardiovascular models can offer a global (0D) or local (1D, 2D, 3D) representation of the flow, $Q(t)$, and pressure, $p(t)$, behaviour under different circumstances.

For instance, considering the pulmonary arterial tree as the system to be represented, a zero dimensional model will provide a general, lumped, description of it. The label 'zero-dimensional' indicates that there is no spatial variation of the parameters in the model: they are functions only of time. On the other hand, the increase of the model's dimensionality will offer a local representation of the fundamental variables ($Q(t)$ and $p(t)$). Distributed models break down the system into compartments in which the flow and pressure can vary in one ($Q(x,t)$, $p(x,t)$), two ($Q(x,y,t)$, $p(x,y,t)$) or three ($Q(x,y,z,t)$, $p(x,y,z,t)$) dimensions [47].

Modelling the pathophysiology of the cardiovascular system requires understanding of the system's behaviour under normal circumstances. In order to achieve today's status, where mathematical models can be used as a non-invasive tool in disease assessment, they have followed an evolutionary path of *in vivo* and *in vitro* experimental validation. The majority of the models were derived at first from animal data, followed by application to human data. For validation the proposed model's outcome was the compared with invasive

measurements. The following sections of this chapter are outlining the underlying concepts of zero and one dimensional models and exemplifying their applications in modelling the pulmonary circulation.

1.1.3 0D models- underlying concepts

The lumped parameter models are represented as analogue electrical circuits, in which voltage represents pressure, $p(t)$, and electrical current represents blood flow, $Q(t)$.

The components of a 0D model are primarily linear, passive (resistor) and active (inductance, capacitance) elements. Each of the elements has a hydraulic equivalent as follows:

- *electrical resistance, R* - represents vascular resistance, associated with the viscous losses
- *capacitance, C* - represents vascular compliance, associated with the elasticity of the blood vessels and their capacity to accommodate volume changes
- *inductance, L* - represents vascular inductance, associated with the inertia of the blood.

Nevertheless, the three elements (R , C and L) stated above are not the only ones that can be included in an electrical analogue circuit. Other electrical elements such as non-linear capacitors and resistors, or diodes can be used to simulate the myocardium's compliance (elastance), variable peripheral vasculature resistance due to respiration, or heart valves as used by [48], [49], [50].

Four of the most commonly encountered configurations of the electrical parameters R , C and L to form a 0D model are exemplified in Figure 1.2.

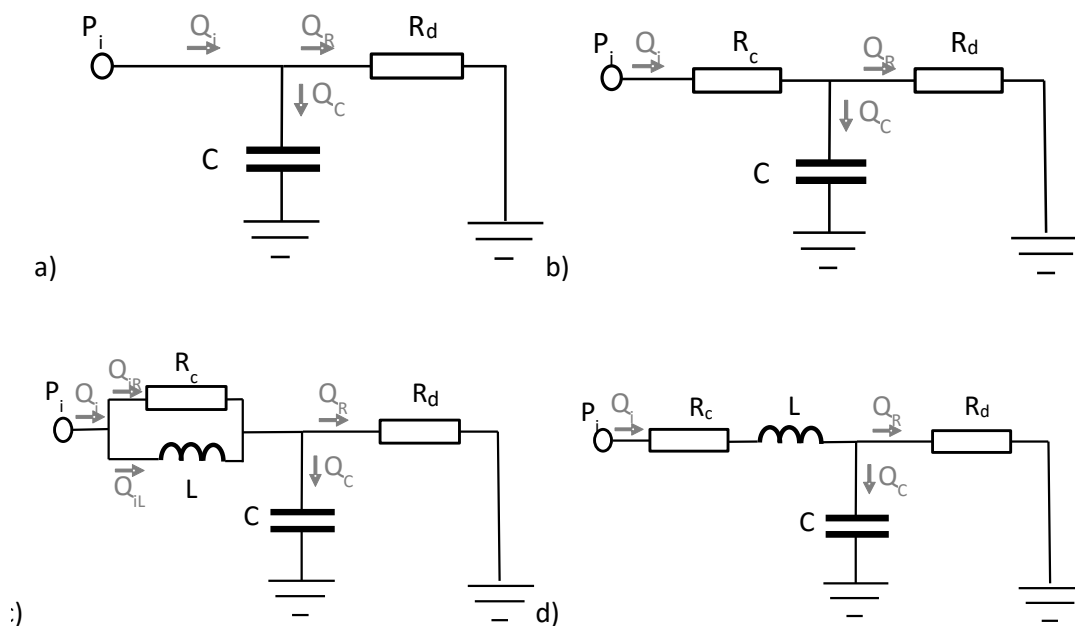


Figure 1.2 OD (Windkessel) models in configuration of 2 (a), 3 (b) and 4 (c-d) electrical parameters

The lumped parameter models can offer a representation of an entire system (systemic/pulmonary circulation) or they can illustrate smaller compartments such as the arterial/venous tree, large arteries, small arteries, veins, venules, capillary bed, etc. The ability to define system models of increasing complexity by assembling OD models of individual components makes the OD approach extremely versatile. OD models can be used as standalone, in a mono or multi-compartment [47] description, or as boundary conditions for higher order models (1D to 3D) [51].

The first zero dimensional model, also known as the Windkessel model (in German, windkessel = air chamber), was mathematically formulated by Otto Frank in 1899 [52], who introduced the concept of using mathematical models to represent the heart afterload [53]. The first proposed Windkessel model was characterised by only two elements: a resistor in parallel with a capacitor (Figure 1.2.a). The compliance of the 2 element Windkessel defined the relationship between the fractional change of volume of blood in the systemic arteries and the change in pressure (Eq. 1.3). The circuit obeys the mass conservation law (Eq. 1.4) (equivalent to Kirchoff's 1st law): any change in volume should equal the difference between the inlet and outlet blood mass flow.

$$C = \frac{dV}{dP} \tag{Eq. 1.3}$$

$$\frac{dV(t)}{dt} = Q_{in}(t) - Q_{out}(t) \quad (\text{Eq. 1.4})$$

$$Q_{out}(t) = \frac{P_{in}(t) - P_{\infty}(t)}{R_d} \quad (\text{Eq. 1.5})$$

where p_{∞} is the distal pressure; for the RC-Windkessel model, $p_{\infty} = 0$ (ground)

Combining the above equations and using the nomenclature illustrated in Figure 1.2 a, leads to an ordinary differential equation (Eq. 1.6) which describes the RC Windkessel model in the time domain.

$$Q_i(t) = \frac{P_i(t)}{R_d} + C \frac{dP_i(t)}{dt} \quad (\text{Eq. 1.6})$$

where, $Q_i(t)$ is the inlet flow, $P_i(t)$ is the inlet pressure, C is the total vascular compliance, R_d is the vascular distal (peripheral) resistance

The electrical-analogue models of the cardiovascular system have since evolved as different authors started to add elements to the initial Windkessel model (Figure 1.2.b-d), and to analyse the results. Some of the fundamental contributions to the literature of OD models are reviewed in the following paragraphs.

Westerhof and co-workers [54] proposed the introduction of an additional element to the Windkessel model to provide a better representation of the system response (Figure 1.2 b). A significant deficiency of the two-element Windkessel is its response at mid to high frequencies. The impedance at each frequency is described by (Eq. 1.7) and (Eq. 1.8).

$$Z_{in}(\omega) = \frac{P(\omega)}{Q(\omega)} \quad (\text{Eq. 1.7})$$

where Z_{in} is the input impedance of a system, described by the ratio between the harmonic pressure and flow components.

$$Z_{in_{2w}}(\omega) = \frac{R_d}{1 + j\omega CR_d} \quad (\text{Eq. 1.8})$$

According to (Eq. 1.8), at high frequency the impedance tends to zero, which is not consistent with experimental data. To address this problem, a resistor R_c , representing the characteristic impedance of the vessel proximal to the measuring site, was added in series with the initial configuration. The impedance of the 3 element Windkessel circuit is given by (Eq. 1.9). At $\omega=0$, corresponding to the direct current (DC) component, the modulus of the input impedance equals the sum of the 2 resistors, whereas at high frequencies, the input impedance modulus equals R_c .

$$Z_{in_{3W}}(\omega) = R_c + \frac{R_d}{1 + j\omega CR_d} \quad (\text{Eq. 1.9})$$

The sum of the distal (R_d) and proximal (R_c) resistances is the total arterial resistance (Eq. 1.10), computed from the ratio of the mean pressure to mean flow [2].

$$R_{total} = R_c + R_d = \frac{\bar{P}}{\bar{Q}} \quad (\text{Eq. 1.10})$$

Although the three element Windkessel model produced more realistic pressure and flow waveforms, it was noticed both for pulmonary and systemic circulation [55], [56], that better fits to measured data could be obtained by using a higher value than the characteristic impedance for the proximal resistance, and a lower value for C than the overall vascular compliance.

The next significant modification was to recognise that the 2 and 3 element Windkessel models do not take into consideration the inertia of the blood. Landes [47] and later Burantini and Gnudi [57] addressed this deficiency by the introduction of an inductance L, in series (Figure 1.2 d) and parallel (Figure 1.2 c), respectively, to the characteristic resistance, R_c .

The difference in the performance of the 2 systems ($Z_{in_{4W_s}}$ and $Z_{in_{4W_p}}$) can be seen in the equations for the input impedance:(Eq. 1.11) and (Eq. 1.12).

$$Z_{in_{4W_s}} = R_c + j\omega L + \frac{R_d}{1 + R_d j\omega C} \quad (\text{Eq. 1.11})$$

$$Z_{in_{4W_p}} = \frac{R_c j\omega L}{j\omega L + R_c} + \frac{R_d}{1 + R_d j\omega C} \quad (\text{Eq. 1.12})$$

At $\omega=0$, the 4 element Windkessel with L in series with R_c returns a DC impedance equal to the one of the 3 element Windkessel, whereas in the higher frequency range, the input impedance does not equal just the characteristic impedance. On the other hand, adding L in parallel with R_c will have at low frequencies a behaviour similar to a 2 element Windkessel, and at high frequencies it will behave as a 3 element Windkessel. The latter approach is considered [58], [57] to better represent the real behaviour of the systemic circulation. It has been argued [58] that since R_c was added to simulate the characteristic impedance, it should not be included in the computation of the total vascular resistance in the 3 element Windkessel or in the 4 element Windkessel with L in series with R_c .

In a study on dogs [58], the C values returned by two Windkessel models (with 3 and 4 elements- L in parallel with R_c) of the systemic circulation, were compared with the ones

returned by classical area and pulse pressure methods for the determination of compliance [59]. The experiment confirmed the previous findings [55], [56] regarding the overestimation of C and underestimation of R_c by the 3 element Windkessel, and showed that the 4 element Windkessel including the inertial effect of the blood returned more realistic values for the total vascular compliance.

Based on experimental data from animals (dogs and pigs), Segers et al. [60] investigated whether there are any circumstances in which a 3 element Windkessel will still return a realistic compliance. The findings showed that the 3 element Windkessel was overestimating the pulmonary compliance when modulus of the input impedance at low frequencies had a value close to the characteristic impedance. The authors suggested that the phenomenon (Z_{in} at $\omega=0$ close to Z_c), was determined by the reduced reflections detected at the entrance of the measurement site.

All the lumped parameter models described above represent mono-compartmental models. As previously mentioned, one major drawback of a 0D model is its global character. To provide some spatial discrimination, a new category of models, the multi-compartmental ones, were introduced. These models, formed by a series of Windkessel circuits added together, are capable of characterising the cardiovascular system in terms of parameters in a series of segments: large arteries, small arteries, arterioles, veins, venules, capillaries etc. For every block of the cardiovascular system, a single R, RC or RLC combination, which better describes the respective segment, is used. In this sense, Formaggia *et al.* [61] proposed four possible configurations of an RLC combination: L-network, L-inverted network, T-network, and π -network, the names being suggestive to the position of each electrical element within the compartment (Figure 1.3). The choice of any one specific configuration as the basis of a particular model depends on the variables of the circuit that are known (inlet flow (Q_i), outlet flow (Q_o), inlet pressure (P_i), outlet pressure (P_o)).

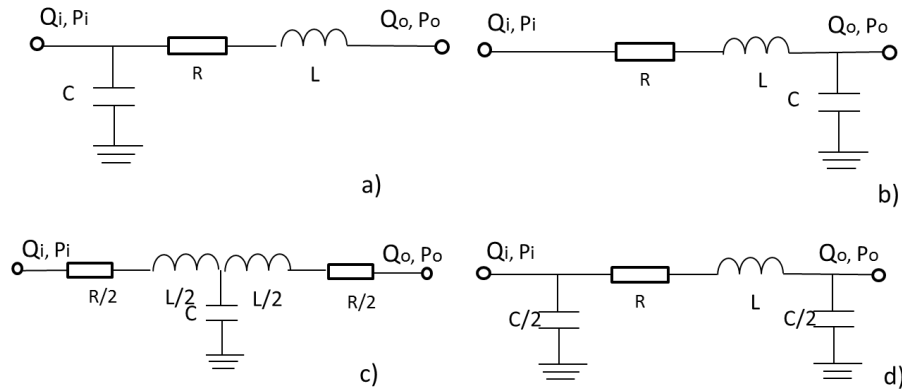


Figure 1.3 The four network configuration for compartmental models, describe by Formaggia [61]

a) 'L' circuit b) 'L inverted' circuit c) 'T' configuration d) 'π' configuration

Based solely on combinations of mono-compartment, complex models had been proposed [62], [63] to represent the systemic, pulmonary or entire circulatory system. Even though these models have the great advantage to describe the vessel's behaviour in more specific points, including segments such as the venous circulation (which is missing in the mono-compartment representation), the multi-compartment models have the disadvantage that the numerical values of each of the R-L-C elements have to be supplied for each single one. However, physiological data available to support the definition of all of the quantitative values for an individual are usually missing.

1.1.4 One dimensional distributed models

One dimensional (1D) distributed models (unlike previous zero dimensional models), represent the continuous variation of pressure and flow along the whole length of the system they describe. Obtained by breaking down the system into segments with known geometrical and mechanical properties, they can capture the effects of wave transmission, and the information that this carries, along the vasculature [64].

The complex phenomenon of blood flow through the circulatory system is governed by the non-linear Navier-Stokes equations, describing the conservation of mass (Eq. 1.13) and momentum (Eq. 1.14).

$$\frac{\partial \rho}{\partial t} + \nabla \cdot (\rho v) = 0 \quad (\text{Eq. 1.13})$$

$$f - \nabla p + \mu \cdot \nabla^2 v = \rho \left(\frac{\partial v}{\partial t} + v \cdot \nabla v \right) \quad (\text{Eq. 1.14})$$

where p is pressure, v is velocity of the blood, μ is the dynamic blood viscosity, ρ is the blood density and f represents the body force [64].

Although three dimensional models (3D) provide the most comprehensive description of the real flow behaviour, they require high computational resources, as well as appropriate boundary conditions, which are sometimes difficult to supply. Nevertheless, comparing the results of 3D with 1D models, it has been shown [65], [66] that the latter approach can produce good results, satisfactorily close to the more complex 3D formulation, and can be used as a simpler and more efficient modelling tool.

The 3D equations can be readily reduced to the 1D form by making assumptions including the representation of blood flowing through axisymmetric thin walled tubes.

The above equations, (Eq. 1.13) and (Eq. 1.14), contain two variables: pressure and velocity, but to reduce to 1D form the velocity has to be integrated across the cross-section to produce flow. This involves a third variable, the vessel area. Another equation is thus required, relating the pressure to the area (Eq. 1.15), often referred as the tube law equation.

$$\frac{\partial p}{\partial A} = \frac{Eh\sqrt{\pi}}{2 \cdot (1 - \nu^2) \cdot A_0} \cdot \frac{1}{\sqrt{A}} \quad (\text{Eq. 1.15})$$

where E is Young's modulus, A is vessel area, ν is Poisson's ratio, p is pressure

The relationship, expressed in here in terms of the derivative represents only one of the many possible relationships that relate the two variables, as reviewed previously by N. Stergiopoulos in [67].

By re-casting the equations in cylindrical form, eliminating the tangential velocity components, considering the axial velocity as dominant and assuming constant pressure over the cross-section, the three dimensional governing equation can be reduced to the 1D form for incompressible flow, through elastic tubes. If the flow and pressure are considered periodic, the 1D linearised equations can be readily solved in the frequency domain.

1D models allow representation of the $Q(t)$ and $p(t)$ at any location along longitudinal direction. However, the most important aspect that the one dimensional models capture is the wave behaviour. It is argued that waves are generated by the heart and travel along the system, exchanging energy with the blood flow and vessels walls [68]. If the travelling wave encounters any discontinuity (e.g narrowing, stenosis, change in vessel diameter, bifurcation), part of the wave will be reflected back to the periphery and part will be

transmitted across the discontinuity. At any position, the measured wave can be described as the sum of forward and backward travelling waves. Measuring the amount of reflections can infer the status of the circulation in health and disease [69], [70].

Waves can be decomposed in the frequency domain from simultaneous measurements of flow, $Q(t)$ and pressure, $p(t)$, using Fourier analysis [52]. This is not however the only method that can separate the wave into forward and backward components. Unlike the frequency domain decomposition (also referred as the impedance analysis), that sees the waves as the superposition of sinusoidal wave trains, the time domain approach, wave intensity analysis (WIA) [71], considers the wave as a successive sum, of infinitesimal wave fronts. The two methods are, however, complementary and mutually consistent, as previously shown [72]. Several models [73], [74], [75], [76], [77], [78], [79], [80], [81], addressing wave reflections in the pulmonary circulation are discussed in the following section. Some of these models were developed in the time domain and some in the frequency domain.

1.1.5 Examples of pulmonary circulation 0D and 1D models

The discussion of 0-D and 1-D models presented in the preceding sections is focused mainly on the underlying concepts and theoretical background. The fundamental theory was developed and tested mainly on models of the systemic circulation. As mentioned in the introductory paragraph of this chapter, despite accommodating the same amount of blood, the systemic and pulmonary circulation have distinct anatomical and functional characteristics. Therefore the differences between the systemic and pulmonary circulation require further discussion.

The first pulmonary models were developed in animals, being supported by experimental data. In 1959, Engelberg and DuBois published measurements of the vascular impedance in the pulmonary network [82], in rabbits. The authors used a 3-element electrical circuit model to represent the entire pulmonary arterial tree. The circuit was formed by an inductance, a capacitance for the compliance of pulmonary arterial vessels and a resistor representing the whole pulmonary bed resistance. The mathematical model neglected the pulmonary veins, and was a reduced version of the previously discussed 4 element Windkessel model, without the characteristic impedance element. Using the proposed electrical analogue model, with the element values measured and computed experimentally, the overall response of the pulmonary arterial tree was tested under different pulsatile pressures. As the authors underlined, finding the pressure and flow waveforms knowing the system's parameters returns a unique solution, whilst trying to infer the system properties from a set of flow and

pressure measurements is rather more difficult. All models produce approximations of the measured flow and pressure curves, and several combinations of parameters can produce solutions with similar errors. Furthermore the variation of the error with the parameters can often be small, or in other words the solution space can be relatively flat, so that a whole range of combinations of parameters can produce equally acceptable fits to the measured data. This issue remains a fundamental one for the methods developed in this thesis.

Since OD models were designed to represent the heart afterload, as Westerhof and co-workers emphasised [54], the electrical analogue impedance of the circuit has to match the real input impedance of the arterial tree. Grant and Paradowski [83] characterised the input pulmonary arterial impedance using eight configurations of lumped parameter models and experimental haemodynamic measurements from cats. They sought to find the model that returns numerical values of characteristic impedance and vascular compliance closest to experimental values, and also which is the best representation of heart afterload. The electrical circuits varied from the simple two Windkessel to circuits with 5 elements.

The model proposed by Engelberg and DuBois [82] performed reasonably well, returning a vascular compliance close to the experimental value, calculated as the ratio between the change in volume to the change in pressure.

The model with the best performance was a modification of the model proposed by Engelberg and DuBois, which accounted for the viscoelastic properties of the vessel wall, by adding a resistor in series with the capacitor.

In their experiment, similar performance was returned by the classical 3 element Windkessel model [54], whereas the 2 element Windkessel scored a lot lower for the comparison criteria. Although the models proposed went up to 5 elements, the 4 element Windkessel with L parallel with R_c was not included in the assessment.

The performance of the 4 element Windkessel with L placed parallel with R_c was tested [84] on a coupled OD-OD model which included 2 compartments, the heart (including variable elastance and heart valve) and the heart afterload (4 element Windkessel). The model performance was tested for both the systemic and pulmonary circulation. The Windkessel parameter values were derived by minimising the residual between the experimentally measured pressure and the one returned by the model, based on a `fminsearch` function. Although for the systemic circulation the results were in good agreement with the experimental data, the ones for the pulmonary circulation were less consistent. This

dissimilarity between the model's performance for the systemic and pulmonary circulations can be either attributed to the different species the models were tested on (pigs for the systemic and dogs for the pulmonary) or raise the hypothesis that the 4 element Windkessel model is not a good representation of the right heart (pulmonary circulation) afterload. However, this suggestion requires further testing, since it was also shown that a 3 element Windkessel overestimated C for the pulmonary circulation [55], as it did for the systemic circulation [58].

Lankhaar *et al.* [20] used a 3 element Windkessel model to evaluate the difference between patients with two types of pulmonary hypertension (CTEPH and IPAH). Based on invasive pressure and flow measurements, the authors computed Z_c , C and R_d and showed that, on average, the analysed parameters showed statistically significant differences between some of the evaluated groups. The vascular compliance, C , decreased from no PH patients to IPAH and CTEPH patients, but the values were similar for the two positive-diagnosis cohorts. The distal resistance and the characteristic resistance were both shown to increase from no disease to disease. Due to the overestimation of C , reported in earlier studies [55], [58], Lankhaar *et al.* [20] computed C through 2 other methods (pulse pressure and stroke volume methods). Although, indeed C was higher for the Windkessel method, between the evaluated groups the decrease in compliance was consistent. This might suggest that even if a 3 element Windkessel model does not return the true compliance, clinically, for the purposes of patient differentiation, it could be a valuable tool.

Moving forward from the mono-compartmental models of the pulmonary circulation, Pollack *et al.* [85], broke down the pulmonary tree into multiple segments to assess the pressure wave travelling effects in each of them and to quantify the reflection. The proposed model of a human pulmonary arterial tree has 55 arterial segments, each segment being represented by an electrical configuration of resistors, compliances and inductances, arranged based on structural rules deduced from a human lung cast. A function generator coupled with a diode simulated the right heart and the pulmonary valve and variable resistors were used at the end of each arterial branch, for branches with radius smaller than 2mm.

Using Fourier analysis, the authors decomposed the pressure wave into harmonic components and quantified the local and global reflection for the first 10 harmonics at several measuring points along the circuit. The local reflection coefficient, defined as the ratio of the reflected wave to incident wave, was found to increase towards the periphery and close to major tapering or bifurcation points within the system. However, the global

reflection coefficient computed as the ratio of all reflected waves generated at and downstream of the measuring point and incident wave, increases towards the inlet and varied with the frequency. Although an 'effective reflection site' was indicated at ~15 cm from the pulmonary valve, derived based on circuit impedance spectrum, the idea of several distributed reflection points was endorsed following the quantification of global and local reflection coefficients.

Huang *et al.* [86] experimentally validated a mathematical model of pulsatile flow for the whole lung. The pulmonary arteries and veins were treated as elastic tubes based on the Womersley [87] pulsatile flow solution, whereas for the capillary bed, a two dimensional sheet model was introduced. It was demonstrated that the modulus of the input impedance derived mathematically matched well the experimental results for frequencies lower than 7Hz. The importance of a good representation of the input pulmonary impedance in the low range frequencies was noted [73], [88] as important, being indicative of the 'pulsatile work' performed by the right ventricle to push the flow through the vasculature.

A 1-D model of the pulmonary circulation in man, with direct clinical application, based on morphometric and patient specific data for the pulmonary arterial tree was proposed by Spilker *et al.* [89]. With the purpose of predicting treatment outcome, the authors developed a 1-D model of the pulmonary arterial tree, with the proximal domain (main arteries) derived based on MRI images of a patient and solved numerically, using 1-D non-linear Navier-Stokes equations. The outflow boundary conditions were specified using arterial trees constructed from morphometric data of human lungs. For each outlet of the main domain, a morphometric arterial tree, solved recursively based on the Womersley solution for pulsatile flow, was tuned to match the inlet flow and pressure. The proposed model was clinically applied to simulate the haemodynamic improvement introduced by stenosis removal for patients with the congenital heart defect of tetralogy of Fallot. The same idea, of using MRI patient specific derived geometry for the main pulmonary arteries, with 1D tree structures for the outlets was later used [44, 45] to simulate haemodynamic changes in normal volunteers under PH conditions. Unlike in the study of Spilker *et al.*, who tuned their outflow trees based on morphometric data, Olufsen *et al.* [44] and Qureshi *et al.* [45] used asymmetric structural trees. Although the first approach has more realistic outlet boundaries, taking into account the observed trifurcations and not only the bifurcations considered in a structured tree, tuning the trees requires measurements of both inlet flow and pressure. The second approach requires the specification of the inlet flow and minimum radius. The latter parameter was shown to influence the input impedance of the structural tree [90]. The

structural trees can be tuned to match the inlet conditions, as showed by Clipp and Steele [50], although they will still miss the level of structural detail that can be achieved through a morphometric model. In this model, the authors proposed a pulmonary arterial 1-D model based on sheep lung cast data for the major arteries, and modified structural trees for the outlet boundary conditions, taking into account the effects of respiration.

Several authors, [44, 45, 89] showed that their models can be used to simulate the pulmonary haemodynamics in health and disease. The stenotic condition in tetralogy of Fallot [89], as well the changes induced by pulmonary hypertension [44, 45], were simulated by altering the parameters of the model, on a healthy volunteer test case. The results provided in [44, 45], concerning the manifestation of PAH, CTEPH and PH associated with a hypoxic lung, were compared with relatively sparse literature data; neither of them was validated directly on a clinical cohort.

Being able to represent the pulmonary pressure and flow waveforms at different levels along the pulmonary circulation, in health and disease, has a crucial importance in quantifying the efficiency of the system. Although wave reflection quantification has shown potential in separating different categories of patients, when applied for the systemic circulation [69], [70], only a few studies [73], [74], [75], [76], [77], [78], [79], [80], [81] have been reported for the pulmonary circulation. Moreover, from these studies, even fewer were concerned with the human pulmonary circulation [75],[74], [81], whereas the others were performed in animals, mainly dogs and sheep. Furthermore all of the studies, both for animals and for human subjects, were performed using invasive pressure measurements.

van den Bos *et al.* [73] quantified the reflection in the pulmonary circulation of dogs under the effect of serotonin (a vasoconstrictor), arguing that this can simulate hypertension conditions. Serotonin increased the total pulmonary resistance, reduced vascular compliance and increased the reflection coefficient, on average, to almost double the control value. In another dog study, Hollander *et al.* [78], confirmed the finding of increased reflections when the subjects were subject to hypoxic conditions, which have a similar effect to serotonin administration. Furuno *et al.* [80], in another study on dogs, artificially induced emboli and constricted the pulmonary arteries. A mid-systolic flow deceleration was reported in half of the subjects with constriction, which was hypothesised to be induced by the backward travelling wave. Since this phenomenon was observed only in 50% of the cases, no clear conclusion was drawn. The wave reflections were found to be higher under constriction, whereas embolization had no significant effect. Later, Castelain *et al.* [81] reported the mid-

systolic flow deceleration in human data. An increase of reflections in pulmonary hypertension patients was demonstrated by Laskey *et al.* [75], who compared humans with and without PH at rest and exercise. As found by van den Bos *et al.* [73], the increase in the wave reflection for the PH condition almost doubled. The effect of exercise was minimal in both patient groups. Huez *et al.* [74] analysed the pulmonary vascular impedance in PAH patients and computed the reflection index as the ratio between the difference and the sum of the input impedance at $\omega=0$ and the characteristic impedance. The results were found to be similar to those of the PH group of Laskey *et al.* [75]. In all of these studies the wave reflections were quantified in the main pulmonary artery. Only Smolich *et al.* [79] and Pollack *et al.* [85] reported reflection indices at levels other than the MPA. Smolich *et al.* [79], in a study on sheep, analysed the effect of embolisation in both main and left pulmonary artery, showing elevated backward reflected waves at both locations. Pollack *et al.* [85], using an electrical analogue, multi-compartment model of the healthy human lung, quantified the local and global reflections at multiple sites. The main pulmonary artery bifurcation was identified [85], [76], [78], [79] as one of the reflection sites, and they attributed the effect to the impedance mismatch introduced by the main arteries tapering.

The above section emphasises the importance of the 0D and 1D computational models in inferring the status of the pulmonary circulation in healthy individuals and subjects with pulmonary hypertension, underlying the value which can be added by integrating them into clinical practice for non-invasive PH diagnosis.

THESIS OUTLINE

The work developed during the course of PhD has been organised into four main chapters aiming to support the non-invasive characterisation of the pulmonary circulation in healthy and patients with pulmonary hypertension. The first chapter, this *Introduction and Literature review*, ‘sets the scene’ by introducing the clinical problem, emphasising the role of computational models for the PH diagnosis. Chapter 2 of the thesis, *From MRI images to area, flow and pressure waveforms as input for the mathematical models of pulmonary circulation*, describes the implementation of a workflow for processing MRI images of the pulmonary arteries in order to supply the mathematical models with personalised, patient specific, measurements: area, flow and radius based pressure surrogate. In Chapter 3, *0-D and 1-D model of a straight elastic thin-walled tube, for non-invasive pulmonary hypertension assessment*, two simple mathematical models are implemented and tested on a cohort of

healthy volunteers and patients who were clinically investigated for PH. Chapter 4, *Alternative, non-invasive PH diagnosis based on combining mathematical models and anatomy derived bio-markers into tree classifiers*, proposes a method which integrates computational markers for PH diagnosis computed in this thesis (chapter 3) with other clinical PH markers existing in the literature into a machine learning algorithm for the non-invasive diagnosis of PH. In order to contribute further to the accurate, non-invasive assessment of pulmonary hypertension, a finite element method (FEM) based model to solve a 1D pulmonary arterial tree linear system was implemented and described in Chapter 5, *Finite Element Model for 1D a Branching Tree of Pulmonary Arterial Circulation*. Finally, Chapter 6, *Conclusions, limitations and future work*, summarises the findings and lays out the new directions.

CHAPTER 2

From MRI Images to Area, Flow and Pressure Waveforms

MOTIVATION

In order to compute the patient-specific parameters in 0D models, including the Windkessel family, pressure and flow waveforms are required [91]. In 1D models the travelling wave can be decomposed into its forward and backward components from pressure and flow waveforms measured simultaneously at a specific location. Phase-contrast magnetic resonance (PCMR) imaging can provide accurate and reliable flow measurements, whilst the pressure in the pulmonary vasculature is currently measured invasively, using right heart catheterisation (RHC).

In this thesis, the focus is on the use of non-invasive in vivo measurements, with radius (again measured by MR imaging) rather than pressure changes over the cardiac cycle as an input. The correlation between changes in radius and pressure over the cardiac cycle has been studied by several groups [92], [93] (aorta), [94], [95] (coronaries) and pulmonary circulation (MPA), [96], [97]. These published correlations, together with data collected in Sheffield, have been used to compute pressure waveforms from measured radius waveforms.

In vivo, the arterial wall is viscoelastic, being composed by both elastin and collagen fibres. Under pressure, the two behave differently and a material made of the two exhibits a non-linear stress-strain relationship. Moreover, during loading and unloading, the changes in radius under pressure follow a different path, best described as a hysteresis curve. It is however assumed, that under very small variations of stress and strains, the hysteresis can be described as a straight line, and therefore, the material can be considered to be elastic. For the simplicity of the area-pressure model applied in this thesis, this assumption has been considered and the vessel wall is considered elastic, obeying the Hooke's law.

These derived pressure waveforms, together with the flow waveforms from PCMR, are the input of the proposed mathematical models of this PhD thesis. The temporal changes in radius, used as pressure surrogate, and the flow waveforms were acquired simultaneously using two co-registered in time and space MRI sequences: radius was measured using a Balanced Steady State Free Precession (bSSFP) sequence and flow using Phase Contrast (PC) sequence. This chapter describes the workflow used to obtain reliable flow and pressure (radius as surrogate) from MRI images of the pulmonary arteries.

PULMONARY ARTERY MR IMAGE ACQUISITION

Magnetic resonance imaging (MRI) is a non-invasive, non-ionizing technique used for both qualitative and quantitative inspection of the cardiovascular system (the heart and blood vessels). The two pulse sequences used for data acquisition are briefly described in the following sub-sections.

2.1.1 Pulse sequences

Phase contrast (PC)

The phase contrast sequence is widely used in clinical practice for blood flow quantification. The sequence is underpinned by the measurement of phase shifts of blood's transverse magnetisation [98]. The sequence depends on the application of bipolar gradients as shown in Figure 2.1. After the positive lobe of the first gradient is applied both stationary and moving spins change their position and register a phase shift. Then, when the negative lobe of the gradients is applied the stationary spins recover their initial phase, but the moving ones acquire some phase. Applying the same procedure with an inverted bipolar gradient and subtracting the two sets of data will eliminate the stationary spins phase shift introduced by the first gradient [99].

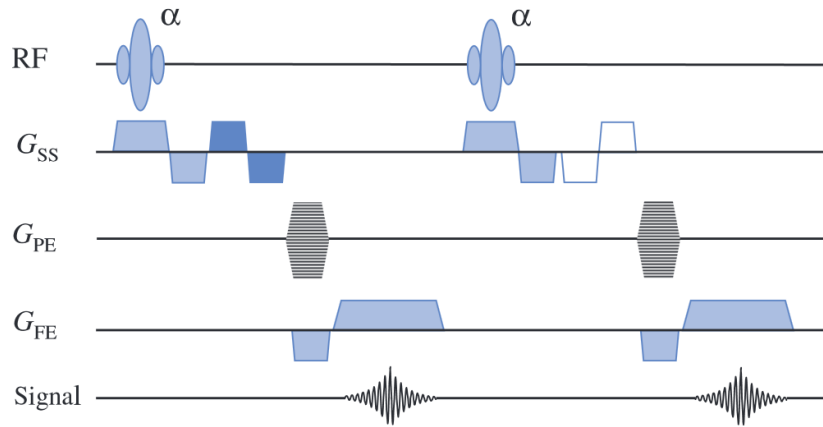


Figure 2.1 Phase contrast (PC) sequence diagram based on a spoiled gradient echo sequence (SPGR)

RF-radio frequency pulse, G_{SS} –slice selection gradient, G_{PE} -phase encoding gradient, G_{FE} – frequency encoding gradient, α –flip angle

Figure 14.9 a, “cine phase contrast velocity mapping”, page 299, Chapter 14, Donald W. McRobbie, E.A.M., Martin J. Graves and Martin R. Prince, *MRI from picture to proton* [98] with permission from Cambridge University Press.

The phase shifts produced by the moving spins with a known constant which links velocity (v) and phase angle ($\Delta\phi$), [98], are used to determine the velocity of the blood flow (Eq. 2.1).

$$v = \frac{\Delta\phi V_{enc}}{\pi} \quad (\text{Eq. 2.1})$$

The V_{enc} parameter is defined by [98] as ‘the velocity that produces a phase shift of π radians’ and is expressed according to relation (Eq. 2.2).

$$V_{enc} = \frac{\pi}{\gamma\Delta M_1} \quad (\text{Eq. 2.2})$$

where, γ is the gyromagnetic ratio and ΔM_1 is the difference between the two moments of the two bipolar gradient pulses used for velocity encoding.

The PC sequence produces two images for each slice, a magnitude image and a phase image. Magnitude images are used for anatomical orientation [100] whereas the phase images contain information about velocity of the fluid in every pixel. Although in principle the magnitude image can be used to delineate the vessel area, the main disadvantage of this approach is that extraction of accurate area during the diastolic period, when there is low flow in the PA and therefore low signal, is difficult because the vessel contour is not as well defined as during systole. To overcome this problem a balanced steady state cine anatomical sequence (bSSFP) with better vessel/blood delineation was used to extract the dynamic radius changes during the cardiac cycle (Figure 2.2).

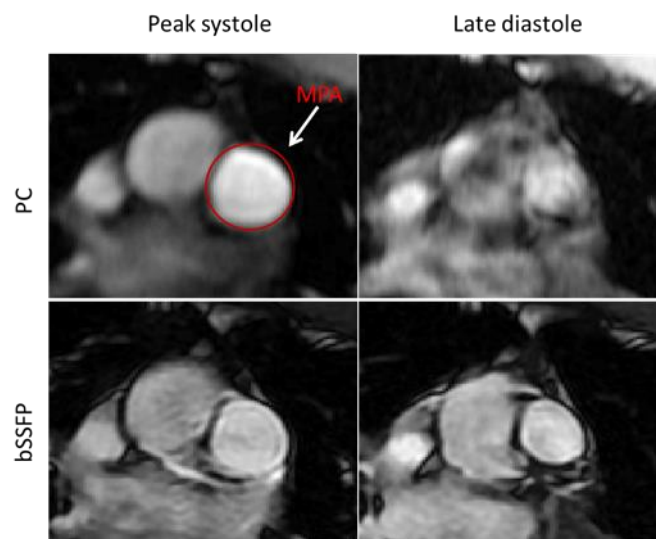


Figure 2.2 Typical PC magnitude and bSSFP images of the MPA, during the peak systole and late diastole

Images acquired using the bSSFP sequence have better blood to vessel delineation than PC magnitude images. The advantages of the bSSFP sequence are visible mainly during the diastole.

Balanced Steady State Free Precession (bSSFP)

The bSSFP sequence is a type of gradient echo sequence, with contrast dependent on the T2/T1 ratio. This technique is often used in clinical application for imaging the blood vessels due to the bright signal from blood (blood presents a high T2/T1 ratio). Also, due to the high signal-to-noise ratio (SNR) and short repetition time (TR) [101], the images can be acquired quickly and give a high level of anatomical detail. The pulse diagram of the bSSFP sequence is shown in Figure 2.3.

The above mentioned advantages make bSSFP a better choice in tracking the contour of the vessel than the SPGR PC images, used by other authors [102], [43]. The use of separate sequences for pressure and flow does, however, introduce its own issues of spatial and temporal registration between separate datasets, discussed in the following sections.

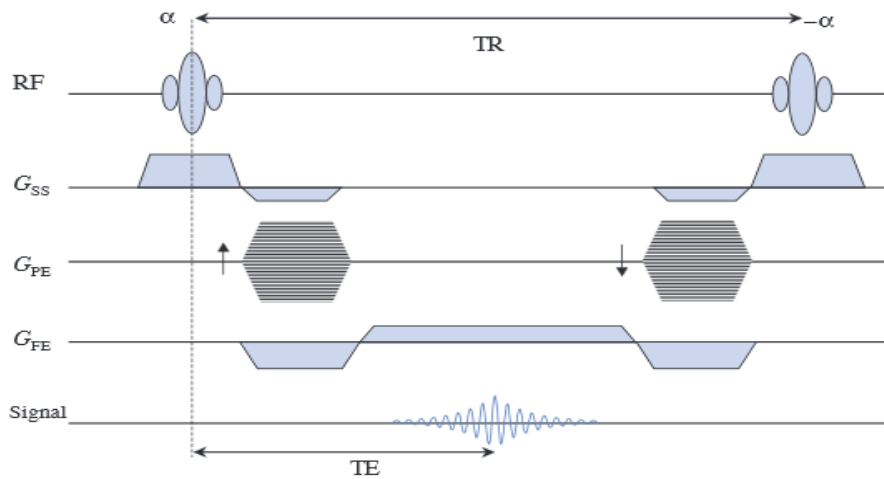


Figure 2.3 Balanced steady state free precession (bSSFP) sequence diagram from [98]
 RF-radio frequency pulse, G_{ss} –slice selection gradient, G_{PE} -phase encoding gradient, G_{FE} – frequency encoding gradient, α –flip angle
 Figure 12.28, “True FISP sequence”, page 247, Chapter 12, Donald W. McRobbie, E.A.M., Martin J. Graves and Martin R. Prince, *MRI from picture to proton* [98] with permission from Cambridge University Press.

2.1.2 Sequences parameters

Using the previously described sequences, 40 cardiac images of the main, right and left pulmonary arteries were acquired for each sequence retrospectively, orthogonal to the pulmonary trunk, using ECG gating, during breath-hold on a GE HD x1.5T scanner.

Figure 2.4 shows an acquisition diagram for an ECG gated MR sequence. The acquisition starts after the R wave is triggered and the number of selected views is sent to the image ‘k-space’.

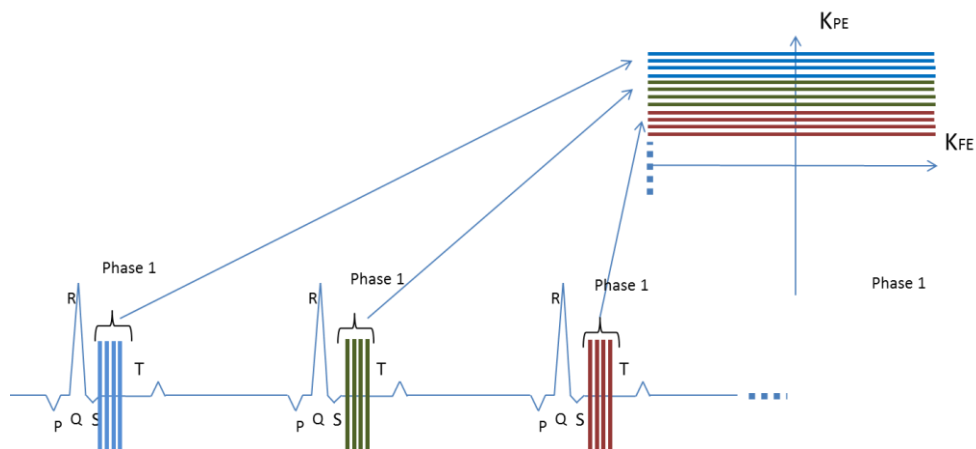


Figure 2.4 ECG gated acquisition with four view per cardiac cycle

Before the parameters for each artery and sequence were established, the arteries were localised using sagittal and coronal views (Figure 2.5).

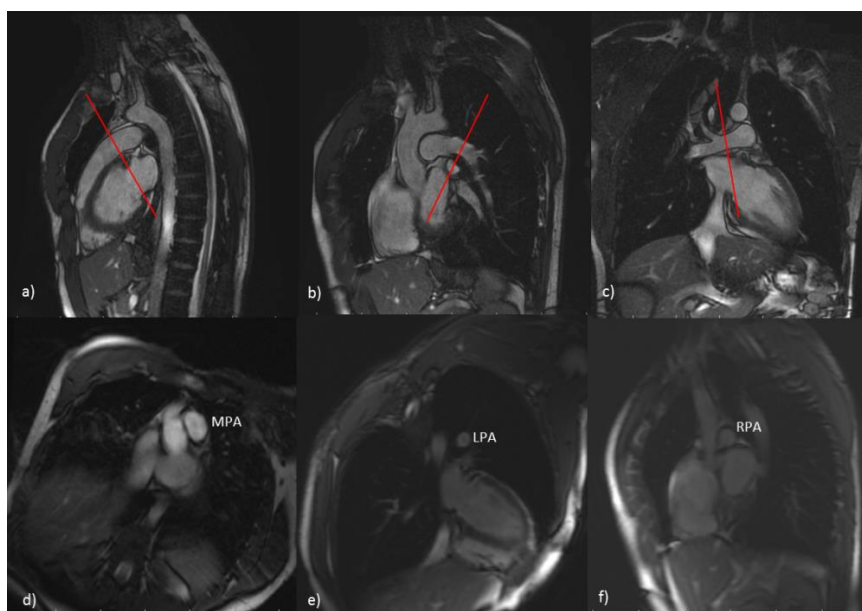


Figure 2.5 The choice of the localizer plans and the corresponding axial view for MPA, LPA and RPA.

a) and d) sagittal and axial view of MPA, b) and e) sagittal and axial view for LPA, c) and f) coronal and axial view for RPA.

The PC and bSSFP images were spatially and temporarily synchronised, using the same pixel size (256x 128 matrix dimensions, 480x 288 mm FOV) and the same number of cardiac images (40). For the PC sequence a value of $V_{enc} = 150\text{cm/s}$, 5.85 ms repetition time (TR) 2.87 ms echo time (TE) and 10% arrhythmia rejection. For the bSSFP acquisition, a 3.73ms TR and 1.62 ms TE were used.

PROCESSING OF MR IMAGES TO DERIVE AREA, FLOW AND PRESSURE WAVEFORMS

2.1.3 Image segmentation

Image segmentation is a type of image analysis and interpretation characterised by separating a digital image into different parts [103], depending on the established aim. A typical 2D MR image of the main pulmonary artery (MPA) is shown in Figure 2.6. Quantification of area and flow in the MPA (or any other blood vessel) requires the vessel

cross-section to be separated from the background and surrounding anatomical structures (heart, blood vessels etc).

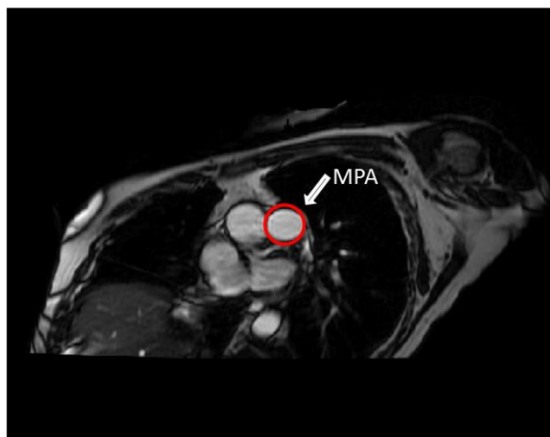


Figure 2.6 MR image of the main pulmonary artery

A 2D cross-sectional slice of the main pulmonary artery from a bSSFP sequence

The extraction of the region of interest (ROI) from an image can be performed in various ways. The current gold standard is by manual segmentation, where the operator has exclusive control on segmenting the appropriate structure. The main drawbacks of the method are: long processing time (especially for segmenting time series images), and reproducibility, being susceptible to high inter- and intra-operator variations. It is expected that an experienced operator will draw the contours of the objects faster and more accurately. At the other extreme, automatic segmentation is reproducible and can be faster, but is not always accurate. The advantages and limitations of automatic segmentation algorithms were addressed by Sharma and Aggarwal [104] in a comprehensive review on MR and CT medical image segmentation. A semi-automatic segmentation approach can be used as a compromise between the two methods. The method adopted in this thesis minimises the operator's intervention to the initialisation and final approval of the segmentations performed automatically.

A Graphical User Interface (GUI) was implemented in MATLAB (The MathWorks, Inc) to test the reproducibility (inter- and intra-observer variability) and efficiency for segmenting the main pulmonary arteries: MPA, RPA and LPA. The manual segmentation was compared with a semi-automatic segmentation approach, based on image registration, applied to derive the

area and flow waveforms used further as input for the mathematical models. Figure 2.7 displays the fields and functions available under the implemented MATLAB GUI.

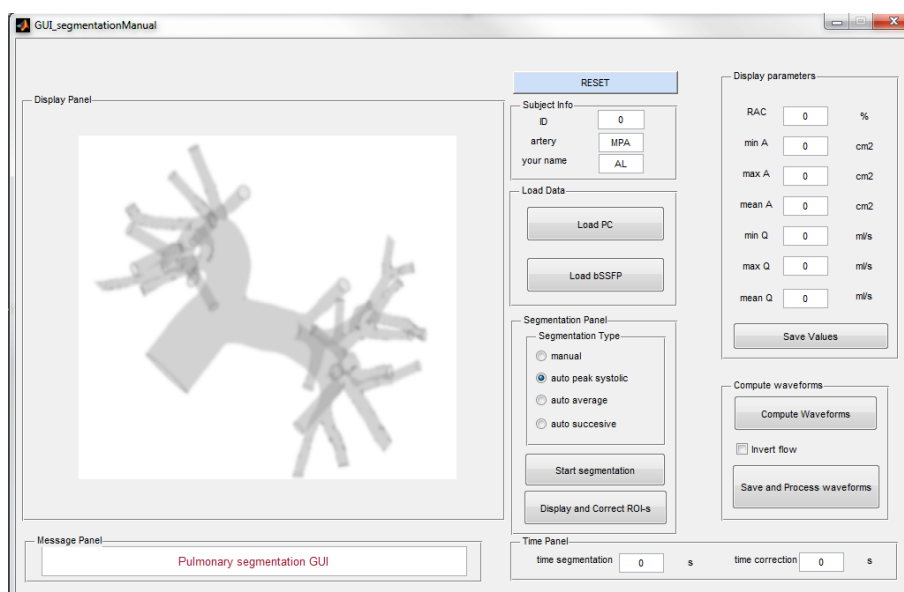


Figure 2.7 MATLAB segmentation GUI
Screen-shot of the starting window for the MATLAB segmentation GUI

The workflow behind the segmentation GUI follows logical steps:

- load the PC and bSSFP data corresponding to the patient to be analysed by pressing the corresponding push-buttons from the *Load Data* panel. The patient study ID, name of the segmented anatomical structure and operator's name are specified within the *Subject Info* panel.
- select the type of segmentation that will be performed from the *Segmentation Panel*. A manual and three semi-automatic, registration-based-segmentations (discussed in details on the following sections), are available under the *Segmentation Type* panel. The segmentation starts at the press of *Start Segmentation* push-button and requires the operator to place a rectangular mask on the vessel to be segmented. All the images are cropped according to the size of the applied mask. The segmentation is performed by placing a series of discrete points around the artery, in each of the 40 time frames for the manual segmentation, or in just one image for the semi-automatic procedures.
- display and correct (if necessary) the generated vessel contours. The images are displayed together with the generated contours, frame-by-frame, allowing for manual corrections.

- compute the area and flow waveforms inside the artery. The flow and area waveforms are computed and displayed on the *Display Panel*.
- save and process the generated waveforms.

Intermediate messages, which serve to guide the operator through the workflow, are displayed in the *Message Panel*.

The segmentation and correction times are displayed and saved after each patient data set is analysed. The segmentation time records for the manual segmentation the time necessary for an operator to draw the contour of all the images in the time series. For the semi-automatic segmentations, it indicates the time an operator takes to segment the initial, start image, added to the actual computation time of the sequence. The correction time, as suggested by the name, indicates the time an operator takes for manual corrections. It is expected that the correction time for the manual segmentation should be minimal (equal to the time of visualising each slice), whereas for the semi-automatic segmentations it will vary; a short semi-automatic correction time will indicate that the automatic algorithm produced segmentation close to the operator expectations, minimising intervention. A longer correction time will suggest additional intervention by the operator on the automatically produced ROIs in order to obtain segmentations close to expectations.

A *Display parameters* panel was added to provide further information, computing and displaying a few simple parameters such as minimum and maximum area and flow, relative area change and mean flow.

2.1.3.1 Manual segmentation

Manual segmentation is considered to be the gold standard in the field of right heart and pulmonary artery MRI analysis. The human eye can distinguish image artefacts from the real anatomical structures and can ignore them. Unfortunately, because of different interpretations about where exactly the vessel wall should lie, manual segmentation is subjective and liable to the inter observer variability. Even more, segmenting a stack of temporal images is not only time consuming, but introduces variation even in the vessel contour appreciation from one time instance to another.

Three operators, two with previous experience in segmenting medical images (operator 1 and 3) and one non-specialist (operator 2), who never performed any type of segmentation, were asked to draw the vessels contours for the principal pulmonary arteries: MPA, RPA and LPA. Each data set corresponded to one artery having 40 time instances. One of the operators

(operator 1) segmented the arteries twice, a week interval between segmentations. The operators were blinded to the results of the other colleagues and no previous training, except the indication of which structure represents the targeted vessel in the image, was offered in the first instance.

2.1.3.2 Semi-automatic segmentation

Minimising operator intervention and reducing the segmentation time, especially in the clinic, where time spent on any intermediate process contributes to the total clinical diagnosis time, is highly desirable. A totally automatic process is ideal, but image artefacts or anatomical structures similar in shape and intensity present in the same image can affect the results of the automatic process. ‘Keeping the operator in the loop’ for initialisation and final approval/corrections of the results can produce a good trade-off between manual and fully automatic segmentation.

The semi-automatic method proposed in this thesis to extract the pulmonary artery cross-section from the MR images in order to derive the area and flow waveforms is based on image registration.

Operator input

The operator input was limited to:

- Reducing the size of the original image by applying a rectangular mask on the area where the PA is positioned. This step was performed for two reasons: to ‘zoom in’ and better position the initial vessel contour and for speeding up the process
- Draw the contour of the vessel in only one image from the time series. The choice of the “drawing image” is explained in the image registration section
- Display, approve and if necessary, correct the slices where the automatically generated segmentation might have failed

Both segmentation and correction time were recorded and compared with the manual segmentation time. The inter- and intra-operator variability was tested in the same manner as for the manual segmentation: three operators, two with previous segmentation experience and one without were asked to initialise and approve the semi-automatic segmentation generated ROIs.

Image registration

Image registration is widely used across different domains such as: cartography, topography, landscape, satellite weather forecast, motion detection, security, photography editing and

processing and medical imaging [105]. The area of medical imaging registration has gained increasing interest for clinical applications. Underlining the differences between registered images can help with: better diagnosis (combining functional imaging PET with anatomy imaging MR), treatment follow-up (images of the same patient acquired before and after surgical intervention), disease classification (by registering the patient image to a medical atlas) etc. In a comprehensive review on medical image registration, Maintz and Viergever [106] highlight the most common applications, in the context of the image acquisition modality as well as of the area of the human body/organ which was investigated.

Registration has been defined [103] as a process of aligning points from two different images using a geometrical transformation. More precisely, for every point in an image, characterised by a set of coordinates, a function can be written that will “move” that point to the corresponding point in the second image. The relationship between the two points is usually known as mapping function [107], and for the two points, characterised by coordinates (x,y) and (x',y') , one can write (Eq. 2.3):

$$\begin{aligned}x' &= u(x,y) + x \\y' &= v(x,y) + y\end{aligned}\tag{Eq. 2.3}$$

where (u,v) is the mapping function in 2D.

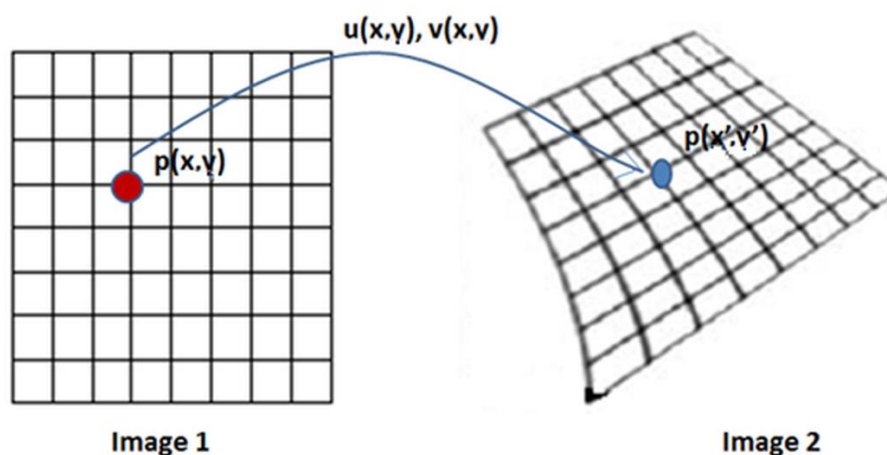


Figure 2.8 Mapping function for a point present in 2 images

Assuming point P is present in both Image 1 and Image 2, but allowing for them to be in different locations within the images, the mapping function will describe the movement required to get from the first location in Image 1 to its corresponding location in Image 2.

The transformation function (mapping) between any pair of images (referred to as fixed and moved, or target and source image) can be used to project any series of points identified in one image into the other image. In this way, if the closed contour of points defines an object in image 1, the same object (if present) can be easily identified in image 2. Separating an object from the surrounding elements and background is exactly how segmentation was defined earlier.

The technique of registration-based segmentation has been already applied in several studies for (semi-) automatic segmentation of different organs or larger anatomical regions, as for example, the abdomen cavity. Few of these applications are included in the following: Barber and Hose [108] were the first proposing this method as a medical application for knee and kidney contour delineation. Odille et al. [109] implemented the method for segmenting the aortic cross-section. Later, the same group applied the technique to a study concerning the bowel movements [110]. Quail et al. [111], used the registration-based segmentation for extracting artery cross-section from 2D time-series of the pulmonary artery. Randall et al. [112] used the registration-based segmentation to extract the contour between two motion regions for identifying abdominal adhesions. The above exemplified applications are concerning the automatic ROI extraction from 2D images. Other applications of the registration-based segmentation technique, although they do not represent the focus of the work described in here, are obtaining the 3D geometry from patient specific data based on model deformation. The method relies upon constructing a general 3D model (usually having an ideal structure of the organ to be segmented), which undergoes shape deformation,

following the registration of the patient's 3D images to the general model, as shown in [113], [114].

The registration algorithm used by Barber and Hose [108] is available under the departmental registration toolkit, ShIRT (Sheffield University Registration Toolkit) and it can be run either from the command line or through the MATLAB to ShIRT interface, IRLab. The pulmonary artery image segmentation process represents in this thesis only one of the steps required for testing the research hypothesis. The reliable results obtained in the previous studies using ShIRT [108, 112, 114-118] were one of the main reasons for taking advantage of the toolkit availability within the department, and use its functionality for the process of non-invasive assessment of pulmonary hypertension.

As described in [108] and later in [113], the registration algorithm implemented under ShIRT minimises the residual between the voxel intensities of the two images, in the sense of the sum of the squares of the difference (SSD). The algorithm deals however with the main limitation of the SSD method (high intensity difference may lead to incorrect mapping), by expanding the images dimensionality by one, in the intensity direction.

More precisely, if u and v are the mapping functions that relate the 2D moved image \mathbf{m} to the fixed image, \mathbf{f} , the relationship between them can be described by (Eq. 2.4):

$$f(x, y) = m(x + u, y + v) \quad (\text{Eq. 2.4})$$

By extending dimensionality, ShIRT's authors expressed \mathbf{f} and \mathbf{m} as binary images, f_b and m_b , in three coordinates: x , y and s . s stores the pixel intensities from the original grey level images, \mathbf{f} and \mathbf{m} (Eq. 2.5).

$$f_b(x, y, s) = m_b(x + u, y + v, s + h) \quad (\text{Eq. 2.5})$$

Equation (Eq. 2.5) is the starting point for defining the cost function which ShIRT minimises during the registration. The final cost function depends on two parameters: the nodal spacing, NS and the smoothness constraint, λ . The mapping functions are defined at discrete points (grid nodes) in x and y , taking interpolated values at the intermediate points. The NS is defined by an integer number and represents the distance (in pixel spacing) between two discrete nodes. The smaller the node spacing, the better the image is registered, but also this would increase the execution time. The λ parameter is a weighting of the smoothness constraint added in order to obtain a unique registration solution. As stated in the description of the registration algorithm [108], λ is chosen to optimise the condition number of the

matrix to be inverted in the solution process and its value depends on the application. A smaller λ will generate a less smooth and less stable mapping. However, a larger λ might constrain the solution too much.

The influence of NS and λ was tested in [113] for the registration of 2 different 3D geometries (aorta and carotid artery). The λ parameter was varied between 5 and 100, while two NS values, 2 and 4, were used to generate the patient specific geometries. The mean diameters of the aorta and carotid artery were compared, while the above mentioned values were applied. At NS of 2 or 4 similar results were obtained, while no clear optimal values could be indicated for λ .

Using a λ value of approximately 30 and NS=4, Fenner et al. [118] obtained reliable results for the registration of abdominal images.

For the purpose of the semi-automatic segmentation of the pulmonary arteries, the default λ value of 30 was used, while the NS values of 2, 4, 6 and 8 were tested. The quality of the segmentations, assessed visually, was similar for all the above stated NS. Based on these observations, and the values stated in [113] and [118] the default NS=4 was also used in this study. Each data set to be segmented contained a series of 40 temporal frames.

As discussed in [109], the choice of the reference image is important. It is recommended to choose an image which is not very different from the moved images. For this, three different approaches (cases) of extracting the blood vessel position and area were evaluated, differentiated by the choice of the fixed image in the registration process: the three choices for the fixed image were the one corresponding to peak systole, the average image over the cardiac cycle and successive registration of each image in the time series.

Case 1: peak systolic image chosen as fixed image

At peak systole the blood flow in the artery reaches the maximum and usually it determines a clear vessel contour, with better defined edges, making it suitable as a reference image. The rest of the images in the time series were considered moved images and registered one by one to the fixed image. The contour of the PA was drawn in the peak systolic images, and the inverse mapping resulting for each moved to fixed image registration was applied to determine the PA ROI for entire set of images. Figure 2.9 shows a schematic representation of the 'case 1' segmentation process

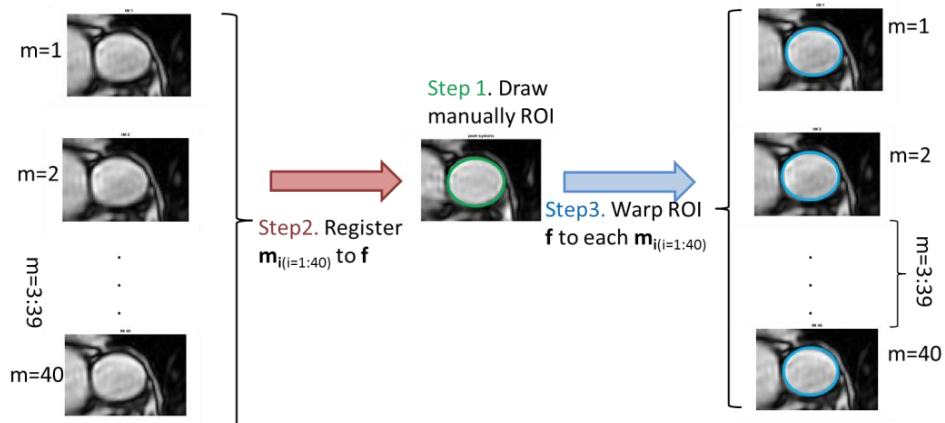


Figure 2.9 Registration-based segmentation: case 1, peak systolic fixed image

At *Step 1* the fixed image, corresponding to the peak systolic image, is displayed and the vessel contour is drawn (green). The rest of the images from the time series are registered one by one into the fixed images, during *Step 2*. At *Step 3*, the inverse mapping is applied to warp the ROI from the fixed image into the moved images, resulting the final ROIs (blue).

Case 2: average image of all the slices used as fixed image

Case 2 is based on the same principle as *case 1*, registering all the moved images, one by one, into a fixed image. This time, the fixed image was chosen to be an average registered image of all slices. The method was proposed by Barber and Hose [108] for segmenting human kidneys. A first average, used as a temporary fixed image, was created from all 40 images of the time series. All 40 images were considered moved images and registered to the temporary frame. The resulting registered images were averaged again, creating a new fixed image where all the original frames were registered as moved images. The rationale of the registered average was that an average can work as a denoising filter, reducing some artefacts, but cannot necessarily guarantee the correct position of the vessel. That is why an intermediate step of registration was necessary.

Case 3: successive registration of each image in the time series

In the third case of segmentation, all the images played a dual role: fixed and moved image. The algorithm starts with the first frame as the fixed image and the second frame as the moved image. After manually defining the borders of the PA in the first frame, the images were registered, and a new ROI, corresponding to the second frame was obtained. On the next time step, the previous moved image was used as the fixed image and the third frame from the sequence was used as the target (moved) image. Instead of drawing again around the artery wall, the ROI generated from the previous time-step was used. The algorithm was then continued until the last slice. A graphical explanation of the process is presented in Figure 2.10.

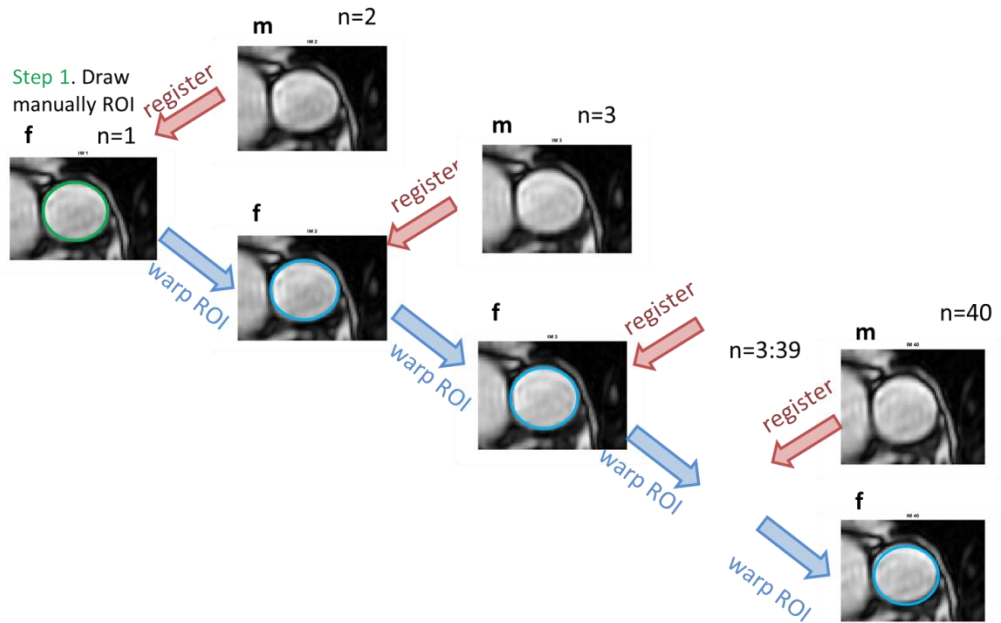


Figure 2.10 Registration-based segmentation, case 3, sequential segmentation of the time series.

At *Step 1* the contour of the vessel is drawn (green) onto the fixed image, selected as the first image of the time series. At *Step 2*, image 2 (moved) is registered to image 1 and ROI 1 manually drawn is warped, generating ROI 2. At *Step 3* image 3 (moved) is registered to image 2 (which became fixed) and ROI 2 is warped into image 3, generating ROI 3. The process continues until image 40 is registered to image 39 and ROI 39 is warped to obtain ROI 40. The only manually drawn contour is the one represented in green in the figure. The blue ROIs are automatically generated.

All three operators segmented the fixed image for the main, right and left pulmonary, for each of the three cases. The resulting binary masks, containing 1 inside the ROI and 0 outside, were used to compute the area of the vessel corresponding to each temporal phase and as a mask for the phase images in order to extract temporal flow waveforms.

2.1.4 Area computation

In each of the 40 temporal frames, cross-sectional area was computed by multiplying the area of a pixel with the number of pixels inside the ROI (Eq. 2.6).

$$A(t) = n_p \cdot ps_x \cdot ps_y \quad (\text{Eq. 2.6})$$

where n_p is the number of pixels with value 1 (all pixels inside the ROI), ps_x is the pixel size in x direction (Eq. 2.7), ps_y is pixel size in y direction (Eq. 2.8)

$$ps_x = \frac{FOV_x}{N_x} \quad (\text{Eq. 2.7})$$

$$ps_y = \frac{FOV_y}{N_y} \quad (\text{Eq. 2.8})$$

where FOV is field of view in x and respectively y direction, N_x is the matrix dimension in x, N_y is the matrix dimension in y

2.1.5 Flow computation

The masks obtained from the segmentation were applied to the phase contrast (PC) images in order to isolate the pixels containing the phase shift introduced by the moving spins inside the pulmonary arteries.

During the PC sequence acquisition, the scanner multiplies the phase image by the magnitude one, in order to suppress the background noise [98]. Because of this aspect, computing the velocity requires the division between the phase and magnitude images.

For each temporal frame, an average velocity was computed (Eq. 2.9)

$$v(t) = \frac{1}{n_p} \sum_{n=1}^{n_p} \frac{\Delta\phi_p V_{enc}}{\pi} \quad (\text{Eq. 2.9})$$

where n_p is the total number of pixels inside the ROI, $\Delta\phi_p$ is the velocity phase shift inside the pixel and V_{enc} is the velocity encoding parameter prescribed within each phase contrast sequence.

For every time step in the cardiac cycle, the average flow was calculated using the area of the vessel multiplied by the corresponding average velocity (Eq. 2.10).

$$Q(t) = v(t)A(t) \quad (\text{Eq. 2.10})$$

2.1.6 From area to pressure waveforms

For a complete characterisation of the 0D and 1D models, information about flow and pressure are essential. The aim of this PhD project, non-invasive characterisation of the pulmonary circulation, requires finding a modality for the pressure waveform estimation.

Simultaneous measurements, during an entire cardiac cycle, of arterial pressure and diameter in animals and humans were reported by several research groups, for the systemic [92], [93] (aorta), [94], [95] (coronaries) and pulmonary circulation [96] (MPA), [97], [119] (RPA), showing strong resemblance between the two waveforms (Figure 2.11).

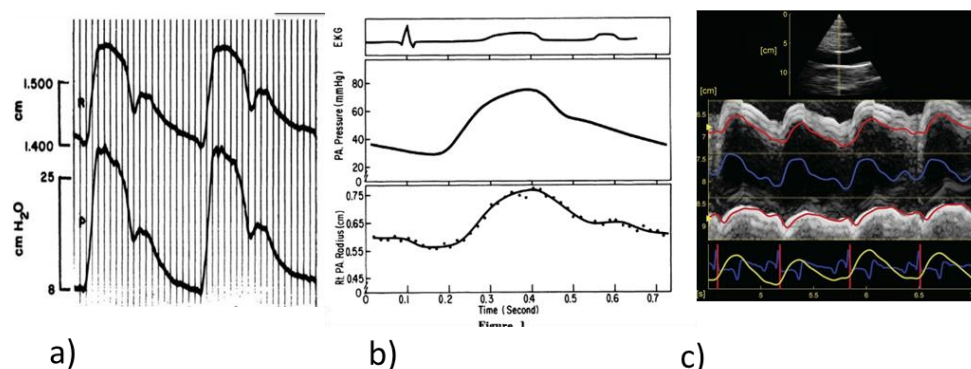


Figure 2.11 Simultaneous recordings of pressure and diameter in the pulmonary circulation

a) MPA (human), from Greenfield, J.C. and D.M. Griggs [96] b) RPA (human) from Jarmakani, J.M.M., et al. [97] c) RPA (calf) from Hunter *et al.* [119]

With permission given through Copyright Clearance Center's RightsLink service

In 1963, Greenfield and Griggs [96] measured the pressure and diameter of the human MPA in 11 patients undergoing open heart surgery (Figure 2.11 a), using a strain-gauge calliper. Three of the patients had pulmonary hypertension, with systolic and diastolic mean \pm SD of 87.37 ± 19.11 mmHg and 39.63 ± 6.01 mmHg, respectively. The systolic and diastolic pressure for the rest of 8 patients with no PH was 28.45 ± 4.68 mmHg and 10.98 ± 4.39 mmHg. The authors reported higher similarity between the MPA diameter and pressure waveforms than the one between the aortic diameter and pressure, studied previously [93].

Jarmakani *et al.* [97] studied the relationship between right pulmonary artery (RPA) radius and pressure in normal and children with congenital heart disease, 7 of whom had pulmonary hypertension. These authors also reported a considerable resemblance between the radius and pressure waveform (Figure 2.11 b).

More recently, using Doppler tonometry, Hunter *et al.* [119] studied the RPA pressure-diameter relationship in the neonatal calf under normal and hypertensive conditions. As displayed in Figure 2.11 c, there are gross similarities between the RPA pressure (yellow line) and diameter (blue line).

The reported similarities are more obviously emphasised by the pressure-diameter (PD) graphs. Figure 2.12 a shows the correlation between the MPA pressure and diameter waveforms reported by Greenfield and Griggs [96] after digitising the waveforms from the original paper. Figure 2.12 b, represents the original PD graph from Hunter *et al.* [119]. The graph distinctly displays the two groups analysed, emphasising that the PD relationship might be linearly approximated, with a different slope of the line for normal and hypertensive subjects.

A direct translation of the vessel diameter into pressure waveform was proposed by Niki et al. [120], in a study using Wave Intensity Analysis (WIA) to non-invasively assess wave reflection in patients with mitral regurgitation.

The authors proposed a linear scaling of the brachial pressure, measured with a cuff-type sphygmomanometer, to the carotid artery diameter. The linear pressure-diameter assumption was further tested by the same group [94], on 6 patients with heart disease, by simultaneous measurements of pressure (catheter) –diameter (echo-tracking) of the left carotid artery. The PD graphs of the study showed small non-linearity and hysteresis, behaviour specific to viscoelastic walls. However, the gross pressure-diameter behaviour was shown to be linear.

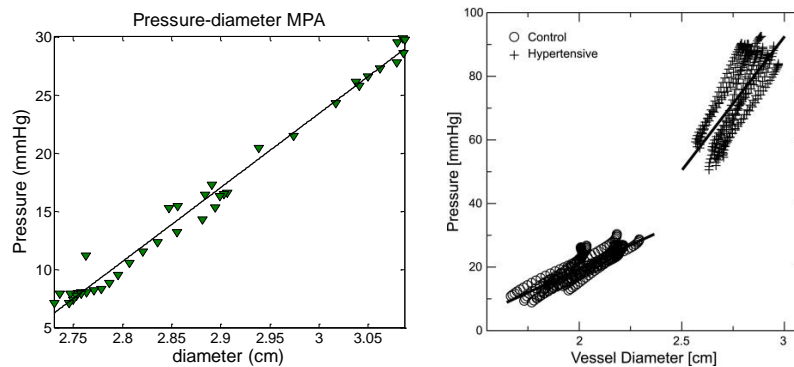


Figure 2.12 Pressure-diameter correlation for the pulmonary circulation
 (a) human MPA (normal) [96] (b) calf RPA (PH and normotensive) from Hunter *et al.* [119]

These experimental observations together with the argument that over small changes of pressure the PD relationship can be considered linear support the choice of a linear pressure-area relationship. A non-linear model taking into account the wall visco-elasticity can be mathematically implemented. Such a model will give a more realistic representation of the vessel wall behaviour but at the expense of a more complicated analysis. As stated in this introduction, the aim of this study is to infer the status of the pulmonary circulation based on simple, but clinically effective mathematical model.

Although the idea of scaling the measured pressure values into an area waveform, as proposed Niki et al. [120] can be valid, the range of pressures that could be obtained with a cuff-type sphygmomanometer from the branchial artery of a patient are outside the pressure range specific to the pulmonary or coronary circulation. Therefore, an alternative method for translating area into pressure is required in order to prescribe realistic pulmonary pressure

values. Feng and Khir [121] proposed a non-invasive WIA analysis which does not require any pressure measurement and no linear pressure-diameter scaling, making the method applicable to sites where no non-invasive pressure can be provided to be scaled as proposed by Niki *et al.* [120]. The principal assumptions in deriving non-invasive WIA method are that the vessel wall is elastic, thin, of circular shape and pulse wave velocity, c , can be derived from the linear slope between blood flow velocity (U) and natural logarithm of vessel diameter $-\ln DU$ loops [122]. Equation (Eq. 2.11) describes the relationship derived by Feng and Khir [121], which relates the small pressure changes to small changes of the vessel diameter (D). The pulse wave velocity, c (Eq. 2.12) is derived from $\ln(D)U$ loops [122], with the assumption that no reflections are occurring during early systole and the pressure and flow are linear for that period.

$$dP = 2\rho c^2 \frac{dD}{D} \quad (\text{Eq. 2.11})$$

$$c = \pm \frac{1}{2} \frac{dU_{\pm}}{d \ln D_{\pm}} \quad (\text{Eq. 2.12})$$

The WIA method of Feng and Khir [121] validated by the authors in vitro, using flexible tubes and a pressure pump generator, was later applied in healthy patients to derive local pulse wave velocity of the femoral and carotid arteries using Doppler echography [123], for evaluating wave reflections in patients with coronary disease, using MRI measurements [69] or in the pulmonary circulation to differentiate PH from no PH patients in a ‘proof of principle’ study of two subjects [124].

Using the same assumptions about the vessel wall (thin, circular shape with viscoelastic and dynamic effects neglected) and also considering that the vessel is formed from a series of rings, tethered axially and in static equilibrium at each time step, a pressure-area relationship is given by the equilibrium condition at the wall of the vessel [125].

The formula can be explained through the circumferential stress-strain relationship. The stress in the circumferential direction σ_{ϕ} is given by (Eq. 2.13).

$$\sigma_{\phi} = \frac{pR_0}{h} \quad (\text{Eq. 2.13})$$

where p – pressure, R_0 – minimum radius, h – wall thickness

The circumferential strain is given by the engineering definition of strain (Eq. 2.14).

$$\varepsilon_{\phi} = \frac{2\pi R - 2\pi R_0}{2\pi R_0} \quad (\text{Eq. 2.14})$$

In the conditions of plane strain for an elastic material, the Cauchy definition of stress relates stress and strain (Eq. 2.15).

$$\sigma_{\phi} = \frac{E}{1 - \nu^2} \varepsilon_{\phi} \quad (\text{Eq. 2.15})$$

where E is the Young's elasticity modulus, ν is the Poisson's ratio

After equating (Eq. 2.13) with (Eq. 2.15) and replacing (Eq. 2.14) the resulting equation relates pressure and radius non-linearly, through Young's modulus and Poisson's ratio.

$$p = \frac{Eh}{1 - \nu^2} \frac{(R - R_0)}{R_0^2} \quad (\text{Eq. 2.16})$$

Replacing the radius terms with the circular cross-sectional area terms in (Eq. 2.16) the tube law equation [125] is obtained.

Young's elasticity modulus and vessel wall thickness are difficult to assess in vivo. Peterson's elasticity modulus, E_p [126], relates diastolic radius to Young's elasticity modulus and wall thickness (Eq. 2.17) and it is derived from the measured changes in diameter and pressure (Eq. 2.18).

$$E_p = \frac{Eh}{R_0} \quad (\text{Eq. 2.17})$$

$$E_p = \frac{\Delta P}{\Delta D} D \quad (\text{Eq. 2.18})$$

At every moment in time during the cardiac cycle a pressure-radius relation, which takes into account the vessel wall elastic properties, can be written (Eq. 2.19).

$$p(t) = \frac{E_p}{1 - \nu^2} \frac{\delta R(t)}{R_0} + P_d \quad (\text{Eq. 2.19})$$

where P_d –diastolic pressure, δR –change in lumen area at every instant in time, R_0 –diastolic radius

The offset diastolic pressure (P_d) and the wall stiffness parameter (Eh), take different values in healthy subjects and in patients with pulmonary hypertension. In order to supply the model with appropriate values for each patient, three approaches are examined in this thesis, considering that both the 0D and 1D models require as input temporal pressure variation in the MPA:

1. Use the invasive reported data of Greenfield and Griggs [96] and create a model which relates P_d and E_p to the relative area change. The data set contains 11 patients,

3 of whom had pulmonary hypertension. The data was acquired during open chest surgery using a strain gauge-calliper device which simultaneously recorded the changes in pressure and diameter. A power law model best described the relationship between E_p and relative change in area ($R^2=0.88$). A strong relationship, ($R^2=0.79$), described also by a power law model, was found between P_d and RAC. Figure 2.13 a) and b), displays the two models on log-log axes.

2. Right heart catheter measured systolic and diastolic pressure and MRI calculated main pulmonary artery relative area change (RAC) acquired from 27 consecutive patients referred to the Sheffield Pulmonary Vascular Unit were used to derive the relationship between E_p and P_d for the second tested approach (Figure 2.13 c and d). A power law model showed good correlation between E_p (computed from the invasive RHC pressure data and diameter using (Eq. 2.18) and RAC ($R^2=0.78$). An exponential law best described the relationship between P_d and RAC, although the correlation is weak ($R^2=0.23$).
3. Combine the data provided by Greenfield and Griggs [127] with the data derived from the RHC available measurements. The main drawback of this approach is given by the different acquisition protocols employed for each data set. As mentioned above, Greenfield and Griggs [127] acquired the diameter and pressure simultaneously using a strain-gauge calliper device, during open heart surgery, while the pressure data from the Sheffield specialist centre were recorded during right heart catheterisation (RHC), and the diameter was measured following MRI images segmentation. However, in this case, the combination of the two data sets has its merit for two important reasons. Firstly, in order to meet the target of developing a diagnostic process for pulmonary hypertension, it is necessary to use underpinning data from individuals who have and do not have this disease. The Greenfield and Griggs data is especially valuable because it includes invasive catheter measurements on individuals who were investigated for another purpose, but did not suffer from pulmonary hypertension. The available RHC dataset is dominated by individuals with the disease, and includes only four cases in which the diagnosis was negative (clinical patients suspected of PH who received negative diagnosis upon RHC intervention – no PH). No invasive data were acquired on healthy volunteers. As for the previous two approaches, a power law best describes the E_p –RAC relationship ($R^2=0.77$). The P_d is best related with area change by an exponential law ($R^2=0.4$). Figure 2.13 e and f, displays the two models, E_p –RAC and P_d -RAC, on log-log and log-lin axes.

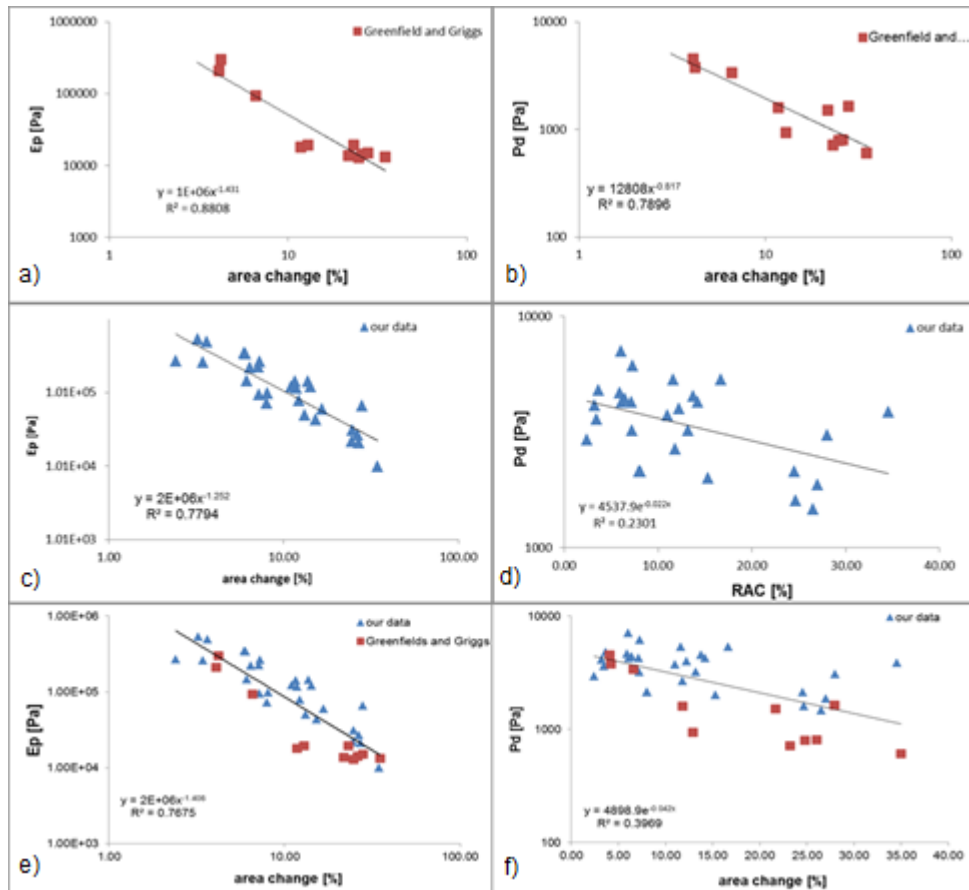


Figure 2.13 Relationship between Peterson’s elasticity modulus (E_p) and diastolic pressure (P_d) with relative area change (RAC) in the human MPA
 a-b) data from Greenfield and Griggs c-d) invasive data from a Sheffield cohort of 27 patients
 e-f) combined datasets from a-b) and c-d)

RESULTS AND DISCUSSION

2.1.7 Image segmentation

Manual segmentation is currently the gold standard for medical image segmentation. It has the advantage of human eye change rationality but this makes it highly operator dependent, introducing inter-operator variability. A semi-automatic registration-based-segmentation method was proposed in order to obtain area and flow waveforms in the principal pulmonary arteries. The operator’s intervention was limited to drawing the contour of the vessel in only one temporal frame, being also allowed to approve and eventually correct the automatically produced contours in the rest of the time frames. Depending on the initial frame, manually segmented, three different semi-automatic approaches were compared between themselves and with the manual segmentation.

The segmentations were performed once by three operators, two with previous image segmentation experience (op 1 and 3) and one unexperienced (op 2), to test inter-operator variability. The intra-operator variability was tested by one single operator (op1), who segmented the images twice, for each of the methods.

The segmentation results were assessed using 2 criteria:

1. *Efficiency*. The criterion tested how fast each of the methods is performing, by considering the segmentation and correction times for each operator.
2. *Reproducibility*. The criterion includes inter- and intra-operator variability, evaluated for area variation. The area waveforms, $A(t)$, were plotted for each operator, together with the mean and ± 1 SD of the mean, corresponding to each of the 40 time frames existing in each data set. The slice-by-slice variation, C.V, was quantified using the coefficient of variation (Eq. 2.20). In order to assess the variation of each method based on a normalised measure, a mean coefficient of variation, expressed as the average of all 40 slice-by-slice C.V, was computed.

$$C.V(\%) = \frac{SD}{\bar{A}} 100 \quad (\text{Eq. 2.20})$$

where \bar{A} is the mean area value computed at each time step from the three area values calculated by the independent ratters, SD is the corresponding standard deviation of \bar{A}

Variability in area segmentation introduces variation in the flow quantification since it depends upon the correct masking of the phase-contrast images and upon the value multiplied with the average velocity, see (Eq. 2.10). The coefficient of variation for each proposed segmentation approach for assessing the variability introduced by area segmentation was reported.

2.1.7.1 Segmentation efficiency

The efficiency criterion takes into consideration the time taken by an operator to segment a set of 40 time frame images of principal pulmonary arteries. The total processing time, t_{total} was computed as sum of the segmentation time, t_s and correction time, t_c . Table 2.1 displays the individual times for each operator, corresponding to each method of segmentation.

Table 2.1 Total segmentation times (t_{total}) for each of the proposed approaches

t_s corresponds to the time of segmenting all 40 time frames for the manual segmentation, while for the semi-automatic cases it accounts for the time taken to draw the vessel contour in the fixed image and actual algorithm computation time. t_c for both manual and semi-automatic approaches is the time to last editing and approving the ROIs before generating $A(t)$.

	segmentation time (s)			correction time (s)			total time (min)			
	t_s			t_c			t_{total}			
	op 1	op 2	op 3	op 1	op 2	op 3	op 1	op 2	op 3	mean
Manual										
MPA	1228.80	893.15	1637.90	75.29	20.11	43.51	21.73	15.22	28.02	21.66
RPA	1473.50	894.75	1574.30	150.50	136.31	94.92	27.07	17.18	27.82	24.02
LPA	1337.00	1701.10	1544.60	123.41	273.70	115.18	24.34	32.91	27.66	28.31
Semi-automatic										
case 1										
MPA	113.44	79.291	121.76	91.97	102.2	202.7	3.42	3.03	5.41	3.95
RPA	90.232	88.597	120.25	267	187.3	601.1	5.95	4.60	12.02	7.46
LPA	94.053	73.425	124.51	50.16	20.4	71.52	2.40	1.56	3.27	2.41
case 2										
MPA	125.12	142.17	108.27	27.93	31.46	60.76	2.55	2.89	2.82	2.75
RPA	129.79	125.55	123.1	42.45	112.7	74.37	2.87	3.97	3.29	3.38
LPA	118.86	104.27	118.45	30.33	19.7	60.31	2.49	2.07	2.98	2.51
case 3										
MPA	90.008	109.49	109.83	25.32	147.6	76.65	1.92	4.28	3.11	3.10
RPA	91.289	82.458	120.89	103.6	115.8	711.6	3.25	3.30	13.88	6.81
LPA	76.496	132.7	93.353	81.26	123.4	55.68	2.63	4.27	2.48	3.13

On average, the manual image processing took in total between 20 to 28 minutes, depending on the segmented structure. About 90% of the t_{total} was taken by the operators to segment all the individual slices, whereas less than 10% was allocated for the final corrections. The main pulmonary artery (MPA) was in general segmented faster than the right (RPA) and left (LPA) arteries. One potential explanation can be given by the relatively smaller size of the latter arteries, making it more difficult for the operators to decide where the vessel boundaries are.

The total processing time of the semi-automatic method was on average 5 times shorter than the manual segmentation, varying from 2.5 to 7.5 minutes. The segmentation time alone, t_s , which represented the time for the operator to draw the vessel contour on the fixed images, together with the computational time for each approach, represented more than half of t_{total} . Comparing with the manual segmentation, the correction time, t_c was as expected longer (approximately double), since at the time of segmentation inspection, minor adjustments were added in the majority of the cases. Analysing the times reported in Table 2.1, two outliers can be noticed for the semi-automatic segmentation. The RPA images contained a

large artefact in 15 of the time frames, which contributed to the partial failure of the semi-automatic algorithm for the first and third proposed approach. Hence, while t_s is similar to that for the other arteries, the correction time was significantly higher. The second semi-automatic approach, which used an average fixed image, was able to deal with the artefact much better, performed in half the time of the other 2 cases, of the same artery.

Overall, operator 3, with previous experience in segmenting medical images (other than blood vessels) took the longest processing time, while the unexperienced operator 2, segmented the fastest. The longer time taken by the experienced operators is reflected in the smoothness of the manually segmented curves, which are less spiky than the ones quickly produced by operator 2, showing that previous experience made them aware of the high variability present in manual segmentation.

2.1.7.2 Segmentation reproducibility

The segmentation reproducibility criterion was evaluated from the perspective of inter- and intra-operator variability assessed for area quantification.

Area waveforms were plotted for each segmentation approach together with the corresponding mean \pm 1SD from the mean. The SD has been calculated using (Eq. 2.21) for each of the 40 area time points segmented by the three individual operators.

$$SD_t = \sqrt{\frac{1}{3} \sum_{n=1}^3 (A_n(t) - \overline{A(t)})^2} \quad (\text{Eq. 2.21})$$

where $\overline{A(t)}$ is the mean area corresponding to a time point, t , $A_n(t)$ is the area value of the n operator at a time point, SD_t is the corresponding standard deviation at that time point, $n=1:3$ and $t=1:40$

The slice-by-slice coefficient of variation (C.V) was computed using (Eq. 2.20) and plotted for every studied case and artery. In order to compare the overall area segmentation reproducibility, a $\bar{A} \pm$ SD of C.V was computed from the slice-by-slice C.V.

Inter-operator variability for area quantification

Figure 2.14, Figure 2.15 and Figure 2.16 display the area waveform variation of the MPA, RPA and LPA respectively, as segmented by the three evaluators. Initially, no training was provided to the operators on how big/small to draw the vessel's contour. The lack of sharp

edges, characteristic to medical images, is the main reason for high variability between operators. Hence how the vessel contour is chosen is subjective to each operator's rationale.

Top to bottom figures display computed area against time frames for each segmentation approach: manual, peak systolic image as fixed image, average image as fixed image and successive registration. The left column contains the individual segmentations of each operator: op 1 -continuous red, op 2 -dashed blue and op 3 -dotted green line.

The three waveforms resulting from the individual operators' segmentations were averaged and displayed on the right column together with ± 1 SD from the mean (\bar{A}). The SD values were calculated for each point on the averaged area waveform which corresponded to one of the 40 time steps acquired. All the manual and semi-automatic cases, for each of the vessels, had the same 'appreciation' trend. The evaluators were consistent with their judgements of where the vessel contour lies. Operator 2 (blue), with no previous segmentation experience, drew the smallest contour, appreciating the artery boundaries to lie where the vessel-background had the highest change in gradient. In opposition, operator 3 (green), with previous clinical experience in segmenting different types of anatomical images (i.e heart, bowel, kidneys) excepting blood vessels, chose to draw the very outside contour, picking the contour at the last grey gradation. Operator 1 (red), from whom the waveforms were plotted as an average of the two measurements (performed for intra-variability assessment), had previous segmentation experience of blood vessels, and appreciated that the real vessel wall lies neither at the higher nor at the lower change in gradient, but rather somewhere in between. Inspecting the smoothness of the curves (Figure 2.14, Figure 2.15 and Figure 2.16), the manual segmentation is highly uneven, especially for the inexperienced operator. The semi-automatic segmentations have a consistent trend for all the proposed approaches, regardless of previous experience. This observation is confirmed by the slice-by-slice coefficient of variation which has a steady variation compared with the manual approach which displays large fluctuations (Figure 2.17).

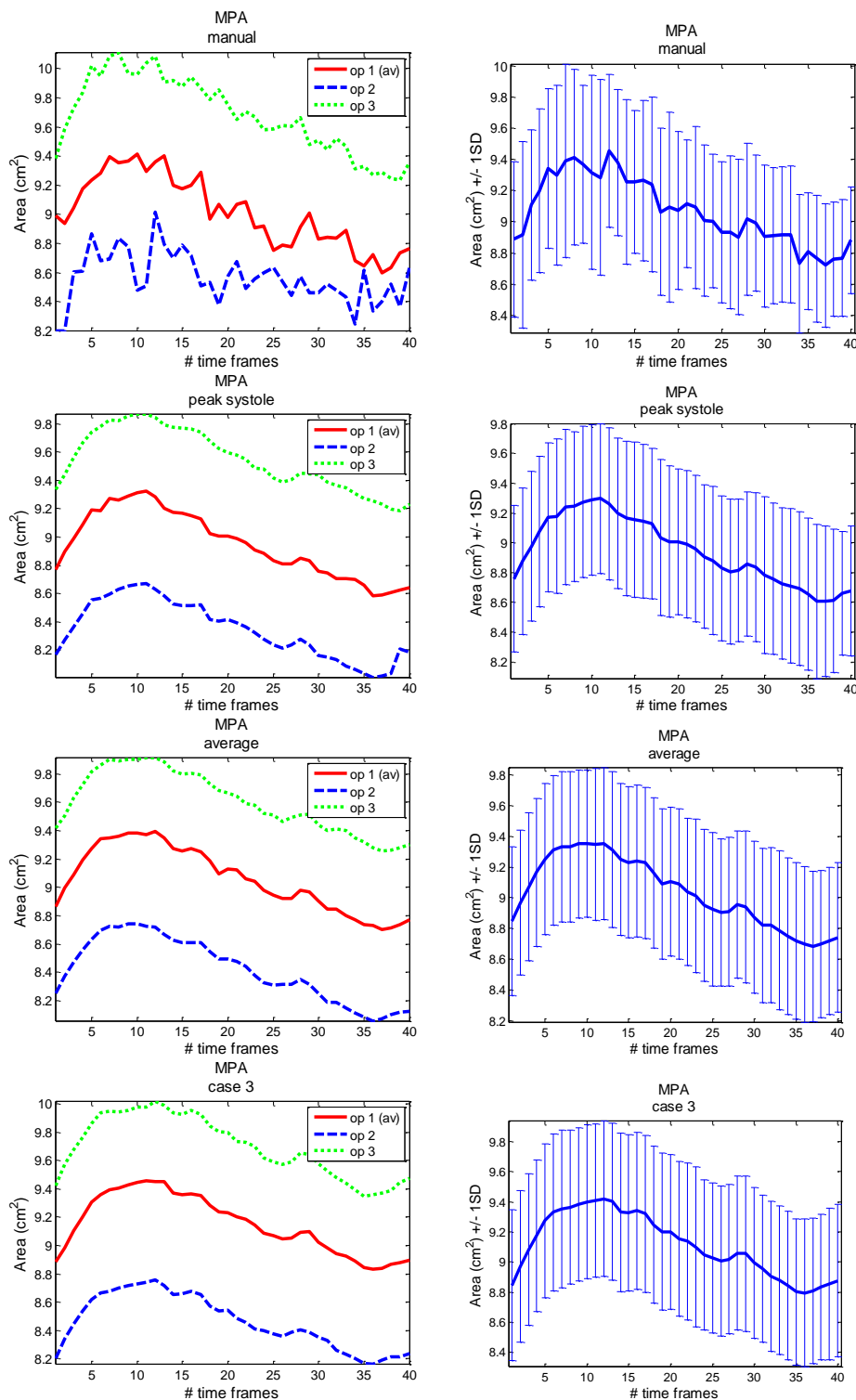


Figure 2.14 Area variation obtained for each operator and every segmentation approach, together with average area and standard deviation for MPA

Top to bottom figures display computed area against time frames for each segmentation approach: manual, peak systolic image as fixed image, average image as fixed image and successive registration. The left column contains the individual segmentations of each operator: op 1 –continuous red, op 2- dashed blue and op 3 –dotted green line. The corresponding averaged temporal area waveforms are displayed on the right column with $\pm 1SD$ from the mean.

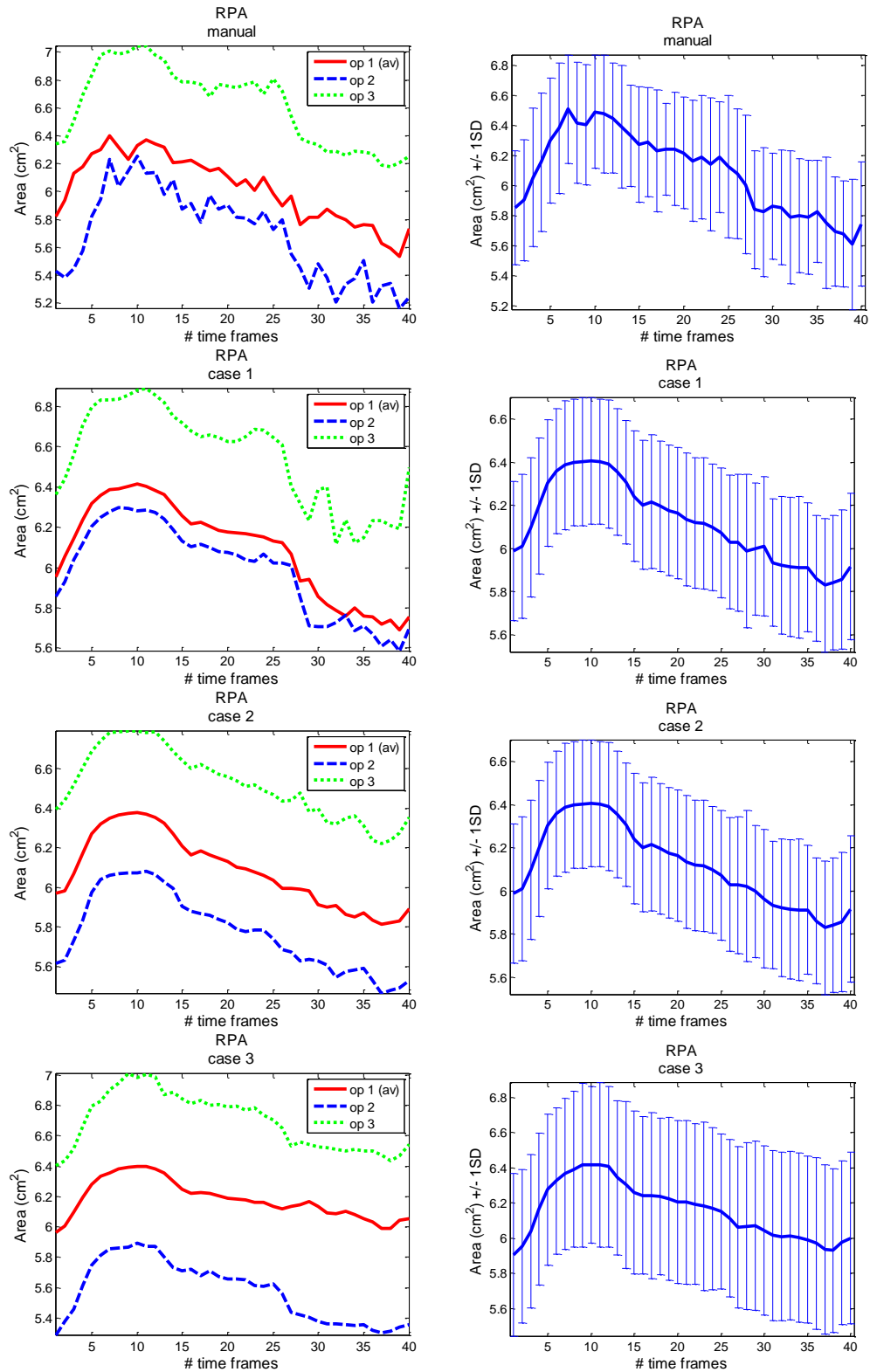


Figure 2.15 Area variation obtained for each operator and every segmentation approach, together with average area and standard deviation for RPA

Top to bottom figures display computed area against time frames for each segmentation approach: manual, peak systolic image as fixed image, average image as fixed image and successive registration. The left column contains the individual segmentations of each operator: op 1 –continuous red, op 2- dashed blue and op 3 –dotted green line. The corresponding averaged temporal area waveforms are displayed on the right column with $\pm 1SD$ from the mean.

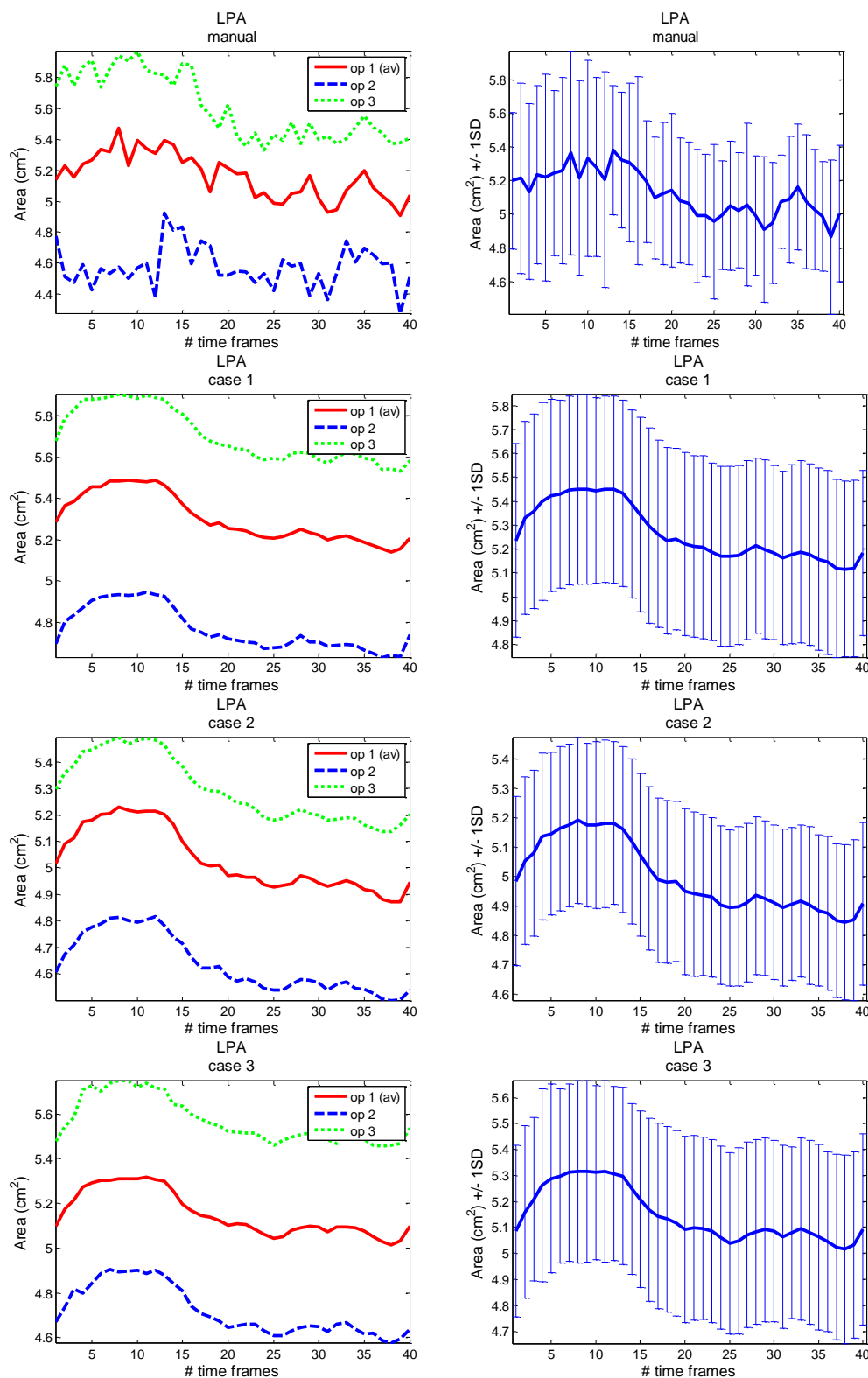


Figure 2.16 Area variation obtained for each operator and every segmentation approach, together with average area and standard deviation for LPA

Top to bottom figures display computed area against time frames for each segmentation approach: manual, peak systolic image as fixed image, average image as fixed image and successive registration. The left column contains the individual segmentations of each operator: op 1 –continuous red, op 2- dashed blue and op 3 –dotted green line. The corresponding averaged temporal area waveforms are displayed on the right column with \pm 1SD from the mean.

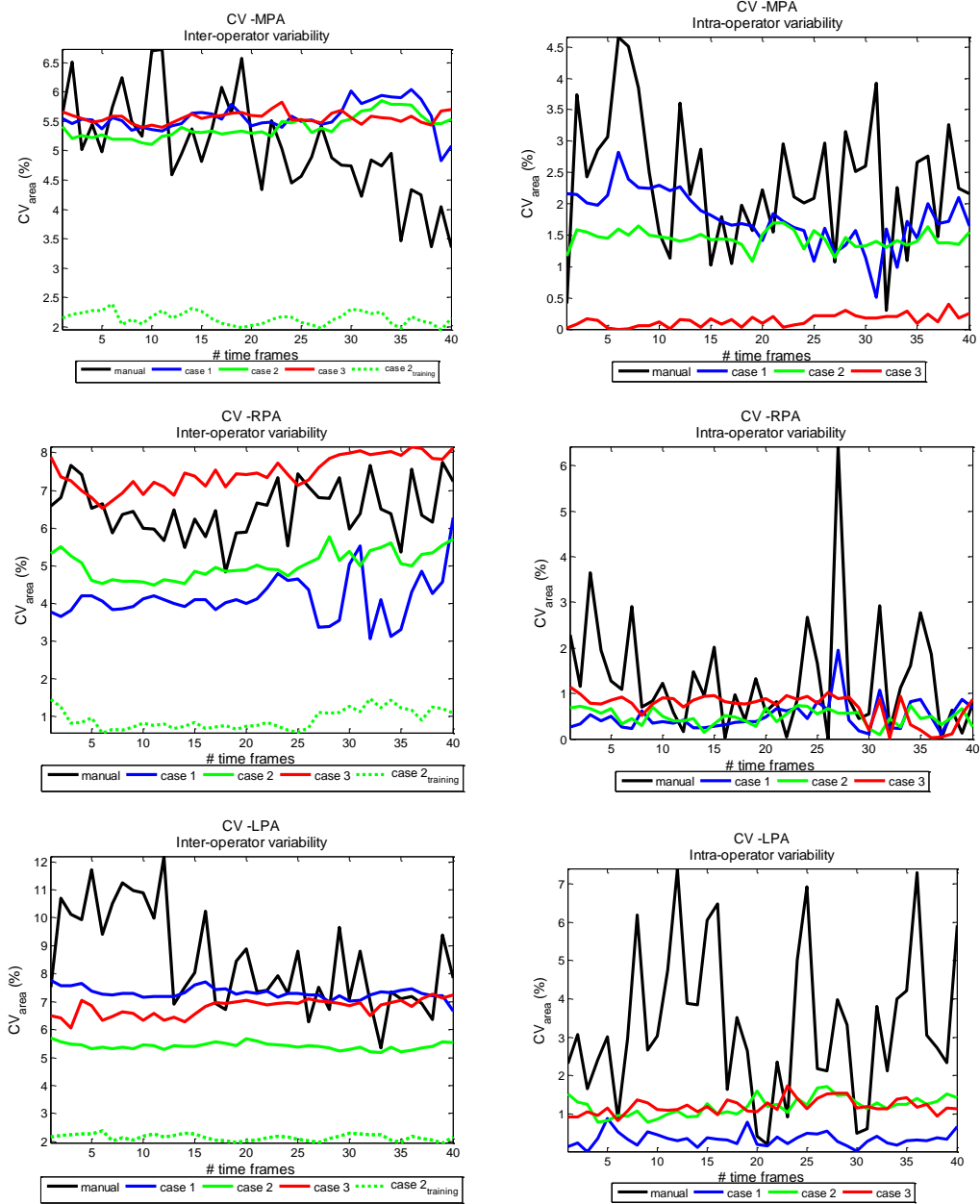


Figure 2.17 Coefficient of variation for inter and intra-operator variability

Top to bottom are displayed the slice-by-slice coefficients of variation for area of MPA (top row), RPA (middle row) and LPA (bottom row) for all segmentation approaches: manual (black), case 1 (blue), case 2 (green) and case 3 (red). The right column corresponds to the intra-operator results, while the left column corresponds to the inter-operator results. The effect of training on inter-operator segmentation variability was tested for the 2nd semi-automatic approach and plotted as slice-by-slice coefficient of variation with green-dotted line on the same graph with the results before training.

Table 2.2 displays mean and standard deviation of the coefficient of variation of each segmentation approach. The inter-operator variability introduced by segmenting the MPA exhibits similar values for all the methods: 5.1 ± 0.8 % for manual and 5.6 ± 0.2 %, 5.4 ± 0.2 % and 5.6 ± 0.1 % for the semi-automatic approaches. Although the manual segmentation exhibits the smallest mean C.V for the MPA, it is not the least varying method. The high

variation during systole is compensated by the smaller diastolic variation, resulting into a mean which it is not necessarily representative. Of the semi-automatic methods evaluated, the approach that uses an average image as a fixed image (case 2) has the smallest mean C.V for the MPA and for the LPA: $5.4 \pm 0.2\%$ and 5.4 ± 0.1 respectively. The smaller artery size of RPA and LPA introduces difficulties for the manual segmentation, displaying a higher mean C.V, $6.5 \pm 0.7\%$ and $8.5 \pm 1.7\%$, than for the MPA, $5.1 \pm 0.8\%$.

Table 2.2 'After-training' mean \pm SD of coefficient of variation (C.V) (inter-operator)

	MPA		RPA		LPA	
	mean (%)	SD (%)	mean (%)	SD (%)	mean (%)	SD (%)
manual	5.06	0.84	6.50	0.70	8.46	1.72
case 1	5.56	0.24	4.14	0.61	7.30	0.20
case 2	5.40	0.19	5.02	0.36	5.41	0.12
case 3	5.56	0.09	7.48	0.45	6.79	0.30
training	2.14	0.11	0.93	0.26	2.14	0.11

It can be argued that in a real clinical scenario, the operators will receive training a priori to the segmentation of any medical images. A test was performed in order to investigate this hypothesis. Using just the second semi-automatic segmentation approach, shown to be fastest and most consistent for all 3 arteries, the 3 operators were requested to segment all the arteries one more time. This time, unlike previously where no indications had been given regarding how to choose the artery boundary in the fixed image, the operators were asked to draw the vessel contour midway between the area with the largest and that with the lowest change in gradient. This criterion is, however, arbitrarily decided, just to evaluate the potential 'after-training' change in variability. The results (Table 2.2), showed a decrease of the mean C.V for all arteries, suggesting that adequate clinical training can reduce the inter-operator variability for semi-automatic segmentations.

Intra-operator variability for area quantification

Operator 1 segmented all three arteries twice, at a one week interval. The results are displayed in Figure 2.18, Figure 2.19 and Figure 2.20 for MPA, RPA and LPA respectively. As noticed for the inter-operator variability, the manual segmentation had the highest slice-by-slice segmentation variation. The automatically produced segmentations were smoother than the manual ones with a smaller slice-by-slice C.V (Figure 2.17 -right column).

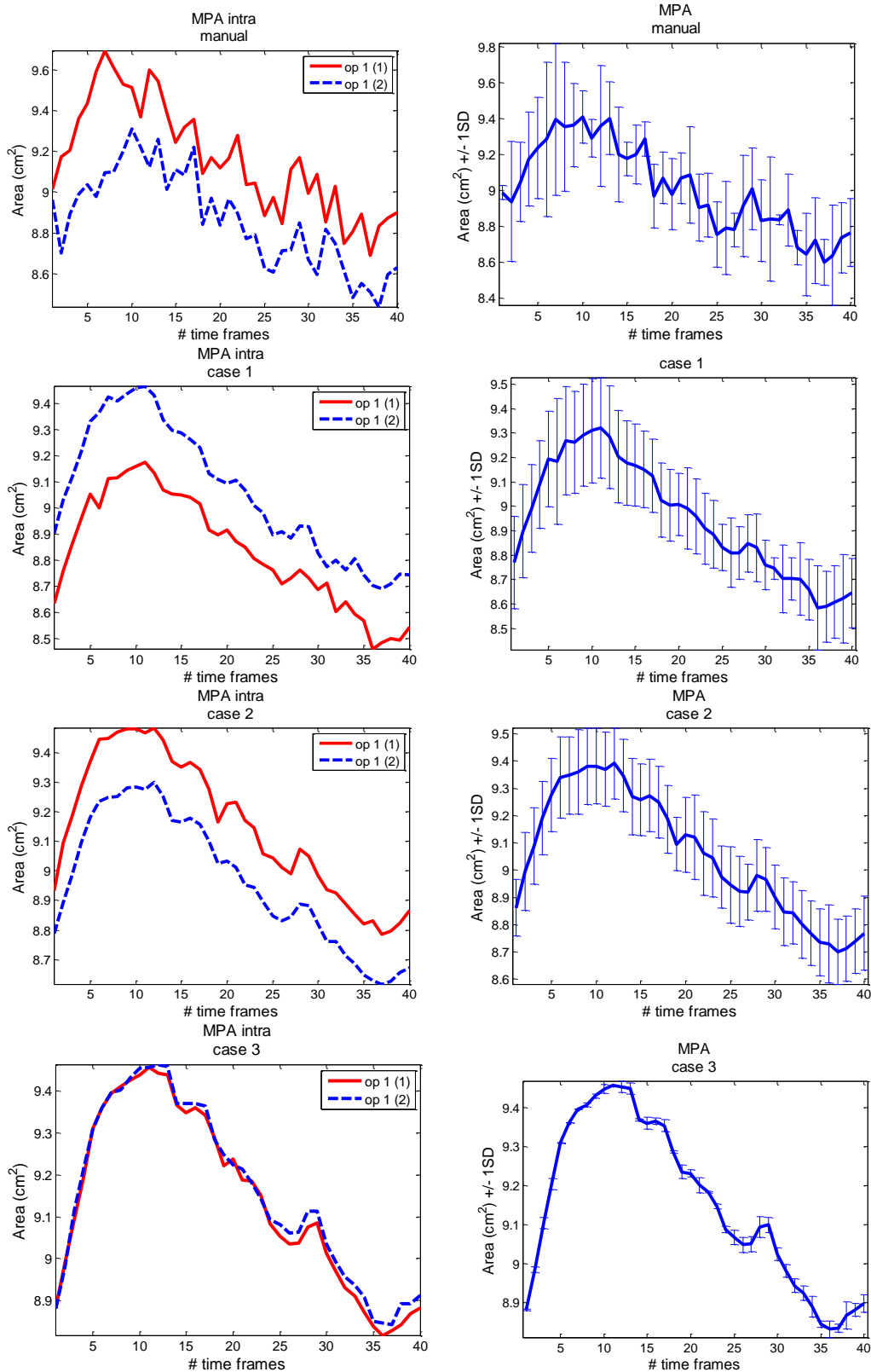


Figure 2.18 Area variation obtained for operator’s 1 segmentations for every segmentation approach, together with average area and standard deviation for MPA

Top to bottom figures display computed area against time frames for each segmentation approach: manual, peak systolic image as fixed image, average image as fixed image and successive registration. The left column contains the 2 individual segmentations of operator 1: (1) –continuous red and (2)- dashed blue. The corresponding averaged temporal area waveforms are displayed on the right column with $\pm 1SD$ from the mean.

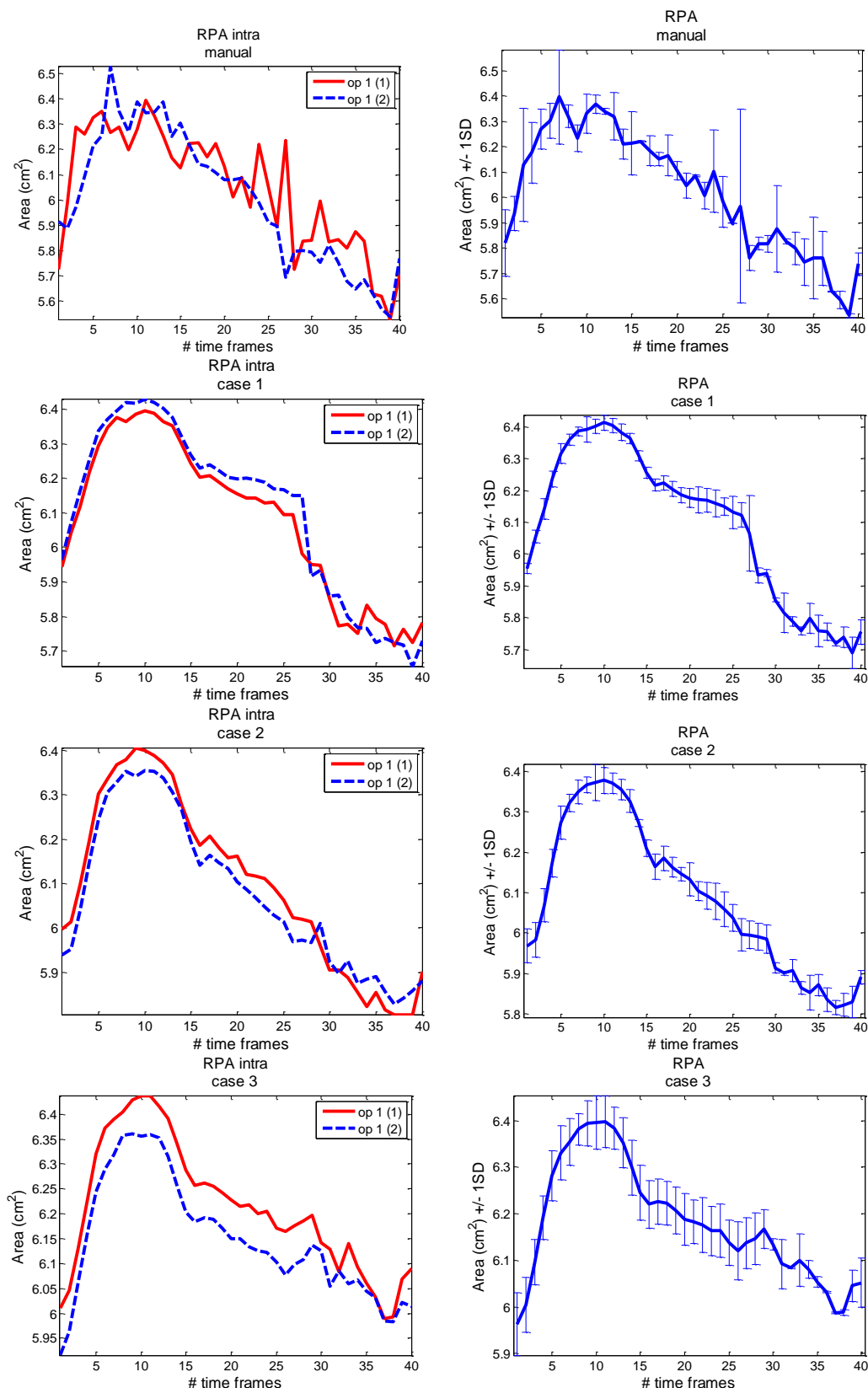


Figure 2.19 Area variation obtained for operator’s 1 segmentations for every segmentation approach, together with average area and standard deviation for RPA

Top to bottom figures display computed area against time frames for each segmentation approach: manual, peak systolic image as fixed image, average image as fixed image and successive registration. The left column contains the 2 individual segmentations of operator 1: (1) –continuous red and (2)- dashed blue. The corresponding averaged temporal area waveforms are displayed on the right column with $\pm 1SD$ from the mean.

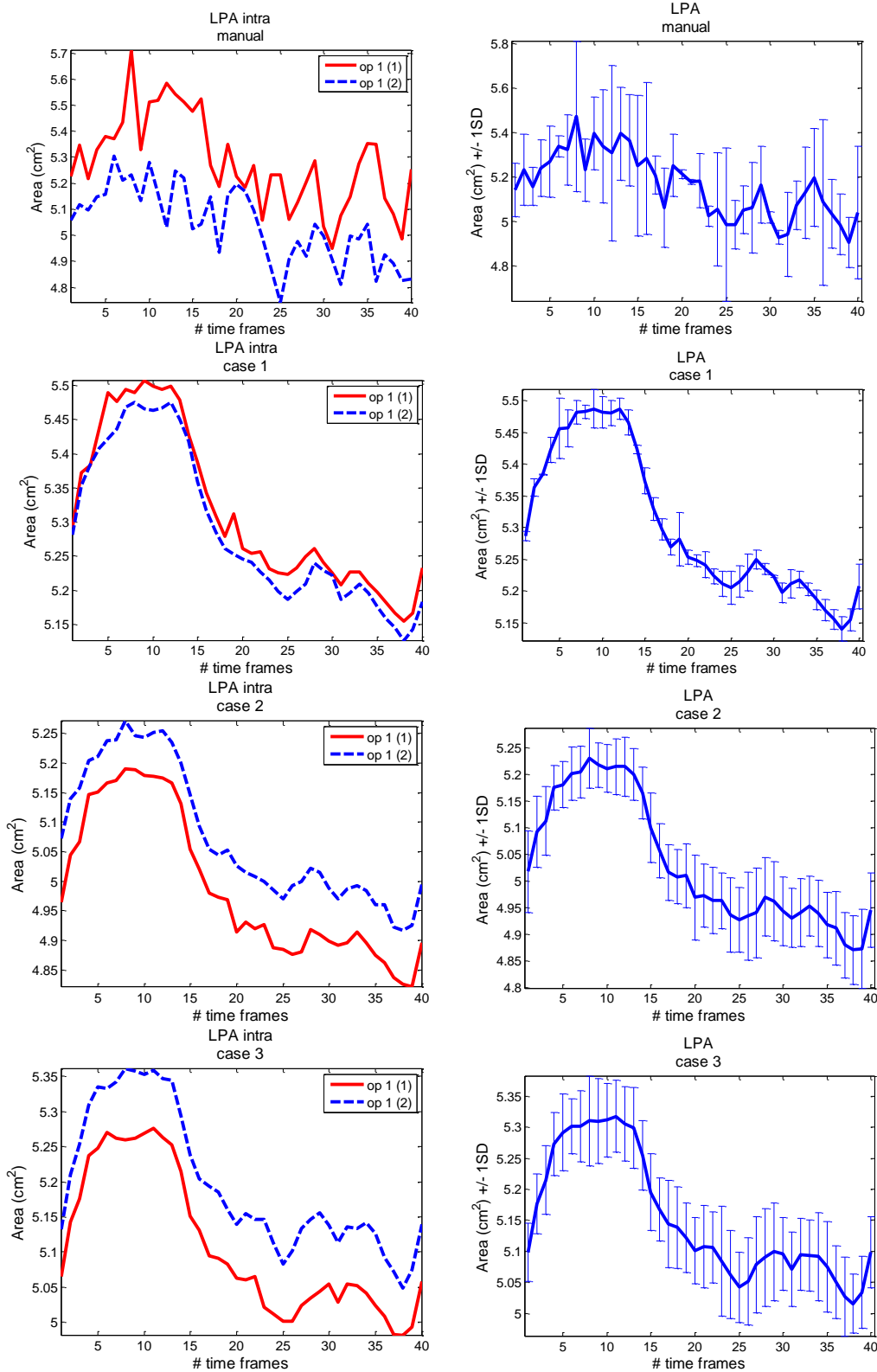


Figure 2.20 Area variation obtained for operator’s 1 segmentations for every segmentation approach, together with average area and standard deviation for LPA

Top to bottom figures display computed area against time frames for each segmentation approach: manual, peak systolic image as fixed image, average image as fixed image and successive registration. The left column contains the 2 individual segmentations of operator 1: (1) –continuous red and (2)- dashed blue. The corresponding averaged temporal area waveforms are displayed on the right column with $\pm 1SD$ from the mean.

The mean C.V and SD are reported in Table 2.3 showing that as expected the intra-operator variability is lower than the inter-operator variability for all the methods tested. Case 1 (peak systolic image as fixed image) as well as case 2 (average image as a fixed image) had a good overall performance, although case 3 showed a much better performance in segmentation of MPA.

	MPA		RPA		LPA	
	mean (%)	SD (%)	mean (%)	SD (%)	mean (%)	SD (%)
manual	2.35	1.03	1.30	1.23	3.31	1.93
case 1	1.77	0.44	0.49	0.33	0.34	0.18
case 2	1.44	0.14	0.48	0.17	1.21	0.24
case 3	0.14	0.09	0.72	0.30	1.25	0.20

Case 1, peak systolic image as fixed image, and case 2, average image as fixed image, produced overall smaller coefficient of variation in segmenting area than case 3 and the manual segmentation approach. Case 3, does not have a consistent performance throughout all the processed cases. Although the idea of registering successive images makes sense, since between two temporal successive frames the differences are minimum, propagating the manually drawn ROI (in the first slice) introduces a cumulative error in the other ROIs.

Flow reproducibility

The average flow during the cardiac cycle was computed by multiplying average velocity with the blood vessel cross-section, as described in Section 2.1.5. Quantification of the blood flow at every time step is doubly influenced by the vessel segmentation, firstly by the masking of the velocity images and secondly by the actual computed cross-section.

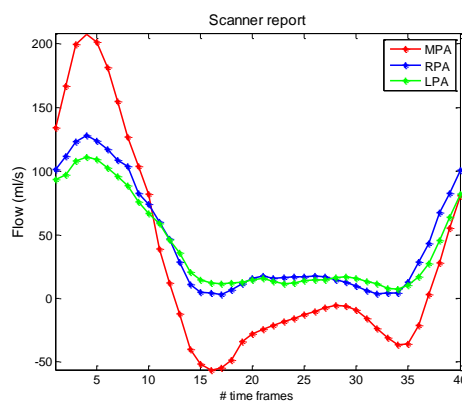


Figure 2.21 Flow waveforms as reported in the MR scanner report for MPA (red), LPA (green) and RPA (blue) of the same patient

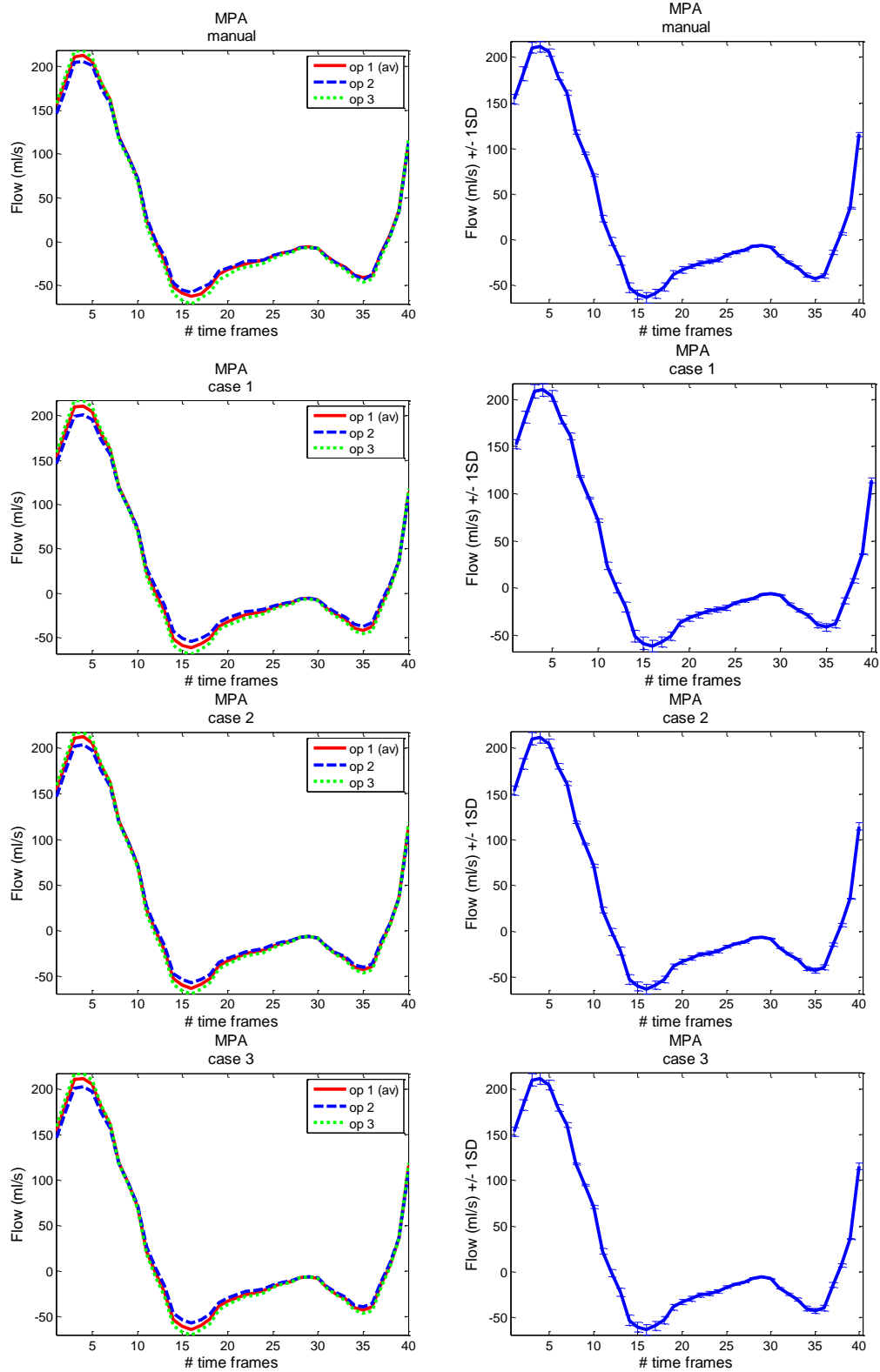


Figure 2.22 Flow variation obtained for each operator and every segmentation approach, together with average flow and standard deviation for MPA

Top to bottom figures display computed averaged flow against time frames for each segmentation approach: manual, peak systolic image as fixed image, average image as fixed image and successive registration. The left column contains the individual segmentations of each operator: op 1 –continuous red, op 2- dashed blue and op 3 –dotted green line. The corresponding averaged temporal flow waveforms are displayed on the right column with $\pm 1SD$ from the mean.

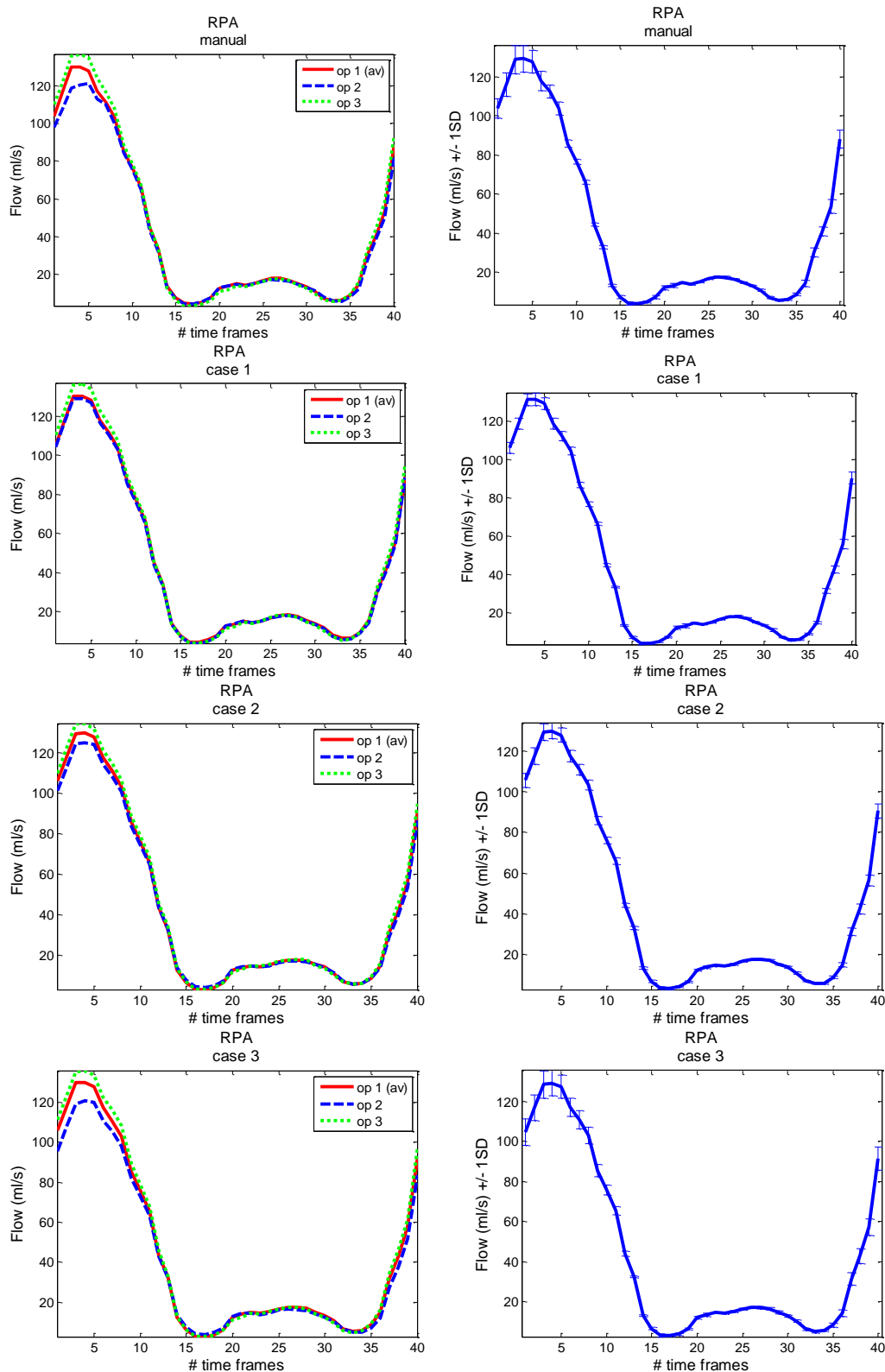


Figure 2.23 Flow variation obtained for each operator and every segmentation approach, together with average flow and standard deviation for RPA

Top to bottom figures display computed averaged flow against time frames for each segmentation approach: manual, peak systolic image as fixed image, average image as fixed image and successive registration. The left column contains the individual segmentations of each operator: op 1 –continuous red, op 2- dashed blue and op 3 –dotted green line. The corresponding averaged temporal flow waveforms are displayed on the right column with $\pm 1SD$ from the mean.

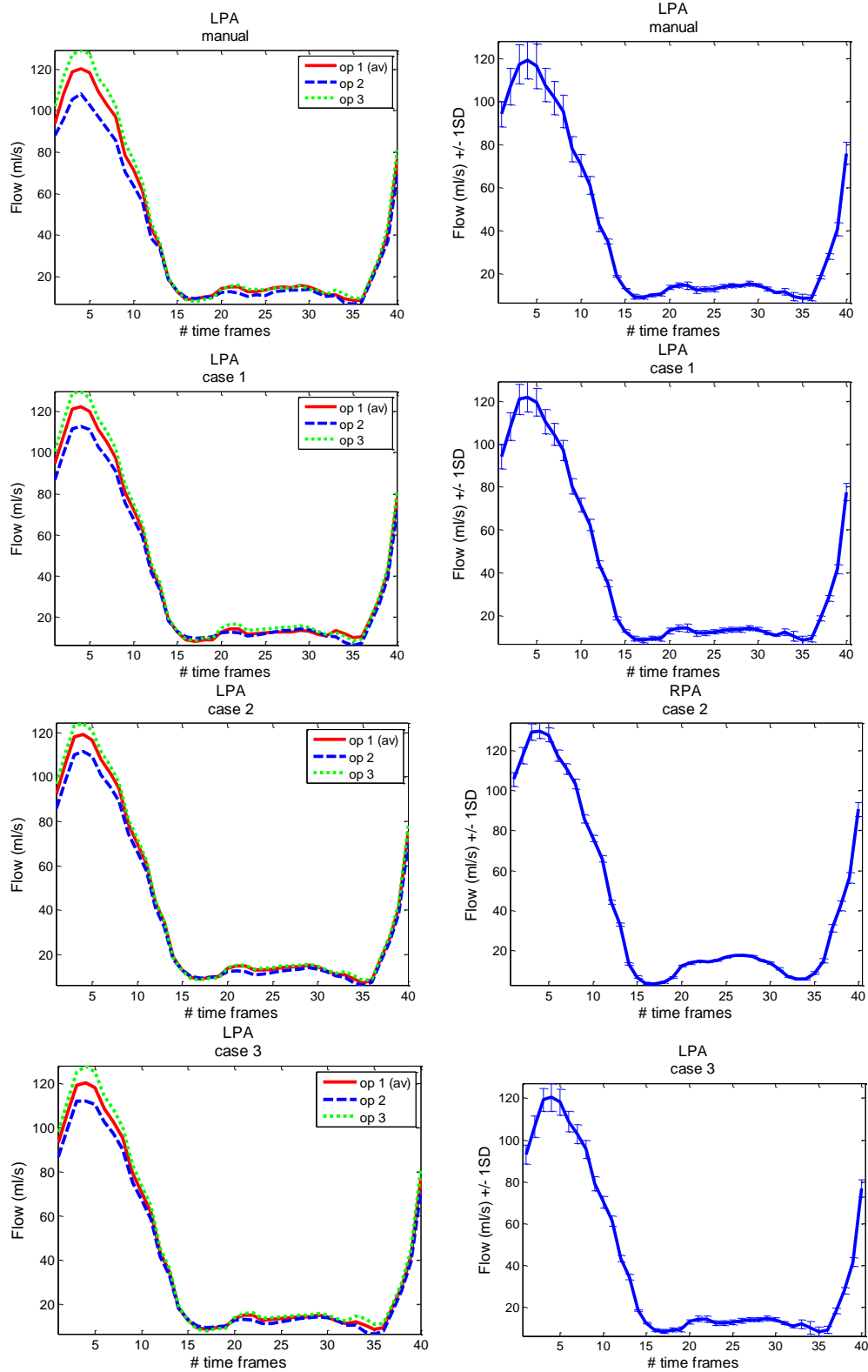


Figure 2.24 Flow variation obtained for each operator and every segmentation approach, together with average flow and standard deviation for LPA

Top to bottom figures display computed averaged flow against time frames for each segmentation approach: manual, peak systolic image as fixed image, average image as fixed image and successive registration. The left column contains the individual segmentations of each operator: op 1 –continuous red, op 2- dashed blue and op 3 –dotted green line. The corresponding averaged temporal flow waveforms are displayed on the right column with $\pm 1SD$ from the mean.

Figure 2.21 displays the blood flow waveforms in the main pulmonary arteries: MPA (red), RPA (blue) and LPA (green), obtained after digitising the graphs from the scanner report. If the scanner result is considered the gold standard, it can be used as a reference for the implemented MATLAB algorithm described in Section 2.1.5 above.

Figure 2.22, Figure 2.23 and Figure 2.24 show the average blood flow waveforms for all the segmentations performed by the three operators based on the described segmentation approaches. It can be noticed that the flow curve shapes are the same for all the cases. The differences introduced by the different segmentation approaches are obvious in signal amplitude. The shape of the flow is however preserved and as can be seen on the graphs (Figure 2.22, Figure 2.23, Figure 2.24), except for the max and min flow, the waveforms overlay is very good. The differences between the scanner results and the MATLAB generated waveforms were quantified through relative error for the maximum ($Q_{\max Er}$) and minimum ($Q_{\min Er}$) flow and root mean squared error (RMS_{error}).

$$Q_{\min Er} = \frac{Q_{\min S} - Q_{\min C}}{Q_{\min S}} 100 \quad (\text{Eq. 2.22})$$

,where $Q_{\min S}$ is the min flow from scanner , $Q_{\min C}$ is the min flow MATLAB

Table 2.4 displays the values for $Q_{\min Er}$ and $Q_{\max Er}$ computed using(Eq. 2.22).

$$RMS_{error} = \frac{\|Q_S - Q_C\|_2}{\|Q_S\|_2} 100 \quad (\text{Eq. 2.23})$$

Table 2.4 Relative errors in flow quantification

		$Q_{\max Er}$ (%)			$Q_{\min Er}$ (%)			RMS_{error} (%)		
		op 1	op 2	op 3	op 1	op 2	op 3	op 1	op 2	op 3
MPA	manual	2.23	1.34	5.10	10.68	2.64	26.23	13.48	10.89	16.61
	case 1	1.67	3.07	4.71	10.08	3.55	21.30	11.20	9.55	15.83
	case 2	1.57	2.20	5.16	12.24	1.22	22.56	13.12	10.03	16.10
	case 3	1.67	5.49	6.36	14.41	1.71	25.15	13.41	10.05	16.59
RPA	manual	2.14	5.28	7.03	24.61	27.97	0.41	12.65	14.13	12.61
	case 1	2.11	0.93	6.99	29.80	9.51	15.69	11.98	12.26	12.25
	case 2	1.57	2.20	5.16	5.13	26.46	1.82	11.68	12.61	11.56
	case 3	1.67	5.49	6.36	20.08	14.27	15.20	11.17	14.07	11.70
LPA	manual	0.17	0.09	0.23	0.41	0.40	0.53	12.78	12.31	16.48
	case 1	0.10	0.02	0.17	0.17	0.07	0.21	13.11	11.26	16.45
	case 2	0.07	0.00	0.12	0.55	0.40	0.54	11.47	11.73	13.27
	case 3	0.08	0.01	0.15	0.62	0.46	0.60	11.58	11.30	14.94

Manual area segmentation introduces the highest relative errors in quantifying maximum flow amplitude, for all the arteries and for all operators. Root mean squared error, RMS_{error} lay however between 11 and 13%, suggesting that flow quantification is not highly influenced by area variability.

2.1.8 Influence of area segmentation of derived pressure waveforms

The first and second semi-automatic segmentation cases showed consistent results for most of the performed analysis. The resulting area waveforms of MPA from the two cases were transformed into pressure waveforms, using eq 2.19 $p(t) = \frac{E_p}{1-\nu^2} \frac{\delta R(t)}{R_0} + P_d$. The equation relates the temporal changes of the vessel's radius, the minimum vessel radius, R_0 , the Peterson's elasticity modulus, E_p and the diastolic pressure P_d . In order to determine the vessel radius at every acquired time step, the pulmonary artery cross-section was considered circular. As previously described in this chapter, the E_p and P_d values were derived from a power law and an exponential relationship respectively that best related the changes in the relative change of the cross-sectional vessel's area to the RHC measured pressure.

The reduction in the variability can be attributed to the relatively constant offset between three segmented areas. Assuming a constant offset at every time point, the relative area change (RAC) would be constant, and therefore, E_p and P_d to be introduced in eq. 2.19 would be the same. Additionally, the $\frac{\delta R(t)}{R_0}$ term in the equation will be the same for a constant segmentation offset.

Therefore if the offset of the three segmentations will be exactly the same at every time step, the pressure waveforms would be identical after applying equation 2.19. This is not the case, and differences between the three resulting pressure waveforms can be noticed. However, due to this almost constant segmentation offset, these differences are small, reducing the coefficient of variation in the case of the pressure waveforms to nearly half of the one obtained for the area waveforms.

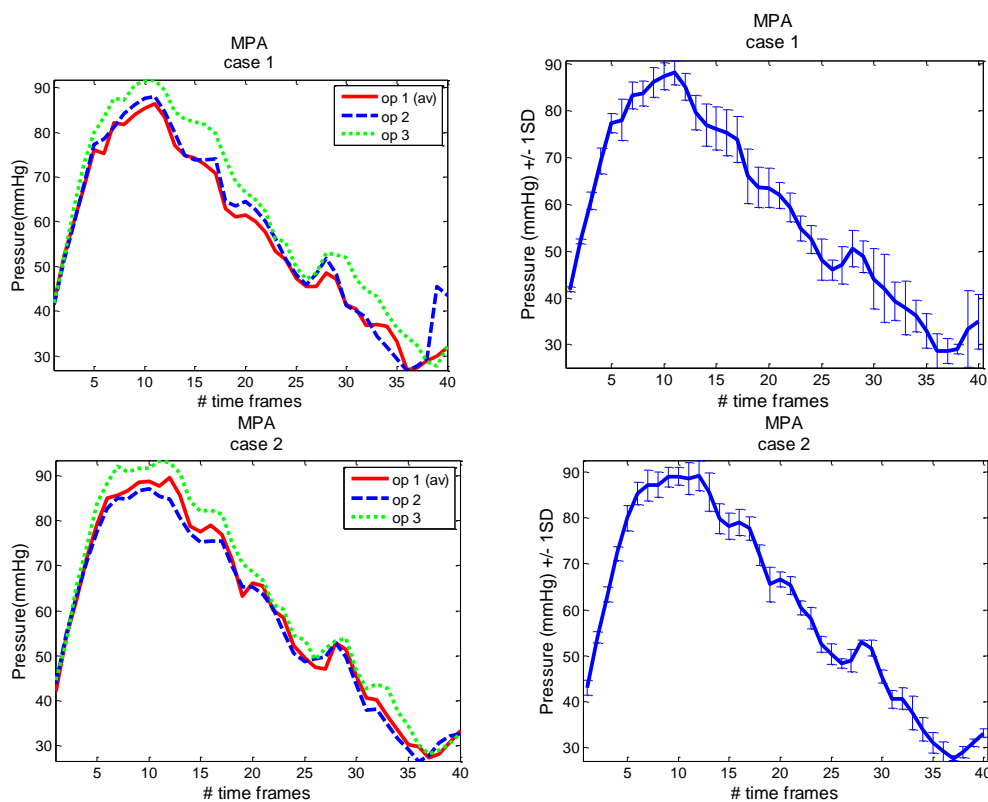


Figure 2.25 Pressure variation in MPA obtained for each operator, for cases 1 and 2 of the semi-automatic segmentation, together with averaged pressure and standard deviation

Top to bottom figures display computed average pressure against time frames case 1 and 2 of semi-automatic segmentation: peak systolic image as fixed image and average image as fixed image. The left column contains the individual segmentations of each operator: op 1 – continuous red, op 2- dashed blue and op 3 –dotted green line. The corresponding averaged temporal pressure waveforms are displayed on the right column with $\pm 1SD$ from the mean.

The graphical results are confirmed by Table 2.5. Minimum and maximum area computed for case 1 and 2 of the semi-automatic process, of all three operators are displayed together with the corresponding coefficient of variation. The area inter-operator C.V varies between 6.27 and 6.85 %, while the corresponding pressure C.V is reduced by a factor of two.

Table 2.5 Coefficient of variation for minimum and maximum area and pressure segmented using semi-automatic cases 1 and 2

		Area (cm ²)				Pressure (mmHg)			
		op1	op2	op3	C.V (%)	op 1	op 2	op 3	C.V (%)
case 1	min	8.58	8.01	9.18	6.85	26.37	26.82	27.76	2.62
	max	9.32	8.67	9.87	6.46	86.39	88.04	91.76	3.10
case 2	min	8.70	8.06	9.26	6.91	27.23	26.57	28.16	2.94
	max	9.39	8.74	9.92	6.27	89.62	87.09	93.47	3.57

SUMMARY AND CONCLUSIONS

Inferring the status of the pulmonary circulation, non-invasively, in patients with PH and healthy volunteers, using 0D and 1D mathematical models requires quantification of flow and pressure waveforms at the same anatomical location.

Two MRI sequences were proposed to be used for deriving accurate flow $Q(t)$ and area $A(t)$ in the pulmonary arteries. A PC sequence was used to quantify the flow variation during the entire cardiac cycle, while a bSSFP sequence, chosen for its high blood-vessel wall delineation, was used to segment the arterial cross-sections and for masking the PC images.

A pressure-radius relationship derived from the equilibrium condition at the wall of the vessel was used to derive pressure waveforms $p(t)$ from radius $r(t)$. The Peterson's elasticity modulus E_p and diastolic pressure P_d , necessary to obtain subject-specific pressure waveforms were derived from two relationships which best fit a mixed data set, containing P_d and E_p variation with relative area change.

Three semi-automatic registration-based segmentation methods were developed and tested against the manual segmentation, considered to be the gold standard in the field. Three operators, with different previous segmentation experience, were asked to manually and semi-automatically segment three data sets, corresponding to main, right and left pulmonary arteries. Although semi-automatic segmentation introduces variability in the resulting waveforms, it has the advantage of human rationale in dealing with images artefacts.

All semi-automatic methods produced results comparable with the manual approach. However, the total segmentation time was considerably higher for the latter. Moreover, the semi-automatic segmentations showed lower slice-by-slice variability, producing smoother curves than the manual segmentation.

Due to its relatively smaller size in comparison with the MPA, the LPA showed overall higher inter-operator variability. On the other hand, the RPA showed similar or even smaller segmentation variability than MPA, supporting the hypothesis of the RPA being more stable. Although it is difficult to quantify categorically which of the three semi-automatic method is better, based on the consistency of the results, better performance in the images with artefacts and total execution times the case using an average image as the fixed image in the registration process was selected as the default option in future analysis. The third semi-

automatic segmentation case, using time-series successive registrations, propagates not only the ROI but also the error.

Segmented bSSFP images were used to mask the PC images and to derive the flow waveforms. The results were compared with the MRI scanner's report and the relative error in maximum and minimum flow differences was quantified. The findings showed that while the flow waveform shape is not affected by the segmented areas, the difference in overall fitting, quantified by RMS_{error} , is approximately 16% in MPA, for all operators and segmentation approaches.

The inter-operator area variability, as expected, influences the derived pressure waveforms. Nevertheless, the variability quantified for maximum and minimum changes are reduced by a factor of two.

A GUI, developed in MATLAB, integrates all the imaging post-processing steps, outputting patient specific area, flow and pressure waveforms, for further use as input to mathematical models. Although it was shown that flow and pressure waveforms are less affected by inter- and intra-operator variability than area itself, it is expected that the final mathematical outputs will reflect this variability to a certain degree. Further variability assessment required for the 0D and 1D model outputs was performed in detail in Chapter 3 of this thesis.

CHAPTER 3

0D and 1D Model of a Thin Walled Straight Elastic Tube for Pulmonary Hypertension Assessment

MOTIVATION

Several authors [73], [74], [75], [76], [77], [78], [79], [80], [81] have described the use of mathematical models to characterise the pulmonary circulation of humans and of animals in health and disease. In the context of this thesis, the focus is on the determination of a diagnosis of pulmonary hypertension (PH). Although published models have proven to have the potential to characterise the status of the pulmonary circulation, in particular to distinguish between normotensive and PH patients, all of these reported studies use invasive pressure catheterisation as an input measure. The challenge of this thesis is to develop and to evaluate diagnostic methods that use only non-invasive, image-based, measures.

There are three pre-requisites for the characterisation of pulmonary hypertension using mathematical models to interpret non-invasive image data:

- Reliable segmentation and flow quantification from time-series image data

The methods developed in this thesis require the measurement of diameter and flow at a cross-section of the pulmonary vessel at each point in time. The achievement of the requisite temporal and spatial resolution is a significant challenge, and utilises state-of-the-art magnetic resonance imaging protocols developed by one of the thesis supervisors and collaborators in Sheffield. The image processing methods are described in Chapter 2.

- Establishment of the relationship between pressure and flow

The mathematical models adopted in this thesis are formulated using pressure and flow as the fundamental variables, because these are routinely used as the basis of such models. Although it is possible easily to replace pressure with a measurement that can be made on the images, for example local vessel diameter, the underlying equations remain the same. The fluid mechanics equations describe the conservation of mass and momentum, and for solution a further equation, an equilibrium equation relating pressure to area, is required. A change of variable would not remove the need for the establishment of a pressure-diameter relationship. The relationships used in this thesis, based on literature and our own measured data, are described in Chapter 2.

- Methods to compute the parameters in the mathematical models that are used to characterise the measured pressure-flow responses of the system.

The thesis describes both 0D and 1D models. For the 0D models the values of resistances and capacitances that best fit the measured time-series pressure and flow data are computed using a customised optimisation process. For the 1D models the wave reflections are characterised based on the 1D wave transmission equation, using a Fourier decomposition of the time series signals. The processing methods are described in Chapter 3.

The current chapter describes the methods used to evaluate the parameters in a three element Windkessel (R_cCR_d) and to determine the wave reflections, based on a 1D straight, thin walled, axisymmetric elastic tube model, to characterise the pulmonary circulation in healthy volunteers and in patients with pulmonary hypertension. The models use as input time varying pressure (computed from the diameter using the relationship described in chapter 2) and flow, simultaneously measured in the main pulmonary artery (MPA) with Magnetic Resonance Imaging sequences.

The methods presented in this chapter were developed in the first two years of this PhD programme and are published, together with an evaluation of statistical significance of the proposed diagnostic measures on a cohort of 35 patients, in [27]. This chapter presents more detail, including additional tests of robustness and application to a larger cohort of 80 subjects.

MATERIALS AND METHODS

3.1.1 Subjects

The cohort of 80 individuals studied comprised 72 patients and 8 healthy volunteers. The 72 patients were referred to the Sheffield Pulmonary Vascular Disease Unit with symptoms of PH. The patients were scanned during routine investigations, approved by the North Sheffield Ethics Committee and no written consent was required. All the patients underwent right heart catheterisation (RHC) and MRI scanning within 2 days. 15 patients were determined by RHC to have mPAP <25 mmHg and were included in the NoPH group. 57 patients were diagnosed with PH, and these were divided into 2 subgroups, according to their measured pulmonary vascular resistance (PVR). PVR is taken as a measure of PH severity [29], [28], [26]. For the current study, a 4 WU threshold, as proposed by [26] was used to separate the PH group. Subgroup 1, with mild PH (PVR<4WU) contained 19 patients, and subgroup 2, severe PH (PVR≥4WU) contained 38 patients.

8 healthy volunteers were investigated to establish the ranges of the proposed parameters in normal individuals. No invasive measurements were performed on the healthy volunteers.

3.1.2 MRI images

Acquisition

MRI images of the MPA were acquired for all the subjects, under breath hold, using phase contrast (PC) and balanced steady state free precession (bSSFP) sequences. The two sets of acquired images were co-registered in time (same number of temporal phases) and space (same matrix dimensions) and were used to obtain simultaneous time varying flow and pressure (from the measured radius). The acquisition protocols, including the sequences parameters were discussed in Chapter 2, Section 2.2.

Post-processing

Using a semi-automatic registration based segmentation method, the images were post-processed in MATLAB in order to extract the MPA cross-sectional area and quantify the flow variation during the cardiac cycle. The chosen segmentation method was discussed in Chapter 2, Section 2.3, being referred as the semi-automatic segmentation approach using an average image as a fixed image.

3.1.3 0D Windkessel model

Pulmonary hypertension is associated with a combination of the phenomena of vasoconstriction, intimal proliferation and vascular remodelling, generally leading to an increase in pulmonary vascular resistance (PVR) and to a decrease in compliance (C). As previously described in Chapter 1, 0D models can offer a global characterisation of the system that they represent, and have been proposed by several authors [83], [54], [55], [84], [20] for the assessment of the status of the pulmonary circulation in healthy and diseased animals and humans.

Using the time varying pressure and flow derived from MR images of the MPA, the values of the electrical parameters of Windkessel model can be computed and used for the assessment of PH.

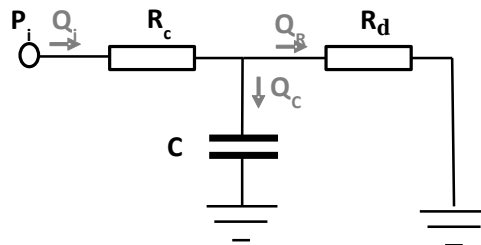


Figure 3.1 Three element Windkessel model (R_cCR_d) used for the analysis of pulmonary circulation in PH

The elements of the circuit are the characteristic resistance R_c , total vascular compliance C and distal resistance R_d . The inlet pressure P_i and flow Q_i are measured in the patient main pulmonary artery (MPA)

3.1.3.1 Optimisation problem for computing Windkessel electrical parameters

The most challenging part in using 0D models is the derivation of the electrical parameter values. The circuit in Figure 3.1 is described in the time domain by an ordinary differential equation (Eq. 3.1).

$$\left(1 + \frac{R_c}{R_d}\right) Q_i(t) + R_c C \left(\frac{dQ_i(t)}{dt}\right) - C \left(\frac{dP_i(t)}{dt}\right) - \frac{P_i(t)}{R_d} = 0 \quad (\text{Eq. 3.1})$$

where $Q_i(t)$ and $P_i(t)$ are the flow and pressure prescribed at the inlet of the domain (MPA)

The problem of solving the OD models can be formulated in the sense of finding the set of electrical parameters (R_c , C , R_d) that together with the measured flow- $Q_i(t)$ will return the measured pressure- $P_{\text{measured}}(t)$. It is unlikely that any combination of the parameter values will return a pressure wave that exactly conforms to the measured one, and so the problem is one of optimisation, or the determination of the optimum set of (R_c , C , R_d) which minimises some measure of the error between the measured pressure $P_{\text{measured}}(t)$ and the analytical pressure solution $P_{\text{optim}}(t)$ for the measured flow $Q_i(t)$.

An optimisation problem comprises of two main parts: defining the cost function (error) and selecting the algorithm which will be applied for minimising that error. The method proposed for solving the three element Windkessel model, was implemented in MATLAB and uses its standard optimisation functions.

3.1.3.2 Searching algorithm

The searching algorithm employed for finding the best set of Windkessel parameters was chosen to reduce operator's input and to be easy to implement on problems with higher degrees of freedom. The approach was to run in the first instance a Genetic Algorithm (GA) optimisation process followed by a gradient-based method for solution refinement. The GA is an algorithm that takes advantage of the randomness in the population, following evolutionary rules to find the best set of values. From an initial population of individual solutions the algorithm randomly selects values that will be used as parents to produce off-springs for the next generation. By allowing enough generations for a population to evolve, it is argued that algorithm will find the best individuals[128].

The GA routine is asking the user to specify an interval where the solution can be found. Gradient based methods, although faster and more efficient are sensitive to the starting point and therefore an erroneous initial guess applied by an operator unfamiliar with the solution space of these models can lead to misleading parameters values.

The bounds interval used by the GA can be modified by the user. However, since the optimisation algorithm is designed to run with minimum input from the operator, default values, showed in Table 3.1 The lower and upper bounds of the interval were decided upon evaluating the physiological values of the pulmonary resistance and compliance already reported in the literature, computed both from invasive measurements or model based. A warning was introduced in the routine to signal when one of the limits have been met by the

optimised parameter. In this way, the user can control the bounds, but also decide if the returned value might be physiologically reasonable or the 0D model cannot represent the input data provided.

Table 3.1 GA parameters' interval

Parameter	Bounds
R_c/R_d	0.0001-10
R_dC (s)	0.01-10

Another method that minimises operator's input is to populate the space with multiple initial values within the same wide range set up for the GA, run the gradient based method for all points and select the solution with the minimum rms. Although the latest method is more intuitive, for a problem with several degrees of freedom it is rather inefficient.

A Bayesian method, based on probabilistic inference, could be implemented as an alternative optimisation method. However, as for the gradient decent method, an initial value is required to supply the model. The method is however a global optimisation technique depending less on a good initial guess, than the gradient based technique. Further work is required to test the feasibility of a Bayesian method for optimising the Windkessel electrical parameters.

3.1.3.3 Defining the cost function

Expressing the error between two waveforms in the sense of the root mean square error (RMS_{er}) (Eq. 3.2) is commonly used in optimisation processes.

$$RMS_{er} = \sqrt{\frac{\sum_{t=1}^n (P_{measured}(t) - P_{optim}(t))^2}{n}} \quad (\text{Eq. 3.2})$$

However, RMS_{er} is an overall waveform fitting error measure and no special consideration is given to any pair of differences, all having the same weight. It has been noticed in practice that two fitting waveforms might have very similar RMS_{er} , but yet the outcome in using one or another would be different. More specifically the optimal fit in the least squares sense, taking into account all of the measured time points, can lead to relatively large errors in the maximum and minimum pressures, at peak systole and in diastole respectively. Systolic and diastolic values are often used as reference points by the clinical community, and it is therefore required in finding a compromise in fitting the overall waveform, but keeping the

minimum and maximum values close to the target waveform. To address this issue a modification of the cost function was introduced (Eq. 3.3) so that extra weight was given to the matching of the extrema over the cardiac cycle.

The cost function, f_{cost} chosen for the optimisation process represents a linear combination of the root mean square error over the cardiac cycle and the error in the peak systolic and minimum diastolic pressure.

$$\begin{aligned} f_{cost} = & C_s \left(\left| \max(P_{optim}(t)) - \max(P_{measured}(t)) \right| \right) \\ & + C_d \left(\left| \min(P_{optim}(t)) - \min(P_{measured}(t)) \right| \right) \quad (\text{Eq. 3.3}) \\ & + C_{RMS} RMS(P_{optim}(t), P_{measured}(t)) \end{aligned}$$

where C_s , C_d and C_{RMS} are multiplication constants for the cost function, defined as proportions

$$C_s + C_d + C_{RMS} = 1 \quad (\text{Eq. 3.4})$$

There is no principled way in which to assign the relative weightings: it is a matter of human judgement as to which combination produces the optimal balance of fitting the extrema and the shape of the curve over the cardiac cycle. Based on a trial and error process and by qualitatively assessing the fitting results of an initial data set of 27 waveforms, the values chosen for processing of all data in this study were: $C_s=0.1$, $C_d=0.1$ and $C_{RMS}=0.8$. These values can be however modified by the user.

3.1.3.4 Analytical solution for the Windkessel inlet pressure

A numerical solution for pressure can be obtained from (Eq. 3.1) in the time domain by using numerical discretisation schemes, and this might be the most appropriate solution methodology if, for example, the resistances and/or capacitance are nonlinear. The solution will be dependent on the discretisation time, dt . A big dt might produce erroneous pressure outputs, whereas a small dt increases computation time.

In this thesis and for this simple linear model, rather than generate a numerical solution, the analytical pressure solution has been derived using the Fourier transform as follows:

Any periodic signal, $F(t)=F(t+T)$, where T is the period of the signal, can be written as a sum of its harmonic components (Eq. 3.5), with A_n and B_n the sine and cosine harmonic coefficients [2].

$$F(t) = \frac{A_0}{2} + \sum_{n=1}^{\infty} A_n \cos(n\omega t) + B_n \sin(n\omega t) \quad (\text{Eq. 3.5})$$

$$\omega = \frac{2\pi}{T} \quad (\text{Eq. 3.6})$$

where n is the number of harmonic components and ω is angular frequency

In complex notation, (Eq. 3.5) is equivalent to (Eq. 3.7).

$$F(t) = \frac{1}{2} \sum_{n=-\infty}^{\infty} (A_n - iB_n) e^{in\omega t} \quad (\text{Eq. 3.7})$$

Considering the pressure and flow measured at the inlet of the R_cCR_d circuit as the sum of the harmonic components they can be expressed using (Eq. 3.12), replacing the generic A and B terms with corresponding flow (Q) and pressure (P) terms (Eq. 3.8) and (Eq. 3.9).

$$P_i(t) = \frac{1}{2} \sum_{n=-\infty}^{\infty} (P_{0cn} - iP_{0sn}) e^{in\omega t} \quad (\text{Eq. 3.8})$$

$$Q_i(t) = \frac{1}{2} \sum_{n=-\infty}^{\infty} (Q_{0cn} - iQ_{0sn}) e^{in\omega t} \quad (\text{Eq. 3.9})$$

where P_{0cn} , P_{0sn} , Q_{0cn} , Q_{0sn} are the harmonic pressure and flow components, P_0 and Q_0 are the direct current (DC) pressure and flow components.

A single harmonic component (n^{th} component) of pressure and flow can be expressed in terms of the amplitude of the cosine and sine coefficients as (Eq. 3.10) and (Eq. 3.11).

$$P_i(\omega) = (P_{0c} - iP_{0s}) e^{i\omega t} \quad (\text{Eq. 3.10})$$

$$Q_i(\omega) = (Q_{0c} - iQ_{0s}) e^{i\omega t} \quad (\text{Eq. 3.11})$$

The inlet pressure and flow are related by the complex input impedance of the circuit (Z_{in3W}) through the transfer function in (Eq. 3.12).

$$P_i(\omega) = Q_i(\omega) Z_{in3W}(\omega) \quad (\text{Eq. 3.12})$$

The complex impedance can be expressed alternatively in terms of Z_{re} and Z_{im} , the real and imaginary parts of the signal.

$$Z_{in3W}(\omega) = Z_{re}(\omega) - iZ_{im}(\omega) \quad (\text{Eq. 3.13})$$

Replacing $P_i(\omega)$ and $Q_i(\omega)$ from (Eq. 3.10), (Eq. 3.11) and (Eq. 3.13) into (Eq. 3.12), (Eq. 3.14) is derived.

$$\begin{aligned}
(P_{0c} - iP_{0s})(\cos(\omega t) + isin(\omega t)) \\
= (Z_{re} - iZ_{im})(Q_{0c} \\
- iQ_{0s})(\cos(\omega t) + isin(\omega t))
\end{aligned} \tag{Eq. 3.14}$$

$$P_{0c} - iP_{0s} = Z_{re}Q_{0c} - iZ_{re}Q_{0s} - iZ_{im}Q_{0c} - Z_{im}Q_{0s} \tag{Eq. 3.15}$$

After equating the real and imaginary part in (Eq. 3.15), the sine and cosine pressure coefficients, P_{0c} and P_{0s} , can be expressed at each harmonic as a function of sine and cosine flow coefficients, Q_{0c} and Q_{0s} , and the real and imaginary part of complex input impedance, Z_{re} and Z_{im} (Eq. 3.16).

$$\begin{cases} P_{0c}(\omega) = Z_{re}(\omega)Q_{0c}(\omega) - Z_{im}(\omega)Q_{0s}(\omega) \\ P_{0s}(\omega) = Z_{im}(\omega)Q_{0c}(\omega) + Z_{re}(\omega)Q_{0s}(\omega) \end{cases} \tag{Eq. 3.16}$$

The equivalent impedance of the three element Windkessel model is given in complex by (Eq. 3.17).

$$Z_{in3W}(\omega) = R_c + \frac{R_d(1 - j\omega R_d C)}{1 + (\omega R_d C)^2} \tag{Eq. 3.17}$$

Which can be further separated into real (Eq. 3.18) and imaginary (Eq. 3.19) components.

$$Z_{re}(\omega) = R_c + \frac{R_d}{1 + (\omega R_d C)^2} \tag{Eq. 3.18}$$

$$Z_{im}(\omega) = -\frac{\omega R_d^2 C}{1 + (\omega R_d C)^2} \tag{Eq. 3.19}$$

Replacing the real and imaginary impedance components, Z_{re} and Z_{im} in P_{0c} and P_{0s} expressions in (Eq. 3.16), and further in (Eq. 3.8), the expression for the analytical pressure at the inlet of the $R_c R_d$ Windkessel circuit is given by (Eq. 3.20).

$$\begin{aligned}
P_i(t) &= \frac{(R_c + R_d)Q_0}{2} \\
&+ \sum_{n=1}^{\infty} \left(\left(R_c + \frac{R_d}{1 + (n\omega R_d C)^2} \right) Q_{0cn} \right. \\
&- \left. \left(\frac{n\omega R_d^2 C}{1 + (n\omega R_d C)^2} \right) Q_{0sn} \right) \cos n\omega t \\
&+ \left(\left(\frac{n\omega R_d^2 C}{1 + (n\omega R_d C)^2} \right) Q_{0cn} \right. \\
&+ \left. \left(\frac{R_d}{1 + (n\omega R_d C)^2} \right) Q_{0sn} \right) \sin n\omega t
\end{aligned} \tag{Eq. 3.20}$$

P_0 from (Eq. 3.8) was replaced in (Eq. 3.20) with the ratio between the sum of the two resistors and the DC flow component, Q_0 .

3.1.3.5 Four element Windkessel model

As discussed in Chapter 1, although the three element Windkessel model produced more realistic pressure and flow waveforms, it was noticed both for pulmonary and systemic circulation [55], [56], that better fits to measured data could be obtained by using a higher value than the characteristic impedance for the proximal resistance, and a lower value for C than the overall vascular compliance. The addition of a fourth (inertial) element, L, in parallel with the characteristic resistance R_c , would behave at low frequencies similar to a 2 element Windkessel, whereas at higher frequencies, the response would behave like a three element model. However, when tested on the pulmonary circulation of animals by Segers *et al.* [84] the four element Windkessel model did not reproduce the satisfactory results that had been demonstrated for the systemic circulation. Nevertheless, the option of using the four element Windkessel for the human system is evaluated in this chapter.

Using the same protocol described for the three element model, a four element Windkessel (Figure 3.2) was implemented and solved for the values of its components.

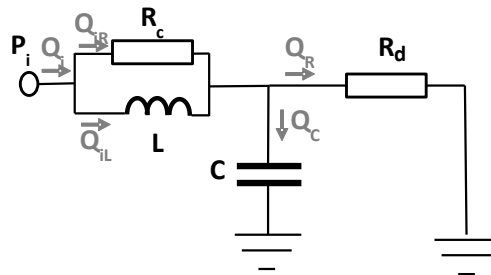


Figure 3.2 Four element Windkessel model (R_c LCR $_d$) used for the analysis of pulmonary circulation in PH

The elements of the circuit are the characteristic resistance R_c , inductance $-L$, total vascular compliance C and distal resistance R_d . The inlet pressure P_i and flow Q_i are measured in the patient main pulmonary artery (MPA)

The real and imaginary impedance of the R_c LCR $_d$ circuit are given by (Eq. 3.21) and (Eq. 3.22).

$$Z_{re} = \frac{\omega^2 L^2 R_c}{R_c + (\omega L)^2} + \frac{R_d}{1 + (\omega R_d C)^2} \quad (\text{Eq. 3.21})$$

$$Z_{im} = \frac{\omega R_d^2 C}{1 + (\omega R_d C)^2} - \frac{\omega L R_c^2}{R_c + (\omega L)^2} \quad (\text{Eq. 3.22})$$

Following the same steps for determining the analytical solution for the inlet pressure of a three element Windkessel model (Eq. 3.20), and using relationships (Eq. 3.21) and (Eq. 3.22),

the analytical expression for the inlet pressure of a four element Windkessel model can be readily determined.

3.1.4 1D model of a straight elastic tube

A 1D model of a straight elastic tube was implemented to locally quantify the wave reflections present in the main pulmonary artery, originating from reflection sites in the downstream vasculature. Since the pulmonary vasculature is characterised by short, tapered tubes with multiple branches and bifurcations (or even trifurcations) with a pulsatile flow, it might be expected that wave reflections will play an important role.

Pulse wave propagation in an elastic tube can be described in the frequency domain [52], or in the time domain using wave intensity analysis (WI) [71]. The classical frequency domain approach has been adopted in the current work, but both approaches produce identical results in terms of the computed power in forward and backward travelling components as proved by Hughes and Parker [72].

Linearization about a reference state of the 1D Navier-Stokes equations returns the standard one-dimensional wave equation (Eq. 3.23).

$$\frac{\partial^2 p}{\partial t^2} - c^2 \frac{\partial^2 p}{\partial z^2} = 0 \quad (\text{Eq. 3.23})$$

The general solution of equation (Eq. 3.23), expressed in terms of forward and backward components is:

$$p(\omega, z, t) = P_f e^{i(\omega t - kz)} + P_b e^{i(\omega t + kz)} \quad (\text{Eq. 3.24})$$

And similarly for flow:

$$Q(\omega, z, t) = Q_f e^{i(\omega t - kz)} + Q_b e^{i(\omega t + kz)} \quad (\text{Eq. 3.25})$$

$$k = \frac{\omega}{c} \quad (\text{Eq. 3.26})$$

where k is the complex wave number, c is the complex wave speed, ω is the angular frequency, P_f , P_b , Q_f and Q_b are the amplitude of the forward and backward pressure and flow waves.

For an inviscid fluid and using real components of the forward and backward pressure flow components, the general pressure and flow solution is given by (Eq. 3.27) and (Eq. 3.28).

$$p(\omega, z, t) = (P_1 \cos(kz - \omega t) + P_2 \sin(kz - \omega t)) + (P_3 \cos(kz + \omega t) + P_4 \sin(kz + \omega t)) \quad (\text{Eq. 3.27})$$

$$Q(\omega, z, t) = (Q_1 \cos(kz - \omega t) + Q_2 \sin(kz - \omega t)) + (Q_3 \cos(kz + \omega t) + Q_4 \sin(kz + \omega t)) \quad (\text{Eq. 3.28})$$

Where,

$$p_f(\omega, z, t) = P_1 \cos(kz - \omega t) + P_2 \sin(kz - \omega t) \quad (\text{Eq. 3.29})$$

$$p_b(\omega, z, t) = P_3 \cos(kz + \omega t) + P_4 \sin(kz + \omega t) \quad (\text{Eq. 3.30})$$

Respectively,

$$Q_f(\omega, z, t) = Q_1 \cos(kz - \omega t) + Q_2 \sin(kz - \omega t) \quad (\text{Eq. 3.31})$$

$$Q_b(\omega, z, t) = Q_3 \cos(kz + \omega t) + Q_4 \sin(kz + \omega t) \quad (\text{Eq. 3.32})$$

where P_1 to P_4 and Q_1 to Q_4 are the real components of pressure and flow waveforms.

At the inlet of the domain, $z=0$, the expressions for pressure and flow are:

$$p(\omega, 0, t) = P_1 \cos \omega t - P_2 \sin \omega t + P_3 \cos \omega t + P_4 \sin \omega t \quad (\text{Eq. 3.33})$$

$$Q(\omega, 0, t) = Q_1 \cos \omega t - Q_2 \sin \omega t + Q_3 \cos \omega t + Q_4 \sin \omega t \quad (\text{Eq. 3.34})$$

Which can be further expressed in terms of sine and cosine pressure and flow coefficients (Eq. 3.35) and (Eq. 3.36).

$$p(\omega, 0, t) = P_{0c} \cos \omega t + P_{0s} \sin \omega t \quad (\text{Eq. 3.35})$$

$$Q(\omega, 0, t) = Q_{0c} \cos \omega t + Q_{0s} \sin \omega t \quad (\text{Eq. 3.36})$$

Equating (Eq. 3.33) with (Eq. 3.35) and (Eq. 3.34) with (Eq. 3.36) and separating the sine and cosine coefficients results in (Eq. 3.37) and (Eq. 3.38).

$$\begin{cases} P_1 + P_3 = P_{0c} \\ -P_2 + P_4 = P_{0s} \end{cases} \quad (\text{Eq. 3.37})$$

$$\begin{cases} Q_1 + Q_3 = Q_{0c} \\ -Q_2 + Q_4 = Q_{0s} \end{cases} \quad (\text{Eq. 3.38})$$

The pressure and flow are related by the vessel characteristic impedance. For a straight, axisymmetric, thin walled elastic vessel, neglecting viscosity, the characteristic impedance is given by (Eq. 3.39).

$$Z_c = \frac{\rho c_0}{A_0} \quad (\text{Eq. 3.39})$$

where c_0 is the Moens-Korteweg wave speed, ρ is the blood density, A_0 - diastolic area

$$Z_c = \frac{P_f}{Q_f} = -\frac{P_b}{Q_b} = \frac{P_1}{Q_1} = \frac{P_2}{Q_2} = -\frac{P_3}{Q_3} = -\frac{P_4}{Q_4} \quad (\text{Eq. 3.40})$$

Using (Eq. 3.37) and (Eq. 3.38) and expressing $Q_{1:4}$, as a function of $P_{1:4}$ and Z_c (Eq. 3.40) a system of simultaneous equations results (Eq. 3.41).

$$\begin{pmatrix} 1 & 0 & 1 & 0 \\ 0 & -1 & 0 & 1 \\ \frac{1}{Z_c} & 0 & -\frac{1}{Z_c} & 0 \\ 0 & \frac{1}{Z_c} & 0 & -\frac{1}{Z_c} \end{pmatrix} \begin{pmatrix} P_1 \\ P_2 \\ P_3 \\ P_4 \end{pmatrix} = \begin{pmatrix} P_{0c} \\ P_{0s} \\ Q_{0c} \\ Q_{0s} \end{pmatrix} \quad (\text{Eq. 3.41})$$

Pressure and flow sine and cosine coefficients (right hand side –RHS) are determined after applying a Fast Fourier Transform (fft) of the measured $Q(t)$ and $p(t)$ signals in MATLAB.

After solving the system of equations (Eq. 3.41), the forward and backward pressure components, $P_{1:4}$ are given by (Eq. 3.42)

$$\begin{cases} P_1 = \frac{1}{2}(P_{0c} + Q_{0c}Z_c) \\ P_2 = -\frac{1}{2}(P_{0s} + Q_{0s}Z_c) \\ P_3 = \frac{1}{2}(P_{0c} - Q_{0c}Z_c) \\ P_4 = \frac{1}{2}(P_{0s} - Q_{0s}Z_c) \end{cases} \quad (\text{Eq. 3.42})$$

The inviscid characteristic impedance was computed by replacing the pulse wave velocity c_0 with a model derived $c_{0\text{model}}$ (Eq. 3.43).

$$c_{0\text{model}} = \sqrt{\frac{E_p}{2\rho(1-\nu^2)}} \quad (\text{Eq. 3.43})$$

Eh/r_0 term from Moens Korteweg wave speed equation was replaced with E_p where Peterson's elasticity modulus was derived as showed in Chapter 2, Section 2.3.

$$E_p = \frac{Eh}{r_0} \quad (\text{Eq. 3.44})$$

$$p_f(\omega, 0, t) = P_1 \cos \omega t - P_2 \sin \omega t \quad (\text{Eq. 3.45})$$

$$p_b(\omega, 0, t) = P_3 \cos \omega t + P_4 \sin \omega t \quad (\text{Eq. 3.46})$$

The amplitude of the forward and backward pressure waves for a single harmonic component are given by (Eq. 3.47) and (Eq. 3.48).

$$P_f = \sqrt{P_1^2 + P_2^2} \quad (\text{Eq. 3.47})$$

$$P_b = \sqrt{P_3^2 + P_4^2} \quad (\text{Eq. 3.48})$$

where P_w can be replaced with the amplitude of the harmonic component of the backward or forward pressure wave.

The power contained in one harmonic wave component, is given by (Eq. 3.49).

$$W_{pw}(\omega) = \frac{P_w^2(\omega)}{2Z_c} \quad (\text{Eq. 3.49})$$

The total power of the forward and backward wave (W_{pft} , W_{pbt}) is given by the sum of the power in the individual harmonics, (Eq. 3.50) and (Eq. 3.51)

$$W_{pft} = \sum_{n_\omega=1}^{\infty} W_{pf}(\omega_n) \quad (\text{Eq. 3.50})$$

$$W_{pbt} = \sum_{n_\omega=1}^{\infty} W_{pb}(\omega_n) \quad (\text{Eq. 3.51})$$

where n is the number of harmonic components considered.

The total power measured at the inlet of the 1D domain was defined as the sum of power contained in the forward and backward waves (Eq. 3.52).

$$W_{total} = W_{pft} + W_{pbt} \quad (\text{Eq. 3.52})$$

3.1.5 Coupled 1D and 0D models

The previous sections describe two simple mathematical models used to represent and infer the status of the pulmonary circulation in health and disease. The 0D Windkessel model can be used to quantify the overall distribution of resistances and compliance, but cannot give any information about the traveling waves. On the other hand, a simple 1D model of a straight elastic tube, described locally by the measured inlet flow and pressure waveforms, quantifies the reflections sensed at the measuring site, without providing any information about where those reflections have come from.

Several authors, [85], [76], [78], [79] have identified the bifurcation of the MPA as one of the reflection sites. Pollack *et al.* [85] argued that in a healthy human, although more local reflection sites are present, an 'effective reflection site' is found at ~15 cm from the pulmonary valve.

Assuming that in the pulmonary circulation an effective reflection site exists and that it is unique, a simple model to determine where it is located can be designed by coupling a 1D model of a straight elastic tube with a 0D Windkessel model. Under this assumption, by

solving the coupled 1D-0D model for the length of the tube and Windkessel parameters, it can be tested whether the effective reflection site can be used as a PH discriminant.

The model is described in the following section.

At the end of a 1D elastic tube, with unknown length l , a 0D ($R_{lc}C R_{ld}$) is added.

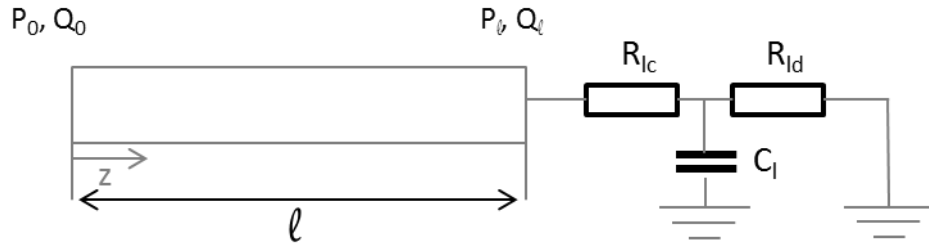


Figure 3.3 A 1D model of a straight elastic tube coupled with a 0D $R_{lc}C R_{ld}$ model

The boundary conditions of the coupled 1D-0D model are the following:

Boundary conditions for the inlet of the 1D domain

$p_0(\omega, 0, t)$ and $Q_0(\omega, 0, t)$ are the pressure and flow at the measuring site, given by (Eq. 3.33) and (Eq. 3.34). The sine and cosine inlet flow coefficients can be written in terms of pressure coefficients and characteristic impedance, for one harmonic (Eq. 3.53).

$$\begin{cases} \frac{1}{Z_c} (P_1 - P_3) = Q_{0c} \\ \frac{1}{Z_c} (-P_2 - P_4) = Q_{0s} \end{cases} \quad (\text{Eq. 3.53})$$

Boundary conditions for the outlet of the 1D domain

From the general expressions of pressure and flow, (Eq. 3.27) and (Eq. 3.28), at an arbitrary position z along the tube, the pressure and flow at the end of 1D domain $p_l(\omega, l, t)$ and $Q_l(\omega, l, t)$, can be written.

$$\begin{aligned} p_l(\omega, l, t) = & (P_1 \cos(kl - \omega t) + P_2 \sin(kl - \omega t)) \\ & + (P_3 \cos(kl + \omega t) + P_4 \sin(kl + \omega t)) \end{aligned} \quad (\text{Eq. 3.54})$$

$$\begin{aligned} Q_l(\omega, l, t) = & (Q_1 \cos(kl - \omega t) + Q_2 \sin(kl - \omega t)) \\ & + (Q_3 \cos(kl + \omega t) + Q_4 \sin(kl + \omega t)) \end{aligned} \quad (\text{Eq. 3.55})$$

Equations (Eq. 3.54) and (Eq. 3.55) can be expressed as a function of sine and cosine coefficients, at the end of the 1D domain (Eq. 3.56) and (Eq. 3.36).

$$p_l(\omega, l, t) = P_{lc} \cos \omega t + P_{ls} \sin \omega t \quad (\text{Eq. 3.56})$$

$$Q_l(\omega, l, t) = Q_{lc} \cos \omega t + Q_{ls} \sin \omega t \quad (\text{Eq. 3.57})$$

Equating the sine and cosine coefficients of (Eq. 3.54) and (Eq. 3.55) with (Eq. 3.56) and (Eq. 3.57), and using relationship (3.40) between flow and pressure individual components, results in (Eq. 3.58) and (Eq. 3.59).

$$\begin{cases} P_1 \cos kl + P_2 \sin kl + P_3 \cos kl + P_4 \sin kl = P_{lc} \\ P_1 \sin kl - P_2 \cos kl - P_3 \sin kl + P_4 \cos kl = P_{ls} \end{cases} \quad (\text{Eq. 3.58})$$

$$\begin{cases} \frac{1}{Z_c} (P_1 \cos kl + P_2 \sin kl - P_3 \cos kl - P_4 \sin kl) = Q_{lc} \\ \frac{1}{Z_c} (P_1 \sin kl - P_2 \cos kl + P_3 \sin kl - P_4 \cos kl) = Q_{ls} \end{cases} \quad (\text{Eq. 3.59})$$

1D-0D 'coupling'

Using the method described in Section 3.1.3, the pressure of the inlet at the 0D domain can be expressed as a function of 0D model equivalent complex impedance and the flow entering the 0D domain.

$$\begin{cases} P_{lc}(\omega) = Z_{lre}(\omega)Q_{lc}(\omega) - Z_{lim}(\omega)Q_{ls}(\omega) \\ P_{ls}(\omega) = Z_{lim}(\omega)Q_{lc}(\omega) + Z_{lre}(\omega)Q_{ls}(\omega) \end{cases} \quad (\text{Eq. 3.60})$$

$$Z_{lre}(\omega) = R_{ld} + \frac{R_{ld}}{1 + (\omega R_{ld} C)^2} \quad (\text{Eq. 3.61})$$

$$Z_{lim}(\omega) = -\frac{\omega R_{ld}^2 C}{1 + (\omega R_{ld} C)^2} \quad (\text{Eq. 3.62})$$

Since the pressure and flow at the end of the 1D domain must be the same as the ones at the inlet of the 0D domain, (Eq. 3.58) can be equated with (Eq. 3.60) at each harmonic, resulting (Eq. 3.64).

$$\begin{cases} P_1 \cos kl + P_2 \sin kl + P_3 \cos kl + P_4 \sin kl - Z_{lre} Q_{lc} + Z_{lim} Q_{ls} = 0 \\ P_1 \sin kl - P_2 \cos kl - P_3 \sin kl + P_4 \cos kl - Z_{lim} Q_{lc} - Z_{lre} Q_{ls} = 0 \end{cases} \quad (\text{Eq. 3.63})$$

After replacing all the known terms, a system of equations can be written in matrix form, as follows:

$$\begin{pmatrix} \frac{1}{Z_c} & 0 & -\frac{1}{Z_c} & 0 \\ 0 & -\frac{1}{Z_c} & 0 & -\frac{1}{Z_c} \\ \left(1 - \frac{Z_{lre}}{Z_c}\right) \cos kl + \frac{Z_{lim}}{Z_c} \sin kl & \left(1 - \frac{Z_{lre}}{Z_c}\right) \sin kl - \frac{Z_{lim}}{Z_c} \cos kl & \left(1 + \frac{Z_{lre}}{Z_c}\right) \cos kl + \frac{Z_{lim}}{Z_c} \sin kl & \left(1 + \frac{Z_{lre}}{Z_c}\right) \sin kl - \frac{Z_{lim}}{Z_c} \cos kl \\ \left(1 - \frac{Z_{lre}}{Z_c}\right) \sin kl - \frac{Z_{lim}}{Z_c} \cos kl & \left(-1 + \frac{Z_{lre}}{Z_c}\right) \cos kl - \frac{Z_{lim}}{Z_c} \sin kl & \left(-1 - \frac{Z_{lre}}{Z_c}\right) \sin kl + \frac{Z_{lim}}{Z_c} \cos kl & \left(1 + \frac{Z_{lre}}{Z_c}\right) \cos kl + \frac{Z_{lim}}{Z_c} \sin kl \end{pmatrix} \begin{pmatrix} P_1 \\ P_2 \\ P_3 \\ P_4 \end{pmatrix} = \begin{pmatrix} Q_{oc} \\ Q_{os} \\ 0 \\ 0 \end{pmatrix} \quad (\text{Eq. 3.64})$$

Solving the above system of equations returns the pressure coefficients (P_1 to P_4) which are dependent on the tube length l and the values of the Windkessel parameters added at the

end of the tube R_{ld} , R_{lc} and C_i . By applying the same optimisation steps described in Section 3.1.3, the length of the tube can be estimated together with the other electrical parameters.

3.1.6 Statistical analysis of the results

Statistical analysis of the results was performed using SPSS for data analysis and GraphPad Prism for graphical representation.

Statistical analysis was performed for: differences between independent variables, variable correlations and measurements of agreement, as following:

Independent sample tests

Independent multiple sample significance tests were performed for the parameters proposed as differentiation criteria in normal and PH subjects: W_b/W_{total} , R_d , R_c and C_i .

A one way ANOVA test for independent groups, with Tukey's post-hoc correction, was applied for the parameters which satisfied the normality and variance homogeneity conditions. The normality criterion was tested by visual inspection of the histograms and confirmed by the Shapiro-Wilk test on each independent group. The homogeneity of variance was tested using Leven's test. The non-parametric Kruskal-Wallis test for independent data was applied for the parameters for which the above criteria were not met [129]. Differences were considered significant for p -values < 0.05 .

Data were represented graphically using box and whiskers plots according to Tukey's method [130]. The significance p -values resulting from pairwise multiple comparisons were marked on the graph.

Agreement between ratters

Intra- and inter- operator variability for the derived metrics of the OD and 1D model were tested using the Bland-Altman method [131] and by computing the intraclass correlation coefficient [132]. MRI image data sets of 20 subjects were selected at random from the entire cohort and segmented by two operators, A and B. Operator A performed the image segmentations twice within one week. Inter and intra operator variability analysis was performed on the final derived parameters: W_b/W_{total} , R_d , R_c and C_i .

The intra class correlation coefficient (ICC) was also used to test the agreement between parameters derived using modified versions of proposed methods.

Correlation

The strength of linear correlations was tested using Pearson's correlation coefficient. Spearman's coefficient was used to express the strength of non-linear relationships.

RESULTS AND DISCUSSION

A cohort of 80 subjects was assessed using two simple mathematical models, a 0D $-R_cCR_d$ Windkessel model and a 1D model of a straight elastic tube, in order to infer the status of the pulmonary circulation. The cohort was divided into 4 groups: healthy volunteers (n=8), NoPH (n=15), PH patients with $PVR < 4WU$, mild PH (n=19) and PH patients with $PVR \geq 4WU$, severe PH, (n=38). The input to the mathematical models was derived non-invasively using MRI images of the MPA acquired during an entire cardiac cycle. The protocol for segmenting the images and computing the area $A(t)$, flow $Q(t)$ and pressure $p(t)$ waveforms was described in Chapter 2 of the current thesis.

The methods describing the two proposed mathematical models were previously published in "*MRI model-based non-invasive differential diagnosis in pulmonary hypertension*" [27] and re-stated in more detail in the above *Materials and Methods* section. The *Results and Discussions* section of the current chapter presents the results following the extension of the cohort from 35 to 80 subjects, together with further amplification of the results corresponding to the pilot study.

Using the non-invasively derived pressure waveforms, the mean, systolic and diastolic pressures were compared with the corresponding invasive RHC values. Figure 3.4 shows the relationship between the invasive and model-derived pressures. Although the trends are consistent, the linear correlation between invasive and model-derived values, as assessed using Person's correlation coefficient, r and goodness of fitness, R^2 values, was weak. The model overestimates mPAP in the NoPH group and underestimates it for the diseased groups.

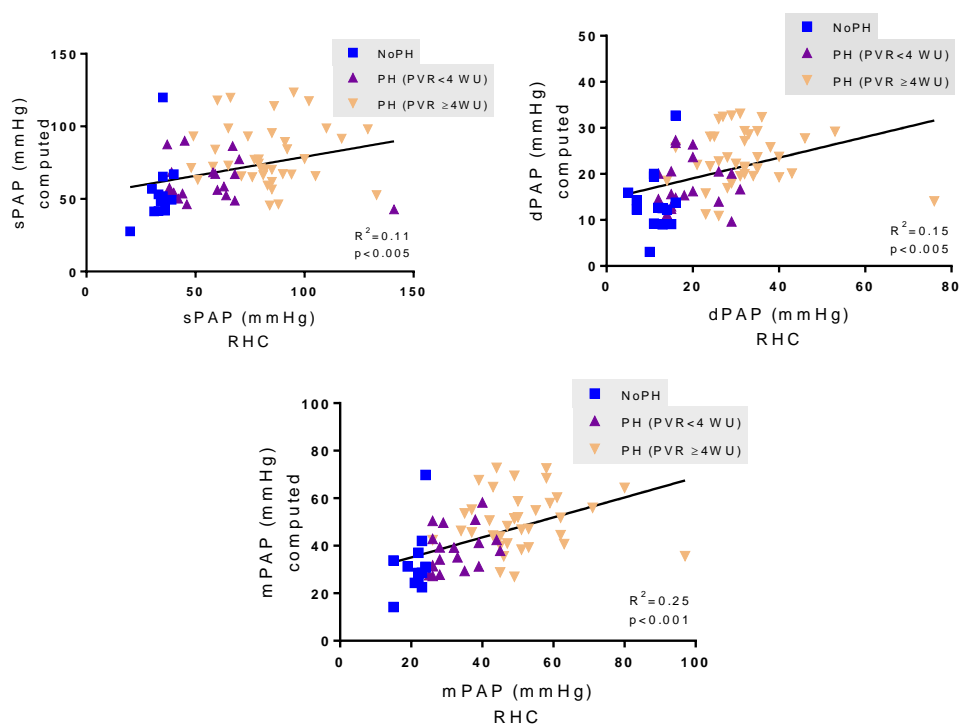


Figure 3.4 Relationship between invasively measured (RHC) and model derived mean (mPAP), systolic (sPAP) and diastolic (dPAP) pressures

The derived model's pressures (computed) show weak linear correlation (Pearson's $r_{sPAP}=0.33$, $r_{dPAP}=0.39$, $r_{mPAP}=0.5$) with the measured (RHC) values.

It is not unexpected that the radius-to-pressure model does not reflect entirely the individual values of measured pressures. At some point during PH manifestation, the PA can continue to enlarge independent of arterial pressure [133]. However, the derived pressure waveforms had been applied together with the flow waveforms as input for the mathematical models described previously, hypothesising that although some parameters values are solely influenced by the magnitude of the waves (R_{total}), others (W_b/W_{total} , R_d , C) depend also on the variations of waveforms during the cardiac cycle and these might prove less sensitive to scaling caused by errors in the pressure-radius relationship.

3.1.7 0D model

3.1.7.1 Results

The electrical parameters of an R_cCR_d Windkessel model were derived using an optimisation method based on stochastic and gradient decent algorithms available in the MATLAB Optimisation Toolbox.

Overall, the parameter fitting process performed reasonably well, returning root mean squared error values with an average of 0.13 ± 0.08 and a 95% CI of 0.11 to 0.14. However, approximately 10% of the analysed cases were fitted poorly, with an error reaching 0.45.

Figure 3.5 shows a few examples, including the best, the worst and two intermediated fitted curves. The fitted waveforms were reconstructed using (Eq. 3.2) using 10 harmonic components. It can be noticed that for the best fitted case the original waveform resembles that expected for an R-C-R circuit response, and therefore the fitting is very good. Conversely, the ‘ripples’ present in the measured signals on the other examples are not characteristic of the expected response of these simple Windkessel representations, and so it is not surprising that the fit was poorer. The model tried to give the best approximation of the original shape, while preserving the systolic and diastolic values, as was defined through the cost function.

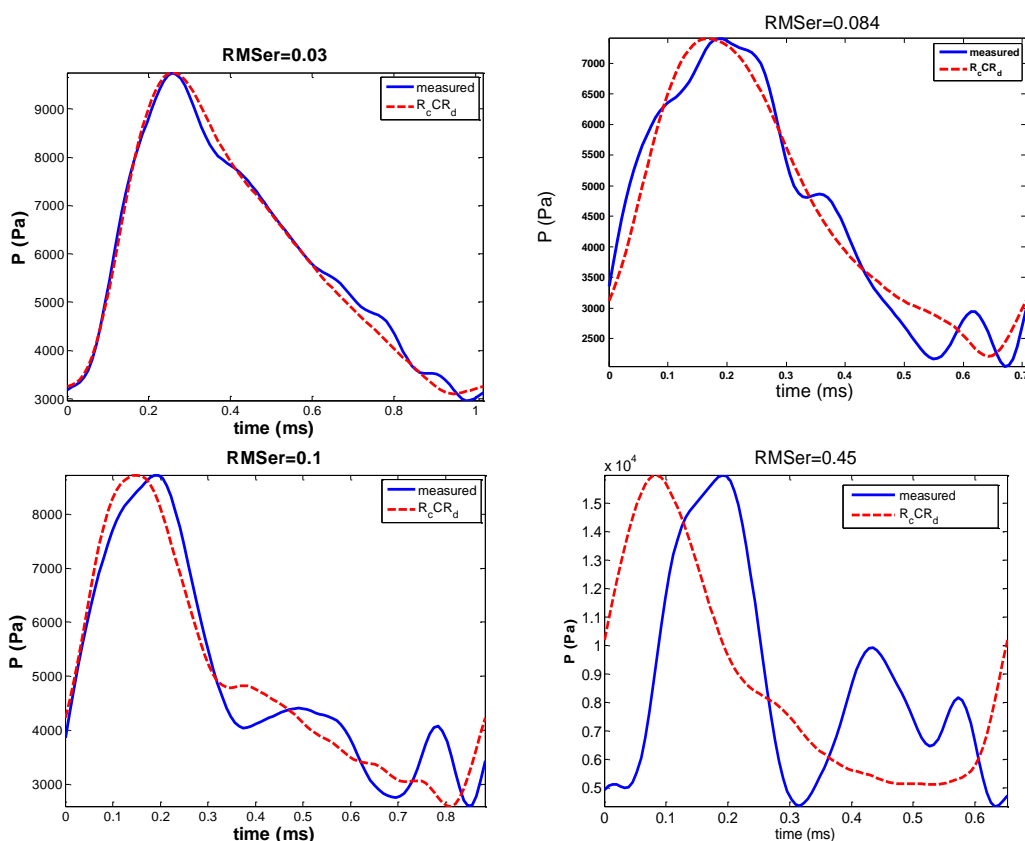


Figure 3.5 Fitting quality of a 3 element Windkessel model: original waveform (continuous blue) and fitted (dashed red).

As outlined above, there were some cases for which the fit was relatively poor, based on the calculated RMSer (Eq.3.2), and visual inspection of the overlaying waveforms. However, all the results were considered for the statistical analysis of the significance of the differences in the parameters for the study cohort. The quality of the fit is discussed in more details in the context of groups’ outlier presence. The derived values were proposed to be used as differentiation criteria between healthy volunteers, clinical patients with no PH and two sub-groups of PH patients, separated according to the measured PVR value in mild and severe PH.

The results of the electrical parameters are shown in Figure 3.6 for all the analysed groups. Data were represented using box and whiskers plots as proposed by Tukey's method [130]. The values that were outside the whisker bands were marked in each group as outliers. The median and mean of the group were marked with a horizontal line and a plus symbol, respectively.

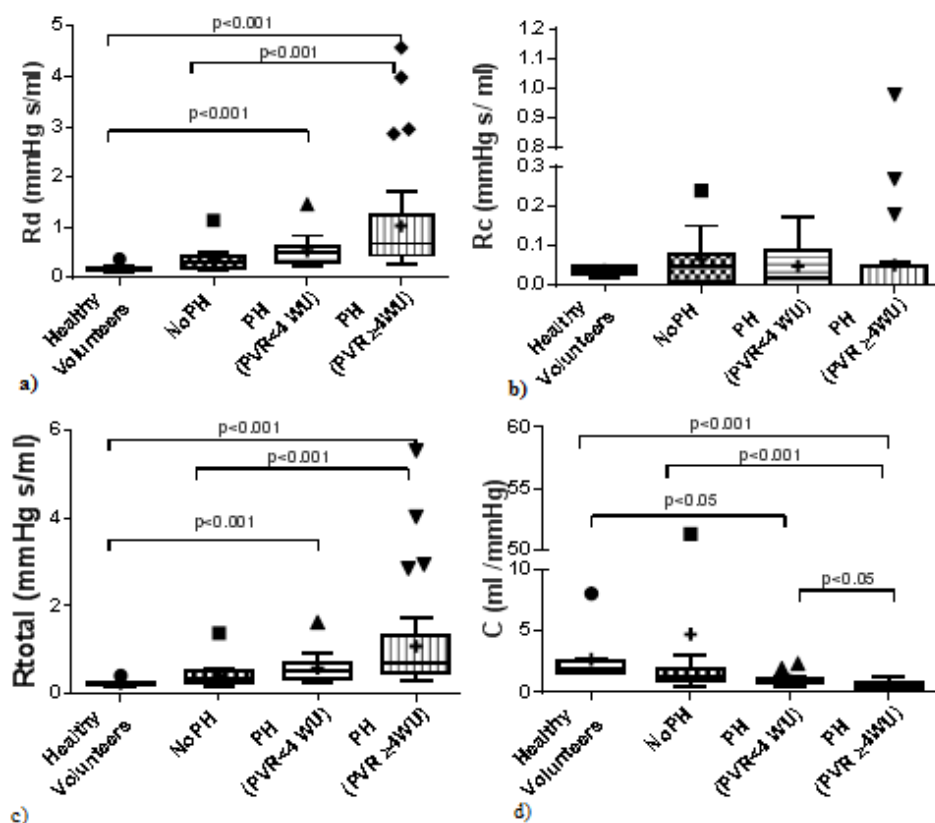


Figure 3.6 The results for the OD Windkessel model on the 80 patient cohort: (a) distal resistance R_d , (b) characteristic resistance R_c , (c) total resistance R_{total} , (d) total compliance C

R_d and R_{total} show statistically significant differences between the healthy volunteers and each of the PH groups and between NoPH and severe PH group. C shows statistically significant differences between healthy volunteers and each of the PH groups, between NoPH and severe PH and between the two PH sub-groups. R_c shows no statistical difference between groups.

All electrical parameters (R_{total} , R_d , C and R_c) of the OD model were not normally distributed within the groups, as assessed visually by histogram inspection and confirmed by Shapiro-Wilk test ($p < 0.05$). Due to the violation of the normality assumption, the non-parametric Kruskal-Wallis test for independent samples, with multiple comparisons, were run for each

variable to determine whether there were statistically significant differences between the 4 subject groups.

R_{total}

The total resistance, R_{total} , defined as mean pressure over mean flow in the MPA, increased, as expected, with the disease status. It increased progressively from 0.24 ± 0.08 mmHg s/ml in healthy volunteers to 0.42 ± 0.3 mmHg s/ml in the NoPH group, to 0.59 ± 0.3 mmHg s/ml and to 1.09 ± 1.1 mmHg s/ml in the mild and severe-disease PH subgroups. The mean R_{total} value of the second PH subgroup is highly driven by the presence of outliers. Therefore, more representative of the group is the median R_{total} value, of 0.68 mmHg s/ml. The total pulmonary resistance showed statistically significant differences between the healthy volunteers and both of the PH subgroups ($p < 0.001$) and between the NoPH and severe PH group ($p < 0.001$).

The values of the total pulmonary resistance are influenced by the mean pulmonary arterial pressure since this metric is defined as the ratio between mean pressure and mean flow. As displayed in Figure 3.4, the non-invasively computed mPAP is overestimated for the NoPH group and marginally underestimated for the two PH groups. Therefore, it is expected that R_{total} of the NoPH group would be overestimated, while for the two PH groups it will be underestimated, if the measured (RHC) mPAP were to be used instead of the computed mPAP.

In order to understand how the surrogate pressure model influences total resistance, the parameter was also computed using RHC mPAP. On average, $R_{totalRHC}$ was lower in the NoPH group while the two PH groups were less affected. However, the trend between the groups remained the same as for R_{total} , showing an increase with the disease status. The total pulmonary resistance computed using RHC mPAP showed statistically significant differences between all the analysed groups. The NoPH group displayed a mean $R_{totalRHC}$ of 0.24 ± 0.1 mmHg s/ml, 43% smaller than the one predicted by R_{total} for this group. The two PH subgroups had mean $R_{totalRHC}$ of 0.49 ± 0.31 mmHg s/ml and 1.04 ± 1.02 mmHg s/ml, being 15% (PH sub-group 1) and 4% (PH sub-group 1) smaller than the non-invasive R_{total} (Figure 3.7).

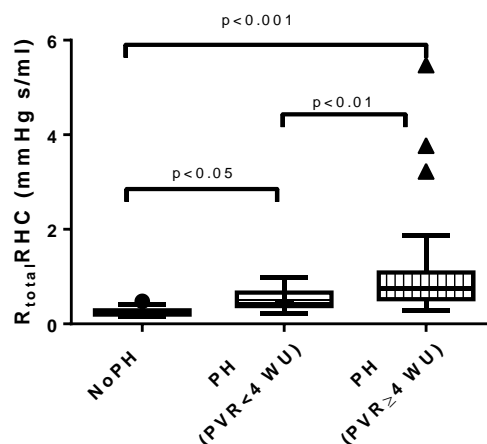


Figure 3.7 Total resistance computed as ratio of invasively measured mPAP (RHC) and mean flow (MRI) $R_{total}RHC$

$R_{total}RHC$ was computed only for the groups where invasive pressure measurements were available. The parameter showed statistically significant mean rank differences between all the tested groups.

Although defined differently, the notion of pulmonary vascular resistance (PVR) and total vascular resistance are used interchangeably, since both represent the steady-state component of the ventricular afterload [134]. The first is defined as the difference between the mean pulmonary artery pressure and mean pulmonary wedge pressure divided by the cardiac output, while the second is defined as the ratio of mean pressure to mean flow. From the definition, it is expected for the two measures to have a strong correlation.

The relationship between R_{total} and PVR can be approximated linearly, but the correlation between the variables is rather poor, Pearson's $r=0.32$, $R^2=0.11$, $p<0.001$. In order to understand once again whether the poor relationship is determined by the pressure surrogate model, the invasive total resistance, $R_{total}RHC$ relationship with PVR was also tested. Although the linear correlation with PVR was stronger for the latter, $r=0.47$, $R^2=0.22$, $p<0.001$, it remains poor. Figure 3.7 displays the relationship between R_{total} and $R_{total}RHC$ with PVR, together with the correlation line which best fits each data set. The differences between slopes and intercepts of the two fitting lines are not statistically significant ($p=0.42$ and $p=0.54$).

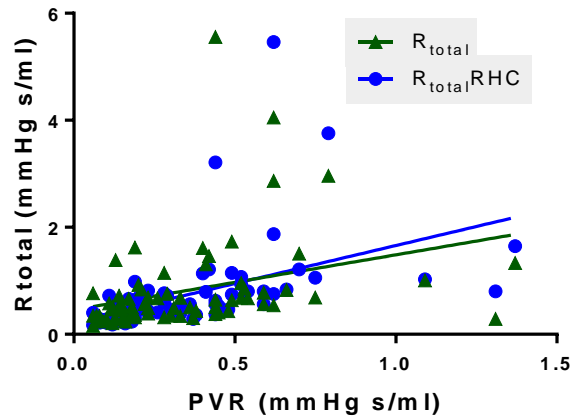


Figure 3.8 Relationship between total resistances measured as mean pressure to mean flow and clinically derived PVR.

R_{total} and $R_{totalRHC}$ were computed as mean pressure to mean flow ratio. For the computation of the first, the model derived mPAP was used, whereas for the second the RHC mPAP was used. Although the trend is similar and consistent, both of the measures correlate poorly with the clinically derived PVR ($r=0.32$, $R^2=0.11$ and $r=0.47$, $R^2=0.22$).

R_d , R_c

The distal resistance, R_d contributes on average $83.2 \pm 5.3\%$ to R_{total} in the healthy volunteers group, $85.8 \pm 11\%$ in the NoPH group, $92.8 \pm 8.3\%$ in the mild PH sub-group and up to $96.7 \pm 2.5\%$ in the severe PH group. R_d , as well as R_{total} , increased with the disease status, varying on average from 0.2 ± 0.07 and 0.35 ± 0.24 mmHg s/ml in the healthy volunteer and NoPH groups to 0.54 ± 0.28 and 1.03 ± 0.9 mmHg s/ml in the two PH sub-groups. Similarly to R_{total} , the severe PH group contains 4 outliers which considerably increase the mean of the group. The median value characteristic of the second PH subgroup is 0.68 mmHg s/ml. Statistically significant differences are shown by the R_d parameter between the healthy volunteers and each of the PH groups ($p < 0.001$), as well as between the NoPH and severe PH group ($p < 0.001$).

The contribution of the characteristic resistance, R_c to R_{total} was much smaller than the R_d contribution, with a R_d to R_c ratio of $\sim 1:8$ in the normotensive groups and $\sim 1:9$ in the PH groups. R_c showed no statistical significance between the analysed groups.

C

The total pulmonary compliance, C decreased with the disease status, from 2.71 ± 2.2 ml/mmHg in the healthy volunteers group, 4.74 ± 12.9 ml/mmHg in the NoPH group, 0.98 ± 0.45 ml/mmHg in the mild PH group and 0.6 ± 0.32 ml/mmHg in the severe PH group. The mean C values in the healthy volunteers and NoPH groups were dragged up by the presence of the outliers. Therefore, the median values of 1.86 and 1.29 ml/mmHg for the healthy

volunteers and NoPH groups are more representative. Statistically significant difference was exhibited by C between the healthy volunteers group and both of the PH sub-groups ($p < 0.05$ and $p < 0.001$), between NoPH and severe PH ($p < 0.001$), as well as between the 2 PH sub-groups ($p < 0.05$).

The total pulmonary compliance, C, inversely correlates to the total pulmonary resistance, R_{total} ($R^2 = 0.66$, $p < 0.001$), distal resistance, R_d (Spearman $r = -0.72$, $R^2 = 0.7$, $p < 0.001$) and invasively measured pulmonary vascular resistance, PVR ($R^2 = 0.79$, $p < 0.001$). The relationships are graphically displayed in Figure 3.9. From the data, the NoPH case which returned an extreme value for C, of 51.3 ml/mmHg, was eliminated because this produced gross distortion of the results.

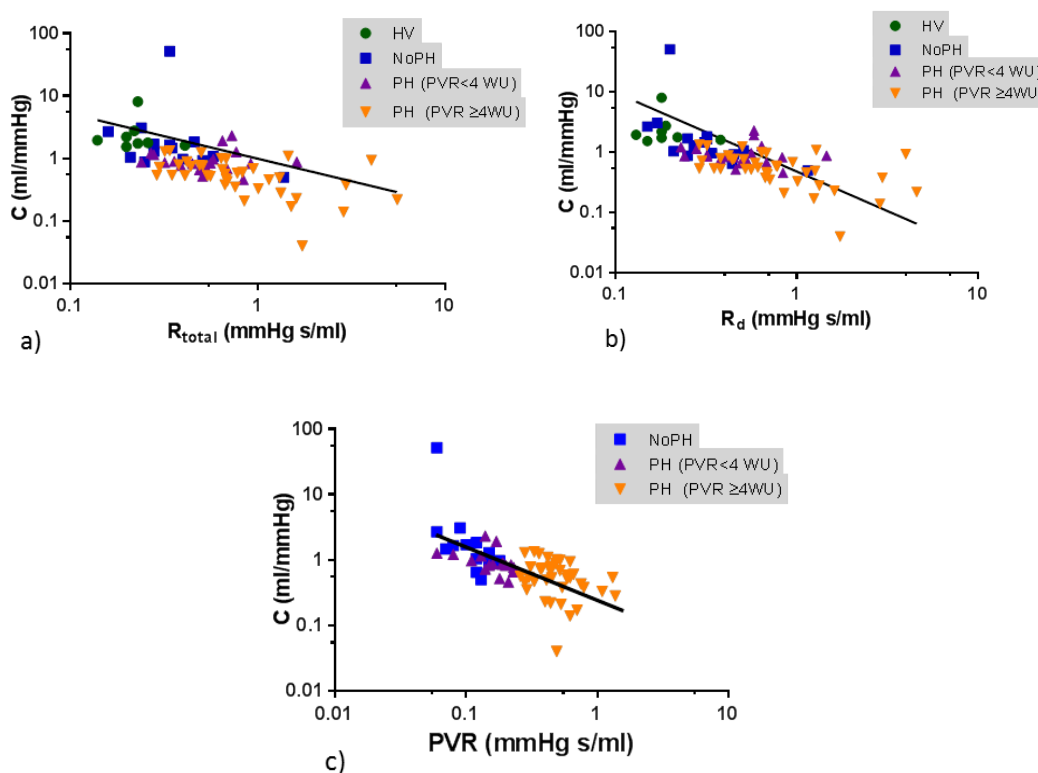


Figure 3.9 Relationship between the total compliance, C and total R_{total} and distal R_d resistances computed from the OD model and total compliance C, and clinically measured PVR, displayed on log-log graphs

C inversely correlates with all the pulmonary resistances. Data is colour coded according to the patient group, showing decreasing compliance and increasing resistance with the disease.

$R_d C$

The product of the distal resistance R_d and total pulmonary compliance, C, of a three element Windkessel model, representing the time constant of the model [135], showed no statistical

differences between the analysed groups Figure 3.10 a. Once again the average values in each group are driven by the presence of extreme outliers, and the median values are more representative: 1.86 ml/mmHg –healthy volunteers, 1.29 ml/mmHg –NoPH group, 0.86 ml/mmHg –mild PH group and 0.54 ml/mmHg –severe PH group. Upon the outliers’ removal, the R_dC product remains almost constant across the groups, with a value of ~ 0.4 s (Figure 3.10 b).

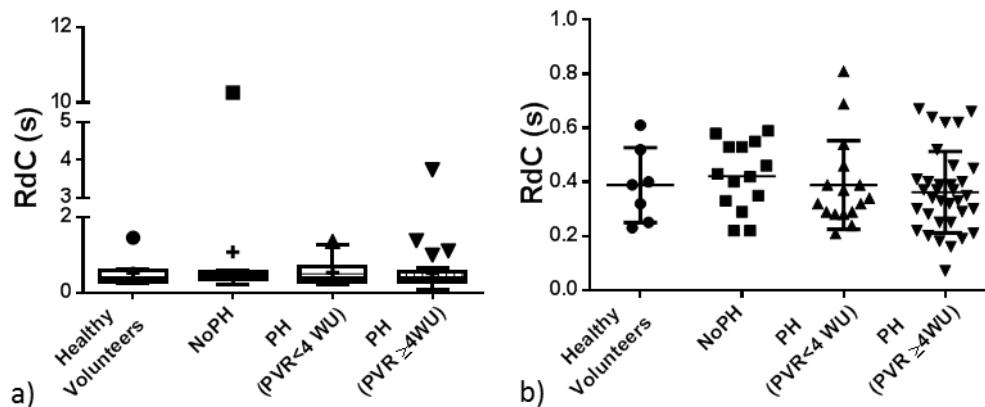


Figure 3.10 The variation of distal resistance-total compliance product within the analysed groups: (a) entire cohort (b) data from (a) without the marker outliers

The circuit’s time constant showed now statistical difference within the groups (a). The removal of the marked outliers, emphasises that the R_dC product stays constant between groups, having an group average value of ~ 0.4 s

Four element Windkessel model

The results of the four element Windkessel are contrasted with those of the three element model in Table 3.2. Overall, the four element model returned similar values to those from the three element model. The waveform fitting to the original data remained on average the same as for the three element model, with $RMS_{error} = 0.13 \pm 0.08$.

Table 3.2 Comparison between parameters values of the three and four element Windkessel model

Metric		HV		NoPH		PH (PVR < 4WU)		PH (PVR ≥ 4WU)		p value
		med	mean ± SD	med	mean ± SD	med	mean ± SD	med	mean ± SD	
Rd	3W	0.18	0.2 ± 0.08	0.31	0.36 ± 0.24	0.49	0.54 ± 0.29	0.68	1.03 ± 0.99	< 0.001
	4W	0.18	0.2 ± 0.08	0.31	0.36 ± 0.25	0.48	0.54 ± 0.29	0.68	1.03 ± 0.98	< 0.001
Rc	3W	0.04	0.04 ± 0.01	0.05	0.07 ± 0.07	0.02	0.05 ± 0.06	0.004	0.05 ± 0.16	0.073
	4W	0.04	0.04 ± 0.01	0.05	0.06 ± 0.06	0.03	0.05 ± 0.06	0.001	0.06 ± 0.18	0.041
C	3W	1.86	2.71 ± 2.2	1.29	4.73 ± 12.9	0.86	0.98 ± 0.45	0.54	0.6 ± 0.32	< 0.001
	4W	1.86	2.42 ± 1.32	1.1	1.5 ± 1.01	0.86	0.85 ± 0.21	0.55	1.48 ± 4.34	< 0.001

3W –three element Windkessel model

4W – four element Windkessel model

The distal resistance, R_d was almost identical for all four groups, with an overall bias of the mean of $0.3 \pm 3.7\%$. The compliance values calculated with the two models were however significantly different on average for the NoPH and severe PH groups. The source of the differences was the existence of two outliers, one in each of these groups

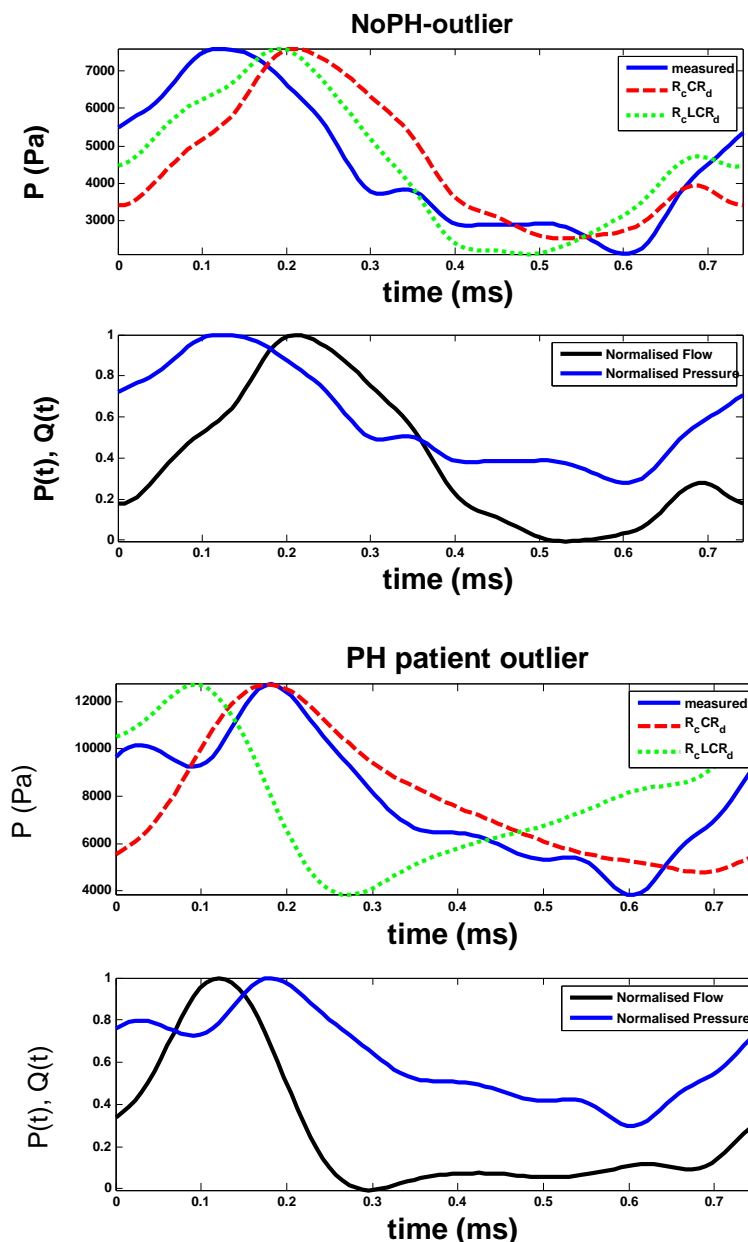


Figure 3.11 Source of outliers in three and four element Windkessel model
 Example of Windkessel model parameters optimisation failure, which represented the cause of some of the outliers in the final model's output.

In each outlier case the RMS associated with the fit was poor, suggesting that the proposed models do not adequately capture the measured responses of these individuals. Figure 3.11 shows the performance of the two OD models in fitting the measured pressure waveforms. For the NoPH outlier case, this illustrates clearly how both of the models are failing in fitting

the pressure waveform. For this particular case, it is observed that flow is leading pressure, which might question the quality of the acquired data. On the second analysed case, of the severe PH group outlier, the Rc C Rd model fits data more closely ($rms=0.2$), whilst the more complex four element model completely fails. Nevertheless it should be emphasised that, whilst this paragraph focuses on the outlier cases and the failure of the model fitting process, overall only 6 cases from the 80 that were studied exhibited this failure, and it is completely plausible that the failure might have been that of the data collection process rather than of the modelling process. These two outlier cases are examined in more detail in the discussion section following this summary.

3.1.7.2 Discussion

In pulmonary hypertension, stiffening and narrowing of the pulmonary vasculature are regarded as major causes of the increased right ventricular afterload, leading to right heart failure [136]. Mathematically, these phenomena can be described by an increase in pulmonary resistance and a decrease in pulmonary compliance. A three Windkessel element model was applied in order to better understand the pulmonary vasculature behaviour in health and disease and to test the hypothesis that the model can be used to compute differentiation criteria for patients with PH.

The results of this study agreed with previous published results [137], [138], [75], [20] in the demonstration of an increase in pulmonary vascular resistance as disease is initiated and progresses. In terms of the quantitative average values of the pulmonary resistance, our study produces results that are consistent with the literature for the diseased groups, but gives higher values for the normotensive ones (healthy volunteers and NoPH groups). These results are discussed in detail in the following paragraphs.

Milnor *et al.* [137], Reuben [138] and Laskey [75] reported average pulmonary vascular resistance in NoPH, measured based on the clinical definition of PVR, between 0.05 and 0.07 mmHg s/ml in patients without PH. Lankhaar *et al.* [20] used a three element Windkessel model to evaluate the differences between NoPH patients and PH patients with idiopathic pulmonary arterial hypertension (IPAH) and chronic thromboembolic pulmonary hypertension (CTEPH). They determined the pulmonary resistance as mean pressure (measured at RHC) to cardiac output (measured using Fick's method), and reported for the normotensive group pulmonary resistance of 0.11 mmHg s/ml. The same value was cited by Saouti *et al.* [134] in an article comparing parameters for the systemic and pulmonary circulations, reporting that the resistance of the latter is on average approximately nine

times smaller than the systemic counterpart. The differences in the above reported values can be attributed to the different methods of calculation. While Milnor *et al.* [137], Reuben [138], Laskey [75] computed the PVR as the ratio of cardiac output (CO) to the difference between the mean pulmonary arterial pressure (mPAP) and the mean wedge pressure (mPWP), Lankhaar *et al.* [20] neglected from the equation the wedge pressure. For the same values of the CO and mPAP, a larger PVR value will be obtained using the second formula.

The higher pulmonary resistance values in the normotensive groups computed in this study are, as expected, influenced by the overestimation of the non-invasive mPAP. There were only 4 noPH cases in the cohort that we used to compute the pressure-radius relationship (methods described in chapter 2). For obvious reasons no invasive data were available for the healthy individuals. For the healthy cohort the model relies on the normotensive data published by Greenfield and Griggs [96]. Given the relative paucity of data, and thus the lower confidence in the pressure-radius relationship in the normotensive range, it is not surprising that the mPAP, and therefore the computed total resistance of the normotensive groups are different between studies. Using the mPAP measured at RHC in our cohort to compute the vascular resistance, the NoPH group average of R_{totalRHC} is 42% smaller (0.24 mmHg s/ml) than that returned by the derived relationship, but it remains high when compared with literature values.

The average values of pulmonary resistance reported in the literature for PH patients are in the same range as those computed in the current study. Laskey [75] and Reuben [138] reported average pulmonary vascular resistance (PVR) for PH patients of 0.66 and 0.54 mmHg s/ml respectively. Saouti *et al.* [139] computed vascular resistance as ratio of mean pressure to mean flow, reporting an average value of 0.51 mmHg s/ml. Huez *et al.* [74], reported an average value of 1.19 mmHg s/ml for the 0 Hz component of the impedance spectrum (a measure equivalent to mean pressure to mean flow ratio) in patients with pulmonary arterial hypertension (PAH). In their two analysed PH groups, IPAH and CTEPH, Lankhaar *et al.* [20] showed that on average the pulmonary resistance is higher for IPAH patients than for CTEPH, quoting the values of 0.73 and 0.64 mmHg s/ml, respectively. Only Milnor *et al.* [137] reported a much smaller value of pulmonary vascular resistance in PH, of 0.27 mmHg s/ml.

By using a three element Windkessel model, the total vascular resistance can be separated in its two components: distal resistance, R_d and proximal resistance, R_c , which was introduced as an approximation of the pulmonary artery characteristic impedance.

The study of Lankhaar *et al.* [20] is the only one in which a three element Windkessel model is used for human patients to differentiate normotensive patients from the ones with pulmonary hypertension. The distal resistance showed increased distal resistance values in the PH groups, when compared with the control group. For the control group, the authors reported a R_d value of ~ 0.25 mmHg s/ml, slightly higher than our derived R_d for healthy volunteers (0.2 ± 0.08 mmHg s/ml) and lower than our NoPH cohort (0.36 ± 0.24 mmHg s/ml). For the diseased groups, separated in patients with CTEPH and IPAH, R_d values of ~ 0.75 mmHg s/ml and ~ 1.2 mmHg s/ml, respectively, were reported. The values are comparable with the computed R_d values from the PH groups of the current study (0.54 ± 0.28 and 1.03 ± 0.9 mmHg s/ml).

Quantification of the characteristic impedance, R_c in the current study, showed an average value of approximately 0.05 mmHg s/ml for each group studied, and the Kruskal-Wallis test for independent variables did not indicate significant differences between the groups. In contrast, Lankhaar *et al.* [20] reported an increase in R_c from normotensive to PH patients. On average, ~ 0.03 mmHg s/ml was found in their study for the no PH group, while ~ 0.1 and ~ 0.18 mmHg s/ml were their reported values for CTEPH and IPAH patients.

Another method of computing the ventricular afterload is based on the analysis of the input impedance spectrum: in this method the characteristic impedance is computed by averaging the impedance moduli following the first input impedance minimum (usually moduli > 2 Hz component). Using this method, Milnor *et al.* [137], reported in normotensive patients a characteristic impedance of 0.02 mmHg s/ml, while in PH the authors found an average characteristic resistance of 0.035 mmHg s/ml. Similarly, Laskey *et al.* [75], found in no PH patients an average characteristic impedance of 0.02, while in PH it doubled. A higher value, of 0.09 mmHg s/ml, closer to the one derived by Lankhaar *et al.* [20] using the Windkessel model, was reported in PH patients by Huez *et al.* [74]. Slife *et al.* [55], applied a three Windkessel model to evaluate the differences between normotensive patients during rest and exercise. The authors computed the values of the electrical parameters by curve fitting algorithms, but also by the means of more traditional methods in which the pulmonary resistance was computed as the 0 Hz input impedance component, the characteristic impedance was obtained by averaging the impedance moduli between the 3rd and the 10th harmonics, and the vascular compliance was computed as ratio of stroke volume to pulse pressure. There was no statistical difference between the average characteristic impedance computed from the Windkessel model and the one computed by impedance spectrum analysis, both indicating at rest a value of 0.016 mmHg s/ml. During exercise, the 2 methods

give different results, but the difference of the averages was not statistically significant. 0.011 mmHg s/ml was given by the Windkessel model, while the impedance spectrum analysis returned a Z_c value of 0.017 mmHg s/ml.

It is noted that the characteristic resistance values computed for our subject groups, although not exhibiting a significant difference between the groups, are on average not far from the values computed using the input impedance spectrum method.

As previously described, for computing the pulmonary resistance there are two approaches usually applied: clinically-measured PVR or the ratio of mean flow to mean pressure. In contrast, in order to compute the arterial compliance, several methods have been reported. One of the most frequent in clinical use is the stroke volume method, in which the compliance is expressed as the ratio of stroke volume to pulse pressure. Sanz *et al.* [30], used the term capacitance to express the same concept, whereas the term compliance was used to define the ratio of maximum and minimum area difference to pulse pressure. The latter can rather be referred as a local compliance, since it accounts for the change in vessel area with the change in pressure, to avoid confusion of terminology.

The pulse pressure method [140], decay time period method [141] and balanced energy method [142] are all used for computing the arterial compliance by using the relationship between flow and pressure waveforms given by the assumption that the heart afterload can be represented by a Windkessel model. Lankhaar *et al.* [20], applied the stroke volume, pulse pressure and energy balanced methods to compute the pulmonary arterial compliance in normotensive and patients with IPAH and CTEPH. All the analysed methods showed that compliance decreases with disease progression. In general, the balanced energy method returned the highest group averages, followed by the stroke volume and pulse pressure results. While in the 2 PH sub-groups reported in this thesis the methods correlated well with the energy balance method, in the normotensive group, the correlation was weaker. Slife *et al.* [55], compared the pulmonary arterial compliance in normotensive patients using two methods: stroke volume and by a curve fitting algorithm used to estimate the elements of a three element Windkessel model. These methods returned different average values, with the stroke volume average compliance approximately one half of that returned by the Windkessel model. In patients with PH, Muthurangu *et al* [143] computed the pulmonary arterial compliance using pulse pressure and stroke volume methods and reported that, although the two methods are in strong agreement, there is a consistent bias between them.

The method implemented in this thesis computes the arterial compliance through a curve fitting optimisation process, seeking to minimise the differences between the measured radius-derived pressure and the pressure expressed analytically based on a three element Windkessel model. Of the methods reviewed above, this approach is the most similar to the pulse pressure method and optimisation method applied by Slife *et al.* [55].

The analysis of the arterial compliance, determined by the optimisation of the three element Windkessel model, showed plausible results. However, two big outliers were identified: one in the healthy volunteer group and one in the NoPH group. The first outlier, with a value 8 ml/mmHg, from the healthy volunteers group, corresponds to a young male athlete (85 kg, 193 cm height). Although this value is rather higher than the range reported in the literature and is extreme in our own cohort, it might not be unreasonable: Lankhaar *et al.* [20] reported an average C of 4.8 ml/mmHg in no PH patients. The second outlier is almost certainly associated with a problem in the data collection or recording. Firstly, the fitting of the two pressure curves was poor, with an RMS error of 0.35. It might be argued that this is simply a failure of the optimisation process but, on a closer analysis of the input pressure and flow waveforms, for a reason which cannot be explained, it can be seen that the measured pressure leads flow in this dataset, conflicting with the statement from [2] that flow leads pressure and pressure gradient leads flow.

After understanding the nature of the two outliers in the estimation of C, the rest of the cohort can also be discussed. As stated in the results section, the total compliance decreased with the disease status, showing statistically significant differences between the healthy volunteers group and each of the PH sub-groups, between the NoPH group and the severe PH group, and between the two PH sub-groups. The average compliance values for the two PH sub-groups of 0.98 and 0.68 ml/mmHg respectively are in agreement with the values reported by Lankhaar *et al.* [20] in IPAH and CTEPH, with averages varying between 0.5 to 1.8 ml/mmHg, depending on the computing method. Similarly, using the time decay period method, Reuben [138] computed the average C in PH of 0.7 ml/mmHg, while in no PH subjects, the reported value is 2.9 ml/mmHg.

It has been clearly demonstrated, both in the literature and in the current study, that the resistance increases and compliance decreases with disease progression. This naturally raises the question of whether there is a consistent correlation between these parameters.

The Windkessel model's derived total pulmonary compliance, inversely correlates with the total resistance, distal resistance and RHC derived PVR, confirming previous findings [135], [20], [144], [138], [143], [145].

Together with the type of correlation existing between the two compliance and pulmonary resistance, a question often concern their product. While for the systemic circulation this product, also known as the time constant, changes with the disease [144], for the pulmonary circulation it is reported to stay constant [139], [135], [20], [144] or at least that changes are small [138]. The current study supports the observation that the time constant does not change significantly in the analysed groups, remaining approximatively constant at 0.4 s, after removal of the outliers.

Reuben [138] reported a time constant of 0.2 s in normotensive patients, while in PH the value was higher, 0.38 s, but not statistically significantly different from the no PH group. Lankhaar *et al.* [135], studied PH patients before and after receiving specialist treatment, and concluded that the pulmonary resistance-compliance product does not change. Computed using clinical PVR and stroke volume compliance, the average time constant before and after the treatment were 0.61 s and 0.59 s respectively. The same group [20] reported a time constant of 0.75 s, computed as the product of distal resistance and compliance determined though the energy balance method. The product was found to be similar in normotensive and patients with IPAH and CTEPH. Saouti *et al.* [139] studied the time constant of the entire circulation and also of separated lungs in CTEPH patients. The authors showed that the time constant of the whole circulation stays constant, at ~ 0.45 s, regardless of whether the site of measurement was the main, right or left pulmonary artery. The difference in the reported values can be justified by the way the pulmonary resistance and compliance were computed. It was discussed in the previous paragraphs how the pulmonary compliance was reported to hold different values, according to the computation method. Additionally, there are discrepancies in the choice of resistance value. In some studies, the resistive component of the product is considered to be the total resistance computed as clinical PVR [138], [135] or as the ratio of mean pressure to mean flow [139], whilst in other studies [20] including the current one, the resistive component included in the product was the distal resistance of the three element Windkessel model. The current choice is justified by the definition of each of the components of the Windkessel model.

3.1.8 1D model

3.1.8.1 Results

The 1D model of a straight elastic tube was used to quantify the wave reflections present in the main pulmonary artery. As described in the Materials and Methods section, based on Fourier analysis, the pressure waveforms were decomposed into their forward and backward components. The power content was computed at each harmonic. The contribution of the reflected wave to the total wave was expressed as the ratio of the sum over all harmonics of the backward wave power to the total wave power.

Figure 3.12 and Figure 3.13 display the decomposition of total pressure wave (blue) into forward (green) and backward (red) wave components and the normalised wave power content for 25 harmonics in a normotensive and a PH patient respectively.

As can be seen, the wave power content is concentrated mainly in the first three harmonic components. In general, the first harmonic contains most of the wave power, while at high frequencies the power content is approaching zero. The finding is not surprising since in order to recompose a pressure or flow waveform from its harmonic components, the first six harmonics will give a very good approximation [146].

The backward (red) and forward (green) power were expressed at each harmonic as the contribution from the total (normalised) wave power at that harmonic. As displayed in Figure 3.12, for the normotensive patient the forward component represents more than 80% of the total power at each harmonic, whereas for the PH case Figure 3.13, the backward component's contribution is increased, reducing the forward to ~65% of total wave power. The ratio of the backward to total power for the normotensive patient, W_b/W_{total} was 0.22, whereas for the PH patient, the ratio went up to 0.35.

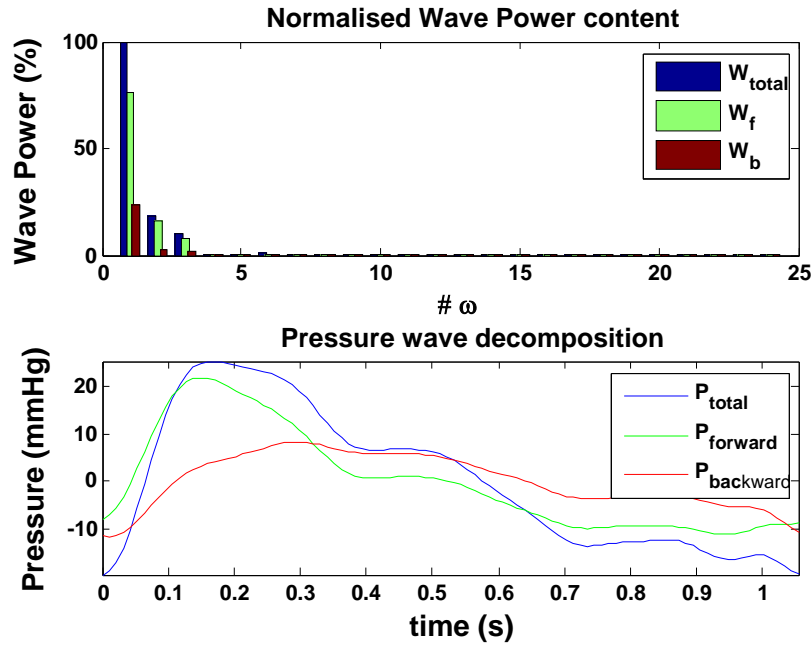


Figure 3.12 (top): wave power harmonic content quantified for the forward (green) and backward (red) pressure components of a NoPH patient. (bottom): Decomposition of the pressure waveform in forward and backward time varying components

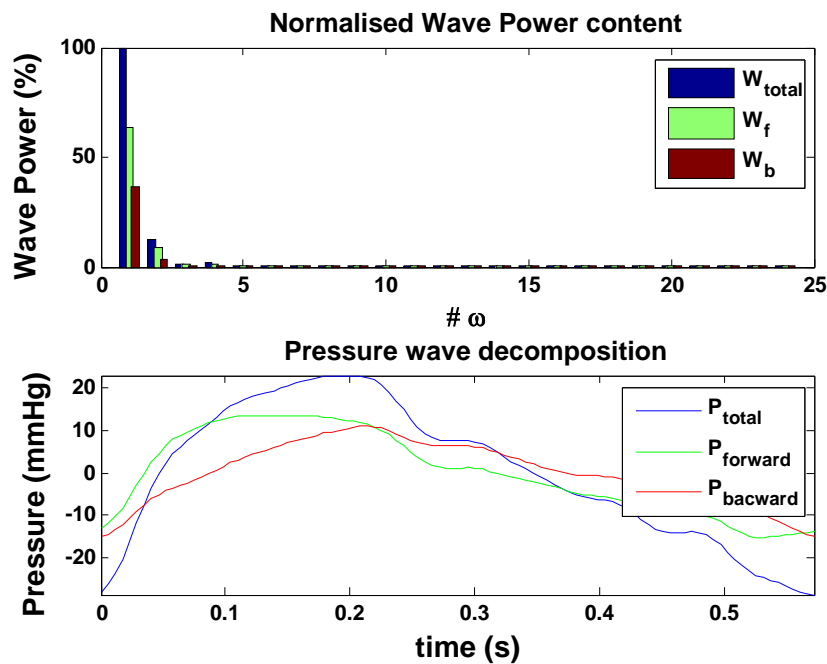


Figure 3.13 (top): wave power harmonic content quantified for the forward (green) and backward (red) pressure components of a PH patient. (bottom): Decomposition of the pressure waveform in forward and backward time varying components

The results are confirmed by the analysis of the whole cohort (Figure 3.14). Data are normally distributed within the groups, as assessed visually by histogram inspection and confirmed by Shapiro-Wilk test ($p > 0.05$). The homogeneity of variance, tested using Leven's test, was not

significant ($p > 0.05$) and one way ANOVA test for independent groups, with Tukey's post-hoc correction was applied to test if there are any significant differences between the group means.

W_b/W_{total} showed significant differences between all the analysed groups. On average, the backward wave contributes $13 \pm 4\%$ to the total wave in the healthy volunteers group, $25 \pm 6\%$ in the NoPH group, $35 \pm 10\%$ in the mild PH group and up to $42 \pm 8\%$ in the severe PH group.

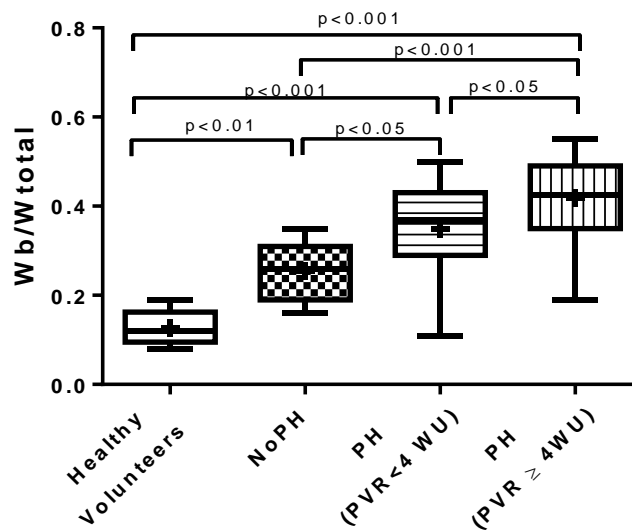


Figure 3.14 Results of the 1D model, within the analysed groups.

The ratio of backward to total pressure wave power increased with the disease status.

W_b/W_{total} shows statistically significant results between all the analysed groups.

3.1.8.2 Discussion

Quantification of wave reflections in the main pulmonary artery showed statistically significant differences between all of the analysed groups, supporting the hypothesis of increased reflections with PH severity.

The results are supported by previous findings in the pulmonary circulation of animals [73], [76], [77], [78], [79], [80] and humans [75], [74], [81], all reported based on invasive measurements.

As stated in the introductory thesis chapter few studies concerning wave reflections have been performed on humans. Laskey *et al.* [75] and Huez *et al.* [74], quantified wave reflections in the pulmonary circulation of man through the means of the reflection

coefficient. The index, defined as backward to forward pressure waves amplitude, showed in the study of Laskey *et al.* [75] significantly increased values in PH, comparing with normal cases. The values found in PH were later confirmed also by Huez *et al.* [74].

Castelain *et al.* [81] argued that the wave reflections are augmenting certain features of the pressure wave, which can be quantitatively evaluated. The metric defined by the authors as augmentation, showed a statistically significant difference between chronic thromboembolic and primary pulmonary hypertension. The method depends on the identification of the second peak of the pressure waveform, which, argued by the authors, corresponds to the arrival of backward wave. In some situations, the identification of this wave feature can be very subtle and the analysis becomes challenging.

3.1.9 Coupled 1D and 0D models

3.1.9.1 Results and discussions

The main research question in implementing the 1D-0D coupled model was focused on whether an equivalent reflection site will be found in patients with PH.

The average root mean square error for fitting a coupled model to the original data had a minor decrease, comparing to the three and four Windkessel models, of 1%. Figure 3.15 shows two of the very few cases in which the coupled model performed better than the simpler 0D models in fitting the measured data.

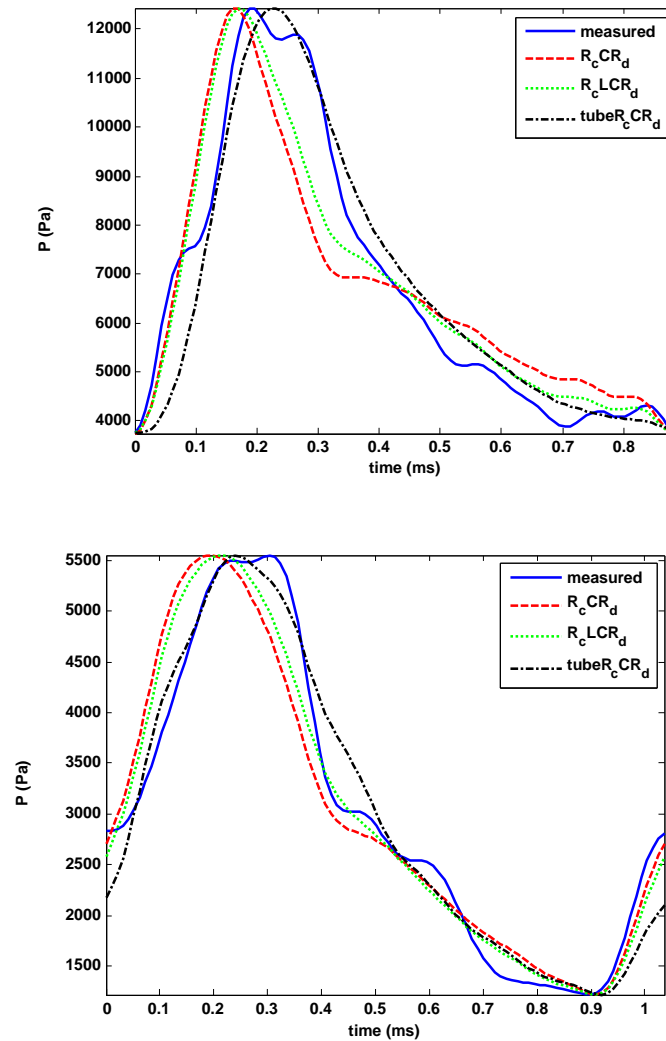


Figure 3.15 Fitting quality of the 3 element Windkessel model: original waveform (continuous blue) and fitted (dashed red).

The length of the tube showed to have a very small average value, statistically not significantly different, between the groups. The mean values varied from 0.23 ± 0.28 m in the healthy volunteers group, 0.19 ± 0.24 m for the NoPH group, 0.12 ± 0.09 m for the mild PH group and 0.13 ± 0.11 m in the severe PH group. With the exception of the mild PH group, data are not normally distributed in the groups, making the median group value more representative. From healthy volunteers to severe PH group, the following median values were found: 0.15 m, 0.14 m, 0.12 m and 0.14 m.

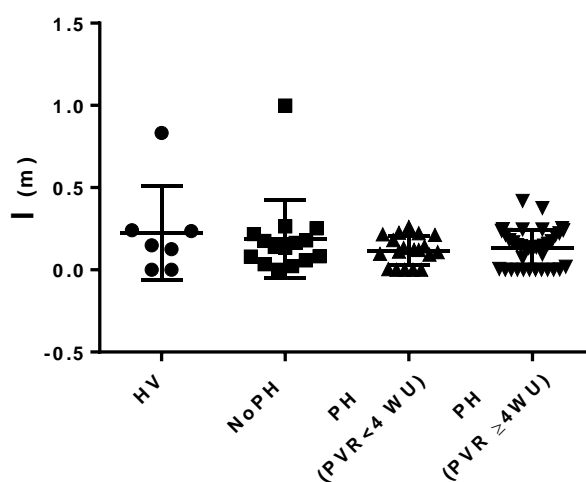


Figure 3.16 Distribution across groups of the length of the 1D domain

3.1.10 0D and 1D models results' influence factors

Throughout the previous sections of the current chapter the results from the 0D and 1D models were analysed and compared with findings reported in the literature. In order to develop the protocol to the models' parameters proposed as differentiation criteria in normotensive and patients with PH, a series of judgements were made. These three decisions are now discussed further in order to understand their influence on the final results. Firstly, the highest uncertainty is that raised by the choice of the non-invasive pressure model. Secondly, the protocol used to compute the area of the main pulmonary artery is semi-automatic, introducing segmentation variability. Thirdly, the type of images proposed to be used to compute the area and flow waveforms came from different sequences.

This section explores the effect on the proposed differentiation parameters (W_b/W_{total} , R_d and C) introduced by the semi-automatic segmentation process, the use of two MRI imaging sequences for deriving area and flow waveforms and by the choice of the pressure model derived from mixed data set.

3.1.10.1 Influence of choosing the pressure model

Chapter 2 describes the process of transforming time varying MPA radius to pressure, necessary for the computation of the Windkessel model parameters and for solution of the 1D wave reflection model. In the proposed methodology, the translation of the radius waveform into a pressure one is dependent on two variables: the diastolic pressure, P_0 and

Peterson’s elasticity modulus, E_p . For each subject, their values were estimated using a relationship between change in area and P_0 and change in area and E_p , obtained by best fitting the data of 27 patients from the current cohort, combined with 11 patient datasets published by Greenfield and Griggs [96]. Combining data sets is not optimal, but this decision was taken because of the paucity of available data: Greenfield and Griggs had only a few PH cases ($n=3$), and the RHC clinical data had only a few no PH cases ($n=4$). Therefore, by their combination, the models are fitted to a larger set of both PH and no PH data.

For a cohort of 35 subjects, the results of the electrical parameters R_d , R_c , C and ratio of backward to total pressure wave power, W_b/W_{total} were computed using pressure waveforms derived only from the Greenfield and Griggs (GG) data and, separately, only from invasively measured (RHC) data and the results compared.

Results and discussions

Figure 3.17 displays the relationship between the ratio of the backward to total pressure wave power, W_b/W_{total} , computed using the pressure model derived from the mixed data sets (RHC +GG) against the same parameter computed from only RHC data (blue circles) and only GG data (green squares). $W_b/W_{total RHC+GG}$ showed strong linear correlation with $W_b/W_{total GG}$ (Pearson’s $r=0.98$, $R^2=0.99$, $p<0.0001$) and $W_b/W_{total RHC}$ (Pearson’s $r=0.99$, $R^2=0.97$, $p<0.0001$). Additionally, the intra-class correlation coefficient, ICC, for absolute agreement is for single measures 0.98.

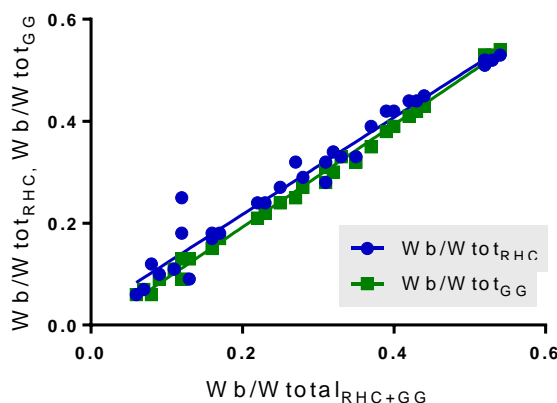


Figure 3.17 Relationship between W_b/W_{tot} determined using mixed data set (GG+RHC) and from solely from RHC and Greenfield and Griggs [96]

Figure 3.18 shows correlation for the distal resistance R_d parameter, computed from the 0D model with pressure waveform derived based on the three data sets. $R_{d RHC+GG}$ shows strong

correlation with $R_{d\text{GG}}$ (Pearson's $r=0.97$, $R^2=0.94$, $p<0.0001$) and $R_{d\text{RHC}}$ (Pearson's $r=0.97$, $R^2=0.95$, $p<0.0001$). The ICC for absolute agreement for single measures is 0.87.

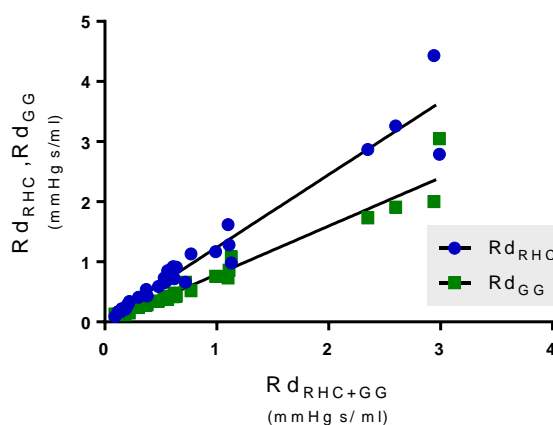


Figure 3.18 Relationship between R_d determined using the mixed data set (RHC+GG) and solely RHC and Greenfield and Griggs [96]

Similarly, the characteristic resistance, R_c , computed using pressure waveforms derived based on the mixed data sets, $R_{c\text{RHC+GG}}$ shows strong correlation with $R_{c\text{GG}}$ (Pearson's $r=0.94$, $R^2=0.96$, $p<0.0001$) and $R_{c\text{RHC}}$ (Pearson's $r=0.98$, $R^2=0.89$, $p<0.0001$). The results showed in Figure 3.19 have an ICC for absolute agreement of single measures of 0.92.

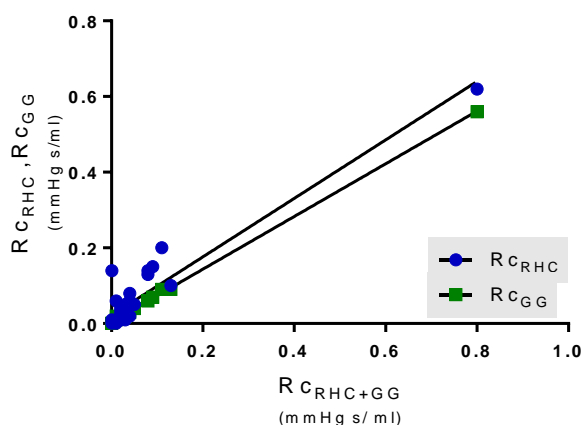


Figure 3.19 Relationship between R_c determined using mixed the data set (RHC+GG) and solely from RHC and Greenfield and Griggs [96]

The total pulmonary compliance, C is the only parameter showing reduced absolute agreement between the values computed from pressure waveforms derived based on the three data sets. The linear correlation between $C_{\text{RHC+GG}}$ and C_{GG} is strong (Pearson's $r=0.99$, $R^2=0.98$, $p<0.0001$), whereas between $C_{\text{RHC+GG}}$ and C_{RHC} it is relatively poor (Pearson's $r=0.63$, $R^2=0.4$, $p<0.0001$). The ICC for absolute agreement of single measures is also poor, 0.38. ICC

is sensitive to outliers. The elimination of the outlier from the C_{RHC} data set increases the ICC value to 0.8.

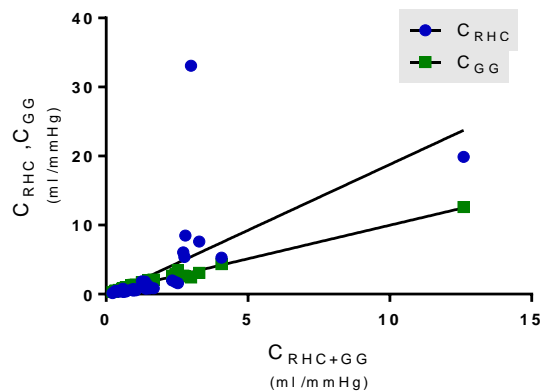


Figure 3.20 Relationship between C determined using the mixed data set and solely from RHC and Greenfield and Griggs [96]

3.1.10.2 Inter and intra operator variability

Computing area of the pulmonary artery at every time step is performed using a semi-automatic segmentation process. Chapter 2 describes the process in details and discuss the intra and inter-operator variability for area, flow and pressure waveforms. The tests performed showed that although there was a high variability in the area waveforms segmented by three operators, there was a consistent bias. Moreover, the effect of training seems to positively influence the results, by reducing the variability. Furthermore the flow waveforms were less affected by the actual value of computed area, as long as the segmentation resulting masks were correctly placed onto the phase contrast images. Likewise, in the process of transforming radius into pressure, the variability was further reduced. Due to the extra processing steps occurring from the images processing to the final result, it is a real challenge to quantify the cumulative error. Therefore, assessing the intra and inter operator variability on the final results is a sensible test.

Results and discussions

Two operators, A and B, segmented at random from the 72 clinical patients of this cohort, 20 MRI images data sets. Operator A, with previous segmentation experience, segmented the images twice, within a week. Operator B, with no previous segmentation experience, received basic, training on MRI images of the pulmonary arteries.

Figure 3.21 and Figure 3.22 displays the inter-observer and intra-observer variability respectively, as Bland-Altman and regression plots for relative area change (RAC), backward

to total pressure power ratio (W_b/W_{total}), distal resistance, (R_d) and arterial compliance (C). As expected, the intra-observer variability is lower (approximately half) for all four metrics, as shown by the Bland-Altman plots and confirmed by the bias and limits of agreement values displayed in Table 3.3. All the metrics are showing very strong correlations ($R^2 > 0.9$) between the sets of measurements. However, the limits of agreement are tighter and the bias is smaller for the RAC and W_b/W_{total} than for the R_d and C metrics, for both inter and intra variability. The RAC metric shows a small negative systematic bias, of 0.9 % between the A and B operators' measurements, and even smaller, of 0.6% between the first and second measurements of operator A, with all data points but one, between the graph's limits of agreement. While the RAC metric directly reflects the segmentation results, the next three metrics, W_b/W_{total} , R_d and C are derived upon the RAC measurements but also influenced by the mathematical model's initial assumptions (the pressure-area relationship) or parameters estimation (optimisation). Therefore the agreement between the computationally derived metrics is influenced by multiple factors, including the operator's segmentations. The W_b/W_{total} displays a similar trend as RAC. The limits of agreement are tight, with small systematic bias of 0.007 for the inter-operator variability and 0.002 for the intra-operator variability. The Windkessel parameters, R_d and C have larger limits of agreement and systematic bias: 0.019 mmHg s/ ml and 0.004 mmHg s/ml for the R_d and -0.074 ml/mmHg and 0.034 ml/mmHg for the C metric, for inter and intra-operator variability. While for the RAC and W_b/W_{total} the values are in general evenly distributed around the bias line, the electrical parameters, R_d and C are showing an increase in the mean differences as the mean value of the measures increase. This disagreement between the calculated values is not surprising, and it can be attributed to the failure of the three element Windkessel model in fitting the input data, as previously discussed in the Results section of this chapter.

Table 3.3 Bias and limits of agreement for the intra and inter-operator variability

Variable	Intra-operator				Inter-operator			
	Bias	SD of bias	95% CI		Bias	SD of bias	95% CI	
			lower	upper			lower	upper
RAC (%)	-0.568	1.321	-3.157	2.021	-0.914	2.375	-5.56	3.741
Wb/Wtot	0.002	0.013	-0.024	0.027	0.007	0.019	-0.03	0.044
Rd (mmHg s/ml)	0.004	0.015	-0.03	0.035	0.019	0.027	-0.04	0.073
C (ml/mmHg)	0.034	0.081	-0.13	0.195	-0.074	0.206	-0.48	0.331

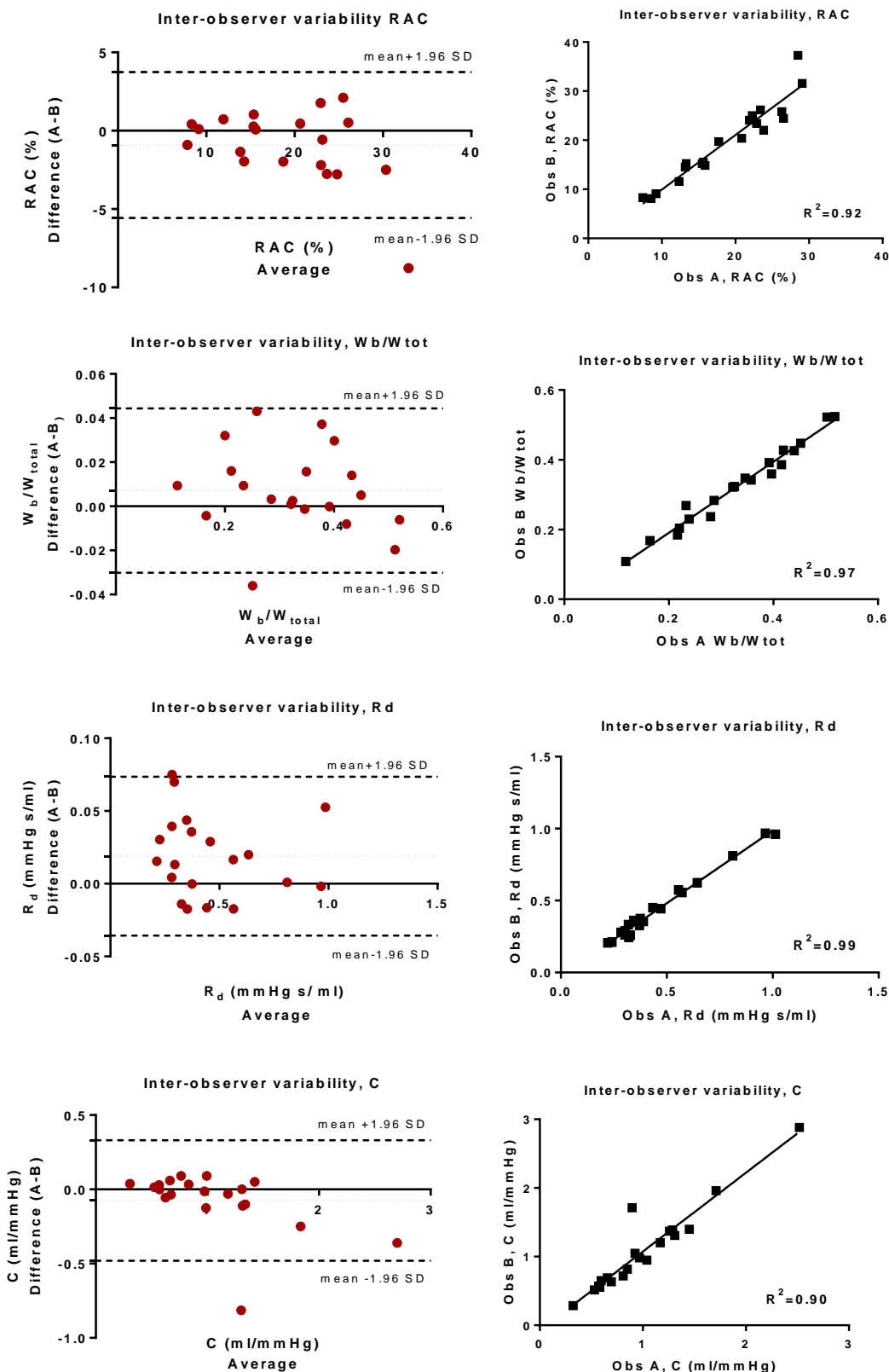


Figure 3.21 Inter-observer variability. Bland-Altman (left) and regression analysis (right), showed for relative area change (RAC), ratio of waves power (W_b/W_{tot}), distal resistance (R_d) and pulmonary compliance (C) performed on 20 cases selected at random (using MATLAB) from the 72 patient cohort.

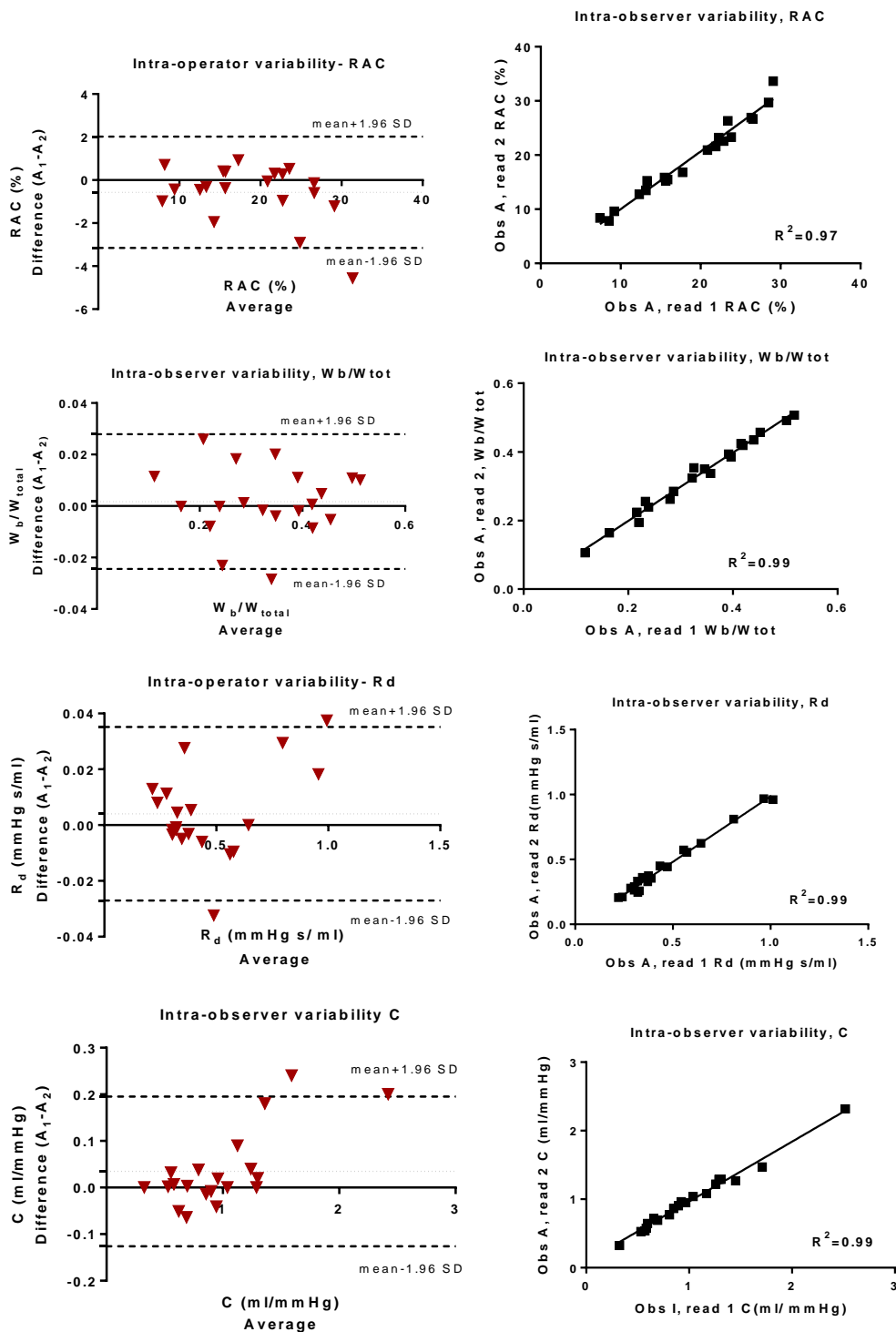


Figure 3.22 Intra-observer variability. Bland-Altman (left) and regression analysis (right), showed for relative area change (RAC), ratio of waves power (Wb/Wtot), distal resistance (Rd) and pulmonary compliance (C) performed on 20 cases selected at random (using MATLAB) from the 72 patient cohort.

3.1.10.3 PC vs bSSFP parameters

Phase contrast (PC) and balanced steady state free precession (bSSFP) images of main pulmonary artery were acquired in order to quantify area and flow waveforms. Due to better blood-vessel delineation, bSSFP images were chosen over PC magnitude images for segmentation.

Although the two sequences are acquired at the same anatomical position, using the same number of cardiac phases and same matrix dimensions, they are acquired at approximately 2 minutes difference. Therefore it is natural to enquire if the results are influenced by the choice of the segmenting images.

For the 35 subject cohort area and flow waveforms were computed after one operator segmented both PC magnitude and bSSFP images.

Results and discussions

Figure 3.23 shows the correlation between the ratio of backward to total wave power W_b/W_{total} measured using bSSFP and PC magnitude images for area segmentation. The parameter derived using the two type of images showed strong correlation (Pearson $r=0.92$, $R^2=0.85$). The intra-class correlation coefficient for absolute agreement of single measures is 0.92.

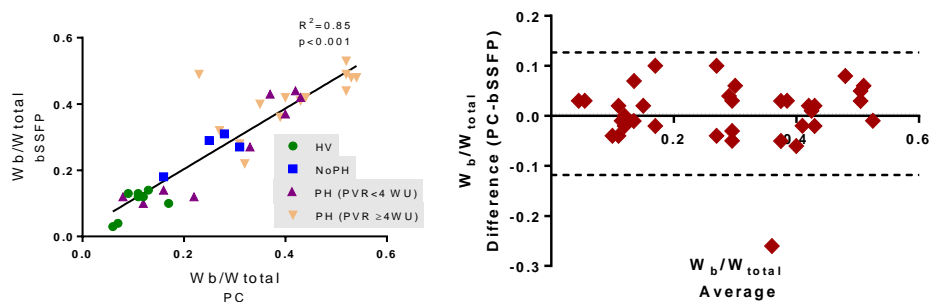


Figure 3.23 Correlation and agreement between W_b/W_{total} derived from solely PC images and bSSFP and PC images.

The parameters derived from the two image sets show strong linear correlation ($r=0.92$, $R^2=0.85$) and strong agreement. With a single exception, the data lay between ± 1.96 SD from the mean, while the bias is minimum.

Figure 3.24 shows the correlation between the distal resistance, R_d , derived using PC magnitude images and bSSFP images for MPA segmentation. R_d derived using the two image sequences show strong correlation (Pearson $r=0.99$), $R^2=0.98$ and high ICC for absolute agreement of single measures 0.98.

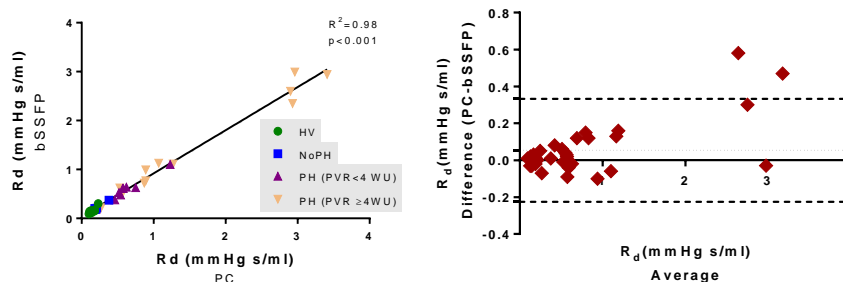


Figure 3.24 Correlation and agreement between R_d derived from solely PC images and bSSFP and PC images.

The parameters derived from the two image sets show strong linear correlation ($r=0.98$, $R^2=0.98$) and good agreement. In general, the data lay between ± 1.96 SD from the mean, with 0.02 mmHg s/ml bias.

Figure 3.25 displays the relationship between total vascular compliance C , derived using bSSFP and PC magnitude images to segment MPA. The two measures correlate strongly (Pearson $r=0.95$, $R^2=0.91$) and have a high ICC for absolute agreement of single measures 0.8.

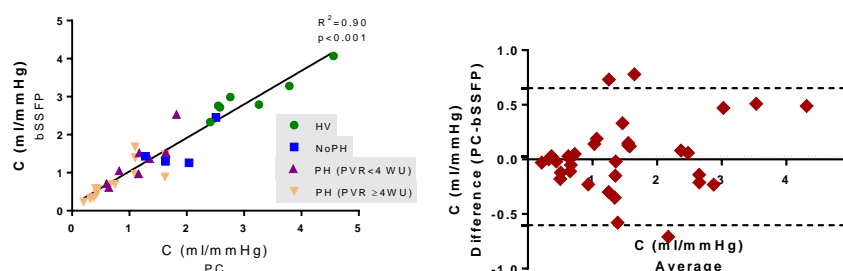


Figure 3.25 Correlation and agreement between C derived from solely PC images and bSSFP and PC images.

The parameters derived from the two image sets show strong linear correlation ($r=0.95$, $R^2=0.91$) and strong agreement. With a single exception, the data lay between ± 1.96 SD from the mean, while the bias is minimum.

Figure 3.26 displays the relationship between characteristic resistance, R_c , derived using bSSFP and PC magnitude images to segment MPA. The two measures show a good linear correlation (Pearson $r=0.89$, $R^2=0.78$). The ICC for absolute agreement of single measures is 0.94.

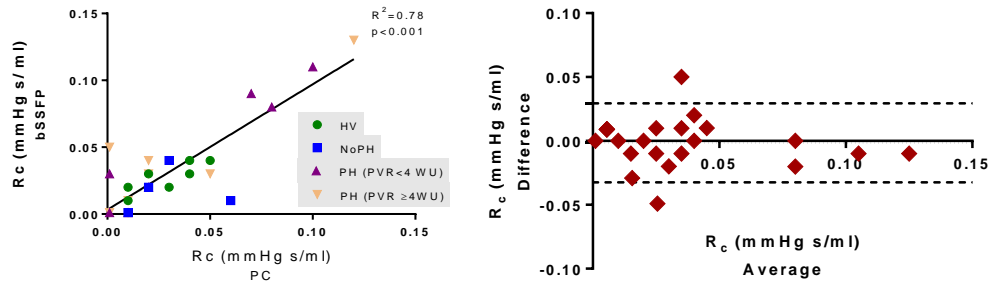


Figure 3.26 Correlation and agreement between R_c derived from solely PC images and bSSFP and PC images.

The parameters derived from the two image sets show strong linear correlation ($r=0.95$, $R^2=0.91$) and strong agreement. With a single exception, the data lay between ± 1.96 SD from the mean.

The above results show that using only PC images to derive the proposed OD and 1D parameters does not have a large influence on the final values, comparing with the ones derived by using spatially and temporally registered bSSFP and PC sequences. Therefore, it can be argued that it is totally justified using an MRI sequence with better blood to vessel delineation (bSSFP) than PC magnitude images, in order to obtain more accurate and quicker segmentations.

SUMMARY AND CONCLUSIONS

The pulmonary status in healthy volunteers and patients with stratified PH was assessed using a OD, three element Windkessel model and a 1D model of a straight elastic tube. The mathematical models used as input non-invasive flow and pressure (radius used as surrogate) waveforms derived from MR images.

The analysis was applied to a cohort of 80 subjects, separated into healthy volunteers, NoPH, PH (PVR < 4WU) and PH (PVR \geq 4WU) groups.

The Windkessel model was solved using an optimisation algorithm constructed from components available in MATLAB's Optimisation Toolbox. In order to minimise the operator's input in selecting the starting value required by gradient search methods, the implemented protocol firstly runs a search based on a Genetic Algorithm (GA) on a large interval. The resulting value is passed to a gradient descent minimisation function, in order to obtain a more accurate solution. During the optimisation process the differences between measured

and analytically defined pressure are minimised based on a mixed cost function, which accounts for overall, peak systolic and diastolic differences. Although the workflow might be unnecessarily complex for the two degree of freedom problem, it was developed as a general tool which can be applied to multiple parameters optimisation. In this thesis a four element Windkessel and a coupled 1D-0D model have also been parameterised following the same protocol.

The three and four element models performed similarly in terms of goodness of fit and values of the derived parameters. Therefore, the use of a more complex model was not justified and the values of the three element Windkessel were proposed as potential differentiation criteria in PH assessment. R_d and C showed statistically significant differences between healthy volunteers and both the PH sub-groups and between NoPH and severe PH group. Additionally, C , showed statistically significant differences between the two PH sub-groups. R_c showed no significant difference between any of the analysed groups. Therefore, only R_d and C are proposed to be further used in the PH diagnosis process.

R_d increased with the disease status, while C decreased. Moreover, their relationship is best described by an inverse correlation and their product showed no significant differences between the groups.

The OD, three Windkessel model's parameters individual values are directly influenced by pressure surrogate mean value. However, the trend is consistent with values reported in the literature computed based on invasive pressure measurements.

The results of the 1D model showed increased wave reflections in the PH groups, when compared with healthy volunteers and NoPH groups. W_b/W_{total} showed statistically significant differences between all the analysed groups. The differences between the healthy volunteers and NoPH group are of great interest. It is suggested that this parameter is able to sense abnormal conditions. However this suggestion should be treated with caution, and the hypothesis should be further tested because the two groups are not age matched.

Inter and intra-operator variability was tested on 20 cases selected at random from the entire cohort for the parameters proposed as differentiation criteria in PH: R_d , C and W_b/W_{total} . The results showed high intra-class correlation coefficient for absolute agreement of single measures for all parameters.

Additional tests were performed in order to understand the robustness of the results. While the OD model's parameters are more susceptible to variations due to change of the pressure

model or using only PC magnitude images for segmenting pulmonary artery, the 1D model parameter gives consistent and robust results for all the tests. Therefore, the 0D model requires further improvement of accuracy and robustness.

Following the 0D and 1D analysis on the study cohort, it can be concluded that both model parameters can be applied as differentiation criteria in PH and hypothesised that added diagnostic value might ensue by their combination under classification algorithms, and this is explored in the next chapter.

CHAPTER 4

Non-invasive PH Diagnosis using Computational and Image Based Indices Integrated into Classification Algorithms

MOTIVATION

Right heart catheterisation (RHC) is currently the standard clinical method for diagnosis, follow-up and evaluation of response to treatment in pulmonary hypertension (PH). In order to eliminate any complications that could be triggered by the invasive procedure, non-invasive PH metrics have been clinically proposed [26, 27, 30-32, 34, 35, 37, 147].

In *Chapter 3*, a three element Windkessel model and a 1D model of a straight elastic tube were solved using non-invasive MRI measurements of the flow in, and the anatomy of, the human main pulmonary artery (MPA). Based on the models' results, three computational parameters, the distal resistance R_d , total vascular compliance C and ratio of backward to total wave power, W_b/W_{tot} were proposed as differentiation criteria between normotensive

and patients with PH. However, for any of these parameters to be proposed as a PH discriminant and to be clinically translated, further work is required.

The current chapter is designed to integrate the simple models' results into direct clinical application. The main research question addressed is whether normotensive and PH patients can be separated by the means of non-invasively derived PH metrics. Cut-off values for the above enumerated computational indices were derived in a data-driven manner and their individual classification accuracies evaluated in terms of sensitivity, specificity and misclassification error.

As introduced in Chapter 1, there is increasing interest in the development of non-invasive methods for PH diagnosis, and a series of image-based-PH-metrics proposed by [26, 30-32, 34, 35, 37, 147] have shown promising results. In this chapter, eight such metrics ((i)- relative area change- RAC, (ii) main pulmonary artery systolic area, (iii) main pulmonary artery diastolic area, (iv) right ventricle end diastolic volume index -RVEDVI, (v) right ventricular ejection fraction -RVEF, (vi) ventricular mass index -VMI, (vii) systolic septal angle, and (viii) right ventricle mass index -RVMI) are evaluated on the same patient cohort used for the derivation of the computational metrics and the individual results are compared.

Finally, in order to maximise the use of MR images for non-invasive PH diagnosis, a machine learning classifier was trained and validated using leave-one-out cross validation, evaluating whether the integration of multiple indices improves the classification accuracy.

MATERIALS AND METHODS

4.1.1 Subjects

72 patients were referred to the Sheffield Pulmonary Vascular Disease Unit with symptoms of PH. All the patients underwent right heart catheterisation (RHC) and MRI scanning within 2 days. Based on the 25 mmHg threshold measured at RHC, as specified by the guidelines [148], the patient cohort was divided in two groups: 'NoPH' (mPAP < 25 mmHg, n=15) and 'PH' (mPAP ≥ 25 mmHg, n=57).

The distribution within the PH group, following Dana Point classification was: 21 patients with pulmonary arterial hypertension (PAH), 11 patients with PH owing to left heart disease (LHD), 8 patients with PH associated with respiratory disease (PH-RESP), 16 patients with chronic thromboembolic PH (CTEPH), 1 patient with unclear/multifactorial PH.

4.1.2 Right heart catheterisation

RHC was undertaken using a balloon-tipped 7.5 Fr thermodilution catheter (Becton-Dickinson, USA). PH was defined by mPAP ≥ 25 mmHg at rest. Cardiac output (CO) was measured using the thermodilution technique. Pulmonary vascular resistance (PVR) was calculated as the ratio between transpulmonary pressure and cardiac output.

4.1.3 MRI images

Acquisition

All patients underwent MRI examination on a 1.5 T GE HDx whole-body scanner (GE Healthcare, Milwaukee, USA), using an 8 channel cardiac coil in supine position.

2D Phase-contrast (PC) and balanced steady state free precession (bSSFP) images of the main pulmonary artery were acquired to quantify flow $Q(t)$ and area $A(t)$ during the entire cardiac cycle. The two sequences were spatially and temporally synchronised using the same imaging dimensions (matrix dimensions 256 x 128, 480 x 288 mm FOV) with the same cardiac gating, generating the same number of cardiac images per heart beat (40). The images were acquired during breath hold, with a slice perpendicular to the pulmonary trunk, at approximately 2 cm distance from the pulmonary valve. The PC parameters were: 5.85 ms repetition time (TR), 2.87 ms echo time (TE), 150 cm/s velocity encoding (V_{enc}), 10% arrhythmia rejection. The bSSFP parameters were: 3.73 ms TR, 1.62 ms TE.

4 chamber and short axis cine cardiac images were acquired using a retrospective cardiac-gated multi-slice bSSFP sequence. A stack of images in the short axis (SA) plane with slice thickness of 8mm with a 2 mm inter-slice gap or 10 mm with no inter-slice gap were acquired fully covering both ventricles from base to apex. The multi-slice bSSFP sequence parameters were: TR 2.8 ms, TE 1.0ms, Flip angle of 50°, FOV=48 x 43.2, 256 x 256 matrix, 125 kHz bandwidth and slice thickness of 8-10 mm.

Post-processing

Following the protocol described in Chapter 2, the 2D MPA images were post-processed by applying a semi-automatic registration-based segmentation to derive the area, $A(t)$, and flow, $Q(t)$, waveforms for each subject. The segmentations were performed by an operator with previous experience in analysing MPA images. The resulting $A(t)$ and $Q(t)$ were used to compute the 0D and 1D model metrics and calculate the relative area change-RAC, main pulmonary artery systolic area-sArea and main pulmonary artery diastolic area -dArea.

An experienced radiographer manually traced the left and right ventricle epicardial and endocardial borders on the stack of SA images using software available on the MR workstation (GE Advantage Workstation ReportCard). The segmentations were used to calculate the cardiac images metrics: right ventricle end diastolic volume index -RVEDVI, right ventricular ejection fraction -RVEF, ventricular mass index -VMI, systolic septal angle and right ventricle mass index -RVMI.

4.1.4 Diagnosis metrics derivation

PH diagnosis metrics discussed in this chapter were separated into three major categories, each group labelled according to the main 'source' of its derivation.

4.1.4.1 Physiology-based computational modelling from image data

A graphical user interface (GUI) was implemented in MATLAB to integrate the workflow of computing the Windkessel electrical parameters (R_d , R_c and C) and the power content in the backward-travelling pressure wave relative to the total wave power (W_b/W_{tot}). The components of the 0D model were chosen as the set that best reproduce the relationship between measured pressure ($p(t)$) and flow ($Q(t)$): the metric for best fit is defined in chapter 3. The 1D model metric was computed from the summation of the wave power at each harmonic, after the total wave was decomposed into its forward and backward components. The methods used for deriving the computational metrics were introduced and extensively discussed Chapter 3 of the thesis.

4.1.4.2 2D MPA metrics

Under conditions of PH the main pulmonary artery dilates to adapt to the increase in pressure, in some cases reaching aortic dimensions [133]. Quantification of the size of the main pulmonary artery was shown to predict treatment failure [40] and low survival rate [31], [26]. Parameters including relative area change (RAC), systolic and diastolic area have also been evaluated in previous studies [32], [34], [26] with respect to their discriminative potential in separating normotensive from PH patients.

From the analysis of the 2D MPA bSSFP images alone, the minimal and maximal areas were selected and used to compute the relative area change -RAC (Eq. 4.3), diastolic -dArea area (Eq. 4.1) and systolic -sArea (Eq. 4.1)..

The measurements were indexed for body surface area (BSA), by dividing the minimum and maximum area of each patient with the individual BSA. The metric was calculated using the

formula proposed by Du Bois and Du Bois [149], where $BSA [m^2] = \text{Weight [kg]}^{0.425} \times \text{height (cm)}^{0.725} \times 0.007184$.

$$dArea = \frac{\min(A(t))}{BSA} \quad (\text{Eq. 4.1})$$

$$sArea = \frac{\max(A(t))}{BSA} \quad (\text{Eq. 4.2})$$

$$RAC = \frac{sArea - dArea}{dArea} 100 \quad (\text{Eq. 4.3})$$

4.1.4.3 CMR metrics

Right ventricle (RV) assessment in patients with suspected pulmonary hypertension plays an important role given that right heart failure is one of the most common causes of death in PH [22]. Several studies [150], [36], [151] reported that RV derived parameters, including right ventricle ejection fraction (RVEF), right ventricle end diastolic volume index (RVEDVI), ventricle mass index (VMI) and stroke volume (SV) are predictors of treatment failure and mortality in PH.

Patients with PH show increased ventricular afterload, clinically quantified by higher pulmonary vascular resistance (PVR) and lower vascular compliance (C), compared with normotensive subjects [20, 135, 144]. The RV tries to compensate for this workload elevation by modifying its morphology and function, including: enlarged RV chamber (RV dilatation), increased wall thickness (RV hypertrophy), inter-ventricular septum (IVS) deformation [9], [152]. RVEDVI, VMI and IVS were shown to be diagnostic metrics of PH in several clinical studies [153], [33], [154], [35], [155], [34]. Due to its higher accuracy and repeatability than Echocardiography, time resolved cardiac imaging, obtained by the means of cine cardiac magnetic resonance (CMR), has become the gold standard for RV assessment [156].

Deriving CMR metrics is part of the standard protocol in our research group. Following the methods described in [147], five CMR indices (right ventricle end diastolic volume index - RVEDVI, right ventricular ejection fraction -RVEF, ventricular mass index -VMI, systolic septal angle, and right ventricle mass index –RVMI) were calculated and their individual accuracies derived on the current patient cohort.

An experienced radiographer manually segmented the endocardial surfaces on the short axes image, used to calculate the right ventricle end-diastolic (EDV) and end-systolic (ESV) volumes. Right ventricle ejection fraction (RVEF) was further calculated as (Eq. 4.4). The RV

epicardial and endocardial borders on each end-diastolic short axis slice image were carefully outlined. During segmentation the inter-ventricular septum was considered part of the left ventricle (LV). The RV and LV volumes were calculated by summation of the area-thickness product over all slices. LV and RV mass were estimated by multiplying the corresponding ventricular volume by the myocardium density, ρ_m -1.05 g/cm³ (Eq. 4.5). VMI was calculated by dividing the RV by the LV mass. Measurements were normalised for BSA where appropriate, using the same approach as for systolic and diastolic area indexing.

$$RVEF = \frac{EDV - ESV}{EDV} \quad (\text{Eq. 4.4})$$

$$RVMI = \frac{(\rho_m \cdot \sum_{n=1}^{n_s} A_{RV} \cdot s_h)}{BSA} \quad (\text{Eq. 4.5})$$

where n_s is the number of cardiac segmented slices, A_{RV} is the segmented area of the right ventricle, s_h is the slice thickness

The inter-ventricular septum was assessed on the mid chamber short axis CINE cardiac images at the phase of maximal septal displacement. Inter-ventricular septal angle was measured by determining the angle between the midpoint of the inter-ventricular septum and the two hinge points.

4.1.5 Clinical diagnosis test

The simplest clinical diagnosis tests are binary, designed to discriminate between two classes the patients could belong to. An ideal classification metric should be able to attribute the correct class to every subject, being both sensitive and specific. Sensitivity (Eq. 4.7) and specificity (Eq. 4.8) measure the ability of a clinical test to correctly classify a patient as having or not having the disease [157]. However, in a real world scenario, a classifier can be either more sensitive, usually used as a screening method, or more specific, used to confirm the absence of the disease. Therefore, it is usually the case that a classifier is chosen based on a trade-off between sensitivity and specificity, dictated by the clinical application of the test.

Two types of classifiers, referred to in this chapter as individual and multiple parameters classifiers, were evaluated on the given PH cohort to segregate the normotensive individuals from patients with PH.

4.1.5.1 Individual metric classifier

In the category of individual metric classifier were included all the calculated PH metrics, which, based on a cut-off value derived in data driven manner, can be applied as a disease/ no disease discriminator.

In the process of selecting the discriminant threshold value, several steps were employed. Firstly, the receiver operator characteristic (ROC) curves were drawn for each of the individual metrics and areas under ROC curves (AUC) were calculated in order to obtain the overall test performances. The optimal threshold value was later selected from the curves as the point that maximises the Youden index (Eq. 4.9).

4.1.5.2 Multiple metrics classification

Machine learning algorithms, such as neural networks, support vector machines, classification and regression trees, are frequently used in the artificial intelligence domain and are gaining more interest for medical applications [158-161].

A direct application in classification of patients with and without pulmonary hypertension was implemented by Dennis *et al.* [161]. Based on heart sounds analysis integrated with a linear support vector machine, the authors proposed a non-invasive method for diagnosis of PH, showing that diseased patients can be differentiated from non-diseased with a 77% accuracy. A random forest algorithm, available in MATLAB, was used to assign the 'PH' and 'NoPH' label to the 72 patients in the study cohort.

A decision tree is used to classify a series of instances from A (eg. clinical patients with unknown diagnostic), described by a set of attributes f_A (eg. metrics) into the corresponding class (eg. disease group). The supervised learning process requires that before the classifier is applied to the unseen data (A), it has to be trained on a separate data set B (eg. clinical patients with known diagnosis) where the class labels (L_B) are known. Once the learning process finishes, the trained classifier will attribute to each element of set A a label L_A , corresponding to its class (Figure 4.1).

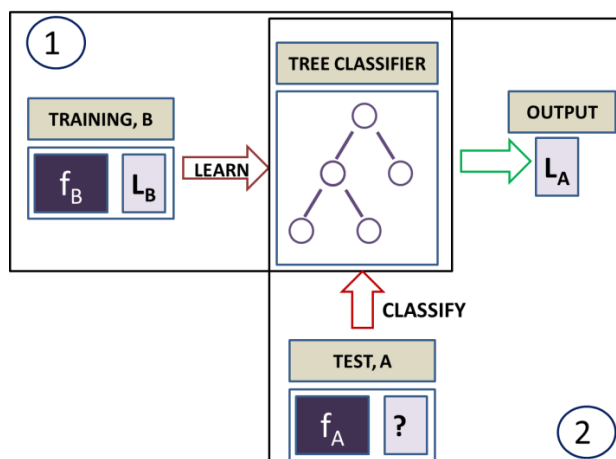


Figure 4.1 Schematic diagram of the single tree classification algorithm

In the first step (1), the model learns on the B data set, based on the values of the attributes, f_B to distinguish between different classes labelled L_B . The trained model is applied during second step (2), to an unseen data set A in order to correctly classify the elements of A into the corresponding classes, labelled L_A .

Although single classification trees are easy to interpret due to their binary format, the variance in the result can be high. An error at the top of the tree propagates to the leaves (final nodes) and alters the results [158]. The random forest algorithm, introduced by Breiman [162] overcomes this problem by using an ensemble of n trees, each of them trained on a subset of data $B_i (i=1:n)$ extracted at random with replacement from B. Every B_i has the same size as B, but some of the data might have been picked twice or more, while some of them will be left out (out-of-bag data). Once the forest is generated, the unseen set A will be tested and each tree of the forest will take a decision, based on the previous learning experience from the different subset B_i . Set A will receive from each tree a set of labels L_{A_i} . The final decision, L_A , will be taken based on the number of votes each element in A will have from all L_{A_i} (Figure 4.2).

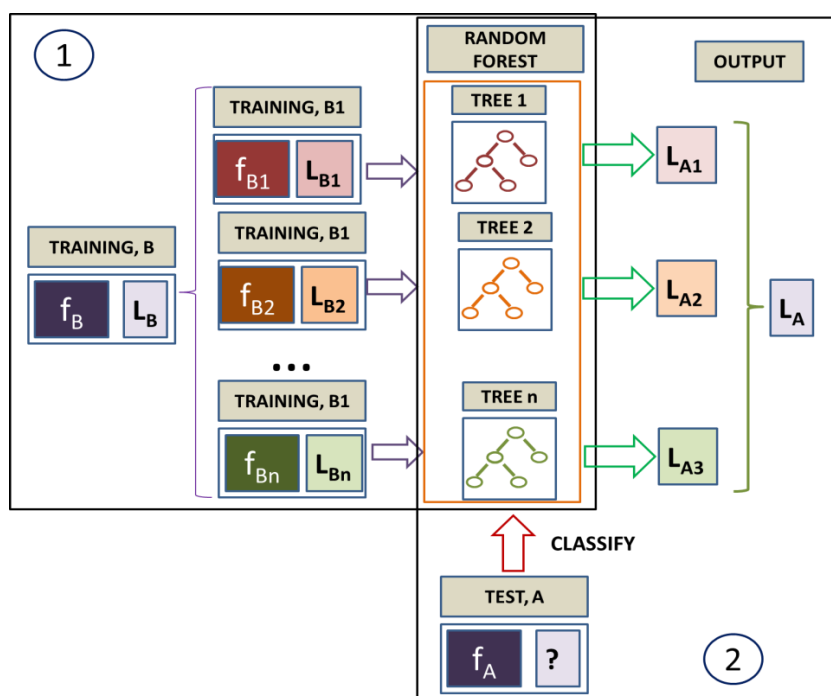


Figure 4.2 Schematic diagram of the random forest classification algorithm.

Feature selection

A classification problem based on machine learning algorithms is dependent on the set of features provided to the learner. It is expected that a feature which performs poorly as an individual discriminant is likely to affect the accuracy of the whole ensemble. Therefore, for deciding which individual markers from the twelve described earlier to include in the random forest algorithm, the following strategy was employed:

Firstly, without excluding any of the features, the change in accuracy given by the in turn addition of MPA and CMR metrics to the 1D-OD models metrics was tested. Secondly, from all individual markers, only the features that would have improved the model's accuracy were selected. Testing all possible combinations of the metrics is computationally expensive even for the small number of attributes available. Therefore a naïve feature selection method was employed, by considering only metrics which showed good individual performance ($AUC > 0.8$).

The metrics included in the classification model following the feature selection were: distal resistance $-R_d$, total pulmonary compliance $-C$, ratio of backward to total pressure wave power $-W_b/W_{tot}$, relative area change- RAC, systolic septal angle, and right ventricle mass index $-RVMI$.

4.1.6 Statistical analysis of the results

IBM SPSS 20 (SPSS, Chicago,IL) was used for statistical analysis. GraphPad Prism 6.0 (San Diego California USA) and MATLAB (R2014a, The MathWorks Inc.) were used for data presentation.

All the variables were tested for statistical differences between groups. The statistical *student t-test* for independent variables was applied where the normality and equality of variances conditions were met. Otherwise, the non-parametric Mann-Whitney test for mean rank differences was applied. The normality condition was tested by visual inspection of histograms and confirmed by the Shapiro-Wilk normality test, whereas Levene's test was applied to verify the equality of variances. A *p-value* < 0.05 was considered significant for all statistical tests.

The diagnostic accuracy of the proposed metrics was tested by computing the area (AUC) under the receiver operator curve (ROC), the misclassification error (Eq. 4.6), sensitivity (Eq. 4.7) and specificity (Eq. 4.8).

$$missclass\ err = 1 - \frac{tp + tn}{tp + tn + fp + fn} \quad (\text{Eq. 4.6})$$

$$sens = \frac{tp}{tp + fn} \quad (\text{Eq. 4.7})$$

$$spec = \frac{tn}{tn + fp} \quad (\text{Eq. 4.8})$$

$$Youden\ index = sens + spec - 1 \quad (\text{Eq. 4.9})$$

where *tp* is the true positive (patients that have PH and were identified by the test as having the condition); *tn* is the true negative (patients that do not have PH and were identified by the model as not having the condition); *fp* is the false positive (patients that do not have PH and were identified by the model as having the condition); *fn* is the false negative (patients that have PH and were identified by the model as not having the condition). Due to the relatively small sample size, the validation of the random forest classification model was performed using leave one out cross-validation -LOOCV. As showed in Figure 4.3, the classification algorithm is operated *n* times, with *n* equal to the number of subjects. For each iteration, one sample (subject) is left out whereas the rest of the *n*-1 samples are used to train the model. Although the method is exhaustive, not being recommended for high sample size, it is considered to be the least bias-affected of all cross-validation methods [163]

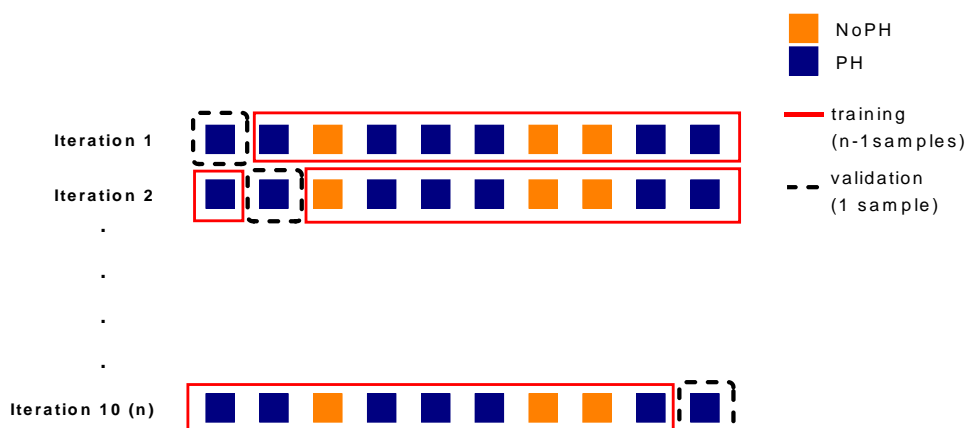


Figure 4.3 Leave-one-out cross-validation diagram

The diagram exemplifies the LOOCV method on a cohort of $n=10$ patients, with both normotensive (NoPH) and PH patients. The model is run for a total of n iterations and at each iteration, one individual is left out (dashed black line), whereas the rest (continuous red line), $n-1$, are used as training set. Following the training, the model will attribute a ‘NoPH’ or ‘PH’ label to the left-out individual, which, compared with the real label, will classify it as true positive, true negative, false positive or false negative.

RESULTS

4.1.7 Demographics and non-invasive metrics group values

Table 4.1 displays the patient demographics together with the median and mean \pm standard deviation (SD) from the mean of the computed invasive (RHC) and non-invasive parameters. Data was found not to be normally distributed for all variables in at least one of the groups. Reported *p-values* from the table correspond to the non-parametric Mann-Whitney test. Excepting right ventricle end-diastolic volume index - RVEDVI, systolic MPA area –sArea and characteristic resistance R_c all the non-invasive indices showed significant statistical difference between the NoPH and PH group.

Table 4.1 Patients demographics, RHC data, mathematical model and images derived parameters

	NoPH				PH				<i>P</i> value
	median	mean ± SD	95% CI		median	mean ± SD	95% CI		
			Lower	Upper			Lower	Upper	
Patient demographics									
Patients, n		15				57			
Male/Female sex		7/8				25/32			
Age,y	59	56 ± 16	47	65	67	64 ± 16	60	68	0.084
Right heart catheter data									
mPAP, mmHg	22	21± 3	19.6	23.0	45	44.7±14.3	40.9	48.5	<0.001
PVR , WU	2	1.9±0.7	1.5	2.3	6	6.9±4.5	5.7	8.1	<0.001
mRAP, mmHg	5	4.9 ± 2.4	3.5	6.2	10	11.3 ± 3.1	9.6	12.9	<0.001
CO, L/min	7	6.5±1.4	5.7	7.3	5	5.2 ±1.5	4.8	5.6	0.005
1D model derived parameter									
W _b /W _{total}	0.26	0.26±0.1	0.22	0.29	0.42	0.4 ± 0.1	0.4	0.42	<0.001
OD model derived parameters									
R _d , mmHg s/ml	0.3	0.36±0.24	0.22	0.49	0.59	0.87±0.73	0.64	1.1	<0.001
R _c , mmHg s/ml	0.038	0.037±0.013	0.027	0.048	0.003	0.051±0.13	0.014	0.087	0.05
C, ml/mmHg	1.29	4.74±12.9	-2.4	11.9	0.69	0.73 ± 0.4	0.62	0.84	<0.001
PA imaging derived parameters									
RAC, %	26.2	25.9±12.52	18.9	32.8	13.9	14.6±7.41	12.6	16.6	<0.001
dArea x 10 ⁴	3.74	3.77 ± 1.01	3.19	4.35	4.74	4.78 ± 1.22	4.46	5.1	0.005
sArea x10 ⁴	3.74	4.77 ± 1.01	3.39	5.52	5.32	5.44 ±1.26	5.1	5.77	0.073
CMR									
RVEDVI, ml/m ²	72.8	69.9 ± 21.9	57.7	82	78	87.6±34.2	78.5	96.7	0.095
RVEF, %	50.3	51.4 ±8.86	46.5	56.3	41	40.3±13.5	36.7	43.9	0.004
VMI , ratio	0.23	0.28 ± 0.15	0.19	0.36	0.37	0.45±0.27	0.37	0.52	0.006
RVMI, g/m ²	10.3	12.1 ± 3.95	9.9	14.3	20.1	21.6±11.2	18.6	24.7	<0.001
systolic septal angle, °	142	144 ± 10.3	138	149	168	168±22.3	162	174	<0.001

*metrics abbreviations

<i>R_d</i>	<i>Distal resistance</i>
<i>R_c</i>	<i>Characteristic resistance</i>
<i>C</i>	<i>Total pulmonary compliance</i>
<i>W_b/W_{total}</i>	<i>Ratio of backward to total wave power</i>
<i>RAC</i>	<i>Main pulmonary artery relative area change</i>
<i>RVEDVI</i>	<i>Right ventricle end diastolic volume index</i>
<i>RVEF</i>	<i>Right ventricle ejection fraction</i>
<i>VMI</i>	<i>Ventricular mass index</i>
<i>RVMI</i>	<i>Right ventricle mass index</i>

It is important to underline that the control group has a high average mPAP value of 21.3±3 mmHg, with a median value of 22mmHg. It is argued [5] that the normal mPAP values are between 17-21 mmHg, whereas higher values, between 21- 24 mmHg are characteristic to borderline PH patients. However, this latter category it is not officially defined in the PH guidelines, remaining an open clinical debate.

4.1.8 Performance of individual parameters

The accuracies of the individual metrics were quantified in terms of AUC, misclassification error, sensitivity and specificity (Table 4.2). Excepting AUC, the other indices were computed for the threshold values which maximised the Youden index.

Table 4.2 Non-invasive metrics' individual accuracies evaluated for a cut-off value corresponding to maximum Youden index

	AUC	missclass. error	Sens.	Spec.	threshold
1D model					
W_b/W_{tot} , ratio	0.88	0.25	0.68	1	0.35
OD Model					
R_d , mmHg s/ml	0.85	0.25	0.72	0.87	0.46
R_c , mmHg s/ml	0.67	0.38	0.56	0.86	0.01
C, ml/mmHg	0.83	0.25	0.72	0.87	0.88
PA imaging					
RAC, %	0.81	0.29	0.67	0.87	16
dAreax10 ⁴ , ratio	0.74	0.21	0.86	0.53	3.75
sAreax10 ⁴ , ratio	0.66	0.38	0.61	0.67	5.01
CMR					
RVMI, g/m ²	0.81	0.26	0.68	0.93	16.01
RVEDVI, ml/m ²	0.64	0.51	0.36	0.93	0.94
VMI, ratio	0.73	0.26	0.74	0.73	0.27
RVEF, %	0.74	0.38	0.56	0.87	43
systolic septal angle, °	0.81	0.35	0.56	1	164

Non-invasive PH metrics (data driven threshold)

Overall, at the selected cut-off values, the PH metrics showed higher specificity than sensitivity, suggesting that these metrics might better be used as confirmation tests, to exclude the NoPH patients, than as screening tests.

The 1D model derived parameter had the highest AUC, at 0.88, of all of the analysed metrics. At the chosen threshold value of 0.35, the ratio of the backward to total wave power, W_b/W_{tot} discriminates between normotensive and patients with PH with a misclassification error of 25%, 68% sensitivity and 100% specificity. Maximum specificity is also shown by the systolic septal angle, at a cut-off value of 164° but its overall accuracy, sensitivity and AUC, of 35%, 56% and 0.81 respectively, are lower than W_b/W_{tot} .

The OD model parameters, distal resistance R_d and total compliance C , performed similarly as discriminators showing good AUC of 0.85 and 0.83 respectively. A misclassification error of 25%, with 72% sensitivity and 87% specificity were found for both R_d and C at the cut-off values of 0.46 mmHg s/ml and 0.88 ml/mmHg respectively. Figure 4.4 displays graphically the ROC for the derived metrics of the computational models.

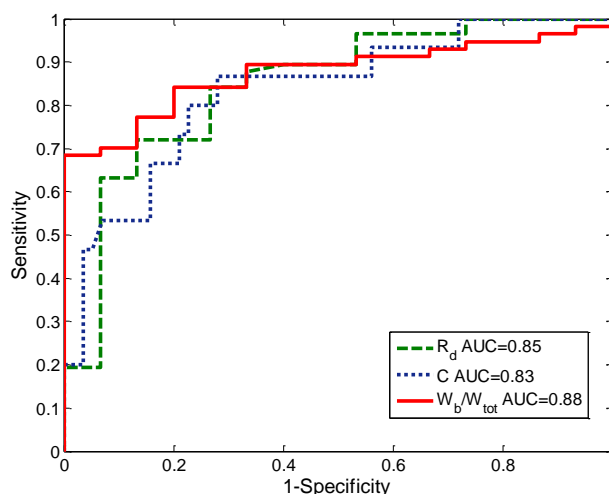


Figure 4.4 ROC and AUC of the physiology-based computational metrics

At a threshold of 16% relative change in area of the MPA, RAC misclassified 29% of the subjects, with 67% sensitivity and 87% specificity. At a chosen threshold value of 3.75×10^4 , the diastolic area misclassified 21% of the subjects, with 86% sensitivity and 53% specificity, being the only metric which had higher sensitivity than specificity from all the analysed data. The BSA indexed systolic area, at a threshold of 5.01×10^4 misclassified 38% of the subjects with 61% sensitivity and 67% specificity. The corresponding ROC curves are graphically displayed in Figure 4.5 for the parameters derived from the 2D MPA images alone.

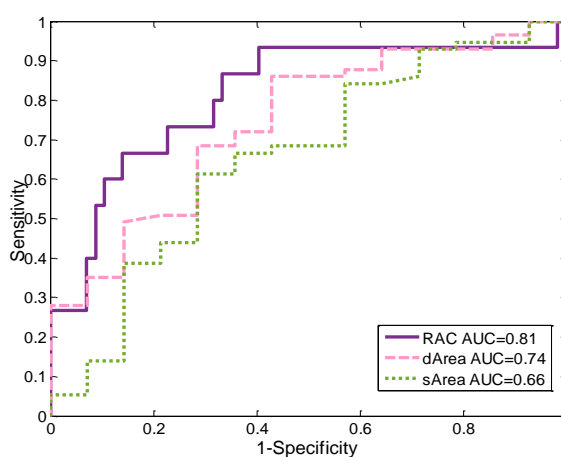


Figure 4.5 ROC and AUC of the MPA derived metrics

The right ventricle mass index, RVMI, and systolic septal angle were the only two parameters derived from cardiac images alone which had, on the analysed cohort, an AUC higher than 0.8. At a chosen threshold of 16.01 g/m^2 , the RVMI misclassified 26% of the subjects, with 68% sensitivity and 93% specificity. The ventricular mass index, VMI, had the same misclassification error, of 26%, with 74% sensitivity and 73% specificity for a cut-off value of 0.27. The accuracy results for the right ventricle end diastolic volume index, RVEDVI were the least satisfactory from all the analysed metrics. For a selected threshold of 0.9 ml/m^2 , only 49% of the patients were correctly classified, with 36% sensitivity and 93% specificity. Figure 4.6 displays graphically the ROC curves for the PH indices calculated solely from CMR images.

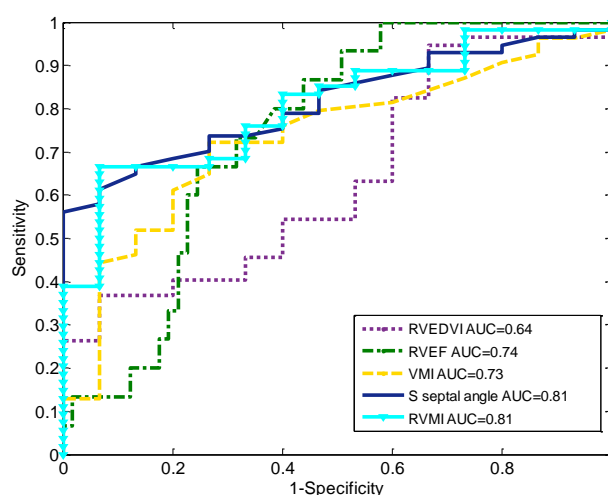


Figure 4.6 ROC and AUC of the CMR derived metrics

4.1.9 Random forest classifier performance

The addition of the OD metrics to the ratio of backward to total wave power metric, W_b/W_{tot} , improved the misclassification error by 4%. The accuracy of the model which combines only OD and 1D computational metrics is similar to the one obtained by Dennis *et al.* [161], using a linear support vector machine classifier combined with heart sound metrics obtained by Doppler Echocardiography. The authors reported a diagnosis accuracy of 77%, with 0.78 AUC for a validation cohort of 31 patients (out of 51).

A decrease of the misclassification error of 6% and increase in both sensitivity and specificity, of 5% and 6% respectively, was obtained by the addition of all MPA metrics. The addition of all CMR metrics, lowered the misclassification error by another 2%, whilst increasing the sensitivity to 97%, and keeping the specificity constant at 53%.

Table 4.3 displays the specificity, sensitivities and misclassification errors resulting from the operation of the random forest algorithm with different combinations of features.

Table 4.3 Classification accuracies for the coupled-PH-metrics models

	AUC	missclass. error	Sens.	Spec.	threshold
LOOCV	0D +1D	0.89	0.21	0.88	0.47
	0D+1D+PA	0.9	0.13	0.93	0.67
	0D+1D+PA+CMR (all)	0.89	0.14	0.97	0.47
	0D+1D+PA+CMR	0.91	0.08	0.97	0.73

The information in Table 4.2 and Table 4.3 is displayed graphically in Figure 4.7, for better understanding of the changes in classification accuracy and sensitivity-specificity trade-off corresponding to individual discriminants and machine learning integrated classifiers.

At the left of the dotted vertical line, representing the individual discriminates accuracies at threshold values maximising Youden index, most of the metrics can be seen to be more sensitive to 'NoPH', having higher specificity than sensitivity. At the right of the dotted line, for all analysed feature combinations, the random forest classifier has higher sensitivity than specificity. It can therefore be suggested that the diagnostic process can be applied in two steps: firstly, a highly sensitive discriminate might be applied as a screening test, identifying patients with PH, followed by a highly specific test to eliminate any false positives.

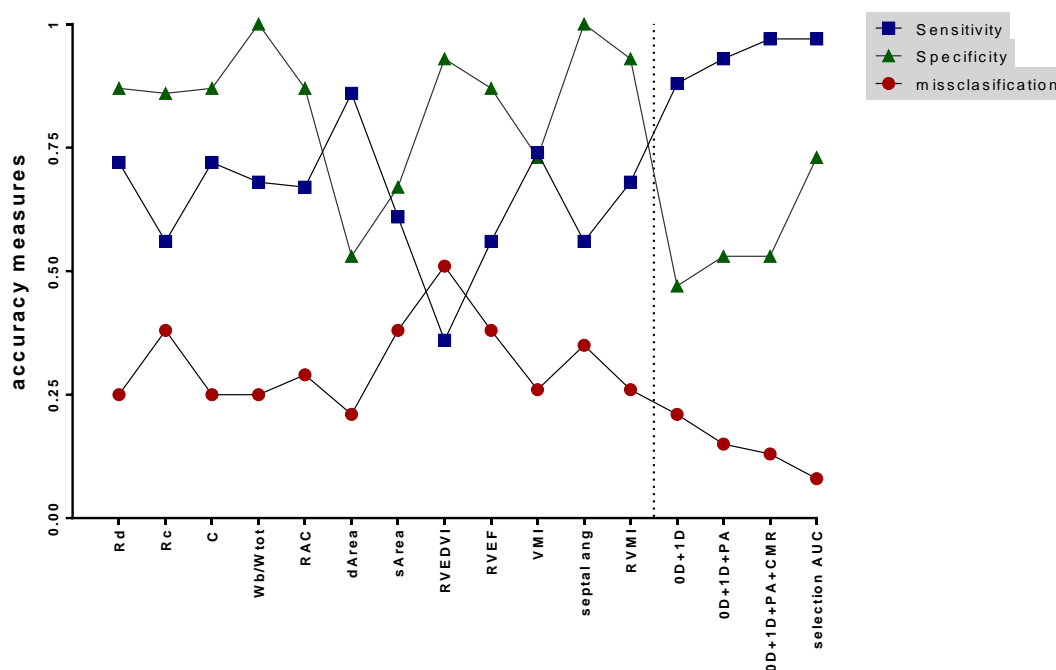


Figure 4.7 Individual and random forest model’s accuracies

Individual PH metrics and random forest’s model’s accuracies are displayed in terms of missclassification error (red circles), sensitivity (blue squares) and specificity (green triangles). The accuracy values corresponding to the individual metrics (left to the vertical dotted line) were calculated for threshold values selected at maximum Youden index, while the ones for the tree ensembles (right of the dotted vertical line) were calculated with leave-one-out cross validation.

The model incorrectly classified 6 out of 72 patients: 2 PH subjects (mPAP >25 mmHg) as not having PH (false negative) and 4 NoPH subjects (mPAP <25 mmHg) as having PH. The high average mPAP of the control group supports the evidence that several of the patients were close to the diagnosis threshold using the gold-standard RHC. This suggested that it should be investigated whether those who were classified incorrectly by the algorithm were close to threshold.

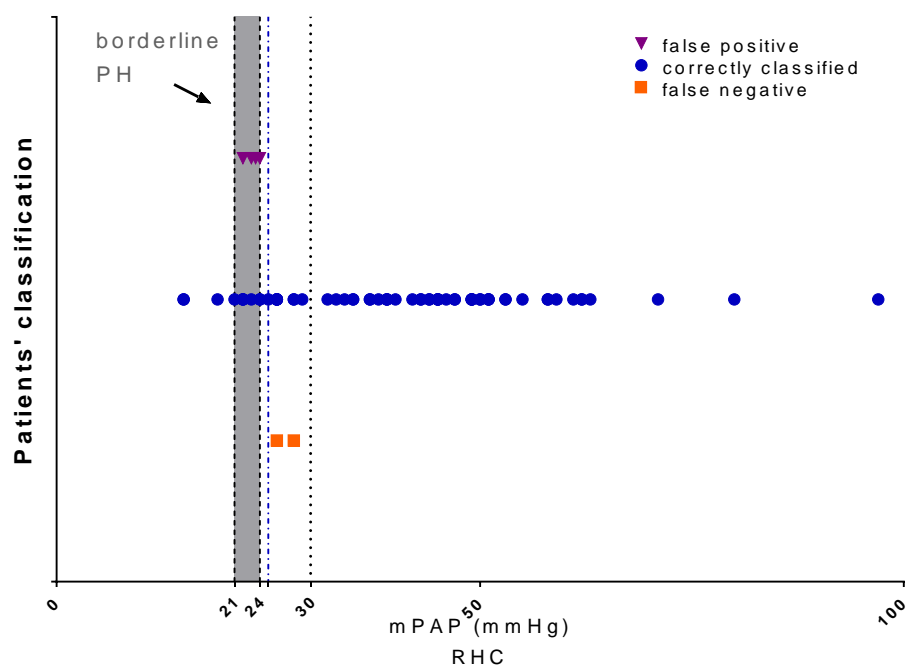


Figure 4.8 The patient classification returned by the ensemble model with the smallest misclassification error and highest sensitivity, at leave-one-out cross-validation.

Six out of the 72 patients were misclassified by the model which included metrics with individual AUC>0.8: two false negative (orange square), who had mPAP> 25mmHg and were identified by the model as not having PH and four false positive (purple triangles), who had mPAP <25mmHg and had been identified by the model as having PH. The mPAP of all misclassified patients was close to the 25 mmHg threshold.

The 2 false negative subjects, had mPAP of 28 mmHg and 26 mmHg respectively, being very close to the 25 mmHg PH threshold. Moreover, their pulmonary vascular resistance was 1.3 WU and 2.7 WU respectively, and so the clinical diagnosis, irrespective of the abnormal mPAP, was that neither of these patients had underlying PAH. All 4 false positive subjects had mPAP between 22 and 24 mmHg. Previous research has found the mPAP of healthy volunteers to be 14mmHg (± 3.3), and patients with mPAP between 21-24mmHg are considered borderline PH [5]. These show that the classification model incorrectly classified only cases which were in the clinically-uncertain area. The overall performance was therefore excellent. This is illustrated in (Figure 4.8), which shows clearly where the incorrect classifications were made.

DISCUSSION

4.1.9.1 Individual metrics

The results showed that computational derived parameters, W_b/W_{tot} , R_d and C , were the non-invasive metrics with the highest individual AUC, confirming the diagnosis potential exhibited by these metrics in the previous work (Chapter 3).

All three computational metrics included in the decision process had the same misclassification error (0.25), when a threshold that maximises Youden index was chosen.

Nevertheless, the combination of 1D and 0D derived metrics using the random forest classification algorithm improves the AUC. The classification accuracy is improved as well, from 75% to 79%, although the improvement is statically not significant ($p=0.32$), when tested with the Mc Nemar statistical test for classification accuracy [164].

Three parameters were derived from the 2D MR images of the main pulmonary artery alone. The results confirmed the results of previous studies, indicating that the size of the artery is a PH discriminant. The normalised diastolic area size performed better than the normalised systolic area, in agreement with the findings of Swift *et al.* [34]. However, while on their analysed cohort Swift *et al.* [34] reported AUCs of 0.82 and 0.77 respectively for the two markers, on the current cohort none of these metrics reached an AUC of 0.8.

Although taken individually, the systolic and diastolic area have not shown a good discriminative performance, the combination of the two, into the pulmonary relative area change metric RAC, showed superior performance. Maximum sensitivity and specificity, according to the data-driven criteria, was obtained for a 16% value. The same cut-off value was found by [31], with measurements performed in the right pulmonary artery, as a mortality predictor. Other authors [26] and [30] indicated 15% and 24% respectively as the diagnosis thresholds for RAC quantified for the main pulmonary artery.

Previous studies [17, 32, 34, 36] have shown good results for PH assessment using CMR derived parameters. The ventricular mass index, VMI, showed high accuracy, 0.92 AUC, in the study of Hagger *et al.* [153]. Similarly, Swift *et al.* reported 0.91 AUC, on a large cohort of naïvely treated patients. However, our results showed poorer performance for VMI, of only 0.73 AUC. Our suggestion is that this reflects the relatively high number of subjects in the current cohort who had mPAP close to the 25mmHg threshold (30% from the entire cohort), making it a more challenging cohort than those used in several previous studies. RV

remodelling occurs secondary to changes in the pulmonary vasculature, suggesting that, for the borderline cases, the CMR derived parameters will have less diagnostic power. Nevertheless, a modification in the distal pulmonary vasculature or any system disturbance leading to an impedance mismatch will determine an increase in the quantity of waves reflected [27], which could be detected by the 0D-1D computational models.

4.1.9.2 Machine learning classifier

The improvement in the classification accuracy occurred gradually (from using just 0D+1D to adding the MPA and CMR metrics), suggesting that the more the model knows about the features defining an individual, the more confidently, with a higher probability, a decision about the unseen data is taken. However not just the quantity but the quality of the input data it is important, since the accuracy of the model using only selective metrics (AUC >0.8) was improved ($p=0.21$) by 5% relative to that using all parameters blindly.

For all the proposed combination of metrics, the random forest model performed better than the individual parameters, in terms of misclassification error and AUC. As reported in this chapter, the misclassification error, sensitivity and specificity of the random forest models were obtained following leave-one-out cross validation, which is considered a robust method, whereas the individual metrics accuracies were based on data-driven criteria, which are known to be biased [165, 166].

SUMMARY AND CONCLUSIONS

Non-invasive PH markers derived through the means of computational models, as well as those measured directly from MRI images of the main pulmonary artery and/ or right ventricle, have been shown to differentiate between normotensive individuals and patients with PH [26, 27, 30-32, 34, 35, 37, 147].

The current chapter was designed to quantify the PH diagnostic accuracy of the 0D and 1D metrics proposed in Chapter 3 (W_b/W_{tot} , R_d , C), to compare their performance with other non-invasive metrics proposed in the literature and routinely calculated in our research group (RAC, $dArea$, $sArea$, RVM, RVEDVI, VMI, RVEF, systolic septal angle), and to test whether combining the available metrics into machine learning classification algorithms can improve the diagnosis accuracy.

Several measures of accuracy were calculated (misclassification error, sensitivity and specificity and area under receiver operator characteristic curve) for each non-invasive metric. As the performance of the classification algorithm is affected by the features included, a naïve selection approach, considering only metrics with $AUC > 0.8$, was applied. The computational metrics, ratio of backward to total pressure wave power (W_b/W_{tot}), distal resistance (R_d) and total compliance (C) showed the highest individual AUC, followed by relative area change (RAC), right ventricle mass index (RVMI) and systolic septal angle, all with $AUC > 0.8$.

The selected imaging metrics were added in turn to the computationally derived discriminants and the performance of a random forest classifier implemented in MATLAB was tested with leave-one-out cross-validation for each proposed metric combination.

Combining the 0D model parameters, R_d and C, with the 1D model parameter, W_b/W_{tot} correctly classified 79% subjects with an AUC of 0.89. Sensitivity, specificity and classification accuracy improved considerably when the anatomical parameters were added to the classification model. The addition of RAC reduced the misclassification error to 13%, increasing both sensitivity and specificity. Coupling all of the non-invasive PH markers with $AUC > 0.8$, correctly classified 66 out of 72 patients (92%), with high sensitivity (97%) and specificity (73%).

It has been shown that a high accuracy non-invasive PH diagnosis can be achieved by maximising the use of MR imaging, by integrating already developed non-invasive PH metrics, derived by the means of different methods, into random forest classifiers. The approach may reduce the need for right heart catheterisation in patients with suspected pulmonary hypertension.

CHAPTER 5

Finite Element Model for a 1D Branching Tree of Pulmonary Arterial Circulation

MOTIVATION

Chapter 3 describes a method of characterising the pulmonary system efficiency in healthy volunteers and patients with stratified pulmonary hypertension through the means of the electrical parameters of a three element Windkessel model and the power contained in the backward pressure wave measured in the main pulmonary artery. Following the analysis, two of the electrical parameters (R_d and C), and the ratio of backward to total pressure wave power (W_b/W_{tot}) showed great potential in differentiating between healthy volunteers and patients with stratified PH. In *Chapter 4*, the discriminative character of the computational metrics together with several other PH metrics calculated from MRI images alone was tested. The individual analysis showed that the W_b/W_{tot} parameter performed the best of all metrics studied. The reflection ratio, in common with all of the analyses presented in the thesis so far, focuses on the interpretation of the pressure-flow relationship at the measured cross-

section to infer the status of the distal vasculature. It is a global measure, providing no immediate information about the spatial distribution of the disease. The distal vasculature that is being characterised is a branching tree structure. Two interesting questions arise.

- How deep into the vascular tree can this technique ‘see’? It seems likely that the strongest signal will come from the vessels that are closest to the reflection site, and that attenuation and wave-trapping effects will diminish the disease signal that returns from the more distal elements of the tree. Is there a point at which the disease cannot be detected, because the signal is lost in noise?
- Might it be possible to characterise the distribution of the disease within the vascular tree? The temporal forms of the pressure and flow signals will be different for wave reflections from different locations, so is it possible to use this information to localise the disease, or to define a spatial spectrum.

In order to answer these questions a model of the branching tree structure is required.

Olufsen *et al.* [44] and Qureshi *et al.* [45] conducted research to investigate the pressure and flow waveforms in healthy and under several simulated PH conditions. Both teams took a similar approach. They used 1D models of the major vessel network, solved numerically, to investigate the performance of the system, with the inlet flow defined from MRI measurements in a healthy volunteer and the outlet boundary characterised by 1D structured tree models. By altering the configuration of the outflow trees to simulate distal vasculature rarefaction, Olufsen *et al.* [44] computationally predicted the changes in pressure and flow waveforms at the inlet of the domain. Similarly, Qureshi *et al.* [45] changed the configuration of the structured tree and altered in turn the compliance of the large and small vessels to predict the haemodynamic changes induced by pulmonary arterial hypertension (PAH), chronic thromboembolic pulmonary hypertension (CTEPH) and hypoxic lung disease (HLD). Recently, Qureshi *et al.* [46] quantified the wave reflections using wave intensity analysis (WIA), on the same simulated conditions, showing an increase in the reflected waves. The proposed models, although they have only been exercised to investigate the consequences of variations on the data measured in a healthy volunteer, are a great tool for understanding the factors affecting the changes that might be measured at the level of major pulmonary arteries. Consistently with the work reported in this thesis, these computational studies emphasise the potential of wave reflections to distinguish not only between healthy volunteers and PH patients but also between PH sub-groups.

The aim of the current chapter is to establish a method to characterise the pressure and flow distribution throughout a pulmonary arterial tree model, with emphasis on the characterisation of the wave reflections and their distribution. It is anticipated that the application of this model will provide new insight as well as further diagnostic information when it is applied to the available patient data. The proposed model predicts the flow and pressure solution in each vessel by solving the 1D linearised Navier-Stokes equations for viscous flow in tubes with thin, elastic walls. The W_b/W_{tot} parameter is computed for each node of the branching tree in order to quantify the amount of backward energy at each bifurcation that is not transmitted proximally towards the measurement site.

The 1D-linear solver developed in this chapter is based on a finite element modelling (FEM) approach implemented in the frequency domain. This is an efficient approach that lends itself to the capture and representation of the wave transmission effects. The results at the top of the tree were validated based on a recursive impedance approach. The latter method, applied in previous studies, [167], [89], [44], [45] is briefly reviewed.

DEFINING THE PULMONARY ARTERIAL TREE

The pulmonary tree has an intricate structure, with arteries and veins closely following the airways. Due to the convoluted nature of the vessel network, its location (hidden behind the thorax) and the small size of the vessels ($< 100\mu\text{m}$ diameter), the pulmonary circulation structure and functions are difficult to image effectively. A compromise between the level of structural tree detail, computational cost and insights gained from simulation of pulmonary functions is often adopted. For constructing the pulmonary tree structure of a 1D model, Spilker *et al.* [89] used patient specific MRI angiography data for the main pulmonary arteries, coupled at each outlet with arterial trees based on morphometric rules derived from human lung casts. The outflow trees were solved recursively based on the Womersley solution for pulsatile flow, being tuned to match the inlet boundary conditions. Similarly, Olufsen *et al.* [44] and Qureshi *et al.* [45] used patient specific MRI based data for the inlet domain, but replaced the outflow morphometric trees with much simpler, asymmetric structural trees.

The structural trees, often used only as outflow boundary conditions for numerical 1D domains [167], [90], [44],[45], have binary, fractal like configurations, defined by simple, length-to-radius and parent-to-daughter radius, rules. Although simpler to construct, the trees are missing the level of detail provided by the morphometric data including, for example, the existence of trifurcations. However, for the purpose of the current work, describing the implementation of a 1D solver based on FEM method to characterise the

pulmonary arterial circulation in terms of wave reflection, a simple geometry is ideal. Therefore, using the set of rules and parameters values implemented by Olufsen *et al.* [44], a pulmonary arterial tree, including small and large arteries, was generated.

Definition of the tree structure

The pulmonary arterial tree is defined based on input (root) radius, output minimum radius and two relationships relating daughter branches to parent branch and vessel length to vessel radius.

- **Root radius, r_0 ,** represents the radius at the inlet of the tree.
- **Output minimum radius, r_{min} ,** is the smallest generated branch radius in the tree and represents the stopping criterion for the depth of the tree.
- **Parent-daughter radius relationship.** The relationship is defined by the values of two coefficients, β_1 and β_2 , describing the parent-to-daughter radius ratio for the two distal vessels branching from the parent vessel.

$$r_{d_1} = \beta_1 r_{parent} \quad (\text{Eq. 5.1})$$

$$r_{d_2} = \beta_2 r_{parent} \quad (\text{Eq. 5.2})$$

As described in [167], the chosen values of β_1 and β_2 values represent some important characteristics of the change in the cross-sectional area of the parent to daughter vessels. The area of each daughter is smaller than the area of the parent vessel ($A_{d1}, A_{d2} < A_p$), whereas the sum of the daughters' area is higher than that of the parent ($A_{d1} + A_{d2} > A_p$).

- **Length to radius relationship.** The length of each vessel is related to its radius by the value of the λ coefficient.

$$l = \lambda r \quad (\text{Eq. 5.3})$$

Tree connectivity and terminology

Following the rules defined above, a function requiring the values of r_0 , β_1 , β_2 and r_{min} was implemented to generate an explicit connectivity matrix. Each generated vessel corresponds to a 1D element with the two ends equivalent to the nodal points. The generations of branches are counted top-down, similarly to Weibel's [168] airways numbering system, with the exception that the first (input) branch corresponds to generation 1 (not generation 0 as specified by Weibel). The generation number increases with 1 after each bifurcation. All the nodes describing a bifurcation (connecting three elements) are referred to as *internal nodes*, whereas the ones connected to only one element, except the inlet node of the first branch, are *terminal nodes*. The latter is referred to as the *root node*, as also described in Figure 5.1.

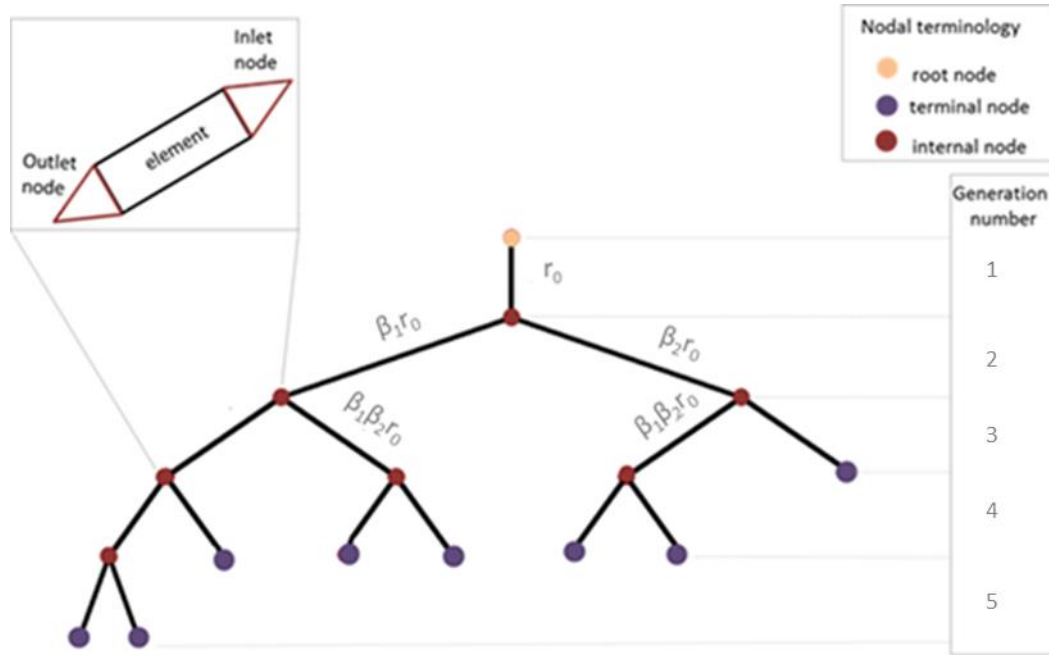


Figure 5.1 Branching tree connectivity and terminology

Each branch of the asymmetric tree represents an element in the connectivity matrix. The elements and nodes are numbered top-down, as well as the generations. All nodes connecting three elements are internal nodes (red) whereas, the ones connected to only one element are the root (orange) and the terminal nodes (purple).

LINEARISED PRESSURE AND FLOW SOLUTION FOR A SINGLE 1D ELEMENT

As introduced in *Chapter 3*, the analytical pressure and flow solution of a linear system can be expressed using Fourier analysis. The oscillatory and steady components of the flow and pressure waveforms are treated separately. The latter does not affect the wave reflection analysis employed in this thesis and therefore the main focus lays on the first.

Oscillatory solution

At any instance in time a travelling wave is the superposition of a forward and a backward travelling wave. The solution for the linearised one-dimensional Navier-Stokes equation of a periodic pressure (p) and flow (q) wave travelling in the z direction, with a complex wave speed, c , is of form:

$$p(\omega, z, t) = P_f e^{i\omega(t-z/c)} + P_b e^{i\omega(t+z/c)} \quad (\text{Eq. 5.4})$$

$$Q(\omega, z, t) = Q_f e^{i\omega(t-z/c)} + Q_b e^{i\omega(t+z/c)} \quad (\text{Eq. 5.5})$$

Where P_f , P_b , Q_f , Q_b are the forward and backward pressure and flow amplitudes, c is the complex pulse wave velocity, ω is the angular frequency of the periodic signal, z is the travelling distance along the longitudinal axis.

The value of c for a wave travelling through a system depends on its physical properties: (visco) elastic properties of the arterial wall and the blood viscosity. For an untethered, thin walled linearly elastic vessel filled with incompressible, inviscid liquid, the pulse wave velocity is real and equal to the Moens-Korteweg wave speed, c_0 .

$$c_0 = \sqrt{\frac{Eh}{2\rho r}} \quad (\text{Eq. 5.6})$$

If the same characteristics of the tube are maintained, but the fluid viscosity is considered, the travelling wave is attenuated and the pulse wave velocity is complex.

$$\frac{1}{c} = \frac{b - ia}{\omega} \quad (\text{Eq. 5.7})$$

where a is the attenuation constant, and b is the phase constant

The complex pulse wave velocity can be expressed using the complex wave number, k . Substituting (Eq. 5.7) and (Eq. 5.8) into (Eq. 5.9), the attenuation and phase constants can be expressed through the real and imaginary parts of k .

$$k = \frac{\omega}{c} \quad (\text{Eq. 5.8})$$

$$k = k_r + ik_i \quad (\text{Eq. 5.9})$$

$$\begin{cases} a = -k_i \\ b = k_r \end{cases} \quad (\text{Eq. 5.10})$$

Using the relationship between c and c_0 given in [87], k complex has the form given by (Eq. 5.12).

$$\frac{c_0}{c} = \sqrt{\frac{1 - \sigma^2}{1 - F_{10}}} \quad (\text{Eq. 5.11})$$

$$k = \frac{\omega\sqrt{1 - \sigma^2}}{c_0\sqrt{1 - F_{10}}} \quad (\text{Eq. 5.12})$$

Where F_{10} parameter is a function of the Womesley parameter α , σ is Poisson's ratio, introduced in the term $(1 - \sigma^2)$ to take into account the longitudinal tethering of the artery.

$$\alpha = r_0 \sqrt{\frac{\omega \rho}{\mu}} \quad (\text{Eq. 5.13})$$

$$F_{10} = \frac{\left(2J_1\left(\alpha i^{\frac{3}{2}}\right)\right)}{\alpha i^{\left(\frac{3}{2}\right)} J_0\left(\alpha i^{\frac{3}{2}}\right)} \quad (\text{Eq. 5.14})$$

where, μ is the dynamic viscosity of the blood, ρ is the blood density, r_0 is the minimum radius of the vessel, J_1 and J_0 are the Bessel functions of the first kind of order 1 respectively 0.

After separating the real and imaginary part of the complex wave number, the pressure and flow waves, travelling in a thin elastic tube, filled with viscous fluid, are given by:

$$p(\omega, z, t) = e^{-(-k_i)z} P_f e^{i(\omega t - k_r z)} + e^{(-k_i)z} P_b e^{i(\omega t + k_r z)} \quad (\text{Eq. 5.15})$$

$$Q(\omega, z, t) = e^{-(-k_i)z} Q_f e^{i(\omega t - k_r z)} + e^{(-k_i)z} Q_b e^{i(\omega t + k_r z)} \quad (\text{Eq. 5.16})$$

Using the same notation introduced in *Chapter 3*, the forward and backward travelling waves can be expressed generally in any element el , for any angular frequency ω , using real components of pressure and flow.

$$\begin{aligned} p_{el}(\omega, z, t) = & e^{-(-k_{iel})z_{el}} (P_{1el} \cos(k_{rel}z_{el} - \omega t) \\ & + P_{2el} \sin(k_{rel}z_{el} - \omega t)) \\ & + e^{(-k_{iel})z_{el}} (P_{3el} \cos(k_{rel}z_{el} + \omega t) \\ & + P_{4el} \sin(k_{rel}z_{el} + \omega t)) \end{aligned} \quad (\text{Eq. 5.17})$$

$$\begin{aligned} Q_{el}(\omega, z, t) = & e^{-(-k_{iel})z_{el}} (Q_{1el} \cos(k_{rel}z_{el} - \omega t) \\ & + Q_{2el} \sin(k_{rel}z_{el} - \omega t)) \\ & + e^{(-k_{iel})z_{el}} (Q_{3el} \cos(k_{rel}z_{el} + \omega t) \\ & + Q_{4el} \sin(k_{rel}z_{el} + \omega t)) \end{aligned} \quad (\text{Eq. 5.18})$$

The flow components can be expressed using the pressure components by replacing (Eq. 5.17) and (Eq. 5.18) into the continuity equation.

$$C' \frac{\partial p}{\partial t} + \frac{\partial Q}{\partial z} = 0 \quad (\text{Eq. 5.19})$$

Where C' is the vessel compliance

$$C' = \frac{A_0}{c^2 \rho} \quad (\text{Eq. 5.20})$$

where A_0 is the vessel unstressed area, c is the complex wave speed and ρ is the blood density

$$\begin{aligned}
& C' e^{-(-k_{iel})z} (P_{1el} \omega \sin(k_{rel}z - \omega t) - P_{2el} \omega \cos(k_{rel}z - \omega t) \\
& \quad - P_{3el} \omega \sin(k_{rel}z + \omega t) + P_{4el} \omega \cos(k_{rel}z + \omega t)) \\
& \quad - (-k_{iel}) e^{-(-k_{iel})z} (Q_{1el} \cos(k_{rel}z - \omega t) \\
& \quad + Q_{2el} \sin(k_{rel}z - \omega t)) \\
& \quad + e^{-(-k_{iel})z} (-Q_{1el} k_{rel} \sin(k_{rel}z - \omega t) \\
& \quad + Q_{2el} k_{rel} \cos(k_{rel}z - \omega t)) \\
& \quad + (-k_{iel}) e^{-k_{iel}z} (Q_{3el} \cos(k_{rel}z + \omega t) \\
& \quad + Q_{4el} \sin(k_{rel}z + \omega t)) \\
& \quad + e^{(-k_{iel})z} (-Q_{3el} k_{rel} \sin(k_{rel}z + \omega t) \\
& \quad + Q_{4el} k_{rel} \cos(k_{rel}z + \omega t)) = 0
\end{aligned} \tag{Eq. 5.21}$$

Since the above equation hold for all z and all t , the coefficients of the terms must be equal, and Q_1, Q_2, Q_3 and Q_4 for a viscous flow can be expressed as:

$$\left\{ \begin{aligned}
Q_{1el} &= \frac{C' \omega}{(-k_{iel})^2 + k_{rel}^2} (k_{rel} P_{1el} - (-k_{iel}) P_{2el}) \\
Q_{2el} &= \frac{C' \omega}{(-k_{iel})^2 + k_{rel}^2} (k_{rel} P_{1el} + (-k_{iel}) P_{2el}) \\
Q_{3el} &= \frac{C' \omega}{(-k_{iel})^2 + k_{rel}^2} (-k_{rel} P_{3el} - (-k_{iel}) P_{4el}) \\
Q_{4el} &= \frac{C' \omega}{(-k_{iel})^2 + k_{rel}^2} (k_{rel} P_{3el} - (-k_{iel}) P_{4el})
\end{aligned} \right. \tag{Eq. 5.22}$$

The viscous characteristic impedance, as determined by Womersley is given by (Eq. 5.23).

$$Z_c(\omega) = \frac{\rho c_0}{A_0 \sqrt{1 - \sigma^2}} \sqrt{1 - F_{10}} \tag{Eq. 5.23}$$

Steady component

For the steady component of the problem, the Poiseuille flow component was considered (Eq. 5.25). The resistance to flow due to blood viscosity in a cylindrical vessel of constant cross-section, R_{dc} , is inversely proportional to radius to the power of four (Eq. 5.24).

$$R_{dc} = \frac{8\mu l}{\pi r^4} \tag{Eq. 5.24}$$

$$Q_{dc} = \frac{P_{dc0} - P_{dc1}}{R_{dc}} \quad (\text{Eq. 5.25})$$

where, P_{dc0} and P_{dc1} are the steady pressure components at the vessel's inlet and outlet, and R_{dc} is the Poiseuille resistance.

PRESSURE AND FLOW SOLUTIONS FOR A BRANCHING TREE ENSEMBLE

The above formulation describes the waves in terms of forward and backward travelling components in one arbitrary element, e_l , of the branching tree. In order to characterise the pulmonary arterial tree globally and to quantify the power contained within the backward pressure wave at each generation of branches, the pressure and flow solutions for the entire ensemble are required.

For a set of given inlet and outlet boundary conditions the linear systems of branching trees are traditionally solved in the frequency domain using a recursive impedance approach. The method computes the input impedance of the tree by starting off with the impedance of the terminal branches and recursively advancing to the top of the tree, where flow or pressure is given. The input impedance and the measured flow or pressure allows the computation of the other fundamental variable at the inlet of the domain. In order to quantify the wave reflections throughout the domain, one of the motivations of the current chapter, a forward solution for the inlet pressure and flow needs to be executed to recover the pressure-flow distribution along the whole tree. Additionally, at each branch, the pressure waves need to be decomposed into their forward and backward components to compute the wave energy transmission characteristics at each bifurcation.

The development of a finite element approach is comprehensively described in this chapter, and is proposed as an alternative to the recursive method. It solves the linear system and decomposes the travelling pressure waves directly, using the same boundary conditions as those imposed in the impedance-based method.

The following sections describe the implementation of both recursive and direct fem-based methods, with a detailed description of the latter. The impedance method was used to validate the FEM approach.

5.1.1 Recursive impedance method

As introduced previously, the recursive method solves the branching tree bottom-up, starting with the outlet boundary conditions and computing, by recursive summation across the bifurcations, the impedance at the root of the tree. The computed impedance relates pressure and flow at the inlet of the domain. Therefore, providing one measurements (flow or pressure) is sufficient for retrieving the other.

$$Z_{in}(\omega) = \frac{P(\omega)}{Q(\omega)} \quad (\text{Eq. 5.26})$$

Input impedance of a single vessel

Considering a single branch of the tree, of length l , as in Figure 5.2, with the complex characteristic impedance Z_c , the impedance at the inlet, Z_1 (node 1) can be computed from the branch terminal impedance, Z_0 (node 2).

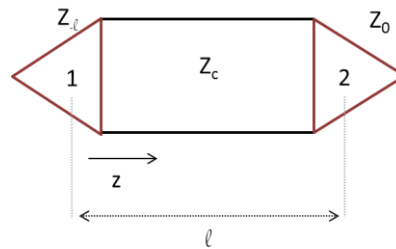


Figure 5.2 Computation of the input impedance, Z_1 for a vascular element using the characteristic Z_c and terminal impedance Z_0

For the ease of the derivation, the reference point ($z=0$) is taken at node 2, whereas at node 1, $z=-l$.

The impedance at node 2 ($z=0$), can be written as the ratio between harmonic pressure and flow (Eq. 5.27).

$$Z_0 = \frac{p_0}{Q_0} = \frac{P_f + P_b}{Q_f + Q_b} \quad (\text{Eq. 5.27})$$

Using the relationship between forward pressure and flow components and characteristic impedance, the outlet impedance Z_0 can be expressed as in (Eq. 5.28).

$$Z_0 = \frac{Z_c \left(1 + \frac{P_b}{P_f} \right)}{1 - \frac{P_b}{P_f}} \quad (\text{Eq. 5.28})$$

From (Eq. 5.28), the ratio of the backward to forward pressure amplitude can be written as (Eq. 5.29).

$$\frac{P_b}{P_f} = \frac{\left(\frac{Z_0}{Z_c} - 1\right)}{\left(\frac{Z_0}{Z_c} + 1\right)} \quad (\text{Eq. 5.29})$$

Similarly, using (Eq. 5.17), (Eq. 5.18) and (Eq. 5.26) the impedance in node 2, at $z=-l$ can be derived (Eq. 5.30).

$$Z_{-l} = \frac{p_{-l}}{Q_{-l}} = \frac{P_f e^{-(-k_i)(-l)} e^{-ik_r(-l)} + P_b e^{(-k_i)(-l)} e^{ik_r(-l)}}{Q_f e^{-(-k_i)(-l)} e^{-ik_r(-l)} + Q_b e^{(-k_i)(-l)} e^{ik_r(-l)}} \quad (\text{Eq. 5.30})$$

Replacing the P_b/P_f ratio from (Eq. 5.29), the inlet impedance Z_{-l} can be expressed as a function of outlet impedance Z_0 and characteristic impedance Z_c .

$$Z_{-l} = \frac{Z_c \left(1 + \frac{Z_0 - Z_c}{Z_0 + Z_c} e^{-2ik_r l} e^{-2(-k_i)l}\right)}{\left(1 - \frac{Z_0 - Z_c}{Z_0 + Z_c} e^{-2ik_r l} e^{-2(-k_i)l}\right)} \quad (\text{Eq. 5.31})$$

Using the definition for the reflection coefficient (Eq. 5.32) provided in [2], the relationship of the input impedance of a straight elastic tube of length l , with known complex characteristic impedance Z_c and distal reflection coefficient, R_f is given by (Eq. 5.32).

$$R_f = \frac{Z_0 - Z_c}{Z_0 + Z_c} \quad (\text{Eq. 5.32})$$

$$Z_{-l} = \frac{Z_c \left(1 + R_f e^{-2ik_r l} e^{-2(-k_i)l}\right)}{\left(1 - R_f e^{-2ik_r l} e^{-2(-k_i)l}\right)} \quad (\text{Eq. 5.33})$$

Outlet boundary conditions for the recursive method

Given relationship (Eq. 5.31) or (Eq. 5.33), the input impedance of a single vessel Z_{-l} , can be computed, provided that the outlet boundary condition is specified (Z_0 or R_f). There are several conditions which can be implemented:

- (i) $Z_0=0$

The condition of null terminal impedance is frequently implemented as boundary condition [167], [89],[90], [44] for structured trees. It is equivalent to a zero distal pressure condition and is often referred in the literature [2] as ‘open end’ – the tube with fluid opens into a huge reservoir.

According to (Eq. 5.32), the distal reflection coefficient, $R_f=-1$.

(ii) $Z_0 = \infty$

The condition of infinite impedance is equivalent to a zero flow distal condition and is referred to in the literature as 'closed end'- the tube with fluid is completely obstructed.

The equivalent distal reflection coefficient, $R_f = +1$.

Both of the conditions produce total wave reflection of the incident wave. The wave reflected from an 'open end' condition will be 180° out of phase with the incident wave, producing a zero total wave.

(iii) $Z_0 = Z_c$

The condition of the terminal impedance being equal to the characteristic impedance is equivalent to a pure-transmission boundary, with no reflections occurring at the interface.

A pure-transmission boundary will have a zero reflection coefficient, $R_f = 0$.

(iv) An arbitrarily Z_0 value, excepting the ones discussed above

The pure reflection and pure transmission boundary conditions might be regarded as limit conditions. In practice there will be a finite value of the terminal impedance that best represents the actual boundary condition in the vascular tree, and in general it will not be equal to the characteristic impedance. The patient-specific terminal impedance could be computed if measurements of both flow and pressure at the distal end were available, but in practice they are not.

Bifurcation conditions

In order to build the way up to the top of the tree by starting with the outlet impedance (or reflection coefficient), the transmission of flow and pressure waves across bifurcation has to be analysed.

In general in fluid mechanics systems the analysis is based on conservation laws. For incompressible flow the conserved quantities are mass and momentum. For the bifurcation it is natural to apply conservation of mass and this is represented by (Eq. 5.35). Conservation of momentum, expressed simply in one dimension under steady flow conditions by Bernoulli's law, dictates that total pressure (dynamic plus static) is conserved. Across a bifurcation, the increase in area ($A_p < A_{d1} + A_{d2}$), which is one of the conditions imposed on the

structured tree, determines a decrease in velocity. Therefore, in order to balance the decrease of dynamic pressure, the static pressure should increase. This would be nevertheless contradictory to the real system behavior, since generally the pressure decreases along the vascular network. The decrease of pressure is partly due to the viscous losses that occurs along the lengths of the vessels, and is represented in the model, but also partly due to losses at the bifurcation itself, associated with local flow structures and vorticity, that are not represented in the model. It would be possible to develop a model system that ensures conservation of total pressure (the model would be inherently nonlinear due to the convective acceleration term), with an empirical loss coefficient at each bifurcation, but in the current work the analysis is based on continuity of static pressure. Olufsen et al. [167] included in their analysis a loss coefficient for all the bifurcations in the systemic circulation. For simplicity, other studies[45], [44] using structured trees are in general neglecting this aspect, and only the static pressure is conserved across the bifurcation. The same approach is adopted in here, and the pressure relationship given by (Eq. 5.34) was used.

$$p_p(\omega, l, t) = p_{d_1}(\omega, 0, t) = p_{d_2}(\omega, 0, t) \quad (\text{Eq. 5.34})$$

$$q_p(\omega, l, t) = q_{d_1}(\omega, 0, t) + q_{d_2}(\omega, 0, t) \quad (\text{Eq. 5.35})$$

From (Eq. 5.34) and (Eq. 5.35) a new relationship, relating the input impedance of the daughter branches to the terminal impedance of the parent branch, Z_{p_0} can be derived. Equation (Eq. 5.36), states that the terminal impedance of the parent vessel (at $z=0$) equals the sum of input impedance of the two daughters (at $z=l$) taken in a parallel configuration.

$$Z_{p_0} = \frac{Z_{d1-l} + Z_{d2-l}}{Z_{d1-l} Z_{d2-l}} \quad (\text{Eq. 5.36})$$

Inlet boundary conditions

Once the input impedance of the tree is retrieved, either measured pressure or flow can be applied to compute the other fundamental variable. Both inlet conditions were implemented for the direct method described on the following sections and therefore both have been also considered for the input impedance.

5.1.2 Direct method

The method is described by building-up the system's solution from a single branch (element) to a bifurcation (three elements connected at a nodal point) and finishing with the whole branching ensemble.

5.1.2.1 Direct method solver based on element's degrees of freedom

Single element

The pressure and flow solutions, together with their forward and backward components, for a single thin elastic tube filled with viscous fluid were specified in Section 0 of this chapter. By replacing the z value in (Eq. 5.17) with 0 and L respectively, the total wave pressure as well as the backward and forward components at the two nodes of the element can be derived. To avoid any terminology confusion during the analysis, the two components of any wave measured locally in the element will be referred as the wave component entering the node (having the subscript *in*), wave component exiting the node (subscript *out*).

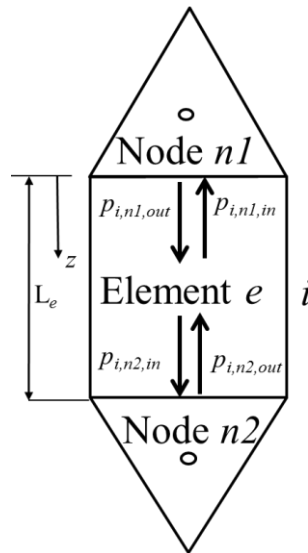


Figure 5.3 Wave direction in one element

At each of the two nodes, a pressure component enters the one (subscript *in*) and another exists the node (subscript *out*). The sum of the two components at *node 1* equals the summed pressure at the inlet of the element ($z=0$). The sum of the two components at *node 2* equals the total pressure at the outlet of the element ($z=L_e$).

For the element ei in Figure 5.3, the inlet and outlet pressures at the two nodal interfaces, $p_{ei,n1,out}(\omega, z, t)$, $p_{ei,n1,in}(\omega, z, t)$, $p_{ei,n2,out}(\omega, z, t)$ and $p_{ei,n2,in}(\omega, z, t)$ can be derived from the total element pressure, $p_{ei}(\omega, z, t)$ given by (Eq. 5.17).

$$p_{ei,n1,out}(\omega, 0, t) = P_{ei_1} \cos \omega t - P_{ei_2} \sin \omega t \quad (\text{Eq. 5.37})$$

$$p_{ei,n1,in}(\omega, 0, t) = P_{ei_3} \cos \omega t + P_{ei_4} \sin \omega t \quad (\text{Eq. 5.38})$$

$$\begin{aligned}
 & p_{ei,n2,in}(\omega, L_{ei}, t) \\
 &= e^{-(k_{iei})z_{ei}}(P_{ei_1} \cos k_{r_{ei}} L_{ei} \\
 &+ P_{ei_2} \sin k_{r_{ei}} L_{ei}) \cos \omega t \quad \text{(Eq. 5.39)} \\
 &+ e^{-(k_{iei})z_{ei}}(P_{ei_1} \sin k_{r_{ei}} L_{ei} \\
 &- P_{e_2} \cos k_{r_{ei}} L_{ei}) \sin \omega t
 \end{aligned}$$

$$\begin{aligned}
 & p_{ei,n2,out}(\omega, L_{ei}, t) \\
 &= e^{(k_{iei})z_{ei}}(P_{ei_3} \cos k_{r_{ei}} L_{ei} + P_{ei_4} \sin k_{r_{ei}} L_{ei}) \cos \omega t \quad \text{(Eq. 5.40)} \\
 &+ e^{(k_{iei})z_{ei}}(-P_{ei_3} \sin k_{r_{ei}} L_{ei} + P_{e_4} \cos k_{r_{ei}} L_{ei}) \sin \omega t
 \end{aligned}$$

Three element bifurcation

For a single element of the tree, the transmission characteristic, represented by the wave speed, is constant along it. At each bifurcation, the wave entering the node (incident wave) encounters a change of transmission characteristics given by the added contribution of the two emerging branches. As a consequence, at the interface, part of the wave is reflected back into the element (interface reflected wave) and part of the wave is transmitted into the emerging branches (interface transmitted wave).

In general, for a system made up from three media, corresponding to a three element bifurcation system, which obey the bifurcation boundary conditions discussed in *Section 5.1.1 Bifurcation conditions*

The continuity of pressure and flow conservation at the bifurcation can be written as follows:

$$p_{inc}(\omega, L, t) + p_{ref}(\omega, L, t) = p_{trn1}(\omega, L, t) = p_{trn2}(\omega, L, t) \quad \text{(Eq. 5.41)}$$

$$Q_{inc}(\omega, L, t) + Q_{ref}(\omega, L, t) = Q_{trn1}(\omega, L, t) + Q_{trn2}(\omega, L, t) \quad \text{(Eq. 5.42)}$$

Where $p_{inc}(\omega, L, t)$, $p_{ref}(\omega, L, t)$, $p_{trn1}(\omega, L, t)$ and $p_{trn2}(\omega, L, t)$ and $Q_{inc}(\omega, L, t)$, $Q_{ref}(\omega, L, t)$, $Q_{trn1}(\omega, L, t)$ and $Q_{trn2}(\omega, L, t)$ are the incident, reflected and transmitted pressure and flow waves. The subscripts 1 and 2 are corresponding to the two emerging branches. The amount of the pressure wave reflected at the interface is given by the bifurcation reflection and transmission coefficients, γ_r and γ_t .

$$p_{ref}(\omega, L, t) = \gamma_r p_{inc}(\omega, L, t) \quad \text{(Eq. 5.43)}$$

$$p_{trn1}(\omega, L, t) = p_{trn2}(\omega, L, t) = \gamma_t p_{inc}(\omega, L, t) \quad \text{(Eq. 5.44)}$$

Making the substitutions into (Eq. 5.41) results:

$$\gamma_t = \gamma_r + 1 \quad \text{(Eq. 5.45)}$$

Using (Eq. 5.41), (Eq. 5.42) and the pressure-flow relationship given by the characteristic impedance, the reflection coefficient γ_r can be generally computed as:

$$\gamma_r = \frac{Z_{c_{parent}} - Z_{c_{daughter}}^p}{Z_{c_{parent}} + Z_{c_{daughter}}^p} \quad (\text{Eq. 5.46})$$

Where $Z_{c_{parent}}$ is the characteristic impedance of the parent vessel, and $Z_{c_{daughter}}^p$ is the characteristic impedance of the two daughter branches added in parallel.

In the general case, for a system made up from three media i, j and k , with the tree elements ei, ej and ek connected by node n , the waves are entering and leaving the interface in all three directions, as illustrated in Figure 5.4 a. Each pressure wave entering the node is an incident wave which is partly reflected back into its own medium, with the appropriate reflection coefficient, and partly transmitted into the other two media.

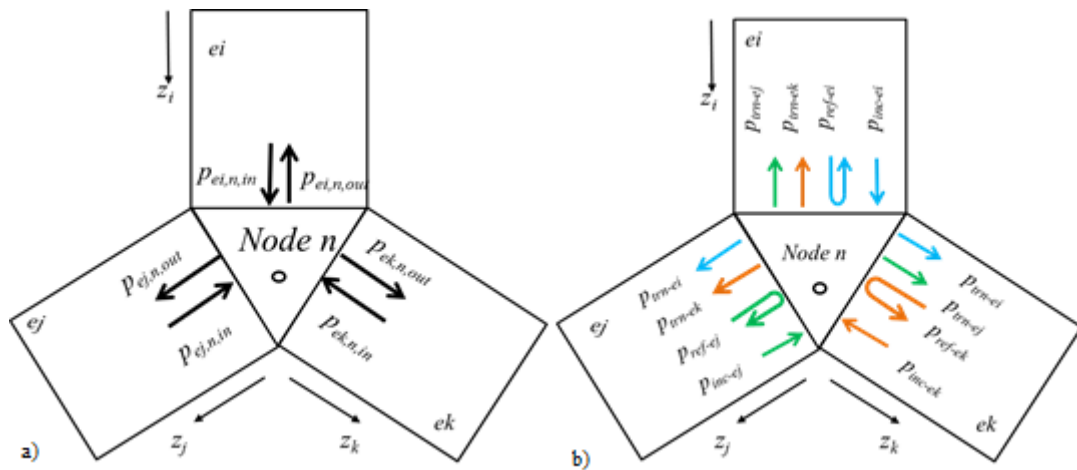


Figure 5.4 Pressure wave components at the interface of a three media system described in terms of a) inlet and outlet components b) incident, transmitted and reflected

The *in* and *out* pressure components of figure a) are divided into *inc*, *trn* and *ref* components in figure b). In each compartment of figure b) the sum of the components orientated in the direction of z equals the component with the same direction and compartment from a). Similarly for the components of which direction opposes z . Each component is coloured according to the incident's wave compartment.

Therefore, the total wave leaving the node is a sum of waves reflected at the interface and transmitted from the other two media (Eq. 5.47) as shown in Figure 5.4 b.

$$\begin{Bmatrix} p_{ei,n,out} \\ p_{ej,n,out} \\ p_{ek,n,out} \end{Bmatrix} - \begin{bmatrix} \gamma_{ii} & \gamma_{ij} & \gamma_{ik} \\ \gamma_{ji} & \gamma_{jj} & \gamma_{jk} \\ \gamma_{ki} & \gamma_{kj} & \gamma_{kk} \end{bmatrix}^T \begin{Bmatrix} p_{ei,n,in} \\ p_{ej,n,in} \\ p_{ek,n,in} \end{Bmatrix} = 0 \quad (\text{Eq. 5.47})$$

,where the γ coefficients correspond to ratios of pressures in waves travelling from medium i to medium j .

Six equations (3 from the cosine and 3 from the sine components) describe the wave behaviour in terms of transmitted and reflected components at the interface (Eq. 5.48).

$$\begin{aligned}
 & \left\{ \begin{array}{c} e^{-(-k_{iei})L_{ei}}(P_{ei_3} \cos k_{rei}L_{ei} + P_{ei_4} \sin k_{rei}L_{ei}) \\ P_{ej_1} \\ P_{ek_1} \end{array} \right\} \\
 & - \begin{bmatrix} \gamma_{ii} & \gamma_{ij} & \gamma_{ik} \\ \gamma_{ji} & \gamma_{jj} & \gamma_{jk} \\ \gamma_{ki} & \gamma_{kj} & \gamma_{kk} \end{bmatrix}^T \left\{ \begin{array}{c} e^{(-k_{iei})L_{ei}}(P_{ei_1} \cos k_{rei}L_{ei} + P_{ei_2} \sin k_{rei}L_{ei}) \\ P_{ej_3} \\ P_{ek_3} \end{array} \right\} \\
 & = 0 \\
 & \left\{ \begin{array}{c} e^{-(-k_{iei})L_{ei}}(-P_{ei_3} \sin k_{rei}L_{ei} + P_{ei_4} \cos k_{rei}L_{ei}) \\ -P_{ej_2} \\ -P_{ek_2} \end{array} \right\} \tag{Eq. 5.48} \\
 & - \begin{bmatrix} \gamma_{ii} & \gamma_{ij} & \gamma_{ik} \\ \gamma_{ji} & \gamma_{jj} & \gamma_{jk} \\ \gamma_{ki} & \gamma_{kj} & \gamma_{kk} \end{bmatrix}^T \left\{ \begin{array}{c} e^{(-k_{iei})L_{ei}}(P_{ei_1} \sin k_{rei}L_{ei} - P_{ei_2} \cos k_{rei}L_{ei}) \\ P_{ej_4} \\ P_{ek_4} \end{array} \right\} \\
 & = 0
 \end{aligned}$$

For a three element system, there are twelve (4x3) unknowns. So far, six equations have been developed to describe the transmission characteristics at the interface. In order to close the system of equations, another six equations are required: two boundary conditions are available at each free end of the elements.

Inlet boundary conditions

The direct method was implemented for the two possible inlet boundaries: inlet pressure and inlet flow.

For each inlet boundary condition, two equations are generated by setting $z=0$ in (Eq. 5.17) or inlet pressure or inlet flow respectively, and equating the sine and cosine coefficients. For the three element system exemplified above, the inlet equations correspond to medium i are:

a) Inlet pressure

$$P_{e1_1} + P_{e1_3} = P_{0c} \tag{Eq. 5.49}$$

$$-P_{e1_2} + P_{e1_4} = P_{0s}$$

b) Inlet flow

$$\frac{P_{e1_1}}{Z_{c1}} - \frac{P_{e1_3}}{Z_{c1}} = Q_{0c}$$

(Eq. 5.50)

$$\frac{-P_{e1_2}}{Z_{c1}} - \frac{P_{e1_4}}{Z_{c1}} = Q_{0s}$$

Outlet boundary conditions

At the outlet of any terminal element e , the relationship between the pressure entering and reflected by the outlet boundary can be expressed using the reflection coefficient γ_{ee} (Eq. 5.48).

$$p_{e,n,out} - \gamma_{ee} p_{e,n,in} = 0 \quad (\text{Eq. 5.51})$$

Where γ_{ee} can take the same values as the reflection coefficient R_f specified for the recursive impedance method: $\gamma_{ee} = 1/-1$ for total wave reflection, 0 for total wave transmission and some intermediate value on the interval $(-1, 1)$, excepting 0 for partial transmission and partial reflection.

Expanding and equating the sine and cosine coefficients of (Eq. 5.51), creates another two equations for each outlet (Eq. 5.52). For the above three element system, the equations correspond to media j and k are:

$$\begin{aligned} e^{(-k_{ie})L_e} (P_{e_3} \cos k_{r_e} L_e + P_{e_4} \sin k_{r_e} L_e) \\ - \gamma_{ee} e^{(-k_{ie})L_e} (P_{e_1} \cos k_{r_e} L_e + P_{e_2} \sin k_{r_e} L_e) \\ = 0 \end{aligned}$$

$$\begin{aligned} e^{(-k_{ie})L_e} (-P_{e_3} \sin k_{r_e} L_e + P_{e_4} \cos k_{r_e} L_e) \\ - \gamma_{ee} e^{(-k_{ie})L_e} (P_{e_1} \sin k_{r_e} L_e - P_{e_2} \cos k_{r_e} L_e) \\ = 0 \end{aligned} \quad (\text{Eq. 5.52})$$

Linear system for direct element P solution

Using the relationships derived for pressure at the interface (Eq. 5.48), inlet (Eq. 5.49) and outlet (Eq. 5.52), a linear system of equations, which directly computes all the element coefficients $P_{e,1}$, $P_{e,2}$, $P_{e,3}$ and $P_{e,4}$ can be constructed .

Once the coefficients $P_{e,1}$, $P_{e,2}$, $P_{e,3}$ and $P_{e,4}$ are known, the proportion of the power of the backward travelling wave in each branch that originates from the reflection site and from the two emerging daughters can readily be computed.

Although forward and backward wave components can be retrieved directly, without further post-processing, the method is much more computationally expensive in comparison to the recursive impedance method. Nevertheless, the results at the inlet of the domain obtained by the direct method are identical to the ones returned by the latter. However, as previously stated, the recursive impedance method recovers the solution at the top of the tree and requires further processing to address the type of problems where the solution is required along the entire domain.

A definite computational advantage of the recursive impedance method is given by the presence of self-similar structures. As implemented by Olufsen *et al* [167], the impedance of a tree with a $\beta_1\beta_2$ root branch is identical for all the $\beta_1\beta_2$ existing trees and the computation is required to be performed only once. As implemented above, the direct proposed method does not benefit from this advantage. In order to reduce the computational cost of the direct method the equations were re-cast and element degrees of freedom were transformed into nodal degrees of freedom. An efficient method designed to solve large problems with self-similarities is the Superelement [169] implementation of the Finite Element Method (FEM)[170].

5.1.2.2 Direct method solver based on nodal degrees of freedom

FEM

In FEM the continuous domain is discretised into finite elements with known geometric and material properties. Similarly, the branching tree can be broke down into vascular elements with length, radius, wall and blood properties known. The forces and displacements at the nodal points of the finite elements can be regarded as the pressure and flow at the inlet and outlet of a vascular element.

The general equation which describes the FEM system is:

$$[k_{FEM}^e]\{u\} = \{F^e\} \quad (\text{Eq. 5.53})$$

Where, k_{FEM}^e is the element stiffness matrix (defined by the element properties), u is the nodal displacement vector and F^e is element force vector.

Similarly, for a vascular element it can be written:

$$[k]\{p\} = \{Q\} \quad (\text{Eq. 5.54})$$

Where k is the stiffness matrix of the vascular element, p is the nodal pressure and Q is the nodal flow.

Previously, the equations have been developed with the $(P_{e_1}, P_{e_2}, P_{e_3}, P_{e_4})$ in each of the elements as the fundamental degrees of freedom. The equations can be however re-cast to use nodal degrees of freedom rather than element degrees of freedom. Writing the nodal equations for n_1 and n_2 and equating the coefficients, the element degrees of freedom (dof) are translated into nodal dof.

Considering the element in Figure 5.3, the oscillatory pressure component at nodes 1 and 2 can be written using both the cosine and sine components and expanded elements components.

Oscillatory component

Node 1

$$p_{n_1}(\omega, 0, t) = p_{c_{n_1}} \cos \omega t + p_{s_{n_1}} \sin \omega t \quad (\text{Eq. 5.55})$$

$$p_{n_1}(\omega, 0, t) = (P_{e_1} + P_{e_3}) \cos \omega t + (-P_{e_2} + P_{e_4}) \sin \omega t \quad (\text{Eq. 5.56})$$

Node 2

$$p_{n_2}(\omega, L_e, t) = p_{c_{n_2}} \cos \omega t + p_{s_{n_2}} \sin \omega t \quad (\text{Eq. 5.57})$$

$$\begin{aligned} & p_{n_2}(\omega, L_e, t) \\ &= \left(\begin{array}{l} e^{k_{i_e} L_e} (P_{e_1} \cos k_{r_e} L_e + P_{e_2} \sin k_{r_e} L_e) \\ + e^{-k_{i_e} L_e} (P_{e_3} \cos k_{r_e} L_e + P_{e_4} \sin k_{r_e} L_e) \end{array} \right) \cos \omega t \\ &+ \left(\begin{array}{l} e^{k_{i_e} L_e} (P_{e_1} \sin k_{r_e} L_e - P_{e_2} \cos k_{r_e} L_e) \\ + e^{-k_{i_e} L_e} (-P_{e_3} \sin k_{r_e} L_e + P_{e_4} \cos k_{r_e} L_e) \end{array} \right) \sin \omega t \end{aligned} \quad (\text{Eq. 5.58})$$

Using the above expressions (Eq. 5.55), (Eq. 5.56), (Eq. 5.57), (Eq. 5.58), a general equation relating nodal dof ($p_{c_{n_1}}, p_{s_{n_1}}, p_{c_{n_2}}$ and $p_{s_{n_2}}$) to element dof ($P_{e_1}, P_{e_2}, P_{e_3}, P_{e_4}$) is given by (Eq. 5.59).

$$\{p\} = [T]\{P_e\} \quad (\text{Eq. 5.59})$$

where

$$\{p\} = \begin{Bmatrix} p_{cn1} \\ p_{sn1} \\ p_{cn2} \\ p_{sn2} \end{Bmatrix} \quad (\text{Eq. 5.60})$$

$$[T] = \begin{bmatrix} 1 & 0 & 0 & 0 \\ 0 & -1 & 0 & 0 \\ e^{k_{ie}L_e} \cos(k_{re}L_e) & e^{k_{ie}L_e} \sin(k_{re}L_e) & e^{-k_{ie}L_e} \cos(k_{re}L_e) & e^{-k_{ie}L_e} \sin(k_{re}L_e) \\ e^{k_{ie}L_e} \sin(k_{re}L_e) & -e^{k_{ie}L_e} \cos(k_{re}L_e) & -e^{-k_{ie}L_e} \sin(k_{re}L_e) & -e^{-k_{ie}L_e} \cos(k_{re}L_e) \end{bmatrix} \quad (\text{Eq. 5.61})$$

$$\{P_e\} = \begin{Bmatrix} P_{e1} \\ P_{e2} \\ P_{e3} \\ P_{e4} \end{Bmatrix} \quad (\text{Eq. 5.62})$$

The distribution of flow, Q , within the element takes the same form as the distribution of p , but with an impedance, pre-multiplying, matrix.

$$\{Q'\} = [T]\{Q_e\} \quad (\text{Eq. 5.63})$$

where

$$\{Q_e\} = [Z]\{P_e\} \quad (\text{Eq. 5.64})$$

where Z is the matrix of the coefficients relating flow to pressure, for a viscous fluid.

$$[Z] = \frac{C'\omega}{(-k_{iel})^2 + k_{rel}^2} \begin{bmatrix} k_{rel} & -(-k_{iel}) & 0 & 0 \\ k_{rel} & (-k_{iel}) & 0 & 0 \\ 0 & 0 & -(-k_{rel}) & (-k_{iel}) \\ 0 & 0 & -k_{rel} & (-k_{iel}) \end{bmatrix} \quad (\text{Eq. 5.65})$$

Therefore, the expression of the nodal flow can be written as follows:

$$\{Q'\} = [T][Z][T]^{-1}\{p\} \quad (\text{Eq. 5.66})$$

The flow through each bifurcation is unknown, but by the simple trick of inverting the sign of the flow at the inlet to each element, making the flow vector point out the domain, continuity dictates that the net flow is zero at all the internal nodes of the domain, and thus the assembly of the right hand side vector becomes trivial.

$$\{Q\} = [F][T][Z][T]^{-1}\{p\} \quad (\text{Eq. 5.67})$$

where F is matrix inverting the flow sign.

$$[F] = \begin{bmatrix} -1 & 0 & 0 & 0 \\ 0 & -1 & 0 & 0 \\ 0 & 0 & 1 & 0 \\ 0 & 0 & 0 & 1 \end{bmatrix} \quad (\text{Eq. 5.68})$$

Equating (Eq. 5.54) with (Eq. 5.67) returns the expression for the stiffness matrix of a vascular element (Eq. 5.69) equivalent to a FEM representation. The stiffness matrix of entire system is given by the assembly of all vascular elements into a global stiffness matrix, K .

$$[k] = [F][T][Z][T]^{-1} \quad (\text{Eq. 5.69})$$

For a single element, e_i , placed between the local nodes n_1 and n_2 , the solution is given by (Eq. 5.70). The same relationship can be written for any element of the branching tree. For simplicity in the algebra presented above, at each node only one degree of freedom was considered. However, one should keep in mind that (Eq. 5.67) was deduced for two degrees of freedom per each node, a cosine and a sine component of pressure and flow, and therefore the following relationships, including the element solution (Eq. 5.70), have two dof per node.

$$\begin{bmatrix} k_{n_1 n_1}^{e_i} & k_{n_1 n_2}^{e_i} \\ k_{n_2 n_1}^{e_i} & k_{n_2 n_2}^{e_i} \end{bmatrix} \begin{Bmatrix} p_{n_1} \\ p_{n_2} \end{Bmatrix} = \begin{Bmatrix} Q_{n_1} \\ Q_{n_2} \end{Bmatrix} \quad (\text{Eq. 5.70})$$

In order to obtain the solution of the whole tree, the individual elements are assembled globally following the methodology employed by the FEM method. At each internal node, the displacements remain constant, which is the same condition as pressure conservation, and the forces are added-up, a condition equivalent with the flow continuity. By changing the orientation of the flow vector at the inlet, for each local element, the flow entering the downstream node in the parent branch is cancelled out by the sum of the flows entering upstream nodes in the daughter branches, reducing to zero all the internal flows.

The assembly of the global stiffness matrix is illustrated in Figure 5.5 for the first three branches at the top of the tree. The values of the element's stiffness matrix corresponding to an internal node add up, whereas the ones of the terminal and first nodes are placed into the global matrix unchanged.

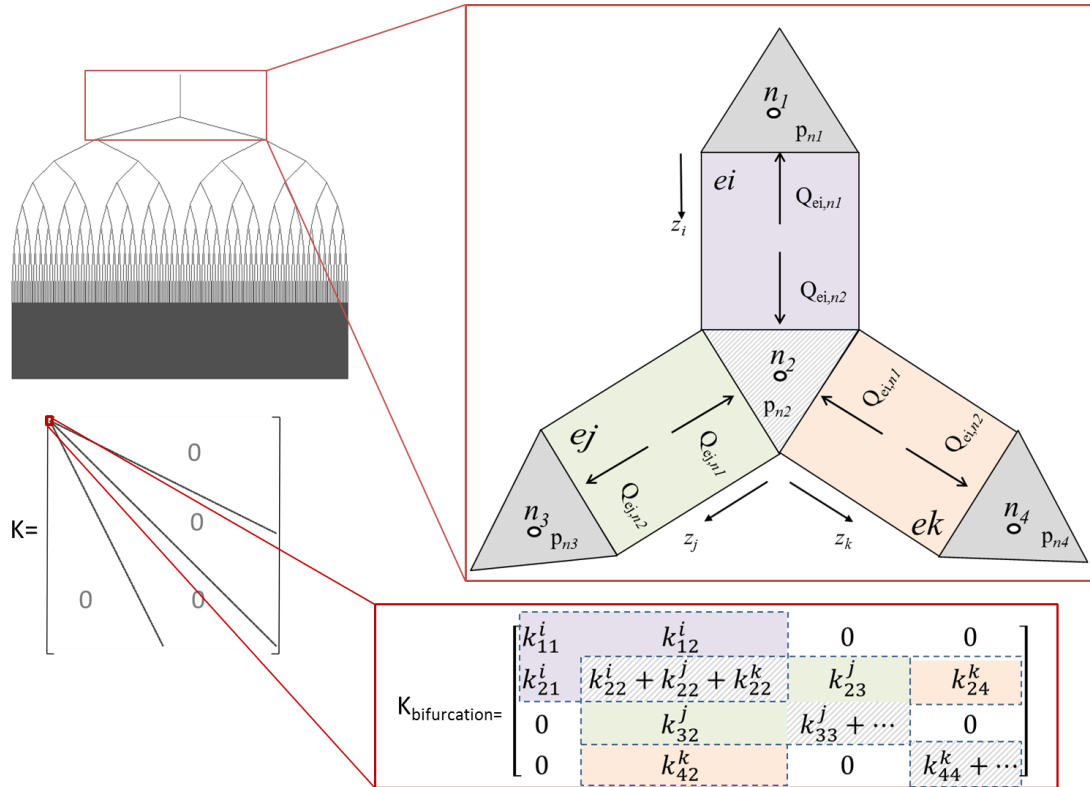


Figure 5.5 Populating the global stiffness matrix with the individual element stiffness
 The first bifurcation of a tree, with the parent and two daughter branches, is considered in detail. The values of the element's stiffness matrix corresponding to an internal node are added up in the global matrix, whereas the ones of the terminal and first nodes are unchanged.

Solving the system requires the specification of the known boundary conditions, followed by the appropriate partitioning of the stiffness, flow and pressure matrices. The pressure and flow matrices were divided into inlet, internal and external blocks, whereas the stiffness matrix is partitioned into 3x3 blocks (Eq. 5.71). The dimensions of each block are determined by the number of nodes and corresponding nodal degrees of freedom per node. Therefore, each block contained by p and Q has one column and two times (2 nodal dof) the number of afferent nodes, rows. Consequently, the latter dictate the size of the k-blocks.

The manipulation on the direction of flow in the element $Q_{internal}=0$, reduced the number of unknowns. Specifying any two boundary conditions is sufficient to solve the linear system of equations.

$$\begin{bmatrix} k_{aa} & k_{ab} & k_{ac} \\ k_{ba} & k_{bb} & k_{bc} \\ k_{ca} & k_{cb} & k_{cc} \end{bmatrix} \begin{Bmatrix} p_{inlet} \\ p_{internal} \\ p_{outlet} \end{Bmatrix} = \begin{Bmatrix} -Q_{inlet} \\ Q_{internal} \\ Q_{outlet} \end{Bmatrix} = \begin{Bmatrix} -Q_{inlet} \\ 0 \\ Q_{outlet} \end{Bmatrix} \quad (\text{Eq. 5.71})$$

Inlet boundary conditions

The zero pressure outlet boundary condition eliminates all the terms containing P_{external} and simplifies the system's equations. Equations (Eq. 5.72) and (Eq. 5.74) correspond to an inlet pressure boundary conditions, whereas, for an inlet flow boundary condition equations (Eq. 5.73) and (Eq. 5.74) are applied.

a) Inlet pressure

$$\{Q_{\text{inlet}}\} = - ([k_{aa}] + [k_{ab}][k_{bb}]^{-1}[-k_{ba}])\{P_{\text{inlet}}\} \quad (\text{Eq. 5.72})$$

b) Inlet flow

$$\{P_{\text{inlet}}\} = - ([k_{aa}] + [k_{ab}][k_{bb}]^{-1}[-k_{ba}])^{-1}\{Q_{\text{inlet}}\} \quad (\text{Eq. 5.73})$$

$$\{P_{\text{internal}}\} = [k_{bb}]^{-1}[-k_{ba}]\{P_{\text{inlet}}\} \quad (\text{Eq. 5.74})$$

$$\{Q_{\text{external}}\} = [k_{bc}]\{P_{\text{inlet}}\} + [k_{bb}]\{P_{\text{internal}}\}$$

Steady component

As stated in the introduction to this chapter, for the quantification of the reflected wave power the oscillatory solution is sufficient. However, the computation of the DC component is briefly outlined in order to demonstrate that the proposed method benefits from the same features as the recursive impedance method, returning identical results.

Using the relationships given by the Poiseuille resistance (Eq. 5.24) and flow (Eq. 5.25), and the condition that the steady state flow component is constant at the two nodes of a vascular element, FEM solution can be formulated as (Eq. 5.75).

$$\frac{1}{R_{dc}} \begin{bmatrix} 1 & -1 \\ 1 & -1 \end{bmatrix} \begin{Bmatrix} P_{dc1} \\ P_{dc2} \end{Bmatrix} = \begin{Bmatrix} Q_{dc1} \\ Q_{dc2} \end{Bmatrix} \quad (\text{Eq. 5.75})$$

$$F_{dc} = \begin{bmatrix} -1 & 0 \\ 0 & 1 \end{bmatrix} \quad (\text{Eq. 5.76})$$

Pre-multiplying the left-hand-side of (Eq. 5.75) by the matrix F_{dc} , the sign of the flow entering the top node is changed and the global linear system can be assembled and solved using the same methods as implemented for the oscillatory components.

The above equations describe the formulation of the branching tree transmission characterisation in terms of nodal degrees of freedom. For a typical tree representing the pulmonary arterial network with a root diameter of 4 cm, a terminal diameter of 0.5 mm, bifurcations ratios of $\beta_1=0.8$ and $\beta_2=0.6$ the number of branches is 131932, and the whole

system has 263864 degrees of freedom. Similar values for the branching ratios were used [44], [45] to represent the asymmetric character of the pulmonary arterial tree. Although the root radius used in these studies is slightly smaller than the above proposed 2 cm (since the used structured trees were attached to the main pulmonary arteries modelled non-linearly) their minimum radius reaches values down to 0.05 mm.

Even taking advantage of the sparsity of the stiffness matrix, the storage and computational requirements for solution of the system of equations remains very challenging. However, in order to understand how far this technique can 'see' (as one of the direct applications described in this chapter), it is important to be able to implement trees of comparable size with the ones previously documented.

The following section explains the concept and implementation of the *Superelement* FEM approach, which by taking advantage of the tree self-similarities, significantly reduces the computation time.

Superelement

A superelement is defined as an ensemble of multiple finite elements which can form an independent structure and can be regarded as a single element [169]. The concept is frequently used in the aerospace engineering. The structural analysis of the main components of an aircraft can be performed independently, in parallel by different specialist teams. Moreover, due to the often encountered symmetric components, the workload can be reduced by solving the self-similar structures only once.

The fundamentals of the method consist in condensing the interior degrees of freedom of the superelement to boundary freedoms in order to reduce the size of the problem. The interior degrees of freedom are defined at the nodes which do not interact with any elements of the main structure.

The Superelement method is implemented by dividing the ensemble corresponding to a tree generated with the r_0 , β_1 , β_2 and r_{\min} parameters into a main domain with attached sub-trees. The main domain is defined in such way that the last generation g_m , has a complete number of terminal branches. All the branches attached to the terminal node of the main domain belong to the first branch of a sub-tree and the terminal nodes of the main domain represent the root nodes of the sub-trees. Each sub-tree is the equivalent of a super-element and the interior degrees of freedom of the Superelement (found at the terminal and internal nodes of the sub-tree) are condensed to the boundary freedoms (the root node of the subtree).

Figure 5.6 shows an example of a branching tree separated into a main subdomain and Superelement structures (dotted marking).

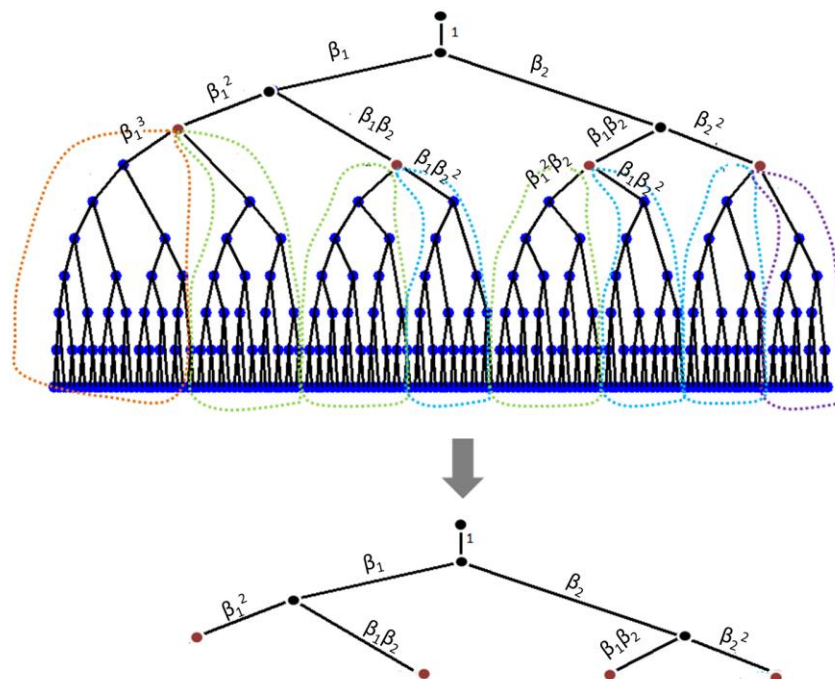


Figure 5.6 Schematic of the interior degrees of freedom condensation in the Superelement approach

Top: the interior degrees of freedom of the superelement (blue) are condensed to the boundary degrees of freedom (red). The condensation process takes place only once for each self-similar tree. Upon condensation, the boundary freedoms concentrate the entire downstream structure. Bottom: the main domain upon condensation

The workflow implemented to solve the pulmonary arterial tree using the FEM Superelement approach can be summarised in six steps as following.

- 1. Generate a small tree ($TREE_{small}$) with the depth given by the number of generations, g_s**

In order to set the limit between the main domain and the sub-trees, a small tree, of g_s number of generations is firstly implemented. Generation g_s of $TREE_{small}$ has a complete number of branches, equal to 2^{g_s} and is one higher than the number of generations of the main domain ($g_s = g_m + 1$).

- 2. Cut the last generation of branches of $TREE_{small}$**

The main domain is obtained by cutting all the branches included in the g_s^{th} generation. Subsequent, all the 2^{g_s} number of terminal branches became the root radii of the attached sub-trees. Due to the fractal character of the tree, only $g_s + 1$ of the 2^{g_s} radii are distinct and therefore the number of sub-tree required to be computed is significantly reduced. Choosing the root radius of each superelements to be equal to the terminal radii of $\text{TREE}_{\text{small}}$, denotes that a sub-tree of minimum 1 element, always exists attached to the main domain.

3. Condensation of the interior degrees of freedom

The interior degrees of freedom of each superelement are condensed to the boundary. In Figure 5.6 the interior dof correspond to the nodes are marked in blue, whereas the boundary dof correspond to the nodes marked in red.

Each superelement is described by a system of linear equations given by (Eq. 5.77) for a one-element sub-tree, and (Eq. 5.80) respectively for higher order trees.

$$\begin{bmatrix} k_{aa}^s & k_{ab}^s \\ k_{ba}^s & k_{bb}^s \end{bmatrix} \begin{Bmatrix} p_{\text{boundary}}^s \\ p_{\text{interior}_o}^s \end{Bmatrix} = \begin{Bmatrix} -Q_{\text{boundary}}^s \\ Q_{\text{interior}}^s \end{Bmatrix} \quad (\text{Eq. 5.77})$$

$$\begin{bmatrix} k_{aa}^s & k_{ab}^s & k_{ac}^s \\ k_{ba}^s & k_{bb}^s & k_{bc}^s \\ k_{ca}^s & k_{cb}^s & k_{cc}^s \end{bmatrix} \begin{Bmatrix} p_{\text{boundary}}^s \\ p_{\text{interior}_i}^s \\ p_{\text{interior}_o}^s \end{Bmatrix} = \begin{Bmatrix} -Q_{\text{boundary}}^s \\ 0 \\ Q_{\text{interior}}^s \end{Bmatrix} \quad (\text{Eq. 5.78})$$

By applying zero pressure at the terminal nodes ($p_{\text{interior}_o}^s = 0$), the condensed equations describing the pressure-flow relationship at the boundary nodes are given by (Eq. 5.79) and (Eq. 5.80) for one and multiple element trees, respectively.

$$[k_{aa}^s] \{p_{\text{boundary}}^s\} = \{-Q_{\text{boundary}}^s\} \quad (\text{Eq. 5.79})$$

$$([k_{aa}^s] + [k_{ab}^s][k_{bb}^s]^{-1}[-k_{ba}^s]) \{p_{\text{boundary}}^s\} = \{-Q_{\text{boundary}}^s\} \quad (\text{Eq. 5.80})$$

4. Assemble the global stiffness matrix with the condensed boundaries

The global stiffness matrix is assembled as shown in Figure 5.5 and described for a branching tree without attached superelements. The major difference consists in populating the cells corresponding to the terminal nodes of the main domain. The boundary stiffness matrices of the two emerging sub-trees are added to each of the main domain terminal nodes.

5. Solve the main domain upon condensation and recover the superelement solution

Upon condensation, according to the implemented inlet boundary conditions, the linear system corresponding to the main domain with condensed boundaries is solved for the inlet solution and internal pressure distribution. Then the pressure solution computed for the terminal nodes of the main domain is applied as the input pressure for each of the subtrees, allowing for the recovery of all internal pressures and external flow solutions.

RESULTS AND DISCUSSION

A direct application of the proposed model is to answer the question: “how deep the technique can see?”. It is important to understand where the quantified reflections are coming from and whether the technique identifies distal or proximal disease. Due to effects such as wave attenuation and wave trapping [71] it seems likely that the strongest detected signal will arrive from the vessels closer to the reflection site. Results obtained from branching tree models, using the geometrical structure proposed initially by Olufsen et al. [167], have been shown to depend on the minimum vessel radius modelled. Cousin et al. [90], showed that the pressure waveform recovered at the top of the tree depends on the value of the minimum radius. One of the main factors influencing the amplitude of the waveform is the direct current (dc) component: the deeper the tree, the higher the value of the resistance in terms of the zero frequency component. Only the harmonic components of the signal are influenced by the wave attenuation effects, while the zero frequency component only adds to the composite harmonic signal.

In order to test this hypothesis, a branching tree defined geometrically in terms of the daughter to parent ratio, vessel length, root and minimum radius, was solved using the Superlement approach. Measured MRI flow from a healthy volunteer was applied for the inlet boundary condition, while zero pressure was specified at the outlet of the domain. Two hundred ten branching trees were solved with minimum radius varying from 0.08 mm to 19 mm. All other parameters were kept constant, parent to daughter ratio ($\beta_1=0.8$ and $\beta_2=0.6$), vessel length ($\lambda_l=15$) and root radius ($r_{root}=20$ mm). The W_b/W_{tot} metric was computed at the inlet of the domain under both viscous and inviscid conditions.

The results with inviscid conditions demonstrated that 50% of the wave power measured at the inlet was contained in the backward wave, independent of the tree depth. More precisely, for an inviscid system as defined here, it makes no difference where the geometrical limit of tree is defined (how deep the tree is), as the wave is totally reflected.

The results of the viscous system, displayed in Figure 5.7 show the amount of power in the backward wave at the root of the tree and the first two branching daughters. For a large minimum radius (>10 mm), 46% of the power is contained in the backward wave, suggesting that the viscous medium attenuates approximately 0.04% of the backward wave. A rapid decay of the W_b/W_{tot} parameter can be noticed for trees with a minimum radius smaller than 4 mm. The ratio of the backward to total wave power reaches 1% for a minimum radius of 0.4 mm. Although not displayed on the graph, an increase in W_b/W_{tot} , which oscillates between 1% and 9%, was noticed for trees with r_{min} between 0.02 mm and 0.3 mm. Due to the very small values of the W_b/W_{tot} metric for $r_{min}=0.4$, it is likely that this increase and oscillations noticed beyond the 0.4 mm minimum radius are generated artificially, representing a numerical effect rather than the real behaviour of the system.

These results show that the minimum radius and implicitly the depth of the tree influence the results at the top tree in terms of the wave power content. The graph in Figure 5.7 shows that the waves are rapidly attenuated, reaching a minimum of 1% reflected wave at the inlet of the system. In order to understand how deep the technique can see, the tree was diseased one generation at a time, while keeping the other generations unchanged. For the asymmetric tree with $r_{min}=0.4$ mm, the radius of the original tree was reduced by 25%, 50% and 75% at each generation. The depth of the tree was 18 generations 11 of which have a complete number of branches. For a generation g_z , a complete number of branches is equal to $2^{(g_z-1)}$. A symmetric tree will have complete number of branches at each generation, whereas this property is not characteristic for an asymmetric structure, due to the different parent-daughter radius ratios. For the above implemented asymmetric tree, the number of branches contained at each generation, g_z after generation 11, is smaller than $2^{(g_z-1)}$ and decreases to only 756 branches at generation 15 (instead of 2^{14}), 212 at generation 16, 32 at generation 17 and 30 at generation 18.

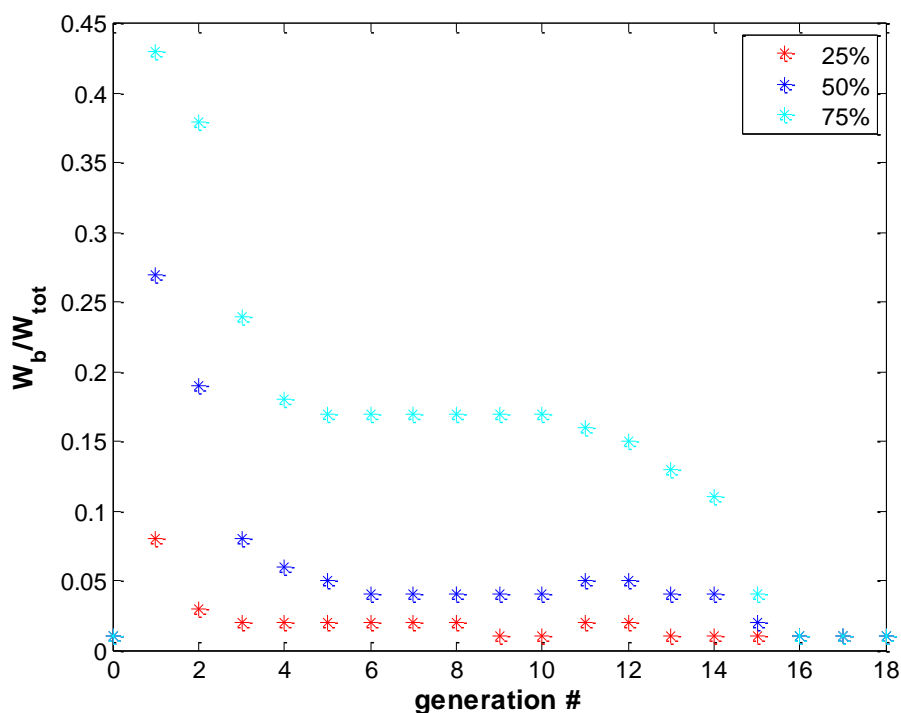


Figure 5.7 The effect of reducing the radius at a generation at the time, on the inlet measured W_b/W_{tot} . A reduction of the vessel radius of 25% (red), 50% (blue) and 75% (cyan) was applied one generation at a time. Generation zero represents the W_b/W_{tot} value computed for the undiseased tree.

Figure 5.7 shows the results following the reduction of the vessel radius by 25%, 50% and 75% from the original tree. Generation zero in the figure corresponds to the W_b/W_{tot} measured in the un-modified tree. It can be noticed that the amount of reflections sensed by the system upon altering the first branch (Generation 1) is 44% in the case of a 75% occlusion, 27% for a 50% occlusion and 0.08 for a 25% vessel occlusion. The signal decays when the radius constriction is applied further down the tree, reaching a plateau region after the 5th generation, for all the levels of radius reduction applied. After the 11th generation, the last generation with a complete number of branches, the signal decays even more, to 1%, value also computed at the root of the original tree. This further reduction can be readily attributed to the reduced number of branches forming the last generations. Between generations 5 and 11, the number of branches grows exponentially (2^{g-1}). However, the value of the W_b/W_{tot} parameter measured at the inlet shows only small oscillations around plateau values, for all three degrees of constriction. This suggests that given the case simulated here, of a generation with the radius of all branches reduced, although the number of branches from a 'complete' generation influences the W_b/W_{tot} measured at the inlet (seen in the oscillations

around the plateau values), this influence is small. By the time the backward waves arrive at the inlet of the domain, viscosity and wave trapping effects are reducing their amplitude, and the signal coming from distal generations (with more branches) has the same value of the signal coming from more proximal generations. The only difference in the amount of reflections sensed in these systems can be noticed for the very proximal generations (1 to 4). However it is difficult to state using this model where exactly and how severe this proximal 'disease' is. As shown in Figure 5.8, a 50% radius reduction applied at generation 2 (left and right pulmonary arteries) will return the same W_b/W_{tot} value as for a 75% reduction applied at generation 4. Similarly, a 25% constriction applied on the main pulmonary artery (generation 1) returns the same W_b/W_{tot} value as a 50% reduction applied to generation 3.

Between generation 12 and 18, the number of branches per generation does not grow with the same exponential law as for the previous ones. Moreover, towards generation 15 the number of branches is small comparing to the upper generations (13, 14). The viscosity and wave trapping effects and the reduced number of branches per generation (incomplete) lead to insignificant backward energy contented being sensed at the inlet of the domain.

In Chapter 3, average values of 11-13% were identified for the W_b/W_{tot} metric in the healthy volunteers (HV) group, while more than 40% was identified for the severe PH patient group, after solving a 1D system of an elastic tube, with flow and pressure prescribed at the inlet of the domain. The 40% backward energy previously quantified for the PH patients can be attributed to an accumulation of reflections from multiple diseased branches, and not only from a single location as simulated here.

There is a large difference between the computed reflected wave in the HV group (assumed to be an efficient system) and the 1% reflection calculated for the asymmetric branching tree discussed in this chapter. This difference can be readily attributed to the simplifications assumed for the branching tree. In reality, the amount of reflections returned at the periphery is produced not only by the bifurcation reflection coefficients (included in this model), but also due to tapering, narrowing of the vessels and other types of impedance mismatch present even in the most efficient system. In spite of the differences between the W_b/W_{tot} values calculated for the asymmetric tree without disease and the 1D model of a tube from Chapter 3, the system implemented here has value in showing that the signal quantified at the inlet might come from proximity. Although the W_b/W_{tot} metric alone cannot make the distinction between a mild constriction applied at the 1st or 2nd generation and a

more severe one applied at the 3rd or 4th generation, a detailed analysis of the individual frequency components might bring further insights on the disease location.

Additionally, further work is required to design a spatial distribution of disease that could simulate different PH conditions not affecting an entire generation of branches, but being distributed across the depth of the tree, in order to clearly understand if the technique is suitable for differentiating between PH sub-groups.

SUMMARY AND CONCLUSIONS

Wave reflection quantification from a simple 1D model of a straight elastic tube showed the best individual PH accuracy within all the analysed metrics in *Chapter 4*. Additionally, as discussed in *Chapter 3*, the metric showed statistically significant results in separating healthy volunteers from patients with stratified PH. Further investigations, quantifying the changes in the transmitted and reflected energy at different branch generations are desirable for understanding the pulmonary circulation in depth.

A new method for solving 1D vascular systems in the frequency domain has been proposed and described in this chapter. The method provides an alternative approach to the recursive impedance method implemented by several authors [171], [172] for solving the flow and pressure distribution along the systemic arterial circulation or as a boundary condition [167], [44], [45], [89] to represent the distal vasculature of a 1D pulmonary domain solved numerically. The primary advantage of the developed method is that it represents the system in an intuitive way from the perspective of the analysis of wave transmission, and immediately yields the reflection characterisation that is central to the work presented in this thesis.

A short section of the chapter was dedicated to briefly describe the implementation of the recursive impedance approach since it was used as 'validation' for the new method. The results evaluated at the inlet of the domain, in terms of the flow waveform computed from outlet pressure boundary conditions are identical for both methods.

Pulmonary trees are large structures and their explicit representation can be computationally challenging. The proposed method, based on a FEM approach, was implemented on an asymmetric pulmonary arterial tree defined based on parent-to-daughter radius ratio and vessel's radius to length rules as implemented by [44]. A structural engineering approach, the Superelement, was used to reduce the size of the problem by taking into account the self-similar structures characteristics to fractal-like geometries.

One of the applications proposed in this chapter that uses the Superelement method is identifying how deep the system can see. Following the running of the method on two hundred ten trees with different minimum radius values, it has been shown that for a viscous system the strongest signal comes from the vessels closer to the measuring point. The backward waves quantified at the inlet decreased with the depth of the tree, reaching a minimum of 1% reflection for a 0.4 mm minimum radius.

In order to understand at which point the reflections are lost in noise and the disease cannot be detected, the vessels' radii of an asymmetric tree were constricted by 25%, 50% and 75% respectively, one generation at a time. While the 'disease' applied at the first generation was immediately identified, it rapidly decayed, reaching a plateau after the 5th generation, suggesting that proximal diseases are more likely to be identified by these systems than distal ones.

Patient specific geometries can be provided to the model by tuning existing morphometric data to match the input measurements as previously shown by [89]. With the support of realistic geometries and patient specific input data, the proposed FEM based method can be applied for simulating a disease spectrum distribution, not only full-generation induced disease, that could help in differentiation of PH sub-groups.

CHAPTER 6

Conclusions, Limitations and Future Work

The research conducted during the PhD and outlined in this thesis has a translational character, focusing on the non-invasive characterisation of the pulmonary circulation in healthy and patients with pulmonary hypertension.

The condition, defined by increased mean pulmonary arterial hypertension over the threshold of 25 mmHg, is currently diagnosed using right heart catheterisation. As for any invasive procedure, RHC is associated with a series of risks [6], [7]. Although if performed in specialist centres the fatal outcome is minimised [8], finding alternative, non-invasive means to diagnose PH is highly desirable.

The research was driven by the primary hypothesis that the physiological status of the pulmonary circulation can be inferred using solely non-invasive flow and anatomy measurements of the pulmonary arteries measured by MRI and interpreted by simple computational models.

The aim was to implement a series of computational 0D and 1D models, taking their inputs from MRI measurements, and to evaluate their potential to support the non-invasive diagnosis and monitoring of pulmonary hypertension.

As outlined in *Chapter 1*, electrical analogue and wave transmission theory based models are extensively described in the literature and their clinical applications on humans is reviewed. However, the majority of the studies that showed potential in distinguishing between normotensive and patients with PH took their input data from invasive RHC pressure measurements. Therefore developing and evaluating non-invasive diagnostic methods for PH represented the main challenge of the thesis.

CONCLUSIONS AND LIMITATIONS

The implementation and clinical testing of two mathematical models, a three element Windkessel model and a 1D model of an axisymmetric straight elastic tube for wave reflections, in healthy volunteers, normotensive and patients with PH represents the central part of the thesis.

The first step in building up towards clinically relevant results was implementing a workflow for processing MRI images of the pulmonary arteries in order to supply the mathematical models with personalised, patient specific, measurements. A MATLAB GUI was designed to semi-automatically segment the pulmonary arteries using a registration-based-segmentation process developed based on the Sheffield University Image Registration Toolkit (ShIRT) [108]. Three different approaches dictated by the choice of the fixed image in the registration process were implemented to quantify the area and the flow passing through the vessels' cross-sections during the entire cardiac cycle.

In order to provide simultaneous measurements of flow and pressure (radius), two spatially and temporally co-registered MRI sequences, phase contrast (PC) and balanced steady state free precession (bSSFP), were used to acquire images of the pulmonary arteries. In the first instance the semi-automatic approaches were tested on a healthy volunteer on a data set consisting of all three pulmonary arteries: main, right and left, in order to establish the segmentation methodology of the clinical study.

Three operators, with different levels of experience in segmenting medical images processed each set of images both manually and using the proposed semi-automatic approaches for testing inter-operator variability of each method. One operator segmented the arteries three times for testing the intra-operator variability. The semi-automatic segmentations were

comparable with the manually obtained ones in terms of waveform shape and relative area change. However, based on the two criteria employed to test the results, efficiency and reproducibility, the manual segmentation was less efficient, being five times slower, and less reproducible, with a higher slice-by-slice coefficient of variation. A limitation of the analysis performed in *Chapter 2* is comparing the segmentation results against the ground truth. Although the manual segmentation is considered the gold standard in the domain, it does not necessarily mean it outputs the true area of the segmented object. A scan on a phantom object of known area can indicate the accuracy of the segmentation process. Yet, the main objective in quantifying the area of the pulmonary arteries was to provide realistic, fast and reproducible anatomy and flow measurements to the mathematical models and not to quantify the area in an absolute sense. The last results of *Chapter 2* emphasised that although the resulting area waveforms showed a consistent inter-operator bias, it had minimum influence on the computed flow waveforms and was reduced by a factor of two on the derived pressure surrogates. These findings were taken forward in *Chapter 3*, by testing the intra and inter-operator variability on the mathematical models' outputs, and confirmed that variability of the results was within the acceptable limits.

The core clinical study of the thesis was employed on an 80 subject cohort divided into healthy volunteers, normotensive clinical patients and patients with mild and severe PH. Datasets of PC and bSSFP images of the main pulmonary artery were semi-automatically segmented based on Chapter 2 pre-established image processing protocol, and passed to an $R_c R_d$ Windkessel model and a 1D model of wave reflections. The mathematical models were solved and the electrical parameters, R_c , C , R_d , and the ratio of the backward to total wave power, W_b/W_{tot} , tested for statistical significance difference between the subject groups.

A major challenge in solving the OD models is finding the appropriate combination of electrical parameters that will satisfy the input pressure-flow relationship. A two-step optimisation process, which minimises the differences between the measured and computed pressure signal, was designed to reduce operator's role and to be readily implemented to circuits of multiple variables. The procedure was limited by the quality of area and flow waveforms obtained in a number of subjects, which could justify the presence of outliers. Although some of the OD results were unsatisfactory due to high RMS fitting values, overall, they were in close agreement to the previously reported results computed on the basis of invasive measurements. The distal vascular resistance, R_d and total vascular compliance, C showed significant statistical differences between several of the analysed groups.

The ratio of the backward to total wave power, W_b/W_{tot} , computed from the decomposition of the pressure wave into its forward and backward components at each harmonic, accentuated the great potential wave reflection analysis has in describing the efficiency of pulmonary system in health and disease. On average, more than 40% of the total power was contained in the backward wave measured in patients with PH, whereas less than 20% was characteristic to the healthy volunteers group.

One of the major limitations in developing the 0D and 1D model is the use of a substitute measurement derived MPA images to replace the time varying pressure data required for solving the models. A pressure-radius relationship, taking into account the elastic properties of the wall, derived on literature and own RHC data was prescribed as a surrogate. The mean, systolic and diastolic computed pressures were following the trend of the invasively measured ones but they were different in absolute value. Although the surrogate pressure model cannot be used to predict the true mPAP value and should not be considered for diagnosis purposes on its own, the underlying equations describing the fluid mechanics remain the same regardless of the variable substitution.

Chapter 3 described the methods and challenges for obtaining robust, reliable and clinically meaningful results from solving the two proposed mathematical models, while *Chapter 4* established a method to directly translate the computational metrics into clinic.

The increased interest for non-invasive PH diagnosis led to the development of metrics calculated directly from the MRI images. The performance of the computationally based metrics (R_d , C and W_b/W_{tot}), quantified as sensitivity, specificity and misclassification error, was compared against image based metrics calculated in our group. Individually, no metric was an excellent discriminant. The best performance of all analysed metrics, tested with a data driven criterion (maximisation of Youden index), was shown by the W_b/W_{tot} parameter developed in this thesis. The metric discriminated between normotensive and patients with PH with an accuracy of 75%, 68% sensitivity and 100% specificity.

The combination of computational and image-based metrics into a decision support classification algorithm classified has shown high classification accuracy (92%). Moreover, all of the subjects who were misclassified by the developed process had mPAP between 21-30 mmHg, which as discussed in *Chapter 4*, represents the area of clinical uncertainty. Combining PH metrics derived computationally and from images alone into classification algorithms maximised the effectiveness of the MR technique for the non-invasive detection and monitoring of PH. The main limitation of the study is the lack of separate train, test and

validation cohorts. To overcome the reduced number of subjects in the study, the results were validated using leave-one-out cross-validation method. Extending the number of patients and dividing them accordingly for a robust validation is desirable.

The simple 1D analysis, quantifying the wave reflections at the inlet of a straight elastic tube, showed in *Chapter 3* statistically significant differences between healthy volunteers, normotensive and patients with stratified PH. Moreover, the W_b/W_{tot} metric displayed in *Chapter 4* the highest individual accuracy of all analysed metrics. The results inspired new research questions regarding the potential of wave reflection quantification in healthy and diseased pulmonary systems emerging from a global analysis. *Chapter 5* proposed a method for quantifying the amount of backward energy transmitted proximally at any location within the branching 1D pulmonary arterial tree.

The newly proposed method was used to solve a 1D linear systems in the frequency domain based on an efficient Finite Element Method (FEM) approach and to quantify the amount of energy reflected and transmitted across each bifurcation. One of the direct applications of the method was testing how deep the technique can 'see'. For an asymmetric branching tree with a zero pressure outlet condition the depth of the tree has no influence on the reflections quantified at the inlet in the inviscid case. In the viscous case the results showed that after 11 full generations, the amount of backward energy at the inlet was reduced to 1%. By reducing the radius of an entire generation of branches by a different percentage, it was observed that the W_b/W_{tot} value reaches a plateau region after the 5th generation. These findings confirm the intuitive suggestion that proximal disease is more likely to be identified in these systems.

However, the backward energy content in pulmonary arterial systems is more likely to be an accumulation of reflections coming from multiple diseased generations. Therefore by applying a disease spectrum affecting several generations further insights into non-invasive PH sub-group classification can be obtained. Other potential clinical applications and limitations of the newly proposed method are further discussed in the *Future Work* section.

FUTURE WORK

The translational research carried out during the PhD outlined the potential of mathematical models integrated with existing non-invasive clinical tools. The results obtained from integrating computationally derived metrics, which showed good discriminative character alone, with other existing clinical metrics into machine learning algorithms indicated that need of invasive PH diagnosis might be reduced.

Further developments of the non-invasive PH diagnosis application can be however implemented: introducing an automatic segmentation option into the segmentation GUI to further reduce operator input and limit the image processing time, improve the robustness and accuracy of computing the OD electrical parameters, extend the number of non-invasive metrics used in the classification algorithm and replace the naïve parameter selection with a more robust feature selection algorithm. Additionally, extend the size of the cohort and use different subsets for training, testing and validation to increase the robustness of the results. Further analysis is also desirable on patients with mPAP close to the clinical diagnosis threshold for increasing classifier's accuracy.

Although an important step towards minimising RHC interventions has been made, the procedure remains essential for establishing the PH sub-group the patient belongs to, and for the response to treatment assessment. The selected machine learning classifier has the advantage that it can be applied to multiple classes. The classifier can be tested on an extended cohort of a homogenous population of PH patients for attributing them to the corresponding PH sub-group. The tests performed in *Chapter 3* emphasised that wave reflections metric W_b/W_{tot} showed significant statistical differences between the healthy volunteers and clinical patients with no PH. On the other hand, the classification algorithm misclassified some patients in the area of clinical uncertainty. Age matched volunteers should be considered for further clinical analysis. The changes in the pulmonary vascular resistance (PVR) occurring after commencement of medication for pulmonary arterial hypertension (PAH) are used as an indicator of treatment response, and RHC follow-up interventions can be as often as every twelve weeks [25]. Perhaps one of the most attractive applications of the OD and 1D model parameters will be in the assessment of patients at follow-up to reduce the need for repeated invasive interventions.

Different PH heterogeneities can be mimicked by modifying the structural and elastic parameters of a 1D pulmonary tree structure [44], [45]. Qureshi and Hill [46] showed increased wave reflections associated with the hypothetical representations of these

conditions in a branching tree model. The method detailed in *Chapter 5* might be applied, with realistic geometry and tuned to match patient specific measurements, to quantify wave reflection at any location along the branching tree, with the potential to differentiate between different PH phenotypes. Moreover, the temporal flow and pressure signals and the resulting wave reflection quantification at different locations in the tree might be used to localise the disease.

A more complex characterisation of the haemodynamics, which can fully resolve the fluid dynamics equations and overcome the limitations introduced by the 1D linearization, is thought to be given by the 3D computational models. Although running CFD analysis is one of the ongoing trends in the translational/clinical research it is not straight-forward. It is highly dependent on both the geometry of the vessel and the boundary conditions. In terms of the pulmonary vasculature dynamics simulation, the challenge will be to define the outlet boundary conditions. There are novel highly accelerated 4D phase contrast pulse sequences that provide simultaneous measurement of blood flow and vessel wall motion. Based on this type of measurement, Windkessel parameters might be tuned in first instance, by using the methods described in the thesis for providing personalised boundary conditions. More realistic personal boundary conditions, able to represent wave behaviour can be applied by tuning the geometry of a structured tree solved with the newly proposed FEM 'like' method.

FINAL THOUGHTS

Finding alternative, non-invasive diagnostic and follow-up assessment methods in pulmonary hypertension is highly desirable in order to minimise the risks associated with the right heart catheterisation (RHC) procedure.

The diagnostic protocols, including the analysis work flow, developed and reported in this PhD thesis can be integrated into the clinical process, with the potential to reduce the need for RHC by maximising the use of available MRI data.

REFERENCES

1. Crapo, J.D., *Baum's textbook of pulmonary diseases*. 2004.
2. Wilmer, W.N. and W.W. Nichols, *McDonald's blood flow in arteries : theoretical, experimental and clinical principles*, ed. M.F. Rourke and D.A. McDonald. 2005, London: London : Hodder Arnold, 2005.
3. Burrowes, K.S., *An Anatomically-Based Mathematical Model of the Human Pulmonary Circulation*, in *Biomedical Engineering*. 2005, The University of Auckland. p. 206.
4. Galie, N., et al., *Guidelines for the diagnosis and treatment of pulmonary hypertension (vol 30, pg 2493, 2009)*. *European Heart Journal*, 2011. **32**(8): p. 926-926.
5. Hooper, M.M., et al., *Definitions and diagnosis of pulmonary hypertension*. *J Am Coll Cardiol*, 2013. **62**(25 Suppl): p. D42-50.
6. Ranu, H., et al., *A retrospective review to evaluate the safety of right heart catheterization via the internal jugular vein in the assessment of pulmonary hypertension*. *Clin Cardiol*, 2010. **33**(5): p. 303-6.
7. Glowny, M.G. and F.S. Resnic, *What to Expect During Cardiac Catheterization*. *Circulation*, 2012. **125**(7): p. e363-e364.
8. Hooper, M.M., et al., *Complications of right heart catheterization procedures in patients with pulmonary hypertension in experienced centers*. *J Am Coll Cardiol*, 2006. **48**(12): p. 2546-52.
9. Kiely, D.G., et al., *Pulmonary hypertension: diagnosis and management*. *BMJ*, 2013. **346**.
10. Ryan, J.J., et al., *The WHO classification of pulmonary hypertension: A case-based imaging compendium*. *Pulm Circ*, 2012. **2**(1): p. 107-21.
11. Swift, A.J., et al., *Quantitative magnetic resonance imaging of pulmonary hypertension: a practical approach to the current state of the art*. *J Thorac Imaging*, 2014. **29**(2): p. 68-79.
12. Simonneau, G., et al., *Updated clinical classification of pulmonary hypertension*. *J Am Coll Cardiol*, 2009. **54**(1 Suppl): p. S43-54.
13. Harris, P., *The human pulmonary circulation : its form and function in health and disease*. 3rd ed. 1986: Edinburgh : Churchill Livingstone.
14. Truong, Q.A., et al., *Reference values for normal pulmonary artery dimensions by noncontrast cardiac computed tomography the framingham heart study*. *Circulation: Cardiovascular Imaging*, 2012. **5**(1): p. 147-154.
15. H.K. Chang, M.P., *Respiratory physiology : an analytical approach*. 1989: New York : Dekker.
16. Kovacs, G., et al., *Pulmonary arterial pressure during rest and exercise in healthy subjects: a systematic review*. *Eur Respir J*, 2009. **34**(4): p. 888-94.
17. Reiter, G., et al., *Magnetic resonance-derived 3-dimensional blood flow patterns in the main pulmonary artery as a marker of pulmonary hypertension and a measure of elevated mean pulmonary arterial pressure*. *Circ Cardiovasc Imaging*, 2008. **1**(1): p. 23-30.
18. Hooper, M.M., *The new definition of pulmonary hypertension*, in *Eur Respir J*. 2009: Switzerland. p. 790-1.
19. Chatterjee, N.A. and G.D. Lewis, *What is the prognostic significance of pulmonary hypertension in heart failure?*, in *Circ Heart Fail*. 2011: United States. p. 541-5.

20. Lankhaar, J.W., et al., *Quantification of right ventricular afterload in patients with and without pulmonary hypertension*. Am J Physiol Heart Circ Physiol, 2006. **291**(4): p. H1731-7.
21. *Pulmonary circulation : diseases and their treatment*. 3rd ed. ed, ed. A.J. Peacock, R. Naeije, and L.J. Rubin. 2011, London: London : Hodder Arnold, 2011.
22. Voelkel, N.F., et al., *Right Ventricular Function and Failure: Report of a National Heart, Lung, and Blood Institute Working Group on Cellular and Molecular Mechanisms of Right Heart Failure*. Circulation, 2006. **114**(17): p. 1883-1891.
23. Ryan, J.J., et al., *Current practice for determining pulmonary capillary wedge pressure predisposes to serious errors in the classification of patients with pulmonary hypertension*. Am Heart J, 2012. **163**(4): p. 589-94.
24. E. Kenneth Weir, J.T.R., *Pulmonary vascular physiology and pathophysiology*. 1989: New York : Dekker.
25. Peacock, A.J., R. Naeije, and L.J. Rubin, *Pulmonary circulation : diseases and their treatment*. 3rd ed. ed, ed. A.J. Peacock, R. Naeije, and L.J. Rubin. 2011, London: London : Hodder Arnold, 2011.
26. Swift, A.J., et al., *Pulmonary artery relative area change detects mild elevations in pulmonary vascular resistance and predicts adverse outcome in pulmonary hypertension*. Invest Radiol, 2012. **47**(10): p. 571-7.
27. Lungu, A., et al., *MRI model-based non-invasive differential diagnosis in pulmonary hypertension*. J Biomech, 2014. **47**(12): p. 2941-7.
28. Chang, P.P., et al., *Mild vs severe pulmonary hypertension before heart transplantation: different effects on posttransplantation pulmonary hypertension and mortality*. J Heart Lung Transplant, 2005. **24**(8): p. 998-1007.
29. Delgado, J.F., et al., *Impact of mild pulmonary hypertension on mortality and pulmonary artery pressure profile after heart transplantation*. The Journal of Heart and Lung Transplantation, 2001. **20**(9): p. 942-948.
30. Sanz, J., et al., *Evaluation of pulmonary artery stiffness in pulmonary hypertension with cardiac magnetic resonance*. JACC Cardiovasc Imaging, 2009. **2**(3): p. 286-95.
31. Gan, C.T., et al., *Noninvasively assessed pulmonary artery stiffness predicts mortality in pulmonary arterial hypertension*. Chest, 2007. **132**(6): p. 1906-12.
32. Sanz, J., et al., *Pulmonary arterial hypertension: noninvasive detection with phase-contrast MR imaging*. Radiology, 2007. **243**(1): p. 70-9.
33. Saba, T.S., et al., *Ventricular mass index using magnetic resonance imaging accurately estimates pulmonary artery pressure*. Eur Respir J, 2002. **20**(6): p. 1519-24.
34. Swift, A.J., et al., *Diagnostic accuracy of cardiovascular magnetic resonance imaging of right ventricular morphology and function in the assessment of suspected pulmonary hypertension results from the ASPIRE registry*. J. Cardiovasc. Magn. Reson., 2012. **14**.
35. Roeleveld, R.J., et al., *Interventricular septal configuration at mr imaging and pulmonary arterial pressure in pulmonary hypertension*. Radiology, 2005. **234**(3): p. 710-7.
36. van Wolferen, S.A., et al., *Prognostic value of right ventricular mass, volume, and function in idiopathic pulmonary arterial hypertension*. Eur Heart J, 2007. **28**(10): p. 1250-7.
37. Garcia-Alvarez, A., et al., *Non-invasive estimation of pulmonary vascular resistance with cardiac magnetic resonance*. Eur Heart J, 2011. **32**(19): p. 2438-45.
38. Swift, A.J., et al., *Black blood MRI has diagnostic and prognostic value in the assessment of patients with pulmonary hypertension*. Eur Radiol, 2012. **22**(3): p. 695-702.

39. Kitabatake, A., et al., *Noninvasive evaluation of pulmonary hypertension by a pulsed Doppler technique*. *Circulation*, 1983. **68**(2): p. 302-9.
40. Jardim, C., et al., *Pulmonary artery distensibility in pulmonary arterial hypertension: an MRI pilot study*. *Eur Respir J*, 2007. **29**(3): p. 476-81.
41. Nogami, M., et al., *Utility of phase contrast MR imaging for assessment of pulmonary flow and pressure estimation in patients with pulmonary hypertension: comparison with right heart catheterization and echocardiography*. *J Magn Reson Imaging*, 2009. **30**(5): p. 973-80.
42. Lanzarini, L., et al., *Two simple echo-Doppler measurements can accurately identify pulmonary hypertension in the large majority of patients with chronic heart failure*. *J Heart Lung Transplant*, 2005. **24**(6): p. 745-54.
43. Bradlow, W.M., et al., *Assessing normal pulse wave velocity in the proximal pulmonary arteries using transit time: A feasibility, repeatability, and observer reproducibility study by cardiovascular magnetic resonance*. *Journal of Magnetic Resonance Imaging*, 2007. **25**(5): p. 974-981.
44. Olufsen, M.S., et al., *Rarefaction and blood pressure in systemic and pulmonary arteries*. *J Fluid Mech*, 2012. **705**: p. 280-305.
45. Qureshi, M.U., et al., *Numerical simulation of blood flow and pressure drop in the pulmonary arterial and venous circulation*. *Biomechanics and Modeling in Mechanobiology*, 2014. **13**(5): p. 1137-1154.
46. Qureshi, M.U. and M.U. Hill, *A computational study of pressure wave reflections in the pulmonary arteries*. *Journal of Mathematical Biology*, 2015.
47. Shi, Y., P. Lawford, and R. Hose, *Review of Zero-D and 1-D Models of Blood Flow in the Cardiovascular System*. *Biomedical Engineering Online*, 2011. **10**.
48. Shi, Y. and T. Korakianitis, *Numerical simulation of cardiovascular dynamics with left heart failure and in-series pulsatile ventricular assist device*. *Artif Organs*, 2006. **30**(12): p. 929-48.
49. Segers, P., N. Stergiopoulos, and N. Westerhof, *Relation of effective arterial elastance to arterial system properties*. *American Journal of Physiology - Heart and Circulatory Physiology*, 2002. **282**(3): p. H1041-H1046.
50. Clipp, R.B. and B.N. Steele, *Impedance boundary conditions for the pulmonary vasculature including the effects of geometry, compliance, and respiration*. *IEEE Trans Biomed Eng*, 2009. **56**(3): p. 862-70.
51. Vignon-Clementel, I.E., et al., *Outflow boundary conditions for 3D simulations of non-periodic blood flow and pressure fields in deformable arteries*. *Computer Methods in Biomechanics and Biomedical Engineering*, 2010. **13**(5): p. 625-640.
52. Nichols, W.W., *McDonald's blood flow in arteries : theoretical, experimental and clinical principles*. 5th ed. 2005: London : Hodder Arnold.
53. Sagawa, K., R.K. Lie, and J. Schaefer, *Translation of Otto frank's paper "Die Grundform des arteriellen Pulses" zeitschrift für biologische 37: 483–526 (1899)*. *Journal of Molecular and Cellular Cardiology*, 1990. **22**(3): p. 253-254.
54. Westerhof, N., G. Elzinga, and P. Sipkema, *An artificial arterial system for pumping hearts*. *J Appl Physiol*, 1971. **31**(5): p. 776-81.
55. Slife, D.M., et al., *Pulmonary arterial compliance at rest and exercise in normal humans*. *American Journal of Physiology - Heart and Circulatory Physiology*, 1990. **258**(6): p. H1823-H1828.
56. Stergiopoulos, N., J.J. Meister, and N. Westerhof, *Evaluation of methods for estimation of total arterial compliance*. *American Journal of Physiology - Heart and Circulatory Physiology*, 1995. **268**(4): p. H1540-H1548.
57. Burattini, R. and G. Gnudi, *Computer identification of models for the arterial tree input impedance: Comparison between two new simple models and first experimental results*. 1982.

58. Stergiopoulos, N., B.E. Westerhof, and N. Westerhof, *Total arterial inertance as the fourth element of the windkessel model*. Am J Physiol, 1999. **276**(1 Pt 2): p. H81-8.
59. Liu, Z., K.P. Brin, and F.C. Yin, *Estimation of total arterial compliance: an improved method and evaluation of current methods*. Am J Physiol, 1986. **251**(3 Pt 2): p. H588-600.
60. Segers, P., et al., *Pulmonary arterial compliance in dogs and pigs: the three-element windkessel model revisited*. Am J Physiol, 1999. **277**(2 Pt 2): p. H725-31.
61. Formaggia L, V.A., *Reduced and multiscale models for the human cardiovascular system*. 2003, Politecnico di Milano.
62. Lu, K., et al., *A human cardiopulmonary system model applied to the analysis of the Valsalva maneuver*. American Journal of Physiology-Heart and Circulatory Physiology, 2001. **281**(6): p. H2661-H2679.
63. Shi, Y., P.V. Lawford, and D.R. Hose, *Numerical Modeling of Hemodynamics with Pulsatile Impeller Pump Support*. Annals of Biomedical Engineering, 2010. **38**(8): p. 2621-2634.
64. van de Vosse, F.N. and N. Stergiopoulos, *Pulse Wave Propagation in the Arterial Tree*. Annual Review of Fluid Mechanics, Vol 43, 2011. **43**: p. 467-499.
65. Moore, S.M., et al., *One-dimensional and three-dimensional models of cerebrovascular flow*. J Biomech Eng, 2005. **127**(3): p. 440-9.
66. Xiao, N., J. Alastruey, and C.A. Figueroa, *A systematic comparison between 1-D and 3-D hemodynamics in compliant arterial models*. International Journal for Numerical Methods in Biomedical Engineering, 2014. **30**(2): p. 204-231.
67. Stergiopoulos, N., *Computer simulation of arterial blood flow*. 1990, Iowa State University: Digital Repository @Iowa State University. p. 194.
68. Bleasdale, R.A., K.H. Parker, and C.J.H. Jones, *Chasing the wave. Unfashionable but important new concepts in arterial wave travel*. American Journal of Physiology-Heart and Circulatory Physiology, 2003. **284**(6): p. H1879-H1885.
69. Biglino, G., et al., *A non-invasive clinical application of wave intensity analysis based on ultrahigh temporal resolution phase-contrast cardiovascular magnetic resonance*. J Cardiovasc Magn Reson, 2012. **14**: p. 57.
70. Koh, T.W., et al., *Analysis of wave reflections in the arterial system using wave intensity: a novel method for predicting the timing and amplitude of reflected waves*. Heart Vessels, 1998. **13**(3): p. 103-13.
71. Parker, K.H., *An introduction to wave intensity analysis*. Med Biol Eng Comput, 2009. **47**(2): p. 175-88.
72. Hughes, A.D. and K.H. Parker, *Forward and backward waves in the arterial system: impedance or wave intensity analysis?* Med Biol Eng Comput, 2009. **47**(2): p. 207-10.
73. van den Bos, G.C., N. Westerhof, and O.S. Randall, *Pulse wave reflection: can it explain the differences between systemic and pulmonary pressure and flow waves? A study in dogs*. Circ Res, 1982. **51**(4): p. 479-85.
74. Huez, S., et al., *Feasibility of routine pulmonary arterial impedance measurements in pulmonary hypertension*. Chest, 2004. **125**(6): p. 2121-8.
75. Laskey, W.K., et al., *Pulmonary artery hemodynamics in primary pulmonary hypertension*. Journal of the American College of Cardiology, 1993. **21**(2): p. 406-412.
76. Dwyer, N., A.C. Yong, and D. Kilpatrick, *Variable open-end wave reflection in the pulmonary arteries of anesthetized sheep*. J Physiol Sci, 2012. **62**(1): p. 21-8.
77. Hollander, E.H., et al., *Direct and series transmission of left atrial pressure perturbations to the pulmonary artery: a study using wave-intensity analysis*. Am J Physiol Heart Circ Physiol, 2004. **286**(1): p. H267-75.
78. Hollander, E.H., et al., *Negative wave reflections in pulmonary arteries*. Am J Physiol Heart Circ Physiol, 2001. **281**(2): p. H895-902.

79. Smolich, J.J., J.P. Mynard, and D.J. Penny, *Simultaneous pulmonary trunk and pulmonary arterial wave intensity analysis in fetal lambs: evidence for cyclical, midsystolic pulmonary vasoconstriction*. *Am J Physiol Regul Integr Comp Physiol*, 2008. **294**(5): p. R1554-62.
80. Furuno, Y., et al., *Reflection as a cause of mid-systolic deceleration of pulmonary flow wave in dogs with acute pulmonary hypertension: comparison of pulmonary artery constriction with pulmonary embolisation*. *Cardiovasc Res*, 1991. **25**(2): p. 118-24.
81. Castelain, V., et al., *Pulmonary artery pulse pressure and wave reflection in chronic pulmonary thromboembolism and primary pulmonary hypertension*. *Journal of the American College of Cardiology*, 2001. **37**(4): p. 1085-1092.
82. Engelberg, J. and A.B. Dubois, *Mechanics of pulmonary circulation in isolated rabbit lungs*. *American Journal of Physiology*, 1959. **196**(2): p. 401-414.
83. Grant, B.J.B. and L.J. Paradowski, *Characterization of pulmonary arterial input impedance with lumped parameter models*. *American Journal of Physiology*, 1987. **252**(3): p. H585-H593.
84. Segers, P., et al., *Systemic and pulmonary hemodynamics assessed with a lumped-parameter heart-arterial interaction model*. *Journal of Engineering Mathematics*, 2003. **47**(3-4): p. 185-199.
85. Pollack, G.H., R.V. Reddy, and Noordergraaf, *Input impedance wave travel and reflections in human pulmonary arterial tree-studies using an electrical analogues*. *IEEE Transactions on Biomedical Engineering*, 1968. **BM15**(3): p. 151-&.
86. Huang, W., et al., *Comparison of theory and experiment in pulsatile flow in cat lung*. *Annals of Biomedical Engineering*, 1998. **26**(5): p. 812-820.
87. Womersley, J.R., *Oscillatory flow in arteries -the constrained elastic tube as a model of arterial flow and pulse transmission*. *Physics in Medicine and Biology*, 1957. **2**(2): p. 178-187.
88. Kussmaul, W.G., A. Noordergraaf, and W.K. Laskey, *Right ventricular-pulmonary arterial interactions*. *Ann Biomed Eng*, 1992. **20**(1): p. 63-80.
89. Spilker, R.L., et al., *Morphometry-based impedance boundary conditions for patient-specific modeling of blood flow in pulmonary arteries*. *Annals of Biomedical Engineering*, 2007. **35**(4): p. 546-559.
90. Cousins, W. and P.A. Gremaud, *Boundary conditions for hemodynamics: The structured tree revisited*. *Journal of Computational Physics*, 2012. **231**(18): p. 6086-6096.
91. Westerhof and Noordergraaf, *Errors in measurement of hydraulic input impedance*. *Journal of Biomechanics*, 1970. **3**(3): p. 351-&.
92. Barnett, G.O., A.J. Mallos, and A. Shapiro, *Relationship of aortic pressure and diameter in the dog*. Vol. 16. 1961. 545-548.
93. Greenfield, J.C., Jr. and D.J. Patel, *Relation between pressure and diameter in the ascending aorta of man*. *Circ Res*, 1962. **10**: p. 778-81.
94. Sugawara, M., et al., *Relationship between the pressure and diameter of the carotid artery in humans*. *Heart Vessels*, 2000. **15**(1): p. 49-51.
95. Giannattasio, C., et al., *Simultaneous measurement of beat-to-beat carotid diameter and pressure changes to assess arterial mechanical properties*, in *Hypertension*. 2008: United States. p. 896-902.
96. Greenfield, J.C. and D.M. Griggs, *Relation between pressure and diameter in main pulmonary artery of man*. *Journal of Applied Physiology*, 1963. **18**(3): p. 557-559.
97. Jarmakani, J.M.M., et al., *In Vivo Pressure-Radius Relationships of the Pulmonary Artery in Children with Congenital Heart Disease*. *Circulation*, 1971. **43**(4): p. 585-592.
98. Donald W. McRobbie, E.A.M., Martin J. Graves and Martin R. Prince, *MRI from picture to proton*. 1st ed. Vol. 1. 2003, Cambridge: Cambridge : Cambridge University Press, 2003. 360.

99. Kaut, C.W.a.C., *MRI in practice*. 2nd ed. 1998, Great Britain, University Press, Cambridge. 326.
100. Lotz, J., et al., *Cardiovascular flow measurement with phase-contrast MR imaging: Basic facts and implementation*. Radiographics, 2002. **22**(3): p. 651-671.
101. Cukur, T. and D.G. Nishimura, *Multiple Repetition Time Balanced Steady-State Free Precession Imaging*. Magnetic Resonance in Medicine, 2009. **62**(1): p. 193-204.
102. Peng, H.H., et al., *Estimation of pulse wave velocity in main pulmonary artery with phase contrast MRI: preliminary investigation*. J Magn Reson Imaging, 2006. **24**(6): p. 1303-10.
103. Beutel, J., et al., *Medical image processing and analysis*. 2000, Bellingham, Wash.: SPIE Press.
104. Sharma, N. and L.M. Aggarwal, *Automated medical image segmentation techniques*. Journal of Medical Physics / Association of Medical Physicists of India, 2010. **35**(1): p. 3-14.
105. Brown, L., *A survey of image registration techniques*. 1992. p. 325-376.
106. Maintz, J.B.A. and M.A. Viergever, *A survey of medical image registration*. Medical Image Analysis, 1998. **2**(1): p. 1-36.
107. Zitová, B. and J. Flusser, *Image registration methods: a survey*. Image and Vision Computing, 2003. **21**(11): p. 977-1000.
108. Barber, D.C. and D.R. Hose, *Automatic segmentation of medical images using image registration: diagnostic and simulation applications*. J Med Eng Technol, 2005. **29**(2): p. 53-63.
109. Odille, F., et al., *Automatic segmentation propagation of the aorta in real-time phase contrast MRI using nonrigid registration*. J Magn Reson Imaging, 2011. **33**(1): p. 232-8.
110. Odille, F., et al., *Quantitative assessment of small bowel motility by nonrigid registration of dynamic MR images*. Magnetic Resonance in Medicine, 2012. **68**(3): p. 783-793.
111. Quail, M.A., et al., *Noninvasive pulmonary artery wave intensity analysis in pulmonary hypertension*. American Journal of Physiology - Heart and Circulatory Physiology, 2015. **308**(12): p. H1603-H1611.
112. Randall, D., et al., *A Novel Diagnostic Aid for Detection of Intra-Abdominal Adhesions to the Anterior Abdominal Wall Using Dynamic Magnetic Resonance Imaging*. Gastroenterology Research and Practice, 2016. **2016**: p. 6.
113. Barber, D.C., et al., *Efficient computational fluid dynamics mesh generation by image registration*. Med Image Anal, 2007. **11**(6): p. 648-62.
114. Lamata, P., et al., *An accurate, fast and robust method to generate patient-specific cubic Hermite meshes*. Med Image Anal, 2011. **15**(6): p. 801-13.
115. Barber, D.C., *Automatic alignment of radionuclide images*. Physics in Medicine and Biology, 1982. **27**(3): p. 387-396.
116. Barber, D.C., et al., *Efficient computational fluid dynamics mesh generation by image registration*. Medical Image Analysis. **11**(6): p. 648-662.
117. Horn, F.C., et al., *Quantification of regional fractional ventilation in human subjects by measurement of hyperpolarized ³He washout with 2D and 3D MRI*. Journal of Applied Physiology, 2014. **116**(2): p. 129-139.
118. Fenner, J., et al., *Towards radiological diagnosis of abdominal adhesions based on motion signatures derived from sequences of cine-MRI images*. Physica Medica, 2014. **30**(4): p. 437-447.
119. Hunter, K.S., et al. *In vivo measurement of proximal pulmonary artery elastic modulus in the neonatal calf model of pulmonary hypertension: development and ex vivo validation*. J Appl Physiol (1985), 2010. **108**, 968-75 DOI: 10.1152/jappphysiol.01173.2009.

120. Niki, K., et al., *A noninvasive method of measuring wave intensity, a new hemodynamic index: application to the carotid artery in patients with mitral regurgitation before and after surgery*. Heart and Vessels, 1999. **14**(6): p. 263-271.
121. Feng, J. and A.W. Khir, *Determination of wave speed and wave separation in the arteries using diameter and velocity*. Journal of Biomechanics, 2010. **43**(3): p. 455-462.
122. Khir, A.W., et al., *Determination of wave speed and wave separation in the arteries*, in *J Biomech*. 2001: United States. p. 1145-55.
123. Borlotti, A., et al., *A comparison between local wave speed in the carotid and femoral arteries in healthy humans: application of a new method*. Conf Proc IEEE Eng Med Biol Soc, 2010. **2010**: p. 2857-60.
124. Quail, M.A., et al., *Abstract 16131: Novel Magnetic Resonance Wave Intensity Analysis in Pulmonary Hypertension*. Circulation, 2014. **130**(Suppl 2): p. A16131.
125. Milisic, V. and A. Quarteroni, *Analysis of lumped parameter models for blood flow simulations and their relation with 1D models*. Esaim-Mathematical Modelling and Numerical Analysis-Modelisation Mathematique Et Analyse Numerique, 2004. **38**(4): p. 613-632.
126. Liao, D., et al., *Arterial stiffness and the development of hypertension. The ARIC study*. Hypertension, 1999. **34**(2): p. 201-6.
127. Greenfield, J.C. and D.M. Griggs, *RELATION BETWEEN PRESSURE AND DIAMETER IN MAIN PULMONARY ARTERY OF MAN*. Journal of Applied Physiology, 1963. **18**(3): p. 557-&.
128. Mitchell, M., *An introduction to genetic algorithms [electronic resource]*. 1998, Cambridge, Mass: Cambridge, Mass : CogNet, 1998.
129. Kittelson, J., *A Review of: "Fundamentals of Biostatistics , 7th ed., by B. Rosner": Boston: Brooks/Cole, 2011, ISBN 978-0-538-73349-6, xvii +859 pp., \$190.95*. 2011, Taylor & Francis Group. p. 1046-1048.
130. Martin, K. and A. Naomi, *Points of Significance: Visualizing samples with box plots*. Nature Methods, 2014. **11**(2): p. 119.
131. Bland, J.M. and D.G. Altman, *Statistical methods for assessing agreement between two methods of clinical*. Lancet, 1986. **1**(8476): p. 307-10.
132. Shrout, P.E. and J.L. Fleiss, *Intraclass correlations: uses in assessing rater reliability*. Psychol Bull, 1979. **86**(2): p. 420-8.
133. Boerigter, B., et al., *Progressive dilatation of the main pulmonary artery is a characteristic of pulmonary arterial hypertension and is not related to changes in pressure*. Chest, 2010. **138**(6): p. 1395-401.
134. Saouti, N., et al., *The arterial load in pulmonary hypertension*. Eur Respir Rev, 2010. **19**(117): p. 197-203.
135. Lankhaar, J.W., et al., *Pulmonary vascular resistance and compliance stay inversely related during treatment of pulmonary hypertension*. Eur Heart J, 2008. **29**(13): p. 1688-95.
136. Wang, Z. and N.C. Chesler, *Pulmonary vascular wall stiffness: An important contributor to the increased right ventricular afterload with pulmonary hypertension*. Pulmonary Circulation, 2011. **1**(2): p. 212-223.
137. Milnor, W.R., et al., *Pulmonary arterial pulse wave velocity and impedance in man*. Circ Res, 1969. **25**(6): p. 637-49.
138. Reuben, S.R., *Compliance of the Human Pulmonary Arterial System in Disease*. Circulation Research, 1971. **29**(1): p. 40-50.
139. Saouti, N., et al., *RC time constant of single lung equals that of both lungs together: a study in chronic thromboembolic pulmonary hypertension*, in *Am J Physiol Heart Circ Physiol*. 2009: United States. p. H2154-60.

140. Stergiopoulos, N., J.J. Meister, and N. Westerhof, *Simple and accurate way for estimating total and segmental arterial compliance-the pulse pressure method*. *Annals of Biomedical Engineering*, 1994. **22**(4): p. 392-397.
141. Stergiopoulos, N., P. Segers, and N. Westerhof, *Use of pulse pressure method for estimating total arterial compliance in vivo*. Vol. 276. 1999. H424-H428.
142. Cappello, A., G. Gnudi, and C. Lamberti, *Identification of the three-element windkessel model incorporating a pressure-dependent compliance*. *Ann Biomed Eng*, 1995. **23**(2): p. 164-77.
143. Muthurangu, V., et al., *Measurement of total pulmonary arterial compliance using invasive pressure monitoring and MR flow quantification during MR-guided cardiac catheterization*. Vol. 289. 2005. H1301-H1306.
144. Westerhof, N., J.W. Lankhaar, and B.E. Westerhof, *The arterial Windkessel*. *Med Biol Eng Comput*, 2009. **47**(2): p. 131-41.
145. MacKenzie Ross, R.V., et al., *Decreased time constant of the pulmonary circulation in chronic thromboembolic pulmonary hypertension*, in *Am J Physiol Heart Circ Physiol*. 2013: United States. p. H259-64.
146. Attinger, E.O., *Pressure transmission in pulmonary arteries related to frequency and geometry*. *Circ Res*, 1963. **12**: p. 623-41.
147. Swift, A.J., et al., *Noninvasive estimation of PA pressure, flow, and resistance with CMR imaging: derivation and prospective validation study from the ASPIRE registry*. *JACC Cardiovasc Imaging*, 2013. **6**(10): p. 1036-47.
148. Galiè, N., et al., *Guidelines on diagnosis and treatment of pulmonary arterial hypertension: The Task Force on Diagnosis and Treatment of Pulmonary Arterial Hypertension of the European Society of Cardiology*. *European Heart Journal*, 2004. **25**(24): p. 2243-2278.
149. Orimadegun, A. and A. Omisanjo, *Evaluation of Five Formulae for Estimating Body Surface Area of Nigerian Children*, in *Ann Med Health Sci Res*. 2014: India. p. 889-98.
150. Katz, J., et al., *Estimation of right ventricular mass in normal subjects and in patients with primary pulmonary hypertension by nuclear magnetic resonance imaging*, in *J Am Coll Cardiol*. 1993: United States. p. 1475-81.
151. van de Veerdonk, M.C., et al., *Progressive right ventricular dysfunction in patients with pulmonary arterial hypertension responding to therapy*, in *J Am Coll Cardiol*. 2011, 2011 American College of Cardiology Foundation. Published by Elsevier Inc: United States. p. 2511-9.
152. Bradlow, W.M., et al., *Measuring the heart in pulmonary arterial hypertension (PAH): implications for trial study size*. *J Magn Reson Imaging*, 2010. **31**(1): p. 117-24.
153. Hagger, D., et al., *Ventricular mass index correlates with pulmonary artery pressure and predicts survival in suspected systemic sclerosis-associated pulmonary arterial hypertension*, in *Rheumatology (Oxford)*. 2009: England. p. 1137-42.
154. Marcus, J.T., et al., *Interventricular mechanical asynchrony in pulmonary arterial hypertension: left-to-right delay in peak shortening is related to right ventricular overload and left ventricular underfilling*, in *J Am Coll Cardiol*. 2008: United States. p. 750-7.
155. Dellegrottaglie, S., et al., *Pulmonary hypertension: accuracy of detection with left ventricular septal-to-free wall curvature ratio measured at cardiac MR*, in *Radiology*. 2007: United States. p. 63-9.
156. Grothues, F., et al., *Interstudy reproducibility of right ventricular volumes, function, and mass with cardiovascular magnetic resonance*. *American Heart Journal*, 2004. **147**(2): p. 218-223.
157. Lalkhen, A.G. and A. McCluskey, *Clinical tests: sensitivity and specificity*. *Continuing Education in Anaesthesia, Critical Care & Pain*, 2008. **8**(6): p. 221-223.

158. Azar, A. and S. El-Metwally, *Decision tree classifiers for automated medical diagnosis*. Neural Computing and Applications, 2013. **23**(7): p. 2387-2403.
159. Podgorelec, V., et al., *Decision Trees: An Overview and Their Use in Medicine*. Journal of Medical Systems, 2002. **26**(5): p. 445-463.
160. Khan, J., et al., *Classification and diagnostic prediction of cancers using gene expression profiling and artificial neural networks*. Nat Med, 2001. **7**(6): p. 673-9.
161. Dennis, A., et al., *Noninvasive diagnosis of pulmonary hypertension using heart sound analysis*, in *Comput Biol Med*. 2010, 2010 Elsevier Ltd: United States. p. 758-64.
162. Breiman, L., *Random Forests*. Machine Learning, 2001. **45**(1): p. 5-32.
163. Arlot, S. and A. Celisse, *A survey of cross-validation procedures for model selection*. Statistics Surveys, 2010. **4**: p. 40-79.
164. Bostanci, B. and E. Bostanci, *An Evaluation of Classification Algorithms Using Mc Nemar's Test*, in *Proceedings of Seventh International Conference on Bio-Inspired Computing: Theories and Applications (BIC-TA 2012): Volume 1*, C.J. Bansal, et al., Editors. 2013, Springer India: India. p. 15-26.
165. Leeflang, M.M., et al., *Bias in sensitivity and specificity caused by data-driven selection of optimal cutoff values: mechanisms, magnitude, and solutions*. Clin Chem, 2008. **54**(4): p. 729-37.
166. Ewald, B., *Post hoc choice of cut points introduced bias to diagnostic research*. Journal of Clinical Epidemiology, 2006. **59**(8): p. 798-801.
167. Olufsen, M., et al., *Numerical Simulation and Experimental Validation of Blood Flow in Arteries with Structured-Tree Outflow Conditions*. Annals of Biomedical Engineering, 2000. **28**(11): p. 1281-1299.
168. Weibel, E.R., *What makes a good lung?* Swiss Med Wkly, 2009. **139**(27-28): p. 375-86.
169. Kuntjoro, W., A.M.H.A. Jalil, and J. Mahmud, *Wing Structure Static Analysis using Superelement*. Procedia Engineering, 2012. **41**(0): p. 1600-1606.
170. Fagan, M.J., *Finite element analysis*. 1992, Harlow: Harlow : Longman Scientific & Technical, 1992.
171. Avolio, A.P., *Multi-branched model of the human arterial system*. Medical and Biological Engineering and Computing, 1980. **18**(6): p. 709-718.
172. O'Rourke, M.F. and A.P. Avolio, *Pulsatile flow and pressure in human systemic arteries. Studies in man and in a multibranched model of the human systemic arterial tree*. Circulation Research, 1980. **46**(3): p. 363-72.

APPENDIX

PUBLICATIONS LIST

JOURNAL ARTICLES

1. **A. Lungu**, A. Swift, D.Capener, D. Kielly, D.R. Hose, J. Wild, Diagnosis of Pulmonary Hypertension from MR image based computational models and decision tree analysis, [accepted **Pulmonary Circulation**, 2016]
2. P. Morris, A. Narracott, H. von Tengg-Kobligk, D.A Silva Soto, S. Hsiao, **A. Lungu**, P. Evans, N. W Bressloff, P. Lawford, D.R Hose, J.P Gunn· Computational Fluid Dynamics Modelling in Cardiovascular Medicine,[published **Heart**, v. **102**, 2015, p. **18-28**]
3. **A. Lungu**, J. Wild, A. Swift, D.Capener, D. Kielly, D.R. Hose, MRI model-based non-invasive differential diagnosis in pulmonary hypertension, [published **Journal of Biomechanics**, Volume **47**, Issue **12**, 2014, pp **2941-2947**]

CONFERENCE PROCEEDINGS AND ABSTRACTS

1. **A. Lungu**, A. Swift, D.Capener, D. Kielly , D.R. Hose, J. Wild, Diagnosis of pulmonary hypertension from MR image based computational models of pulmonary vascular haemodynamics and decision tree analysis, **European Respiratory Journal**, 2015. **46(suppl 59)**
2. A. Swift, **A. Lungu**, H.Walker, D.Capener, C. Hammerton, C.Elliot, R. Condliffe, D.Kiely, J.Wild, Improved diagnostic accuracy of MRI in patients with suspected pulmonary hypertension with combined right ventricle and pulmonary artery metrics, **European Respiratory Journal**, 2015. **46(suppl 59)**
3. A. Swift, **A. Lungu**, H.Walker, D.Capener, C. Hammerton, C.Elliot, R. Condliffe, D.Kiely, J.Wild, Estimation of mPAP with MRI in pulmonary hypertension subgroups: Comparison with echocardiography, **European Respiratory Journal**, 2015. **46(suppl 59)**

4. **A. Lungu**, J. Wild, A. Swift, D. Capener, D. Kielly, D.R. Hose, Automatic, simultaneous, non-invasive measurements of flow and area in the human pulmonary arteries from MRI images, **International conference on advancements of medicine and health care through technology, IFMBE Proceedings Volume 44, 2014, pp 259-264**

5. J. Peters, **A. Lungu**, F.M. Weber, I. Waechter-Stehle, D.R. Hose, J. Weese, Comparison of CFD-Based and Bernoulli-Based Pressure Drop Estimates across the Aortic Valve Enabled by Shape-Constrained Deformable Segmentation of Cardiac CT Images **Lectures Notes in Computer Science, Volume 8789, 2014, pp 211-219**

6. Le Luong, H. Duckles, T. Schenkel, N. Arnold, W. Gsell, **A. Lungu**, T. Spencer, D.R. Hose, I. Halliday, P. C. Evans, A pharmacological approach to promote shear stress-dependent anti-inflammatory mechanisms in arteries, **Arteriosclerosis, Thrombosis, and Vascular Biology, 2014. 34(Suppl 1): p. A258-A258**

Third party copyright permissions

1. Figure 1.1

Figure 1 from Kiely, D.G., et al., Pulmonary hypertension: diagnosis and management. BMJ, 2013. **346** with permission through Copyright Clearance Center's RightsLink service

Order Details

Licensee: Angela Lungu

License Date: Oct 22, 2015

License Number: 3734260780350

Publication: The BMJ

Title: Pulmonary hypertension: diagnosis and management

Type Of Use: Dissertation/Thesis

Total: 0.00 GBP

2. Figure 2.1 and Figure 2.3

Figure 14.9 a, cine phase contrast velocity mapping, page 299, Chapter 14 and Figure 12.28 True FISP sequence, page 247, Chapter 12, from Donald McRobbie, Elizabeth A. Moore, Martin J. Graves, Martin R. Prince, MRI from picture to proton

Dear Angela Lungu

Thank you for your request to reproduce two figures in your forthcoming PhD thesis, for non-commercial publication, in electronic format. Cambridge University Press are pleased to grant non-exclusive permission free of charge for this specific one time use, on the understanding you have checked that we do not acknowledge any other source for the figures.

Please ensure full acknowledgement appears in your work.

There is further information on our website at the following link:

<http://www.cambridge.org/about-us/rights-permissions/permissions/>

Yours sincerely

Claire Taylor

Senior Publishing Assistant

Cambridge University Press

University Printing House

Shaftesbury Road

Cambridge CB2 8BS

UK

3. Figure 2.11 a)

Figure 2 from Greenfield, J. C., and D. M. Griggs, 1963, Relation between pressure and diameter in main pulmonary artery of man: Journal of Applied Physiology, v. 18, p. 557-559

Permission requested through Copyright Clearance Center's RightsLink service for "reuse in a thesis/dissertation"



RightsLink®

Home

Account
Info

Help



Title: Relation between pressure and diameter in main pulmonary artery of man

Author: Joseph C. Greenfield, Douglas M. Griggs

Publication: Journal of Applied Physiology

Publisher: The American Physiological Society

Date: May 17, 0010

Copyright © 10, The American Physiological Society

Logged in as:
Angela Lungu
Account #:
3000968204

LOGOUT

Permission Not Required

Permission is not required for this type of use.

BACK

CLOSE WINDOW

Copyright © 2016 Copyright Clearance Center, Inc. All Rights Reserved. [Privacy statement](#). [Terms and Conditions](#).
Comments? We would like to hear from you. E-mail us at customer@copyright.com

4. Figure 2.11 b)

Figure 1 from Jarmakani, J.M.M., et al., In Vivo Pressure-Radius Relationships of the Pulmonary Artery in Children with Congenital Heart Disease. *Circulation*, 1971. **43**(4): p. 585-592. with permission through Copyright Clearance Center's RightsLink service

Order Details

Licensee: Angela Lungu

License Date: Oct 22, 2015

License Number: 3734260501062

Publication: *Circulation*

Title: In Vivo Pressure-Radius Relationships of the Pulmonary Artery in Children with Congenital Heart Disease

Type Of Use: Dissertation/Thesis

Total: 0.00 USD

5. Figure 2.11 c) and Figure 2.12 b)

Figure 1 and Figure 3 from Hunter, K.S., et al. In vivo measurement of proximal pulmonary artery elastic modulus in the neonatal calf model of pulmonary hypertension: development and ex vivo validation. *J Appl Physiol* (1985), 2010. **108**, 968-75 DOI: 10.1152/jappphysiol.01173.2009.

Permission requested through Copyright Clearance Center's RightsLink service for "reuse in a thesis/dissertation"



RightsLink®

Home

Account
Info

Help



Title: In vivo measurement of proximal pulmonary artery elastic modulus in the neonatal calf model of pulmonary hypertension: development and ex vivo validation

Author: Kendall S. Hunter, Joseph A. Albiez, Po-Feng Lee, Craig J. Lanning, Steven R. Lammers, Stephen H. Hofmeister, Philip H. Kao, H. Jerry Qi, Kurt R. Stenmark, Robin Shandas

Publication: Journal of Applied Physiology

Publisher: The American Physiological Society

Date: Apr 1, 2010

Copyright © 2010, The American Physiological Society

Logged in as:

Angela Lungu

Account #:
3000968204

LOGOUT

Permission Not Required

Permission is not required for this type of use.

BACK

CLOSE WINDOW

Copyright © 2016 Copyright Clearance Center, Inc. All Rights Reserved. [Privacy statement](#). [Terms and Conditions](#).
Comments? We would like to hear from you. E-mail us at customercare@copyright.com